Sensors and actuators for the cochlear implant using inherently conducting polymers

Yanzhe Wu
University of Wollongong

SENSORS AND ACTUATORS FOR THE COCHLEAR IMPLANT USING INHERENTLY CONDUCTING POLYMERS

A thesis submitted in fulfilment of

the requirements for the award of the degree

DOCTOR OF PHILOSOPHY

from

UNIVERSITY OF WOLLONGONG

by

YANZHE WU, BSc (HONS), MSc

Intelligent Polymer Research Institute

Department of Chemistry

June 2006

To my parents for their endless love.

To my wife Yun Dai for her support and patience.

CERTIFICATION

I, Yanzhe Wu, declare that this thesis, submitted in fulfilment of the requirements for the award of Doctor of Philosophy, in the Department of Chemistry, University of Wollongong, is wholly my own work unless otherwise referenced or acknowledged. The document has not been submitted for qualifications at any other academic institution.

Yanzhe Wu

June 2006

ACKNOWLEDGEMENTS

Sincere gratitude is given to my supervisors Prof. Gordon Wallace, Dr. Dezhi Zhou and Prof. Geoff Spinks for supervision throughout this work. Their guidance and support will not be forgotten in my life.

I would particularly give thanks to Dr. Chee O. Too for his guidance and advice, to Dr. George Tsekouras for his careful proof reading and help on the first draft of this thesis.

I greatly appreciate the help and friendship from all colleagues in IPRI. In particular I would like to thank Dr. Simon Moulton, Dr. Peter Innis, Dr. Violeta Misoska, Dr. Philip Whitten, Dr. Jun Chen, Dr. Jie Ding, Jakub Mazurkiewicz, Scott McGovern, Adrian Gestos, Vahid Motaghitalab, Dr. Jian Wu, Dr. Jiazhao Wang, Jenny Causley, Dr. Mark Imisides and Dr. Carol Lynam for their unforgotten help in the laboratory and in proof-reading of this thesis.

I would also like to thank Dr. Gursel Alici from Mechanical Materials & Mechatronics, UoW, Claudiu Treaba and Peter Gibson from Cochlear Corp., Carrie Newbold and Bob Cowan from the Cooperative Research Centre for their help and advice.

Finally I am grateful to the Intelligent Polymer Research Institute and the Cooperative Research Centre for Cochlear Implant and Hearing Aid Innovation for the award of the postgraduate scholarship.

.

PUBLICATIONS

1. Wu, Y., Alici. G., Spinks, G.M., and Wallace, G.G., "Fast trilayer polypyrrole bending actuators for high speed applications", *Synthetic Metals*, Submitted.
2. Wu, Y., Zhou, D., Spinks, G.M., Innis, P.C., Megill, W.M. and Wallace G.G., "TITAN: A conducting polymer based microfluidic pump", *Smart Mater Struct* 14 (2005) 1511-1516.
3. Wu, Y., Moulton, S. E., Too, C.O., Wallace, G. G., and Zhou, D., "Use of inherently conducting polymers and pulsed amperometry in flow injection analysis to detect oligonucleotides" *Analyst*, 129 (2004) 585-588.
4. Spinks, G.M., Zhao, L., Li, W., Wu, Y., Zhou, D., Wallace, G.G., "Synthesis, modelling and characterization of conducting polymers", *SPIE International Symposium on Smart Materials, Nano-, and Micro-Smart Systems*, Sydney, Australia, Dec 2004.
5. Li, W., Spinks, G.M. Zhao, L., Wu, Y., Zhou, D., Wallace, G.G., "Characterisation of conducting polymer based bimorph vibration sensors", *SPIE International Symposium on Smart Materials, Nano-, and Micro-Smart Systems*, Sydney, Australia, Dec 2004.
6. Wu, Y., Moulton, S.E., Too, C.O., Wallace, G.G., and Zhou, D., "Detection of Oligonucleotides: Polypyrrole - Oligonucleotide Modified Electrodes Using a Pulsed Potential Method", *The International Conference on The Science and Technology of Synthetic Metals*, University of Wollongong, Australia, July 2004.

7. Wu, Y., Zhou, D., Wallace, G.G., Spinks, G.M., Cowan, R., and Newbold, C., "Polypyrrole/PVDF Laminates as Mechanical Sensor", *26th Australasian Polymer Symposium*. Noosa, Australia, July 2003.

8. Zhou, D, Wallace, G.G., Spinks, G.M., Wu, Y., Cowan, R., and Newbold, C., "High Performance Polypyrrole Based Electromechanical Actuators", *26th Australasian Polymer Symposium*. Noosa, Australia, July 2003.

ABSTRACT

This study considered the use of various inherently conducting polymer (ICP)-based devices for utilisation with the cochlear implant. Investigations centred on the use of polypyrrole (PPy) to produce a mechanical sensor, actuators and controlled release devices. The development of a novel force sensor using the electrodes that are an integrated part of the cochlear implant itself was also investigated.

Investigation into mechanically induce electrical signals using PPy-based mechanical sensors showed that the polarity of the voltage output was dependent on the dopant ion in the conducting polymer. In addition, it was found that the signal amplitude was related to the redox state of the PPy and the concentration of mobile dopant ions within the PPy. This led to the "stress induced ion flux" mechanism being proposed for the first time to explain such observations.

Actuator systems developed in this study included a PPy trilayer bending actuator, a PPy microfluidic pump and a PPy-coated hollow fibre. The study of PPy trilayer actuators led to several findings including a high amplitude harmonic vibration using a PPy/TFSI trilayer actuator, the first time that such behaviour has been observed for ICP-based mechanical actuators. A study of the blocking forces generated using such actuators in ionic liquid electrolytes suggested that switching from cathodic contraction to cathodic expansion occurs under the application of reducing potentials. This switching behaviour was found to depend on the amplitude and time of the electrochemical stimulation employed. It was shown that the expulsion of the dopant anion (PF_6^-) from the reduced polymer (- 0.8 V *vs.* Ag/Ag^+) did not support the previously claimed cathodic expansion model.

An ion diffusion controlled mechanism was proposed to explain the results obtained.

Investigations into the novel “tube in tube actuator nodule” (TITAN) microfluidic pump based on PPy had led to the significant finding that, for the first time, the intrinsic resistance of PPy can be utilised to carry out peristaltic actuation for the purpose of fluid transport.

The electrochemically controlled release of a model anion from the internal volume of a PPy-coated platinised PVDF hollow fibre was successfully demonstrated. Such controlled release was ascribed to the electrochemically activated incorporation / expulsion of small anions upon redox switching of polypyrrole resulting in enhanced ion transport across the concentration gradient from the internal volume of the hollow fibre to the receiving solution. The experimental findings suggested that electrochemically controlled release of anionic drugs is a real possibility using a device configuration consisting of a reservoir coated with an ICP membrane.

By studying the electrochemical impedance changes in response to impact forces on the tip of a cochlear implant in artificial perilymph solution, it was found that the cochlear implant electrode itself can be used to detect impact forces. The findings were significant because such an approach provides a simple and safe method for the detection of possible dangers during surgical implantation of the cochlear implant. Factors influencing the response were investigated and these included solution composition and the orientation of the impact forces encountered.

ABBREVIATIONS

A	Ampere
A^-	Anion
AC	Alternating current
ACN	Acetonitrile
Ag/Ag^+	Silver/silver ion reference electrode
Ag/AgCl	Silver/silver chloride reference electrode
$BMI.BF_4$	1-Butyl-3-methyl-imidazolium tetrafluoroborate
C	Coulomb
C_{dl}	Double layer capacitance
cm	Centimetre
conc.	Concentration
CV	Cyclic voltammetry
D	Diffusion coefficient
DBS^-	Dodecylbenzene sulfonate
e^-	Electron
E	Potential
E_{app}	Applied potential
EC	Electrochemical/Electrochemistry
EE	Electrochemical efficiency
EE_{ox}	Electrochemical efficiency during oxidation process

EE_{red}	Electrochemical efficiency during reduction process
E_f	Final potential
E_i	Initial potential
EIS	Electrochemical impedance spectroscopy
E_{lower}	Lower limit potential
EMI.TFSI	1-ethyl-3-methylimidazolium (bis) trifluoromethanesulfonimide
E_p	Peak potential
E_{pa}	Anodic peak potential
E_{pc}	Cathodic peak potential
E_{upper}	Upper limit potential
F	Faraday constant
g	Gram
i	Current
i_p	Peak current
i_{pa}	Anodic peak current
i_{pc}	Cathodic peak current
iR	Ohmic drop
L	Litre
M	Molar
mA	Milliampere
min	Minute
ml	Millilitre

mV	Millivolt
n	Number of electrons
PAn	Polyaniline
PC	Propylene carbonate
PF_6^-	hexafluorophosphate
PPy	Polypyrrole
PPy/Cl	Polypyrrole chloride
PPy/ClO_4	Polypyrrole perchlorate
PPy/NO_3	Polypyrrole nitrate
PPy/DBS	Polypyrrole Dodecylbenzenesulfonate
PPy/PF_6	Polypyrrole hexafluorophosphate
PPy/*p*TS	Polypyrrole p-toluene sulphonate
PVDF	Polyvinylidene fluoride filter membrane
Pt	Platinum
*p*TS.Na	p-toluene sulphonic acid sodium salt
Q	Charge
R	Gas constant
R	Resistance
R_s	Solution resistance
R_p	Polarisation resistance
s	Second
S	Siemens
t	Time

T	Temperature
TBAP	Tetrabutylammonium perchlorate
$TBA.PF_6$	Tetrabutylammonium hexafluorophosphate
$TFSI^-$	(bis) trifluoromethanesulfonimide
V	Volt
μ	Micro (prefix)
υ	Scan rate
X^+	Cation

LIST OF FIGURES AND TABLES

1. FIGURES

2. TABLES

CONTENTS

CHAPTER 1 GENERAL INTRODUCTION

1.1 MOTIVATION

Micro mechanical sensors and actuators have become of interest in the development of the next generation of medical implants including cochlear implant electrodes. Inherently conducting polymers (ICPs) provide some interesting possibilities in this regard.

ICPs are polymers capable of conducting electricity and have the ability to sense and actuate, leading many researchers to envisage "Intelligent Polymer Systems" based on ICPs [1]. The following sections present a review of the cochlear implant, the need for mechanical sensors and actuators and the motivation for the study of ICP based devices.

1.1.1 BACKGROUND OF THE COCHLEAR IMPLANT

The cochlear implant represents a successful biomedical device. It has provided the opportunity to hear for severely to profoundly deaf children and adults. This is achieved through direct stimulation of the hearing nerve via an array of electrodes (Figure 1-1). The external sound is picked up by the microphone and converted / encoded by the speech processor to electrical signals according to specific sound coding strategies. This electrical signal is then packaged by radio wave to transmit a signal through the skin to the implanted receiver. Finally, a multichannel electrode array is used to electrically stimulate the different auditory nerve fibres at different places in the cochlear resulting in speech perception in the human brain [2].

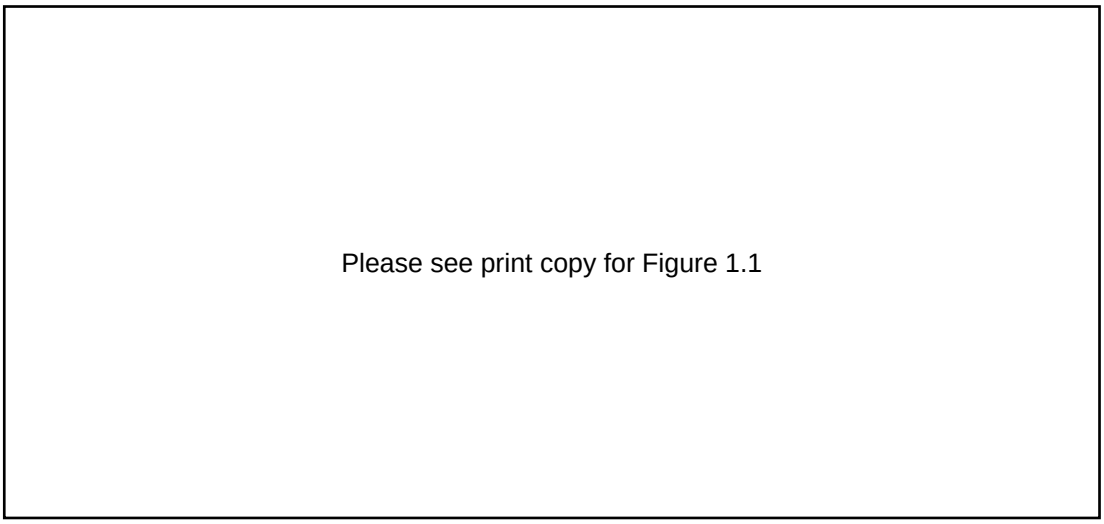

Figure 1-1 The cochlear implant consists of a speech processor and a cochlear implant electrode in order to create the sensation of sound in severely to profoundly deaf people [2].

The breakthrough in research on the cochlear implant was made in 1982 by Clark and co-workers at the University of Melbourne, Australia, who first made meaningful sound available to profoundly deaf adults using a multichannel electrode [3]. The invention of the multichannel electrode was motivated from a frequency analysis theory, called place theory [4]. According to Georg von Bekesy's pioneering work in the 1950s [4], place theory states that low frequency sounds cause the basilar membrane to vibrate with larger amplitudes of displacement at the apex of the membrane, while high frequency sounds cause the largest amplitude of displacement at the base of the basilar membrane (near the stapes). Complex sounds would then be decomposed into their frequency components along the inner ear turns where the hair cells were organised at different places according to the frequency at which they were most sensitive. For multichannel implants, the electrodes near the base of the cochlear are stimulated with high-frequency signals, while electrodes near the apex are stimulated with low-frequency signals, thereby allowing complex sounds to be decoded using different

strategies (F0/F2 [3, 5], F0/F1/F2 [6] and MPEAK [7, 8]) and allowing the exploitation of various stimulation methods (bipolar, pulsatile) [4].

The Cochlear Nucleus® 22 electrode consists of 22 pure platinum ring electrodes. Every ring electrode is 0.3 mm wide and spaced at 0.45 mm intervals with each connected to a Pt/iridium leadwire. All of the electrodes are embedded in a soft silicone body to form a well-defined electrode array. The electrode is tapered from a diameter of 0.6 mm at the base to a tip diameter of 0.4 mm at the tip [9]. Unlike the straight Cochlear Nucleus® 22 electrode, the Nucleus ® 24 Contour™ Electrode Array utilises a pre-curled structure. The aim of such a structure is to exploit the possible benefit of closer proximity to the modiolus that resides in the cochlear, since individual electrodes placed at appropriate positions close to the spiral ganglion cells can reduce stimulus threshold and provide more discrete neural excitation with wider dynamic range at lower power consumption [10, 11].

1.1.2 THE NEED FOR SENSORS AND ACTUATORS

During surgical implantation, highly experienced surgeons and complicated and delicate insertion operations are normally required in order to avoid possible insertion trauma to the fragile cochlear structure. This would result in the loss of residual hearing and impaired implant performance [10]. Kennedy [12] has suggested that any insertion trauma would be mainly ascribed to the impact of electrode tip, the upward displacement of the proximal electrode, and accidental insertion into the scala media or scala vestibuli as illustrated in Figure 1-2. Recent experimental results [10] using the Nucleus® 24 Contour™ electrode suggest that the above risks remain, and so the development of sensors and/or actuators designed to reduce insertion risks would be advantageous.

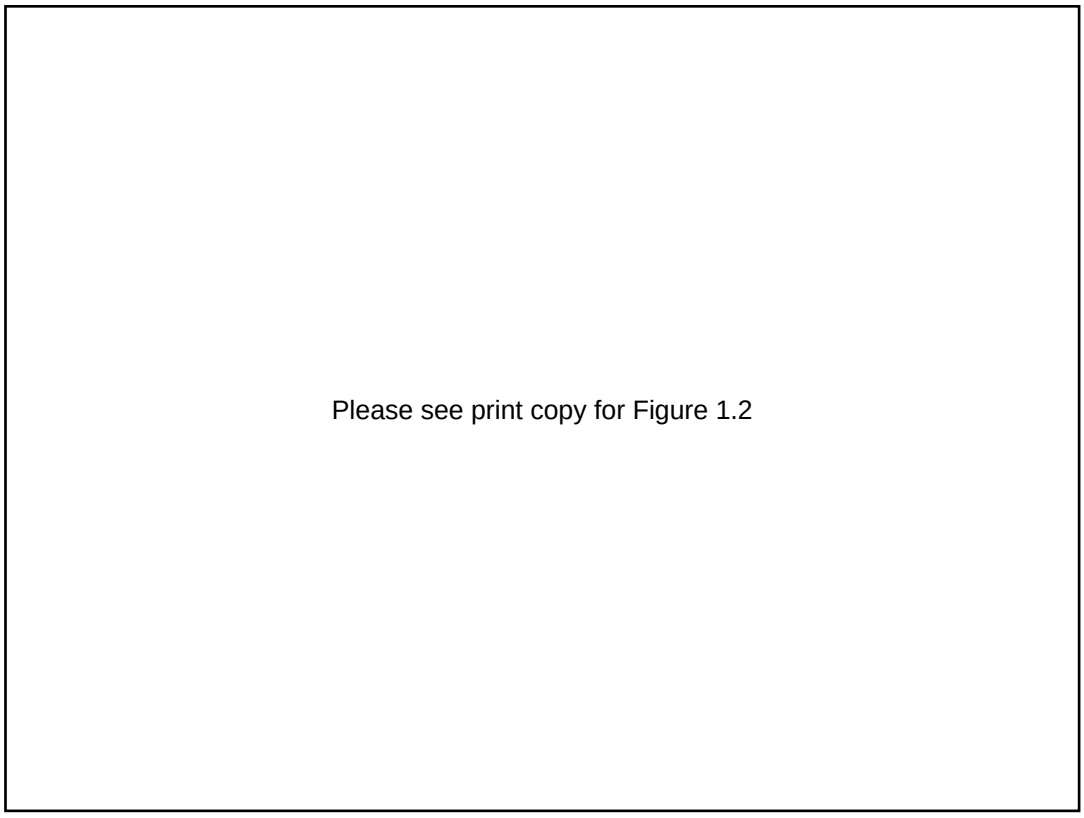

Figure 1-2 Schematic illustrating insertion trauma that may occur during the surgical implantation of the cochlear implant. A. The electrode tip tears the spiral ligament in the lower basal turn, B. The tear has increased and there is slight upward movement of the basilar membrane, C. The electrode tip has met resistance against the outer wall in the upper basal turn causing slight buckling of the electrode, further tearing of the spiral ligament, and upward dislocation of the osseous spiral lamina and basilar membrane [12].

Current approaches to avoid the occurrence of insertion trauma during implantation of the cochlear implant involve improvements in the surgical insertion technique. For the straight ring electrode array, it was suggested that the insertion should be via the antero inferior opening and that twisting of the electrode anticlockwise should be enacted if an insertion resistance was encountered by the surgeon [13]. For the pre-curled Nucleus® 24 Contour™ electrode (Figure 1-3, a), the insertion would be more difficult because the pre-curled electrode is straightened by a platinum stylet for ease

of insertion and this stylet needs to be withdrawn following insertion to allow the electrode array to adopt the required shape in the cochlea. It was suggested that the insertion of the Nucleus® 24 Contour™ electrode should be into the scala tympani and a partial removal of the stylet (1-2 mm) should be considered before full insertion if resistance is encountered during insertion (Figure 1-3, b) [10]. The use of an injection type of insertion technique in conjunction with an electrode array called the Advance Off-Stylet™ (AOS™) has been advocated [14]. This modified version of the Nucleus® 24 Contour™ electrode utilises a soft material at the very end of the tip to minimise impact force and guide the advance of the implant electrode [14].

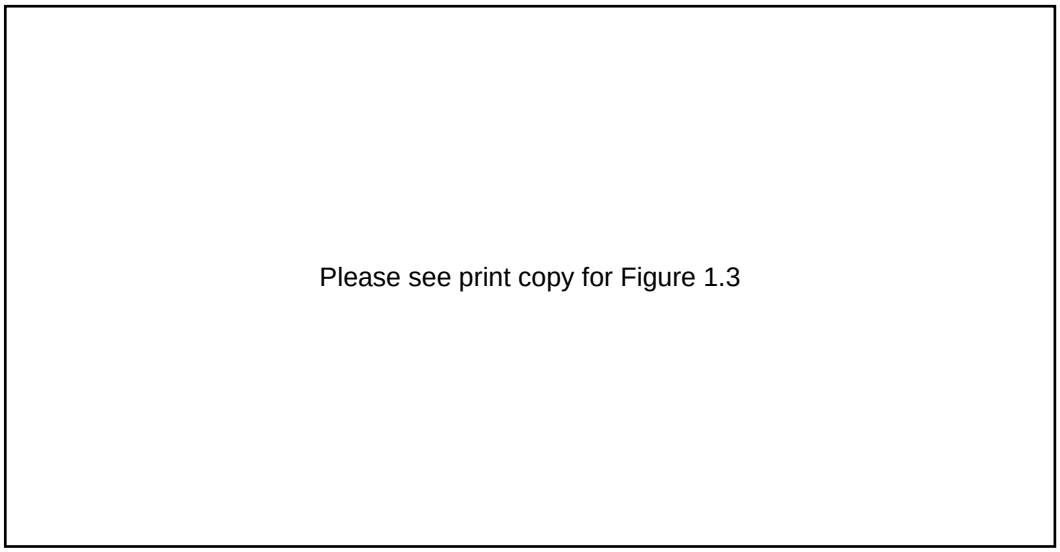

Figure 1-3 the Nucleus® 24 Contour™ electrode. (a) the pre-curled electrode, (b) the pre-curled electrode straightened by a platinum stylet for ease of insertion and the suggested alternative technique if resistance is felt during surgical implantation [10].

Besides improvements in surgical insertion techniques, a long term approach to solving the problem of insertion trauma would be to integrate micro sensors and actuators into the cochlear implant. A micro mechanical sensor could be used to monitor the possible danger of impact and frictional

force to the fragile cochlear structure and provide a feedback mechanism for the controlled steering of the cochlear implant electrode using a micro actuator. The micro actuator would also be used for precise placement of the electrode for better proximity to the modiolus where the auditory neurons reside.

It has been noted that, in some patients after long term implantation, implant performance decreases. This might be attributed to the continuous electrical stimulation resulting in deterioration of the residual auditory nerve cells, discouraging growth and resulting in further loss of hearing [15]. However, this may be minimised with the integration of actuators capable of the controlled release of drugs to encourage the outgrowth of auditory nerve cells. Growth of spiral ganglion cells can be facilitated by providing neurotrophic factors [16] as shown by in vitro or in vivo animal experiments, respectively. Inherently conducting polymers (ICPs) represent a very promising class of materials that have the potential to be utilised as micro sensors or micro actuators for the cochlear implant.

1.1.3 WHY INHERENTLY CONDUCTING POLYMERS?

Candidate materials for possible micro sensors and micro actuators for utilisation in the cochlear implant must provide several functions and be able to do so when scaled down to micro dimensions. Although a number of classes of materials are capable of providing one or more functions, it is considered that only ICPs have the possibility to meet all of them, especially at the micro scale. ICP-based actuators can generate stresses and strains higher than or comparable to natural skeletal muscle [17, 18]. Based on this, a micro actuator / robot for biomedical application has already been demonstrated [19, 20]. ICPs also show an ability to convert mechanical energy to electricity [21], a property that can be utilised in mechanical

sensors. Moreover, the use of ICPs for controlled drug release has been demonstrated by a number of researchers [22-24]. In these respects, ICP based "Intelligent Polymer Systems" that possess the ability to sense, process information and actuate based on a feedback mechanism [1] have been envisaged.

In this Chapter, ICPs, as well as sensors, actuators and controlled release devices based on them are reviewed. Previous work on micropumps and micro-mechanical sensors using other materials and technologies are reviewed separately in the introduction sections of Chapter 5 and Chapter 7.

1.2 INHERENTLY CONDUCTING POLYMERS

ICPs are materials that exhibit electrical conductivity approaching that of metals. The discovery of ICPs by Shirakawa, MacDiarmid and Heeger [25-27] in 1977, led to the Nobel Prize in Chemistry in the year 2000. They first discovered that, upon exposure to halogen vapours, polyacetylene films increased in electrical conductivity (σ) by 10^9 times to as high as 10^5 $S.cm^{-1}$ [28]. Such conductivities are even higher than that of mercury ($\sim 1.04 \times 10^4$ $S.cm^{-1}$) and comparable to that of copper ($\sim 5.65 \times 10^5$ $S.cm^{-1}$). Following this discovery, many ICPs (with a common π-conjugated structure) have been discovered, including polypyrrole (PPy) [24, 29-33], polyaniline (PAn) [31, 34-37] and polythiophene (PTh) [38-40] (Figure 1-4).

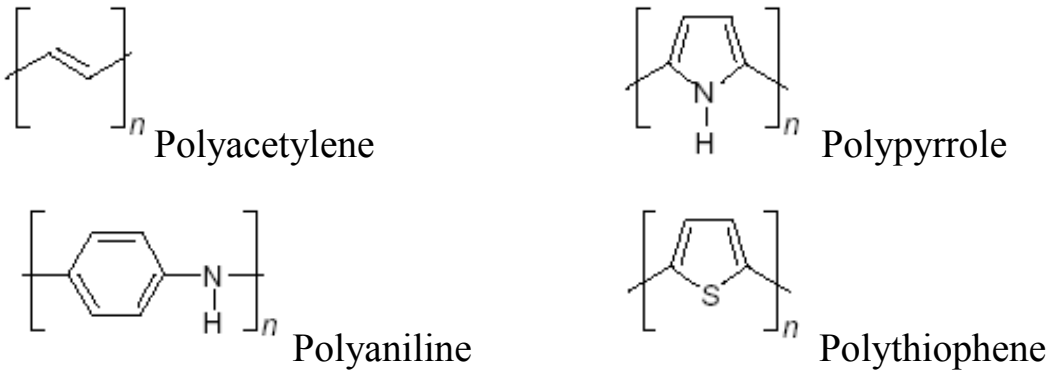

Figure 1-4 Chemical structures of selected π-conjugated inherently conducting polymers (ICPs) in the dedoped form.

Due to their unique electrical, chemical and physical properties, ICPs have found many applications in different areas, including chemical sensors [41-43], composite membranes for gas separations [44-47], rechargeable batteries [30, 38, 48-50], electrochromic displays [51, 52], light emitting devices [53-57], electrocatalysts [58-60], electromagnetic interfence shielding [61, 62], mechanical actuators [63-70] and controlled drug release [22, 24, 71].

Electrical conduction in ICPs is achieved through a unique oxidised π-conjugated system in which mobile charge carriers are created. Such charge carriers are radical cations, called polarons that are partially delocalised across ~ 3-4 monomer units. When enough electrons are removed, the polaron concentration gets high enough that special dications, called bipolarons, form in place of individual polarons. Bipolarons are energetically more favourable than the separated polaronic states [72, 73], as shown in Figure 1-5 (taking PPy as an example). Polarons and bipolarons are mobile in an electric field and are responsible for the electrical conduction properties of ICPs.

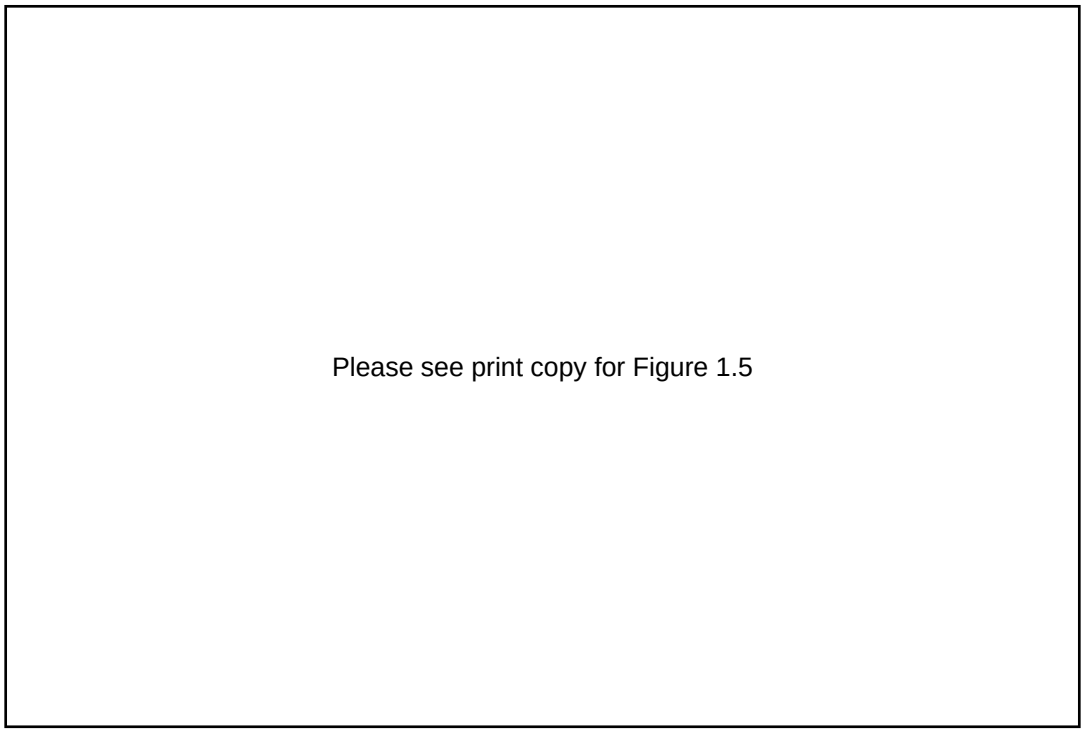

Figure 1-5 Schematic showing the formation of polaron and bipolaron states in PPy [72, 73].

The positive charge in the polaron and biopolaron states is stabilised by negatively charged counter ions, incorporated in close vicinity. In this unusual charge transport structure, all charged dopants are spatially removed from the quasi-one-dimensional conduction pathway [74-77], so that the resistive back scattering of electrons is reduced and this leads to a theoretical conductivity of up to 2×10^{7} S.cm^{-1}, which is far higher than the conductivity of metals such as copper [78]. However, in real situations, individual polymer chain lengths of ~ 100 – 1000 monomer units [79] would be too short to allow electrical conduction over appreciable distances. In addition, almost all ICPs prepared either chemically or electrochemically inevitably have defects that lead to the loss of conjugation. Therefore, an inter chain charge hopping mechanism [80, 81] has been proposed to explain the discontinuous charge transport in ICPs. In this mechanism, the electrical conduction between two terminated chains is achieved by the

hopping of mobile charge carriers (e.g. polarons, bipolarons) from one polymer chain on to adjacent chains. Chain defects reduce the electrical conductivity of ICPs to generally less than 1000 $S.cm^{-1}$ and the inter chain charge hopping mechanisms also explains why the electrical conductivity of ICPs generally increases with temperature, which is opposite to the behaviour observed for metals.

Among the available ICPs, PPy is attractive since it has relatively high mechanical strength (tensile strength at break: 18-33 MPa [82-85]), is stable in air, electroactive in both organic and aqueous solutions, and especially suitable for use in physiological environments [33]. PPy is easy to prepare via chemical or electrochemical oxidation of the monomer in solution. Incorporation of wide range of dopants is possible giving rise to polymers with varying properties. In particular, PPy has been identified as a non-toxic, potentially biocompatible material for the immobilisation of biologically active molecules, such as enzymes, antibodies, receptors, or even whole living cells [33, 86, 87]. Microrobots using PPy-Au bilayer actuators have been used to move and position other microcomponents such as bioentities [19, 20, 88]. Strain gauges and pressure sensors using PPy for biomedical applications have been constructed [89, 90]. The use of PPy as a model ion gate membrane for controlled drug delivery has also been demonstrated [91, 92].

PPy can be synthesised by chemical [93, 94] or electrochemical polymerisation [95, 96]. Both processes involve the incorporation of anionic species into the oxidised polymer. Chemical polymerisation generally involves mixing the pyrrole monomer with chemical oxidant in a suitable solvent or in the vapour phase. On the other hand, electrochemical polymerisation is carried out by oxidising pyrrole monomer in a supporting electrolyte at a suitable anode. The formation of PPy at an anode undergoes

several electrochemical steps, as shown in Figure 1-6. Generally, the first step involves the electrochemical oxidation of the monomer to form a delocalised radical cation. The next step is dimerisation of the monomer radicals, which occurs via radical-radial coupling at the α position and accompanied by the expulsion of two H^+ ions to leave the neutral dimer. Chain propagation then proceeds via electrochemical oxidation of the neutral dimer to form the dimer radical cation since the neutral dimer and higher molecular weight oligomers oxidise more easily than the neutral monomer [97, 98]. The radical dimer can combine chemically with other monomeric, dimeric or oligometric radical cations to extend the chain. Chain growth is generally terminated when the radical cation of the growing chain becomes too unreactive or more likely when the reactive end of the chain becomes sterically hindered from further reaction [99].

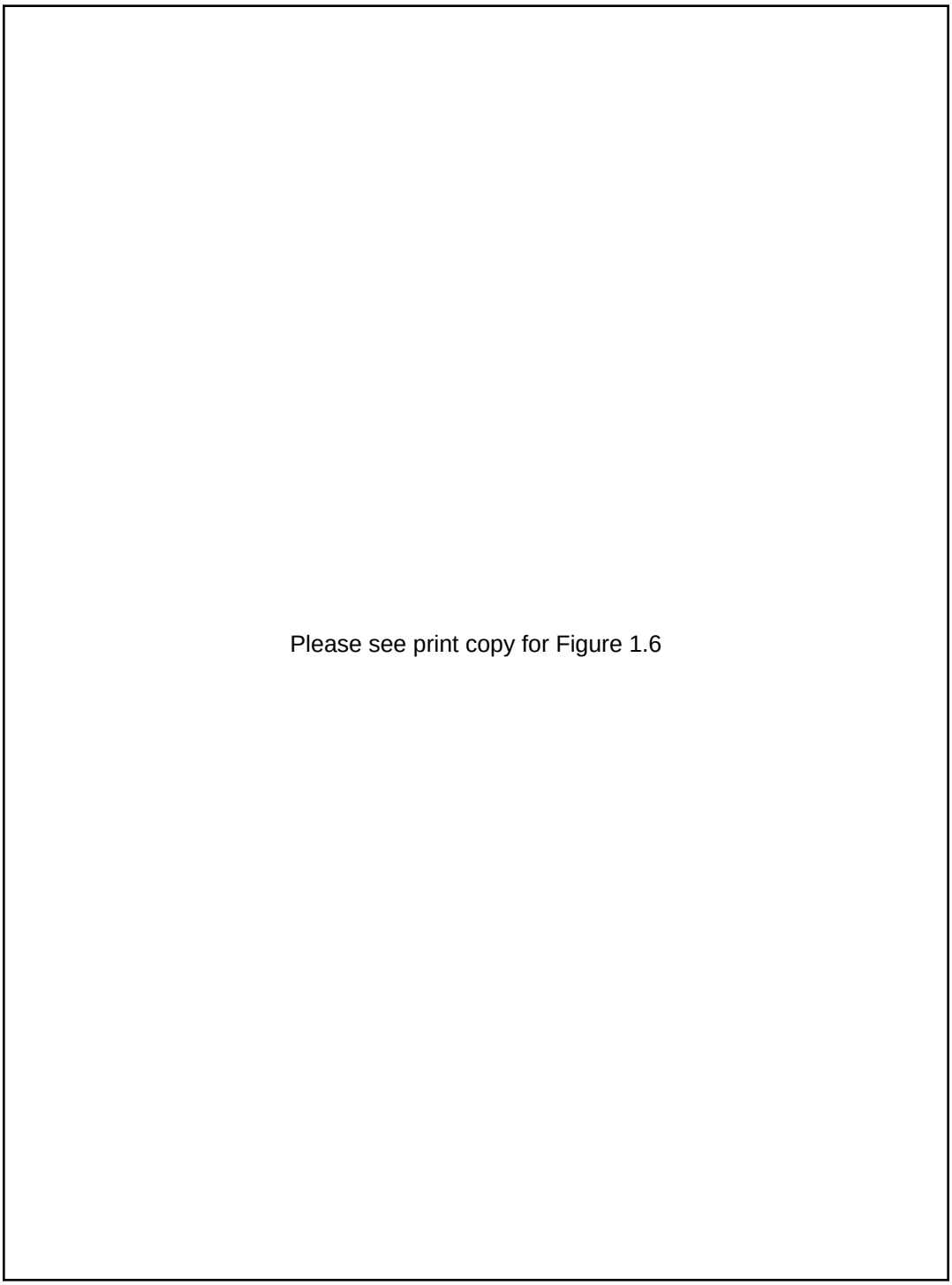

Figure 1-6 Mechanism of the electrochemical polymerisation of pyrrole to form PPy [100].

The electrochemical polymerisation method is versatile and provides a simple, clean and efficient route to prepare PPy and allows the incorporation of a great range of dopant from inorganic [101], organic [102, 103] to biological species [33, 104, 105] even live cells [86]. For the electrochemical polymerisation method, the rate and extent of the polymerisation reaction can be carefully controlled by the choice of appropriate electrochemical conditions. In addition, electrical, chemical and physical properties of the resulting polymer can be controlled by the electrochemical conditions employed during synthesis [106]. Therefore, electrochemical polymerisation has been extensively employed in this study.

The nature of the solvent used is critical in that it can affect the morphology, conductivity, electroactivity and other chemical and physical properties of the polymer film [106]. Ideally, the solvent should possess a high dielectric constant, low viscosity and allow the monomer and supporting electrolyte to be dissolved readily. The best polymers are generally prepared from non-nucleophilic solvents [106] since nucleophilic solvents would react with the monomeric, dimeric and oligomeric radical cation intermediates of the polymerisation reaction and quickly terminate chain growth. Acetonitrile and propylene carbonate have proved useful in this regard [106]. However, electrochemical polymerisation promotes rapid pyrrole protonation and hence to improve the quality of electrodeposited polymer, a small amount of water is normally added to non-nucleophilic solvents [107]. Water itself has also been extensively used as the solvent for the electrochemical preparation of PPy since it has the ability to dissolve a much wider range of electrolytes (such as biomolecules) compared to organic solvents. However, studies have shown that PPy films prepared from water have conductivities that are typically one order of magnitude lower than those grown form acetonitrile or propylene carbonate [106].

PPy can be switched between the oxidised and reduced states allowing dynamic control of electrical, chemical and mechanical properties. Generally small anionic species are incorporated in the oxidised state and expelled in the reduced state in order to maintain charge neutrality (Equation 1-1). However, in the case of bulky and immobile dopants, charge neutrality would be achieved via the incorporation of cations from the electrolyte upon reduction (Equation 1-2). With further oxidation, the expulsion of cations or addition of anions would occur. In most cases a combination of both processes occurs. The dominant process would depend on how firmly the anions are trapped in the polymer, and how easily the cations could enter the polymer.

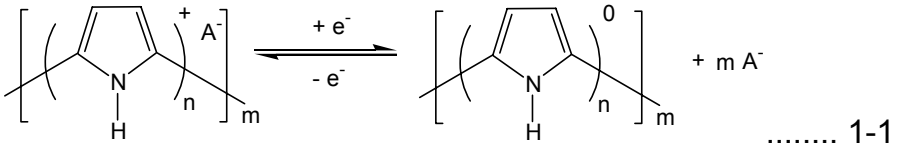

..... 1-1

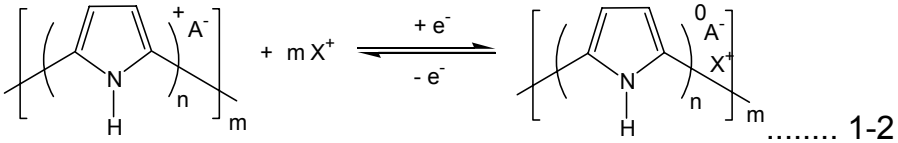

..... 1-2

Where A^- is the dopant anion incorporated into the PPy during synthesis, X^+ represents a cation from the electrolyte, n is the number of pyrrole units for each A^- incorporated, and m is the numbers of PPy repeat units that determine the molecular weight of polymer.

To achieve a higher performance in devices based on the ICP electrochemical switching properties, electrolyte systems that provide mobile ions in a supporting liquid environment are extremely important. Large electrochemical window (> 1V), high ionic conductivity ($>10^{-4}$ $S.cm^{-1}$), fast ion mobility during redox switching ($>10^{-14}$ $m^2V^{-1}S^{-1}$), low

volatility and environmental stability are generally preferred [108]. However, the use of aqueous electrolyte systems is limited by the intrinsic narrow electrochemical potential window and the high volatility of water. Nonaqueous electrolytes such as that using propylene carbonate have a broader electrochemical potential window (-1.9 to +1.7V *vs.* saturated calomel electrode), but in general those systems are still susceptible to evaporation [108]. In comparison, ionic liquids represent an ideal electrolyte system that could potentially meet all of above requirements. Ionic liquids are pure salts that exist as liquids at room temperature. The existence of the electrostatic attraction between the cations and anions means an intrinsic lack of measurable vapour pressure. They are therefore non-volatile, non-flammable, and have high thermal stability. Moreover, the large variety of available cations and anions provide ionic liquids with tailored properties desirable for specific applications [109-111], such as to enhance electrochemical stability of ICP based devices [112]. The exceptional enhanced cycle life - up to 1 million cycles without failure has been demonstrated for a polyaniline based electrochromic device using ionic liquid 1-butyl-3-methyl-imidazolium tetrafluoroborate ($BMI.BF_4$) [108] and up to 6000 cycles with only 17% decrease in measured displacement has also been demonstrated for a polypyrrole based electrochemical mechanical actuator system with the use of 1-butyl-3-methyl-imidazolium hexafluorophosphate ($BMI.PF_6$) [108].

The incorporation and expulsion of ionic species (either from normal electrolyte system or ionic liquid) during the electrochemical switching process results in considerable volume changes, which form the basis of ICP mechanical actuators. It also results in ion exchange between the polymer and the surrounding solution forming the basis of electrochemically controlled release of ionic drugs using ICPs. Moreover, such switching

properties are also responsible for electrical signal generation in ICP mechanical sensors. The following sections considers advances in the fields of ICP based mechanical actuators, controlled release devices using ICPs and ICP based mechanical sensors.

1.3 CONDUCTING POLYMER MECHANICAL ACTUATORS

The mechanical work produced from ICP actuators is based on the volume change related to the electrochemical switching process. In general and where relatively small and mobile anions are considered, an applied oxidising potential leads to the removal of electrons from the polymer backbone and induces a conformational change to accommodate the anions in order to maintain electrical neutrality. The positive charges on the polymer backbone provide coulombic repulsion forces between polymer chains to allow conformational changes. Following conformational changes, the penetration of anions (often solvated) occurs from the supporting electrolyte solution. If solvent molecules are also associated with anions, then electroosmotic interactions occur. Conformational change and the incorporation of anions and solvent molecules all contribute to the overall volume increase upon oxidation of PPy. Under reducing potentials, electrons are injected to neutralise the positively charged polymer backbone, leading to the cancellation of attractive forces of the polymer chains to the anions and solvent molecules. At the same time, electrostatic repulsion forces disappear allowing conformational changes to occur. As a result of these processes, anions and solvent molecules diffuse out of the polymer and into the bulk solution. These combined processes result in the contraction of the polymer upon reduction. Besides the incorporation / expulsion of counter ions, it is generally agreed that intrinsic volume changes are also due to conformational changes of polymer chains induced

by the delocalisation of charge in π-electron system, electrostatic repulsion between charged polymer chains [113-118], and osmotic effects [119].

Where relatively bulky and immobile dopant anions (e.g. dodecylbenzenesulfonic anion, DBS^-) are considered, the application of a reducing potential would lead to the incorporation of cations to balance the negative charges on entrapped bulky anions [118, 120-122] as shown by equation 1-2. Therefore, an opposite mechanism encompassing cathodic expansion and anodic contraction of the polymer would occur compared to the case of small and mobile dopant anions.

However, in some cases it has been shown that large anions can cause anodic expansion. For example, a bulky anion called 2-di-butoxy-2-ethoxy ethyl ester of sulfosuccinic acid (DBEEESSA) (Figure 1-7) was shown to produce anodic expansion in polyaniline. Takashima *et al* [123] reported that DBEEESSA-doped PAn exhibited anodic expansion in aqueous HCl. It was likely that large conformational changes occurred to overcome the anodic contraction due to the expulsion of small protons, resulting in net anodic expansion. In another example, PPy doped with bis(trifluoromethane-sulfonyl) imide (TFSI) also showed anodic expansion to produce an extremely large strain in aqueous LiTFSI electrolyte [124]. It was suggested that the PPy films had gel-like properties that enabled the polymer to swell enough to enable the penetration of large anions such as TFSI [124].

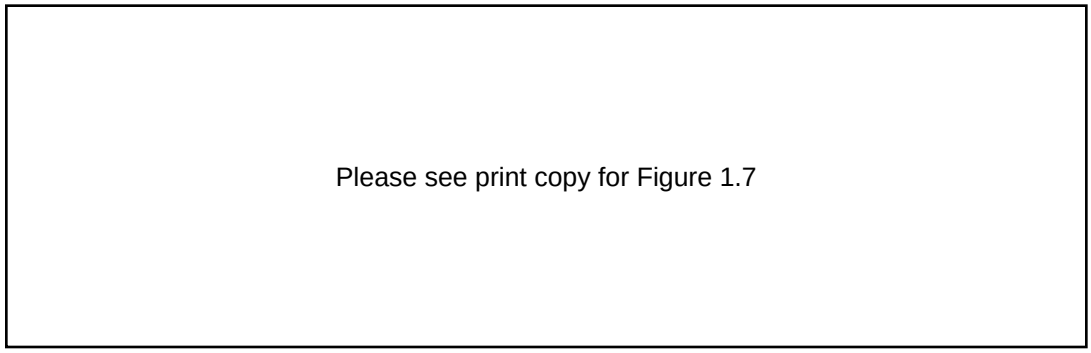

Figure 1-7 Chemical structure of di-2-butoxy-2-ethoxy-ethyl ester of sulfosuccinic acid (DBEEESSA) [123].

Interesting actuation behaviour has been reported when using ionic liquids as electrolytes [108, 110, 125]. Ding *et al* [108] reported that for PPy doped with hexafluorophosphate (PF_6^-), the application of a reducing potential resulted in expulsion of PF_6^- and subsequent contraction in propylene carbonate (PC) containing 0.25 M tetrabutylammonium texafluorophosphate ($TBA.PF_6$) electrolyte. Over the same potential range and in pure 1-butyl-3-methyl imidazolium hexafluorophosphate ($BMI.PF_6$) ionic liquid, reduction induced an expansion, presumably owing to the incorporation of the large imidazolium cation. It has also been shown [126] that cathodic expansion can be observed in the ionic liquid ethylmethylimidazolium bistrifluoromethanesulfonimide (EMI.TFSI), even through an anodic expansion in aqueous or PC-based Li.TFSI electrolyte [124] was observed for the same PPy actuator. It has been suggested [127] that the rate of ion diffusion / migration dominates what determines the volume change of PPy actuators. To illustrate this, it has been shown that for ionic liquids including EMI.TFSI and $BMI.BF_4$, the cation diffuses faster than the anion, even though the cationic radii are larger than the anionic radii [128-130].

Therefore, the incorporation of ions between polymer chains appears to be primarily responsible for dimensional increases in PPy actuators. However, the net volume change depends on a number of simultaneous electrochemical processes, such as conformational change and solvent flux, and may also relate to competitive ion diffusion rates in a particular electrolyte system.

Although still in the early stages of development, ICP basd mechanical actuators can be made to achieve average stresses ~ 10 to 20 times those generated from natural muscle[131], and theoretical predictions of up to 200 MPa [132] have been made. Strains are normally from 1 % to 10 % [17, 63, 131] and as high as 26 % [124]. Such strains are comparable to those in muscle (~ 20%). Generally, oxidised ICPs are harder and show higher tensile modulus values due to the de-localisation of π-electrons and the increased inter-chain interactions associated with incorporation of dopant anions [116]. Under isotonic conditions, the strain decreases as the applied force increases [119, 133]. Strain rates in ICP mechanical sensors are normally around 3.2 $\%s^{-1}$ to give strains of 1.1 % [134], and up to 16 $\%s^{-1}$ can be achieved using a helix tube configuration [70]. A cycle life of 6000 cycles with only an ~ 17 % decrease in actuation strain if cycled in an ionic liquid ($BMI.PF_6$) has been reported [108]. Recently, over one million redox cycles have been reported using an ionic liquid ($BMI.BF_4$) / polyaniline fibre actuator system with minimal decrease in actuation strain [112].

A number of ICP mechanical actuator configurations have been demonstrated, e.g. PPy hollow tube actuators incorporating a platinum helix structure for use in a multi-dot Braille cell [135], the use of ICP micro actuators in constructing a "cell clinic" [20] for the manipulation of biological entities, such as cells, bacteria and multi-cellular organisms from

one site to another site for diagnostic testing and a micro-robots [136] for the picking up, lifting, moving and placing micro dimensional objects in an aqueous solution.

Among the available configuration, compact laminated ICP mechanical actuators have frequently been used as mechanical amplifiers to generate large deflections. A triple layer structure has been described [137], in which double sided tape was laminated between two polymer films. Such a structure improved energy efficiency since oxidation on one side and reduction on the other side were coupled, thereby removing parallel reactions such as bubble generation at the counter electrode. To enable operation out of solution, a new trilayer configuration was reported by Sansinena and Olazabal [138], in which a porous polyvinylidene fluoride (PVDF) sheet was used as the middle layer to store electrolyte. This structure was further developed by Andrews *et al*. [139] as part of an integrated electrochemical sensor-actuator system that gave reliable and repeatable mechanical behaviour for about 50 hours.

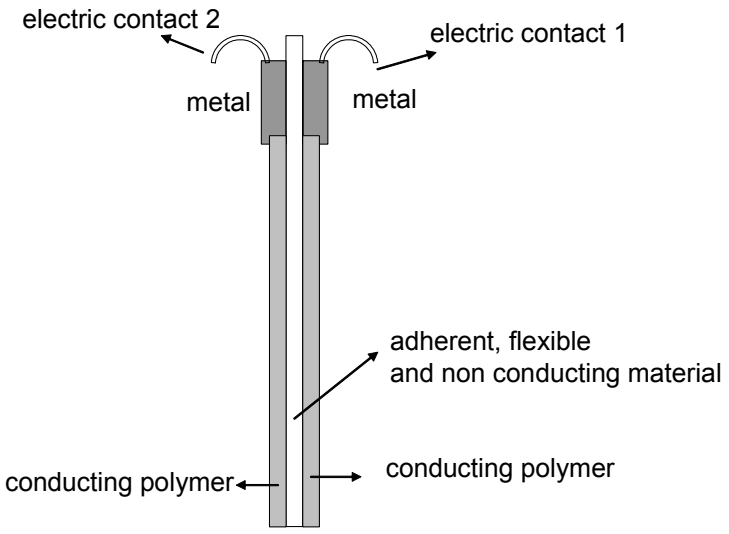

Figure 1-8 A triple layer laminated actuator formed by a double-sided tape sandwiched between two layers of conducting polymer films.

One of the major problems in the cycle life of laminated actuators is delamination of the ICP layers from supporting substrates. Supporting substrates have generally been made of adhesive tapes [137], polymer films [140, 141] or thin metal layers [19, 88]. Physical adhesion between supporting substrates and ICP layers, however, could not sustain repeated volume alterations at the interfaces, resulting in delamination. For operation within a solution, Sansinena *et al* reported a novel monolithic configuration based on a single PAn asymmetric membrane [142] to allow the actuator to produce a bending movement without the possibility of any delamination. In another approach, Bohn [143] addressed the delamination problem by using a Au electrochemical plating technique to increase the surface roughness of the supporting layer and thereby improve adhesion to the PPy film. However, for stand alone actuators that can operate out of solution, improved fabrication techniques need to be investigated.

1.4 ICPs FOR CONTROLLED RELEASE

One aspect associated with the switching properties of ICP materials during actuation is controlled ion exchange into the external environment. The expulsion of small dopant anions at reducing potentials or the expulsion of cations at oxidising potentials from polymers doped with bulky anionic dopants provide a novel platform from which to perform controlled release. Miller and co-workers [22] demonstrated that either cations (e.g. dopamine, a neurotransmitter) or anions (e.g. salicylate) could be controllably delivered upon electrical stimulation. It was shown that the amount of ions released was roughly proportional to the charge passed. Cationic dopamine had been loaded into poly (N-methylpyrrole) doped with polystyrenesulfonate (PMP^+/ PSS^-) film [22] by reduction of the film at – 0.6 V (*vs.* SCE). The release efficiency (moles of ions released / unit of charge) was ~ 50 % for

dopamine from PMP^+/ PSS^- upon oxidation, which was presumably due to the partial retention of dopamine and the incorporation of anionic species from the bulk solution. Similar electrochemically controlled release of quinones [24] and dithiocarbamates [144] has also been demonstrated. Studies of the cathodic release of anions from PPy [145] showed similar yet opposite partial retention of anions in the PPy film. The repetitive pulse method seems to be a good option for practical controlled release applications, and has been demonstrated for glutamate delivery from a PPy film [23]. Significant control over the amount of glutamate released was achieved by controlling the pulse time and potentials used.

The principle of controlled exchange of ions can also be extended to active ion transportation, in which an applied electrical stimulation enhances ion transport across a polymer membrane placed between reservoir and receiver solutions. It has been demonstrated that simple ions [146], small organic molecules [147] and even proteins [148] can be transported across polymeric membranes in a controlled manner. Parameters influencing electrochemically controlled transport have been investigated by Zhao *et al* [149] for small cations across PPy membranes. It was shown that the dopant ion affected transport selectivity, the placement of counter electrode affected transport efficiency due to the ion migration effect, transport efficiency can be affected by the hydrodynamics of the receiving solution, the electrical connection geometry affects the redox efficiency of the polymer membrane and therefore transport efficiency, and that higher and more sustainable fluxes can be achieved by using a square wave pulsed potential waveform compared to using constant or ramped potentials.

The dynamic ion exchange properties possessed by ICPs make them promising candidates for controlled release applications. However, ICP films do have capacity limitations due to the doping level, and on the other

hand complete transport cells incorporating ICP membranes are bulky and therefore not suitable for implantable biomedical devices. In this respect, it has been envisaged by Wallace and Maguire [150] that the amount of ions released can be enhanced by using structures (e.g. capsules, hollow fibres) to contain the active materials and then surrounding such structures with ICP membranes of small dimensions. In such systems, the release capacity would be determined by the internal volume rather than the dopant capacity of the ICP itself.

Low *et al* [151] reported a sphincter configuration using microvalves for responsive controlled drug delivery, for which a blend of ICP and hydrogel was placed within an array of holes with opening and closing achieved by the shrinkage and expansion of the polymer blend upon electrical stimulation. It was suggested that this approach offers better reproducibility and easier control than drug release achieved by passive diffusion out of a polymer host matrix. In addition, Fang *et al* [152] investigated micro fabrication of patterned structures and demonstrated a micro PPy O-ring structure as a seal for microvalves. PPy was electrodeposited on gold electrodes micro patterned on Si wafers in a defined structure. This was advantageous in making micro valves and micro pumps for controlled delivery in fluidic chips or even in lab-on-chip applications

1.5 ICP BASED MECHANICAL SENSORS

ICP based mechanical sensors can be constructed using different working principles, including the use of energy conversion properties, or the use of conductivity or other measurable parameters that can be associated with mechanical deformation.

Takashima and co-workers [21] reported on the conversion of mechanical movement to electricity using ICPs. The authors observed mechanically induced electrochemical current in a freestanding film of PAn. The results observed showed that the induced charge was dependent upon tensional load and the degree of doping within the PAn. It was suggested that the stretching of longer main chain molecules in PAn may have resulted in a narrowing of the band gap and a change in the density of states, which was reflected in the energetic spread in the charge transport levels of chain segments due to fluctuation in conjugation lengths and structural disorder [153]. A change in the density of states near the chemical potential would result in a redox current. Although the observed phenomenon was significant, further research on the mechanism and use in mechanical sensors has not been reported in the literature.

ICPs can be thought of as analogous to metal coated ionic polymer membranes in terms of the coupling of charge and ion motion. Ionic polymers, such as Nafion®, behave like solid-state electrolytes. This particular example consists of a Teflon backbone with pendant sulfonic acid side groups and allows the conduction of cations. Metal-coated Nafion films are capable of transducing mechanical deformation to electricity via a cation redistribution process [109], with the charge generated at the surfaces of the membrane proportional to the strain in the material [154, 155]. ICPs in the oxidised state behave like solid-state polycationic electrolytes filled with mobile ions, however, instead of having a thin metal coating, the ICP itself is an intrinsically electrical conductor. Therefore, mechanical displacement would induce an ion redistribution process in ICPs, resulting in electrical signal output similar to that in ionic polymers.

The intrinsic conductivity changes exhibited by ICPs in response to external deformation has been utilised to construct mechanical sensing

devices, such as ICP-coated textiles as flexible strain gauges [89, 156, 157] and ICP-coated foams [90] or ICP-based nano composites [90, 158] as deformation sensors. Flexible strain gauges using ICP-coated textiles have been investigated by De Rossi and co-workers [156, 157], while the use of PPy-coated wearable strain gauges based on nylon lycra textile substrates has been applied to biomechanical monitoring [89, 159]. It has been shown that the presence of ICPs gives these composite materials piezoresistive properties and enables the detection of local strains on the fabric [156, 157]. Whitten [160] stated that ICP-based textile strain gauges have the possibility of detecting large strains, up to at least 80 %, and also suggested that the mechanical interaction of the coated fibres within the textile contributed to the overall conductivity change. In addition, the use of PPy-coated polyurethane foam as wearable mechanical sensors has recently been demonstrated [90]. ICPs have also been incorporated into various other non conductive materials to form composites for deformation sensor applications. Flandin *et al* [158] demonstrated a PPy nanocomposite as a deformation sensor and suggested that the correlation between electrical conductivity and mechanical stress was due to the deformation-induced conductivity change of the percolating network of conductive PPy.

Moreover, Otero *et al* [161] reported that ICPs can be utilised to sense mechanical variables indirectly by considering the variation of the consumed electrical energy during a constant movement of a triple layer ICP actuator and relating this to the load on the tip of the actuator. However, it is worth noting that this sensing method would be problematic if strictly controlled conditions were not possible, since the mechanically induced energy change was much smaller than the total energy consumed by the device. In addition, other factors might also make significant contributions to the variation in consumed energy. These might include ageing effects, the

polymer structural changes during current cycling, and the electrolysis of the electrolyte solution.

1.6 ORGANISATION OF THIS THESIS

A general background to this project and the relevant literature to the tasks carried out in this study have been introduced and reviewed in this Chapter.

The general experimental techniques used for materials preparation, device construction and characterisation are described in Chapter 2.

The result Chapters on the development of sensors and actuators using ICPs are contained in Part 1 of this thesis. The development of the capacitive force sensor considering the use of the cochlear implant itself is described in Part 2 (Chapter 7).

In Chapter 3, the preparation and characterization of PPy mechanical sensors is described. The effects of the nature of the dopant, polymer redox state, electrolyte composition and displacement frequency on induced voltage or charge output were investigated. The correlation between the induced charge and static displacement was determined.

PPy trilayer bending actuators were constructed and investigated (Chapter 4). The effect of the stimulation waveform on energy consumption has been investigated. The correlation between strain and charge, the effect of electrolyte on cycle life, the effect of frequency on the amplitude of deflection, the correlation between blocking force and applied voltage, and the effect of using ionic liquids on the blocking force were also investigated. Finally, the possibility of using the PPy trilayer actuator to straighten the Nucleus® 24 Contour™ electrode was evaluated.

In Chapter 5, the construction and characterisation of a novel microfluidic pump (TITAN) is described. The effect of applied voltage, and applied backpressure on the volume displaced were investigated and discussed. The use of an electronic switching sequence to carry out switching and the use of the intrinsic resistance of PPy to perform 'peristaltic' actuation were considered.

In Chapter 6, the construction and characterisation of PPy-coated hollow fibre devices for electrochemically controlled release is described. The effect of dopant size in PPy on electrochemically controlled release was investigated and discussed. Electrochemically controlled release using three-electrode or two-electrode setups configuration was also investigated.

In Chapter 7, Part 2, a novel capacitive force transducer using the cochlear implant itself is described. The electrochemical impedance spectra of the electrode in artificial perilymph, the correlation between capacitance and applied force on the electrode tip, the capacitance response in a simulated insertion, and the influence of buffer composition were investigated and discussed.

Finally, general conclusions for this study are presented in Chapter 8, including comments on the suitability of ICP sensors and actuators for application in the cochlear implant.

1.7 REFERENCES

1. Wallace, G.G., Spinks, G.M. and Teasdale, P.R. *Conductive Electroactive Polymers - Intelligent Materials Systems*; Technomic Publishing: Switzerland, 1997.
2. *What is the Cochlear Implant*: www.cochlear.com, April 2003.
3. Clark, G., *Advances in Oto-Rhino-Laryngology*, 38 (1987) 1-189.
4. Loizou, P., *IEEE SIGNAL PROCESSING MAGAZINE*, (1998) 115-119.
5. Seligman, P., Patrick, J., Tong, Y., Clark, G., Dowell, R. and Crosby, P., *Acta Otolaryngologica*, Suppl. 411 (1984) 135-139.
6. Blamey, P., Dowell, R. and Clark, G., *Journal of the Acoustical Society of America*, 82 (1987) 38-47.
7. Patrick, J., Seligman, P., Money, D. and Kuzma, J. In *Cochlear prostheses*; G. Clark, Y. Tong and J. Patrick, Eds.; Churchill Livingstone: Edinburgh, 1990, pp 99-124.
8. Patrick, J. and Clark, G., *Ear and Hearing*, 12 (1991) 3-9.
9. Clark, G.M., Blamey, P.J. and Brown, A.M. In *Advance in Oto-Rhino-Laryngology*; C. R. Pfaltz, Ed.; Basel: Karger, 1987; Vol. 38.
10. Briggs, R. and Saunders, E. *The Nucleus 24 Contour Electrode Array - A training guide;* in the surgical training guide, Cooperative Research Centre for Cochlear Implant & Hearing Aid Innovation, 2002.
11. Seldon, H.L., Dahm, M.C. and Clark, G.M., *Biomaterials,* 15 (1994) 1161-9.
12. Kennedy, D.W., L*aryngoscope,* 97 (1) (1987) 42-9.
13. Webb, R.L., Clark, G.M., Shepherd, R.K., Franz, B.K. and Pyman, B.C., *Am. J. Otol.,* 9 (1) (1988) 8-13.
14. Update on the development of the Advance Off-Stylet (AOS insertion tool In *2004 Cochlear Collaborative Research Report;* Cochlear Limited, 2004, pp 2.
15. Associate Prof. Robert Cowan, *Personal Communication:* CRC for Cochlear Implant and Hearing Aid Innovation, East Melbourne, April 2003.
16. Paasche, G., Bogel, L., Leinung, M., Lenarz, T. and Stover, T., *Hearing Research,* In Press, Corrected Proof.

17. Baughman, R.H., *Synthetic Metals,* 78 (3) (1996) 339-353.

18. Otero, T.F. In *Handbook of Organic Conductive Molecules and Polymers;* H. S. Nalwa, Ed.; John Wiley & Sons Ltd.: Chichester, 1997; Vol. 4, pp 558.

19. Smela, E., Ingamas, O. and Lundstrom, I., *Science,* 268 (5218) (1995) 1735-1738.

20. Jager, E.W.H., Immerstrand, C., Peterson, K.H., Magnusson, K.E., Lundstrom, I. and Inganas, O., *Biomedical Microdevices,* 4 (3) (2002) 177-187.

21. Takashima, W., Fukui, M., Uesugi, T., Kaneko, M. and Kaneto, K., *Synthetic Metals,* 85 (1-3) (1997) 1395-1396.

22. Miller, L.L., Smith, G.A., An-Cheng Chang and Qin-Xin Zhou, *Journal of Controlled Release,* 6 (1) (1987) 293-296.

23. Zinger, B. and Miller, L.L., *J. Am. Chem. Soc.,* 106 (22) (1984) 6861-6863.

24. Lin, Y. and Wallace, G.G., *Journal of Controlled Release,* 30 (2) (1994) 137-142.

25. Shirakawa, H., Louis, E.J., MacDiarmid, A.G., Chiang, C.K. and Heeger, A.J., *Chem. Soc. Chem. Commun.,* (1977) 578.

26. Chiang, C.K., Fincher, C.R., Park, Y.W., Heeger, A.J., Shirakawa, H., Louis, E.J., Gua, S.C. and MacDiarmid, A.G., *Phys. Rev. Lett.,* 39 (1977) 1098.

27. Chiang, C.K., Druy, M.A., Gua, S.C., Heeger, A.J., Shirakawa, H., Louis, E.J., MacDiarmid, A.G. and Y. W. Park, *J. Am. Chem. Soc.,* 100 (1978) 1013.

28. Reynolds, J.R., *Chemtech,* 18 (7) (1988) 440.

29. Diaz, A.F., Kanazawa, K.K. and Gardini, G.P., *J. Chem. Soc. Chem. Commun.,* (1979) 635.

30. Wang, J., Too, C.O., Zhou, D. and Wallace, G.G., *Journal of Power Sources,* 140 (1) (2005) 162-167.

31. Spinks, G.M., Xi, B., Truong, V.-T. and Wallace, G.G., *Synthetic Metals,* 151 (1) (2005) 85-91.

32. Jin, G., Norrish, J., Too, C. and Wallace, G., *Current Applied Physics,* 4 (2-4) (2004) 366-369.

33. Wallace, G.G. and Kane-Maguire, L.A.P., *Advanced Materials,* 14 (13-14) (2002) 953-+.

34. Kane-Maguire, L.A.P., MacDiarmid, A.G., Norris, I.D., Wallace, G.G. and Zheng, W., *Synthetic Metals,* 106 (3) (1999) 171-176.

35. Kane-Maguire, L.A.P., Norris, I.D. and Wallace, G.G., *Synthetic Metals,* 101 (1-3) (1999) 817-818.

36. Dominis, A.J., Spinks, G.M., Kane-Maguire, L.A.P. and Wallace, G.G., *Synthetic Metals,* 129 (2) (2002) 165-172.

37. Diaz, A.F. and Logan, J.A., *J. Electroanal. Chem.,* 111 (1980) 111.

38. Wang, C.Y., Ballantyne, A.M., Hall, S.B., Too, C.O., Officer, D.L. and Wallace, G.G., *Journal of Power Sources,* In Press, Corrected Proof.

39. Barisci, J.N., Stella, R., Spinks, G.M. and Wallace, G.G., *Synthetic Metals,* 124 (2-3) (2001) 407-414.

40. Tourillon, G. and Garnier, F., *J. Electroanal. Chem.,* 135 (1982) 173.

41. Barisci, J.N., Wallace, G.G., Andrews, M.K., Partridge, A.C. and Harris, P.D., *Sensors and Actuators B: Chemical,* 84 (2-3) (2002) 252-257.

42. Nguyen, T.A., Barisci, J.N., Partridge, A. and Wallace, G.G., *Synthetic Metals,* 137 (1-3) (2003) 1445-1446.

43. Ngamna, O., Morrin, A., Moulton, S.E., Killard, A.J., Smyth, M.R. and Wallace, G.G., *Synthetic Metals,* 153 (1-3) (2005) 185-188.

44. Zhou, D. *Development of Conducting Polymer Membrane Structures for Protein and Gas Separation;* PhD thesis, University of Wollongong, 1997.

45. Morales, J.A., O'Sullivan, S.J. and Cassidy, J.F., *Sensors and Actuators B: Chemical,* 105 (2) (2005) 266-270.

46. Reece, D.A., Ralph, S.F. and Wallace, G.G., *Journal of Membrane Science,* 249 (1-2) (2005) 9-20.

47. Shao, Y., Jin, Y., Wang, J., Wang, L., Zhao, F. and Dong, S., *Biosensors and Bioelectronics,* 20 (7) (2005) 1373-1379.

48. Wang, J., Too, C.O. and Wallace, G.G., *Journal of Power Sources,* 150 (2005) 223-228.

49. Karami, H., Mousavi, M.F. and Shamsipur, M., *Journal of Power Sources,* 117 (1-2) (2003) 255-259.

50. Gurunathan, K., Amalnerkar, D.P. and Trivedi, D.C., *Materials Letters,* 57 (9-10) (2003) 1642-1648.

51. Somani, P.R. and Radhakrishnan, S., *Materials Chemistry and Physics,* 77 (1) (2003) 117-133.

52. Somani, P., Mandale, A.B. and Radhakrishnan, S., *Acta Materialia,* 48 (11) (2000) 2859-2871.

53. Tengstedt, C., Crispin, A., Hsu, C.-H., Zhang, C., Parker, I.D., Salaneck, W.R. and Fahlman, M., *Organic Electronics,* 6 (1) (2005) 21-33.

54. Saxena, V. and Malhotra, B.D., *Current Applied Physics,* 3 (2-3) (2003) 293-305.

55. Muller, D., Gross, M., Meerholz, K., Braig, T., Bayerl, M.S., Bielefeldt, F. and Nuyken, O., *Synthetic Metals,* 111-112 (2000) 31-34.

56. Chinn, D., DeLong, M., Fujii, A., Frolov, S., Yoshino, K. and Vardeny, Z.V., *Synthetic Metals,* 102 (1-3) (1999) 930-932.

57. Onoda, M. and MacDiarmid, A.G., *Synthetic Metals,* 91 (1-3) (1997) 307-309.

58. Choi, J.-H., Park, K.-W., Lee, H.-K., Kim, Y.-M., Lee, J.-S. and Sung, Y.-E., *Electrochimica Acta,* 48 (19) (2003) 2781-2789.

59. Diab, A.S., Hathoot, A.A., Abdel-Azzem, M. and Merz, A., *European Polymer Journal,* 36 (9) (2000) 1959-1965.

60. Chen, J., Too, C.O., Wallace, G.G. and Swiegers, G.F., *Electrochimica Acta,* 49 (5) (2004) 691-702.

61. Dhawan, S.K., Singh, N. and Rodrigues, D., *Science and Technology of Advanced Materials,* 4 (2) (2003) 105-113.

62. Courric, S. and Tran, V.H., *Polymer,* 39 (12) (1998) 2399-2408.

63. Spinks, G.M., Liu, L., Wallace, G.G. and Zhou, D.Z., *Advanced Functional Materials,* 12 (6-7) (2002) 437-440.

64. Ding, J., Liu, L., Spinks, G.M., Zhou, D., Wallace, G.G. and Gillespie, *J., Synthetic Metals,* 138 (3) (2003) 391-398.

65. Lewis, T.W., Moulton, S.E., Spinks, G.M. and Wallace, G.G., *Synthetic Metals,* 85 (1-3) (1997) 1419-1420.

66. Spinks, G.M., Xi, B., Zhou, D., Truong, V.-T. and Wallace, G.G., *Synthetic Metals,* 140 (2-3) (2004) 273-280.

67. Bar-Cohen, Y., *SPIE,* Bellingham*, (*WA 2001).

68. Zhou, D., Wallace, G.G., Spinks, G.M., Wu, Y., Cowan, R. and Newbold, C. In *26th Australasian Polymer Symposium;* Royal Australian Chemical Institute: Noosa, Australia, 2003, pp B2/3.

69. Jeong, B. and Gutowska, A., *Trends in Biotechnology,* 20 (7) (2002) 305-311.

70. Ding, J., Liu, L., Spinks, G.M., Zhou, D., Wallace, G.G. and Gillespie, J., *Synthetic Metals,* 138 (2003) 391-398.

71. Massoumi, B. and Entezami, A., *European Polymer Journal,* 37 (5) (2001) 1015-1020.

72. Bockris, J.O.m. and Miller, D. In *Conducting Polymers - Special Applications;* L. Alcacer, Ed.; D. Reidel Pub. Co.: Holland, 1987, pp 1-36.

73. Bredas, J.L. and Street, G.B., *Acc. Chem. Res.,* 18 (1985) 309.

74. Winokur, M., Moon, Y.B., Heeger, A.J., Barker, J. and Bott, D.C., *Phys. Rev. Lett.,* June 1 (1987).

75. Wieners, G., Weisenhofer, R., Monkenbusch, M., Stamm, M., Leiser, G., Enkelmann, V., Wegner, G. and Makromo, L., *Chem. Rapid Commun.,* 6 (1985) 425.

76. Baughman, R.H., Shacklette, L.W., Murthy, N.S., Miller, G.G. and Elsenbaumer, R.B., *Mol. Cryst. Liq. Cryst.,,* 118 (1985) 253.

77. Pouget, J.P., Oauxviel, J.C., Robin, P., Comes, R., Begin, D., Billaud, D., Feldblum, A., Gibson, H.W. and Epstein, A.J., *Mol. Cryst.,* 117 (1985) 75.

78. Kivelson, S. and Heeger, A.J., *Synthetic Metals,* 22 (1988) 371 - 384.

79. Street, G.B., Lindsey, S.E., Hazzal, A.I. and Wynne, K.J., *Mol. Cryst. Liq. Cryst.,* 118 (1985) 137.

80. Roy, R., Sen, S.K., Digar, M. and Bhattacharyya, S.N., *J. Phys. Condens. Matter.,* 3 (1991) 7849.

81. Roth, S. In Hop*ping Transport in Solids; M*. Pollak and B. Shklovski, Eds.; Elsevier Science Publishers: B.V. Amsterdam, 1991.

82. Bates, N., Cross, M., Lines, R. and Walton, D., *Chem. Commun.,* (1985) 871.

83. Buckley, L.J., Roylance, D.K. and Wrek, G.E., *J. Polym. Sci., Part B: Polym. Phys.,* 25 (1987) 2179.

84. Cvetko, B.F., Brungs, M.P., Burford, R.P. and Skyllas-Kazacos, M., *J. Mater. Sci.,* 23 (1988) 2102.

85. Ansari, R. and Wallace, G.G., *Polymer,* 35 (1994) 2372.

86. Campbell, T.E., Hodgson, A.J. and Wallace, G.G., *Electroanal.,* 11 (1999) 215.

87. Gooding, J.J., Wasiowych, C., Barnett, D., Hibbert, D.B., Barisci, J.N. and Wallace, G.G., *Biosensors and Bioelectronics,* 20 (2) (2004) 260-268.

88. Smela, E., Kallenbach, M. and Holdenried, *J., IEEE Jounal of Microelectromechanical Systems,* 8 (4) (1999) 373-383.

89. Wu, J., Zhou, D., Too, C.O. and Wallace, G.G., *Synthetic Metals,* 155 (3) (2005) 698-701.

90. Brady, S., Lau, K.T., Megill, W., Wallace, G.G. and Diamond, D., *Synthetic Metals,* 154 (1-3) (2005) 25-28.

91. Kontturi, K., Pentti, P. and Sundholm, G., *Journal of Electroanalytical Chemistry,* 453 (1-2) (1998) 231-238.

92. Kontturi, K., Murtomaki, L., Pentti, P. and Sundholm, G., *Synthetic Metals,* 92 (2) (1998) 179-185.

93. Gardini, C.P., *Adv. Heterocyclic Chem.,* 15 (1973) 67.

94. Kanazawa, K.K., Diaz, A.F., Geiss, R.H., Gill, W.D., Wak, J.F., Logan, J.A., Raboly, J.F. and Street, G.B., *J. Chem. Soc. Chem. Comm.,* (1979) 854.

95. Dall'Olio, A., Dascola, Y., Varacco, V. and Bocchi, V., C. *R. Acad. Sci. Ser, C,,* 267 (1968) 433.

96. Bowen, W.R., Kingdom, R.S. and Sabuni, H.A.M., *J. Membr. Sci.,* 40 (1989) 219.

97. Genies, E.M., Bidan, G. and Diaz, A.F., *J. Electroanal. Chem.,* 149 (1983) 101.

98. Diaz, A.F., Crowley, J., Bargon, J., Gardini, G.P. and Torrance, J.B., *J. Electroanal. Chem.,* 121 (1981) 355.

99. Mukherjee, D., *Progress in Rubber and Plastics Technology,* 6 (1990) 30.

100. Deronzier, A. and Moutet, J.C., *Coordination Chemistry Reviews,* 147 (1996) 339-371.

101. Akhtar, P., Too, C.O. and Wallace, G.G., *Analytica Chimica Acta,* 341 (2-3) (1997) 141-153.

102. Akhtar, P., Too, C.O. and Wallace, G.G., *Analytica Chimica Acta,* 339 (3) (1997) 201-209.

103. John, R. and Wallace, G.G., *Journal of Electroanalytical Chemistry,* 283 (1-2) (1990) 87-98.

104. Garner, B., Georgevich, A., Hodgson, A.J., Liu, L. and Wallace, G.G., *Journal of Biomedical Materials Research,* 44 (2) (1999) 121-129.

105. Yang, X., Too, C.O., Sparrow, L., Ramshaw, J. and Wallace, G.G., *Reactive and Functional Polymers,* 53 (1) (2002) 53-62.

106. Imisides, M.D., John, R., Riley, P. and Wallace, G.G., *Electroanal.,* 3 (1991) 879.

107. Otero, T.F. In *Handbook of Organic Conductive Molecules and Polymers;* H. S. Nalwa, Ed.; John Wiley & Sons Ltd.: Chichester, 1997; Vol. 4, pp 535.

108. Lu, W., Fadeev, A.G., Qi, B., Smela, E., Mattes, B.R., Ding, J., Spinks, G.M., Mazurkiewicz, J., Zhou, D., Wallace, G.G., MacFarlane, D.R., Forsyth, S.A. and Forsyth, M., *Science,* 297 (5583) (2002) 983-987.

109. Bennett, M.D. and Leo, D.J., *Sensors and Actuators A: Physical,* 115 (1) (2004) 79-90.

110. Mazurkiewicz, J.H., Innis, P.C., Wallace, G.G., MacFarlane, D.R. and Forsyth, M., *Synthetic Metals,* 135-136 (2003) 31-32.

111. Murray, P.S., Ralph, S.F., Too, C.O. and Wallace, G.G., *Electrochimica Acta,* In Press, Corrected Proof.

112. Lu, W. and Mattes, B.R., *Synthetic Metals,* 152 (1-3) (2005) 53-56.

113. Takashima, W., M.Fukui, Kaneko, M. and Kaneto, K., *Jpn. J. Appl. Phys.,* 34 (1995) 3786-3789.

114. Kaneto, K., Kaneko, M. and W.Takashima, *Jpn. J. Appl. Phys., 3*4 (1995) L837-L840.

115. Kaneko, M. and Kaneto, K., *Synth. Met.,* 102 (1999) 1350-1353.

116. Kaneto, K. and M.kaneko, *Appl. Biochem. Biotechnol.,* 96 (2001) 13-23.

117. Kaneto, K., Sonoda, Y. and Takashima, W., *Jpn. J. Appl. Phys.,* 39 (2000) 5918-5922.

118. Takashima, W., Pandey, S.S. and Kaneto, K., *Tin Solid Films,* 438 (2003) 339-345.

119. Bay, L., Jacobsen, T., Skaarup, S. and West, K., *J. Phys. Chem.B, 1*05 (2001) 8492-7.

120. Fedorko, P., Fraysse, j., Dufresne, A., Planes, J., Travers, J.P., Oligna, T., Kramer, C., Rannou, P. and Pron, A., *Synth. Met.,* 119 (2001) 445-446.

121. Takashima, W., Pandey, S., Fuchiwaki, M. and Kaneto, K., *Jpn. J. Appl. Phys.,* 41 (2002) 7532-7536.

122. Takashima, W., Pandey, S.S. and Kaneto, K., *Sensors and Actuators B: Chemical,* 89 (1-2) (2003) 48-52.

123. Takashima, W., Dufour, B., Pandey, S.S., Kaneto, K. and Pron, A., *Sensors and Actuators B: Chemical,* 99 (2004) 601-607.

124. Hara, S., Zama, T., Takashima, W. and Kaneto, K., *J. Mater. Chem.,* 14 (2004) 1516-1517.

125. Lu, W., Fadeev, A.G., Qi, B. and Mattes, B.R., *Synthetic Metals,* 135-136 (2003) 139-140.

126. Ding, J., Zhou, D., Spinks, G.M., Wallace, G.G., Forsyth, M. and MacFarlane, D.R., *Chemistry of Materials,* 15 (2003) 2392-2398.

127. Dr. Philip Whitten, *Personal Communication:* IPRI, University of Wollongong, 2005.

128. Prof. West, K., *Personal Communications*, The Danish Polymer Centre, Department of Chemical Engineering, The Technical University of Denmark, Lyngby, Den.: 2006.

129. Tokuda, H., Hayamizu, K., Ishii, K., Susan, M.A.B.H. and Watanabe, M., *J. Phys. Chem. B.,* 108 (2004) 16593-600.

130. Noda, A., Hayamizu, K. and Watanabe, M., *J. Phys. Chem. B,* 105 (2001) 4603-10.

131. Hayamizu, K., Aihara, Y., Nakagawa, H., Nukuda, T. and Price, W., *J. Phys. Chem. B,* 108 (2004) 19527-32.

132. Della Santa, A., Rossi, D.D. and Mazzoldi, A., *Smart Materials and Structures,* 6 (1997) 23.

133. Baughman, R.H., Shacklette, I.W. and Elsenbaumer, R.L. *Microelectromechanical actuators based on conducting polymers;* Kluwer, Dordrecht, 1991; pp 267.

134. G.M, S., L, L., D, Z. and G, W.G., *Adv. Funct. Mater.,* 12 (2002) 437-40.

135. Madden, J.D., Cush, R.A., Kanigan, T.S., Brenan, C.J. and Hunter, I.W., *Synthetic Metals,* 105 (1999) 61-64.

136. Wallace, G.G., Zhou, D., Ding, J., Xi, B., Innis, P.C., Mazurkiewicz, J.H., Spinks, G.M., Gillespie, J., MacFarlane, D.R., Forsyth, S. and

Forsyth, M. In *Proc. SPIE Smart Structures and Materials,* 2003; Vol. 12, pp 468-472.

137. Jager, E.W.H., Inganas, O. and Lundstrom, I., *Science,* 288 (2000) 2335.

138. Otero, T.F. In *Handbook of Organic Conductive Molecules and Polymers;* H. S. Nalwa, Ed.; John Wiley & Sons Ltd.: Chichester, 1997; Vol. 4, pp 553.

139. Sansinena, J.M. and Olazabal, V. In *Electroactive Polymer (EAP) Actuators as Artificial Muscles: Reality, Potential, and Challenges, International Society for Optical Engineering (SPIE);* Y. Bar-Cohen, Ed.: Bellingham, WA, 2001, pp 193-221.

140. Andrews, M.K., Jansen, M.L., Spinks, G.M., Zhou, D. and Wallace, G.G., *Sensors and Actuators A: Physical,* 114 (1) (2004) 65-72.

141. Pei, Q., Inganas, O. and Lundstrom, I., *Smart Mater. and Struct.,* 2 (1993) 1.

142. Kaneko, M. and Kaneto, K., *React. Funct. Polym.,* 37 (1998) 155.

143. Sansinena, J.-M., Gao, J. and Wang, H.-L., *Adv. Funct. Mater.,* 13 (9) (2003) 703-709.

144. Pyo, M., Bohn, C.C., Smela, E., Reynolds, J.R. and Brennan, A.B., *Chem. Mater.,* 15 (2002) 916-922.

145. Lin, Y., Riley, P.J. and Wallace, G.G., *Anal. Lett.,* 22 (1989) 669.

146. Beck, F., Braun, P. and Schloten, F., *Journal of Electroanalytical Chemistry,* 267 (1-2) (1989) 141-148.

147. Price, W.E., Wallace, G.G. and Zhao, H.J., *Electroanal. Chem.,* 334 (1992) 111.

148. Zhao, H., Price, W.E. and Wallace, G.G., *J. Memb. Sci.,* 100 (1995) 239.

149. Price, W.E., Too, C.O., Wallace, G.G. and Zhou, D., *Synthetic Metals,* 102 (1-3) (1999) 1338-1341.

150. Zhao, H., Price, W.E., Too, C.O., Wallace, G.G. and Zhou, D., *Journal of Membrane Science,* 119 (2) (1996) 199-212.

151. Wallace, G.G. and Kane-Maguire, L.A.P. *In Advances in Synthetic Metals - Twenty Years of Progress in Science and Technology;* P. Bernier, S. Lefrant and G. Bidan, Eds.; Elsevier Science S.A.: Lausanne, Switzerland, 1999, pp 376.

152. Low, L.-M., Seetharaman, S., He, K.-Q. and Madou, M.J., *Sensors and Actuators B: Chemical,* 67 (1-2) (2000) 149-160.

153. Fang, Q., Chetwynd, D.G., Gardner, J.W., Toh, C. and Bartlett, P.N., *Materials Science and Engineering A,* 355 (1-2) (2003) 62-67.

154. Salaneck, W.R., Seki, K. and Kahn, A. *Conjugated Polymer and Molecular Interfaces;* Marcel Dekker, 2001; pp 514.

155. Newbury, K.; Virginia Tech, 2002.

156. Newbury, K. and Leo, J.D., *J. Intell. Mater. Syst. Struct.,* 13 (1) (2002) 51-60.

157. Mazzoldi, A., Rossi, D.D., Lorussi, F., Scillingo, E.P. and Paradiso, R., *J. AUTEX Res.,* 2 (4) (2002).

158. Rossi, D.D., Santa, A.D. and Mazzoldi, A., *Mater. Sci. Eng., C*7 (31) (1999).

159. Flandin, L., Brechet, Y. and Cavaille, J.-Y., *Composites Science and Technology,* 61 (6) (2001) 895-901.

160. Munro, B.J., Steele, J.R. and Wallace, G.G., *J. Sci. Medicine Sport,* 5 (4) (2002) suppl: 10.

161. Whitten, P. *Flexible Strain Sensors;* in Honour Thesis, Materials Engineering, University of Wollongong, 1998; pp 70.

162. Otero, T.F. and Cortes, M.T., *Sensors and Actuators B: Chemical, 9*6 (1-2) (2003) 152-156.

CHAPTER 2 GENERAL EXPERIMENTAL

2.1 INTRODUCTION

In this Chapter, the instrumentation and techniques used in this thesis are described. This includes Cyclic Voltammetry (CV), Chronoamperometry, Chronopotentiometry, Electrochemical Impedance Spectroscopy (EIS), Ultraviolet Visible Spectroscopy (UV-Vis), the Dual Lever Arm System, the Magnetron Sputter Coater system and the Four Point Probe for conductivity measurement.

To avoid repetition, experimental techniques common to more than one chapter will be described here. More specific experimental techniques will be described in relevant individual Chapters.

2.2 CYCLIC VOLTAMMETRY

Cyclic voltammetry (CV, also called potentiodynamic waveform) uses a triangular waveform to scan the potential at the working electrode between certain set potential limits as shown in Figure 2-1 [1, 2].

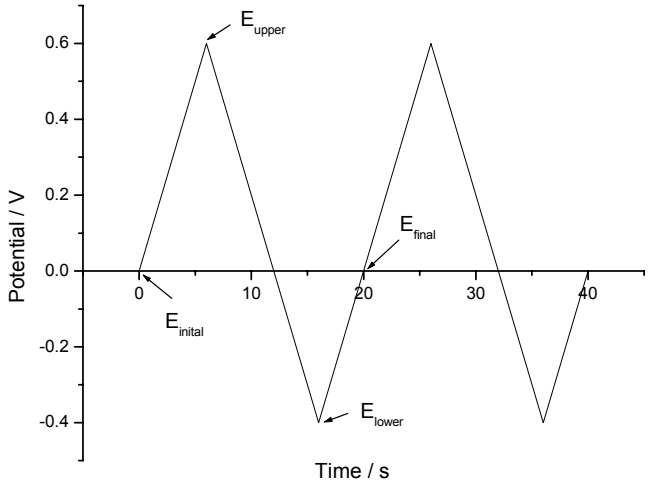

Figure 2-1 The potential waveform in a typical CV experiment. The potential is scanned between +600 mV and -400 mV at a scan rate of 100 $mV.s^{-1}$ for 2 cycles.

CV involves the measurement of current at the working electrode as a function of the applied potential, which is controlled versus a reference electrode (e.g. Ag/AgCl). The resulting 'electrochemical spectrum' (Figure 2-2 and Figure 2-3) indicating the potentials at which processes occur can provide useful qualitative and quantitative information on the nature of particular electrochemical systems. Peak potential, current magnitude, and peak potential separation have been widely used in the literature to identify, for example, the mobile ions in polypyrrole [3], for the characterisation and concentration determination in a sequence-selective biosensor for DNA [4, 5] and for the characterisation of electroactive ICP actuators [6]. CV is nearly always the technique of choice when studying an electrochemical system for the first time.

In a CV experiment, the important parameters include the initial, final, upper and lower potentials, and the potential scan rate (v). The initial potential ($E_{initial}$) is usually set at a potential where no charge transfer occurs between the active species and the working electrode. Starting from $E_{initial}$, the potential is continuously swept between the upper potential limit (E_{upper}) and the lower potential limit (E_{lower}) for a number of cycles until the experiment comes to an end at the final potential limit (E_{final}), which is most often equivalent to $E_{initial}$.

In a typical study, CVs are usually recorded over a wide range of sweep rates and for various values of $E_{initial}$, E_{upper} and E_{lower}. Often there will be several peaks, and by observing how these peaks appear and disappear as the potential limits and sweep rate are varied, it may be possible to identify the role of adsorption, diffusion and coupled homogeneous chemical reactions. The potential scan rate dependence of the peak current can reveal important diagnostic information. It is also important to compare the first and subsequent cycles, from which, potentially useful mechanistic

information may be obtained. Note that the kinetic data can only be accurately obtained from an analysis of the first potential sweep.

The following subsections consider the CV of soluble electroactive species and electroactive species immobilised onto an electrode surface.

2.2.1 CYCLIC VOLTAMMETRY OF SOLUBLE ELECTROACTIVE SPECIES

If the redox couple formed between species *O* (to be reduced) and species *R* (to be oxidised) is soluble, then a simple and reversible one electron transfer reaction can be expressed $O + e^- \rightleftharpoons R$, Only the reduction process is considered here because oxidation is simply the reverse of reduction. It is assumed that only *O* is initially present in solution. To understand the current peak formation, the shape of the concentration profiles of *O* as the function of the applied potential need to be considered.

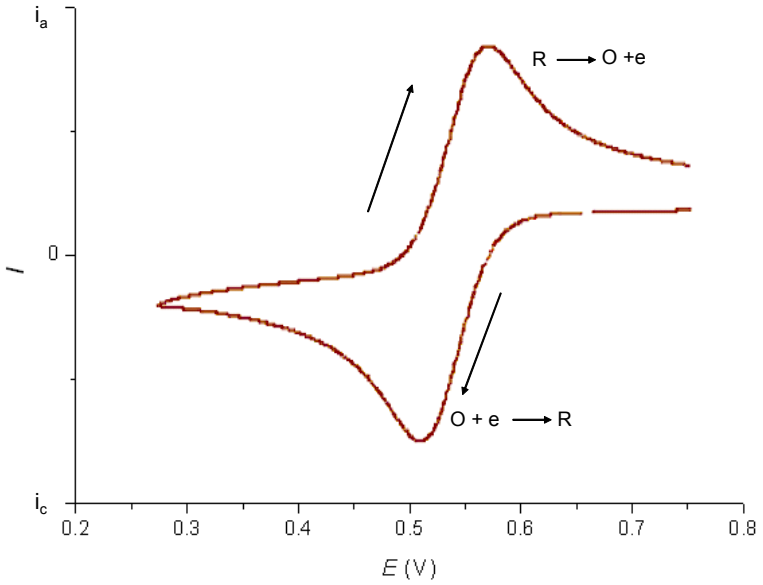

Figure 2-2 Cyclic voltammogram for a diffusion limited reversible redox couple where both the oxidized and reduced species are solution soluble.

It is generally assumed that the concentration of electroactive species a certain distance from the working electrode (also called 'bulk' concentration) is maintained uniformly by natural convection. The region immediately next to the electrode is called the *Nernst diffusion layer*. Within this region, the concentration ratio of redox couple species (C_O^σ / C_R^σ) can be determined by the Nernst equation:

$$E_e = E_e^e + \frac{RT}{nF} \ln \frac{C_O^\sigma}{C_R^\sigma} \qquad \text{..... 2-1}$$

where E_e^e is the standard electrode potential, E_e is the equilibrium potential, C_R^σ and C_O^σ are the surface concentrations of redox couple species R and O..

Considering the case when the potential is scanned to more negative values, the electrode surface concentration of reactant *O* is progressively decreased and a concentration gradient is thereby set up. As a result, an electrical current flows proportionally to the concentration gradient. Clearly this concentration gradient will decrease owing to diffusion. In a CV experiment using a moderately rapid scan rate, the diffusion layer will not have enough time to relax to its equilibrium state because the potential applied on the working electrode is continuously changing to more negative values. At this juncture, the concentration gradient is further increased until the surface concentration of the reactant *O* eventually reaches zero. After this point and due to the depletion of the reactant *O*, the concentration gradient starts to decrease and induces the electrical current to decrease as well. This is how the peak shape is formed in CV. Increased potential scan rate can drive the concentration gradient to a higher value, so that larger peak currents are observed at higher scan rates. Diagnostic information is usually obtained by evaluating the relationship between the anodic peak current (I_{pa}), anodic potential (E_{pa}), cathodic peak current (I_{pc}) and cathodic peak potential (E_{pc})

at various scan rates. The graphical determination of above peak currents and potentials is described in Figure 2-3.

Theoretically for planar diffusion using a conventional disk electrode, the peak current in a CV experiment is given by the *Randles-Sevcik* equation:

$$I_p = -0.4463\ nF\left(\frac{nF}{RT}\right)^{1/2} C_O^{\infty} D^{1/2} v^{1/2} \qquad \text{..... 2-2}$$

where I_p is the peak current density (in $A.cm^{-2}$), n is the stoichiometric number of electrons transferred; C_O^{∞} is the bulk concentration of the reactant species (in $mol.L^{-1}$), D is the diffusion coefficient (in $cm^2.s^{-1}$) of the species being reduced and v is the scan rate (in $V.s^{-1}$). From Equation 2-2, I_p is directly proportional to the square root of the scan rate.

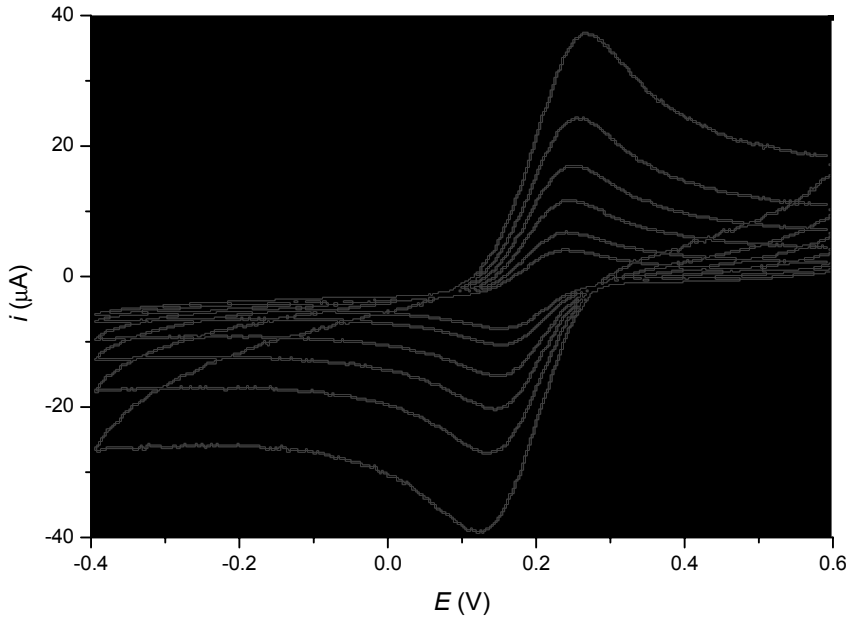

Figure 2-3 A typical cyclic voltammogram and the graphical method for determining peak potentials and currents for a reversible process. Data is from a CV experiment using a bare platinum working electrode in 5 mM potassium ferricyanide in aqueous 0.1 M sodium perchlorate supporting electrolyte at various scan rates.

CV can be used to perform diagnostic tests to identify the reversibility of electrochemical processes in solution. At 25ºC, if both species *O* and species R are stable and the kinetics of the electron transfer process are fast (i.e. the electron transfer rate at all potentials is significantly greater than the rate of mass transport), a reversible CV should satisfy the following diagnostic tests [1]:

$$\Delta E = E_p^A - E_p^C = 59/n \ mV \quad \text{..... 2-3}$$

$$\left|E_p - E_{p/2}\right| = 59/n \ mV \quad \text{..... 2-4}$$

$$\left|I_p^A / I_p^C\right| = 1 \quad \text{..... 2-5}$$

$$I_p \alpha \ v^{1/2} \quad \text{..... 2-6}$$

E_p is independent of *v* and at potential beyond E_p, $I^{-2} \alpha \ t$

Where ΔE is the peak separation between the anodic and cathodic peak potentials, $E_{p/2}$ is the half peak potential where the current is the half of the peak current and t is the time of the i-t transient. This holds for ideal systems and may not be observed in real systems partly due to the uncompensated solution resistance.

2.2.2 CYCLIC VOLTAMMETRY OF SURFACE IMMOBILISED ELECTROACTIVE SPECIES

If the redox species are immobilised on the working electrode (the *O* / *R* redox couple is considered for simplicity) and the electron transfer is reversible, the effect of diffusion / mass transfer can be ignored. In this situation, redox peaks originate from the direct charge transfer from the fixed amount of adsorbed reactant to the electrode and are therefore often sharper and more symmetrical than peaks from diffusion processes of solvable redox species (Figure 2-4). Moreover, the redox charge is equal

and there is little or no peak separation. CV of surface immobilised electroactive species is particularly useful in understanding the electrochemical process of inherently conducting polymers (ICPs) modified electrodes because the amount of reactant (ICP) is fixed on the electrode surface.

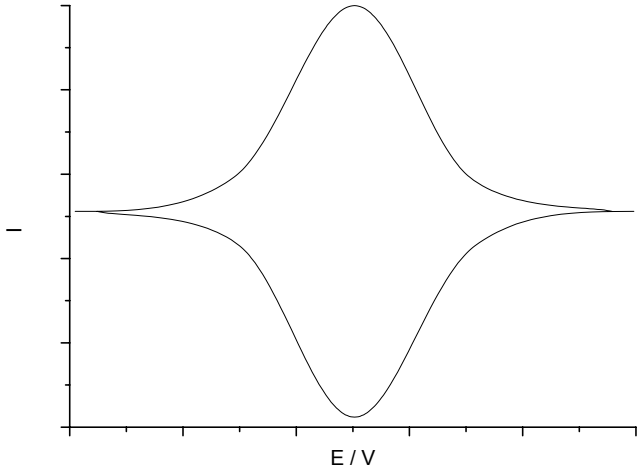

Figure 2-4 Cyclic voltammogram for a reversible surface immobilised electroactive species.

A possible problem for both soluble and surface immobilised redox species occurs when the uncompensated resistance / iR drop is considered, The following CV distortions may be observed in such a case: (A) anodic and cathodic peaks will shift apart and the peak separation is usually larger than the ideal value at a given scan rate, (B) redox peaks become broader and asymmetric and (C) anodic and cathodic peaks will further shift apart with an increase in scan rate. CVs obtained using ICPs as the working electrode are affected by iR drop since the conductivity of the polymer is limited. In the reduced state, conductivity is further reduced. For ICPs, the CV can be further distorted by the large capacitive effect of the conductive and porous ICP layer. The capacitive charging current is given by:

$$i_c = \frac{dQ}{dt} = C_{dl} \times \frac{dE}{dt} = C_{dl} \times \nu \qquad \text{..... 2-7}$$

where i_c is the non-faradic charging current, Q is amount of double layer charge; C_{dl} is the capacitance at the double layer interface of solution and electrode and ν is the potential scan rate.

In the oxidative potential region, an ICP modified electrode is at its oxidised and conductive state and is often associated with larger capacitance. Owning to this capacitance, a large change in current can often be observed at E_{upper} when the direction of the potential scan is changed as shown in Figure 2-5.

Owing to its diagnostic nature, CV was quite often used for the electropolymerisation of ICPs with the advantage of having the ability to simultaneously monitor electroactive quality.

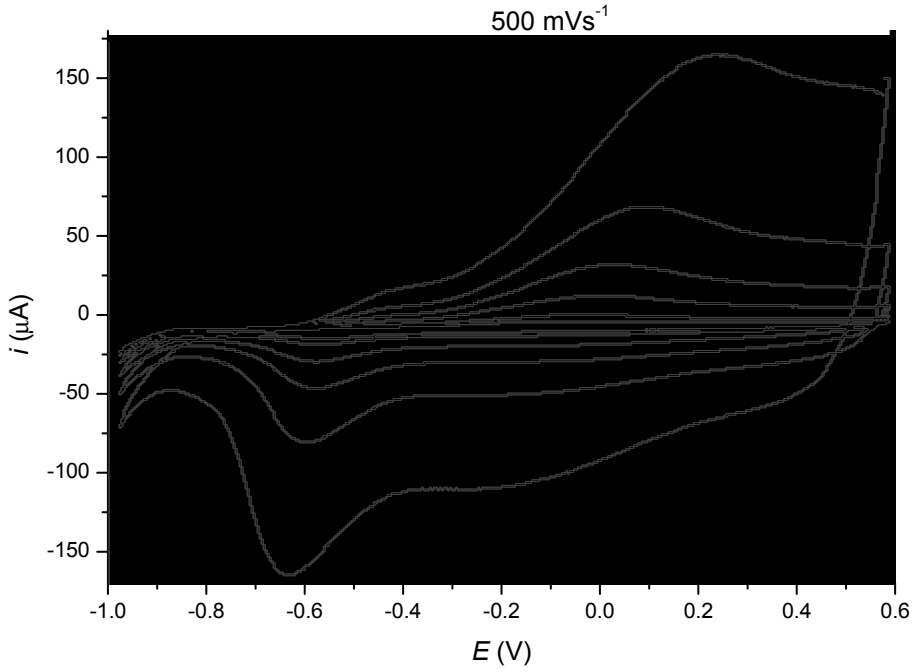

Figure 2-5 Cyclic Voltammograms of polypyrrole/para-toluenesulfonate modified glassy carbon electrode in 100 mM aqueous sodium perchlorate supporting electrolyte at scan rates of 10 to 500 $mV.s^{-1}$.

2.3 CHRONOAMPEROMETRY

Chronoamperometry involves instantaneous switching from one potential (E_i) to another (E_f) and the monitoring of the current response with respect to time. The oxidation of pyrrole on a Pt disk electrode at 0.61 V vs. Ag/AgCl can be monitored using chronoamperometry (Figure 2-6). The chronoamperogram of PPy/*p*TS growth initially showed a transient increase of charging current upon applying the potential. During the growth, continuous rise in current indicates that the conducting polymer has been deposited on the electrode resulting in an increase in the electrode surface area. On the other hand, a decrease in current may be evidence of no deposition or resistive material being deposited. Chronoamperometry has been used for the synthesis and characterisation of polypyrrole in aqueous solution [7] and for oligonucleotide detection in flow injection analysis [8].

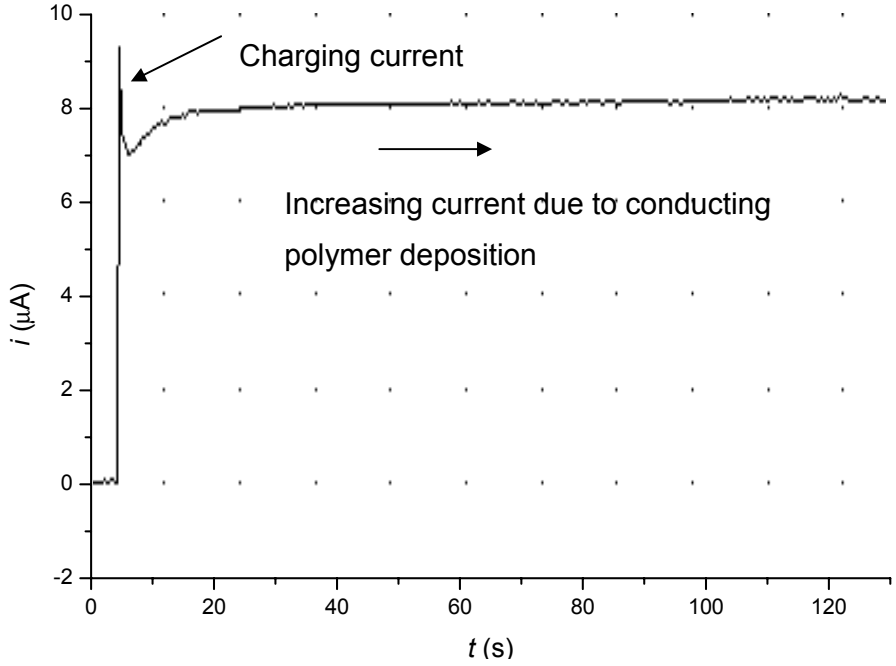

Figure 2-6 A typical chronoamperometry experiment using a standard Pt disk electrode (Ø1.5 mm) for the electrochemical deposition of polypyrrole from an aqueous solution containing 0.2 M pyrrole and 0.05 M sodium *p*TS at a constant potential of 0.61 V vs. Ag/AgCl.

Typically in chronoamperometry a decaying current can be observed and is characteristic of electroactive species present in solution or on the electrode surface. For a system using a conventional disk electrode under diffusion control, this current density is given by Cottrell equation [1]:

$$i = \frac{nFCD^{1/2}}{\pi^{1/2} t^{1/2}} \qquad \text{..... 2-8}$$

where the n is the stoichiometric number of electrons, F is the Faraday constant, C is the bulk concentration of electroactive species, D is its diffusion coefficient and t is the time of the I-t transient. The slope of an i vs. $t^{-1/2}$ plot is often used to determine important parameters, such as the diffusion coefficient.

If the potential were to be switched in a region where no charge transfer would occur between the electrode and the electroactive species, chronoamperometry could be used to determine the "*RC*" time constant of an electrochemical cell, where *R* is the uncompensated resistance and *C* is the double layer capacitance.

In this study, chronoamperometry was often used to determine the electrochemical efficiency of ICP actuators by measuring and comparing the charge associated with oxidation and reduction processes. Such charge measurements were made by integration of chronoamperograms (since $Q = I \times t$).

2.4 CHRONOPOTENTIOMETRY

Chronopotentiometry involves the application of a controlled current at the working electrode. The potential with respect to time during the experiment is monitored. A typical chronopotentiogram is shown in Figure 2-7. The current applied at the working electrode is controlled by a galvanostat in such as way as to drive the electroactive species to exchange

electrons with the electrode at a constant rate. The maximum current level is limited by the concentration of electroactive species and the maximum duration of a galvanostatic experiment is dependent on the amount of electroactive species presented in solution.

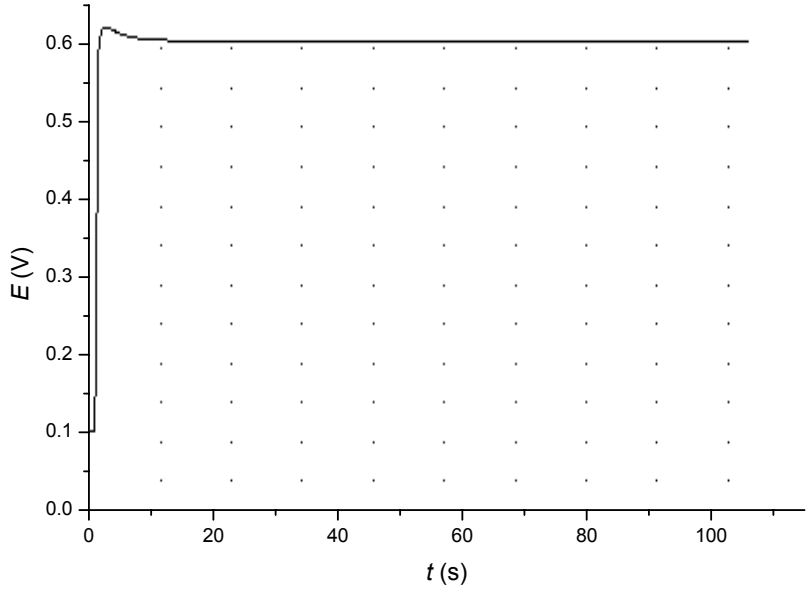

Figure 2-7 A typical response of a chronopotentiometric experiment for the electrochemical polymerisation of pyrrole to form polypyrrole on a standard Pt disk electrode (Ø1.5 mm) in an aqueous solution containing 0.2 M pyrrole and 0.05 M sodium *p*TS. Constant current density of 0.5 mA.cm^{-2} was applied.

Chronopotentiometry was extensively used in this study for electrochemical synthesis of ICP films. In a chronopotentiogram, a steady decrease or rise in potential during electrochemical polymerisation of conducting polymer indicates that the deposited PPy is of good or poor conductivity, respectively. If the potential remains relatively low and stable, the polymer film deposited on the electrode is in a conductive form. On the contrary, if the potential remains relatively high or even increases with time during growth, this indicates resistive film deposition or no film deposition at all. Considering Figure 2-7 of the growth of PPy/*p*TS at a constant current

density of 0.5 $mA.cm^{-2}$, the steady constant potential at low level (~ 0.61 V *vs.* Ag/AgCl) indicates that the PPy/*p*TS film had deposited onto the electrode surface and is conductive. In particular, this technique allowed simple control of the amount of charge (Q) passed by controlling the duration of experiments (since $Q = I \times t$).

2.5 ELECTROCHEMICAL IMPEDANCE SPECTROSCOPY

Electrochemical impedance spectroscopy (EIS) involves the application of a small amplitude sinusoidal AC potential excitation on top of a constant DC potential. The resulting AC current response (frequency and amplitude) is monitored. Analysis of the current response with variations in the amplitude and frequency of the AC potential produces useful information such as charge transfer rate, diffusion and surface coating properties. Studies using EIS include surface characterisation of thin film cochlear implant electrode arrays in biological environments [9], impedance characterisation of an ICP hydrogel electrode for use in neural communication [10], impedance study of single or a small number of cells in a microvial activated by polypyrrole / Au microactuators [11] and electrochemical stability of polypyrrole / PF_6 films [12].

The underlying principle of using a small amplitude sinusoidal AC potential is to maintain the current response of an electrochemical system in a pseudo-linear region [13]. The current response to sinusoidal potential will be a sinusoid at the same frequency (no harmonics) but shifted in phase. Therefore, it is possible to express the impedance (defined as the property that hinders the current flow) as a complex function. The potential is described as:

$$V(t) = |V| \exp(jwt) \quad \text{..... 2-9}$$

and the current response as:

$$I(t) = |I| \exp j(wt - \phi) \quad \text{..... 2-10}$$

the impedance can be represented as:

$$Z = \frac{V}{I} = \frac{|V|}{|I|} \exp(j\phi) = |Z| \exp(j\phi) \quad \text{..... 2-11}$$

or

$$Z = |Z| \cos\phi + |Z| j \sin\phi = Z_{RE} + Z_{IM} = Z' + jZ'' \quad \text{..... 2-12}$$

where $V(t)$ is the potential at time t, $|V|$ is the peak potential amplitude, ω is the radial frequency (radians per second) of sinusoidal AC excitation potential, $I(t)$ is the responsive current at time t, $|I|$ is the peak amplitude of current and φ is the frequency phase shift in respect to potential, Z_{RE} or Z' is the real part and Z_{IM} or Z'' is the imaginary part of impedance. Both $|Z|$ and ϕ are functions of excitation frequency [2, 14].

In practice, rather than direct analysis of the potential and current responses, impedance data is normally plotted in the complex impedance plane (sometimes called Nyquist Plots) (Figure 2-8, a), where the X axis is $Z_{RE} = |Z| \cos\phi$ and the Y axis is $Z_{IM} = |Z| j \sin(\phi)$. The semicircle is characteristic of a single "time constant". Electrochemical impedance plots often contain several time constants. Often only a portion of one or more of their semicircles is observed. However, the Nyquist plot can not be used to tell the frequency of an individual datum point. Therefore, Bode plots are useful (Figure 2-8, b), where both the magnitude of impedance in log |Z| and phase-shift (theta, θ) are plotted on the Y-axis with respect to the frequency plotted on the X axis as log (f).

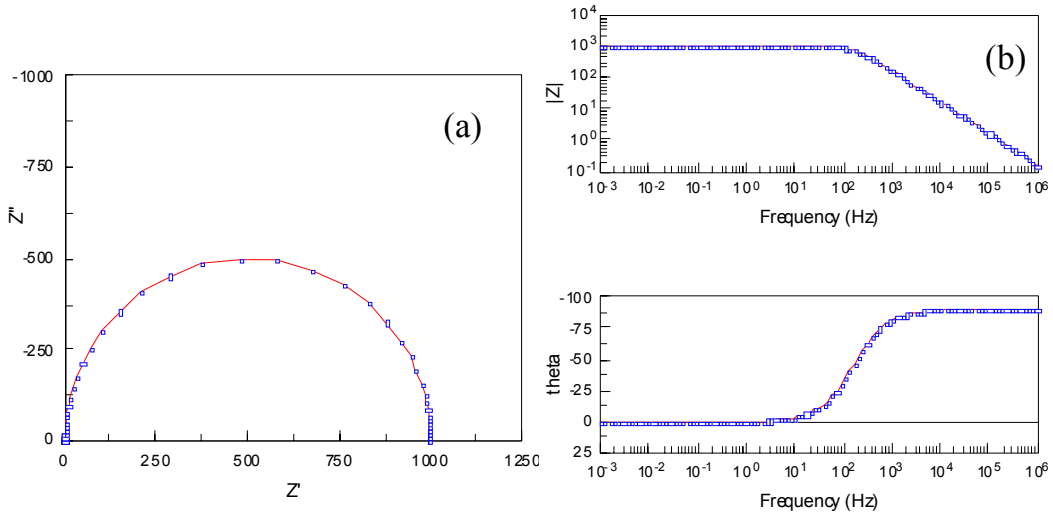

Figure 2-8 Impedance spectra of (a) Nyquist plot and (b) Bode plot.

In the study of a particular system using EIS, the impedance spectrum plots are generally modelled with an equivalent electrical circuit that is able to produce a similar spectrum, as shown in Figure 2-9. A range of different components may be used. Such components may exist physically such as resistors, capacitors and inductors, or exist as mathematical equivalents for a particular process, such as constant phase elements and Warburg impedances. An experimental impedance spectrum may be modelled by more than one possible equivalent circuit, meaning that electrochemical knowledge of the system is generally required for the correct interpretation of impedance data, which includes selection of the most appropriate equivalent circuit. Considering the system in Figure 2-9 again, the serial resistance R_s represents solution resistance of PBS buffer, which has the effect of translating the |Z| plot along the |Z| axis in the Bode plot. The constant phase element represents the non-ideal capacitance of an electrochemical ionic double layer formed on an electrode surface, which usually results in a depressed semicircle in the complex plane, as though the axes were rotated by a fixed angle. Often a small proportion of it is obtained in a practical measurement.

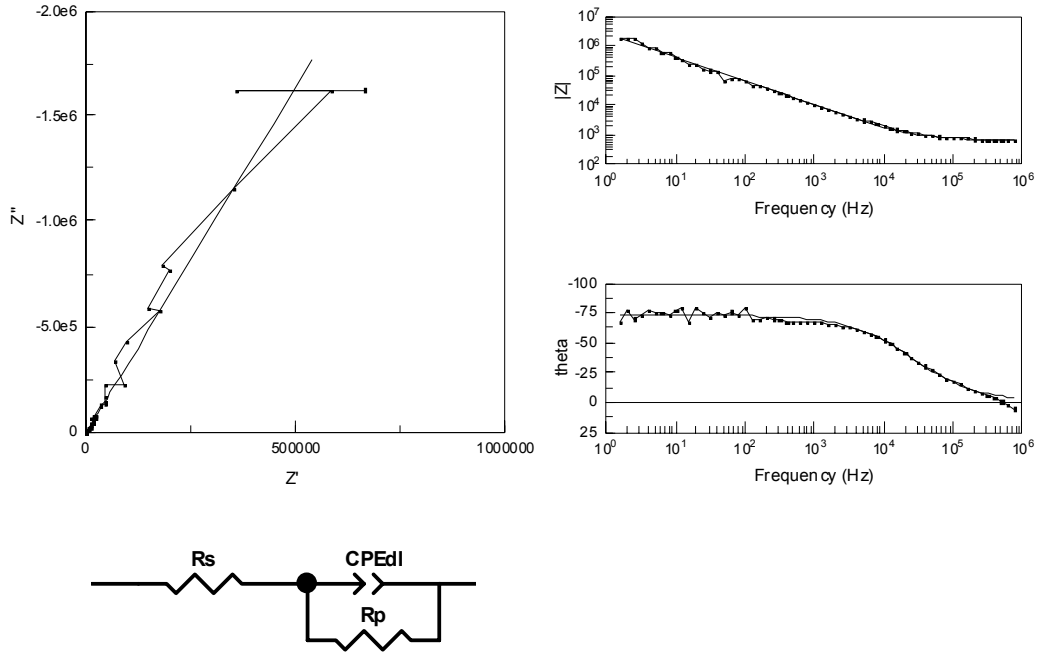

Figure 2-9 EIS spectra of cochlear ring electrode in PBS buffer and its equivalent circuit model, where R_s stands for the solution resistance, CPE_{dl} for the nonlinear nature of double layer capacitance at the electrode-solution interface and R_p for the polarisation resistance (also called charge transfer resistance).

2.6 ULTRAVIOLET VISIBLE (UV-vis) SPECTROSCOPY

UV-vis spectroscopy measures the light absorption of samples in the ultraviolet and visible regions. It comprises a radiation source, sample container, monochrometer, the photomultiplier tube detector and detector output.

A UV-vis spectrum is characteristic of a material with particular chemical structures. The absorption maximum of a band reflects the most probable transition (i.e. the vibrational frequency of valence shell electrons) in the region of absorption. The position of UV-vis spectral peaks have been extensively employed to characterise ICPs in thin layer coatings or in solution.

Besides the use of UV-vis spectroscopy as a useful tool to probe the chemical structure of molecules, the Beer-Lambert law states that the absorbed incident light is proportional to the number of molecules in the path, which is particularly useful in determining the concentration of a dissolved substance. The correlation between the absorption intensity ratio and solution concentration is given by [15]:

$$\log_{10}(\frac{I_0}{I}) = \varepsilon CL \qquad \text{..... 2-13}$$

where ε is the extinction coefficient, C is the substance concentration in mol L^{-1}, and L is the path length in cm.

Note that the solvent used should not have any absorption at the wavelength used for the concentration measurement. In addition, ε may not be constant at different concentrations so calibration over a range of concentrations is required for the quantitative determination of a substance in solution. The reasons for this include molecular interaction at high concentration, solute ionisation and fluorescence.

A Shimadzu UV 1601 Spectrophotometer was employed for UV-vis measurements in this study for the quantitative determination of the concentration of dye released from an ICP controlled release device.

2.7 DUAL LEVER ARM SYSTEM

In this study, an Aurora Dual-Mode Lever Arm system (305B) was employed for the controlled displacement of polypyrrole based mechanical sensors and the measurement of blocking force generated from polypyrrole trilayer actuator. The system employs a very high performance rotary moving coil motor to control/measure the force and a high performance

capacitive position detector to sense the length at the same time and capable of measuring force range from 0 to 5.0 N at the signal resolution of 1.0 mN and length excursion in the range of 20 mm with the length signal resolution of 1 μm [16].

The sample of either actuator or sensor was prepared as rectangular shape and clamped by plastic tweezers with electrical contacts made of platinum wire to minimise the electrochemically induced corrosion troubles. The tip of the lever arm was physically attached to the free end of the rectangular sample strip so that the measurement of force and the controlled displacement could be made possible as illustrated in Figure 2-10. In particular, the consistent attachment of the lever arm to the sensor must be met and a small range of sliding of the lever arm along the sensor must be allowed. The initial bending of the sensor against the lever arm and the existence of liquid electrolyte between the sensor and level arm helped the consistent attachment. Consistent attachment over the frequency range of displacement used in this study (from 0.01 Hz to 10 Hz) was also checked according to the sinusoidal voltage output from the sensor by ensuring the absence of signal distortion due to the detachment of the lever arm from the sensor.

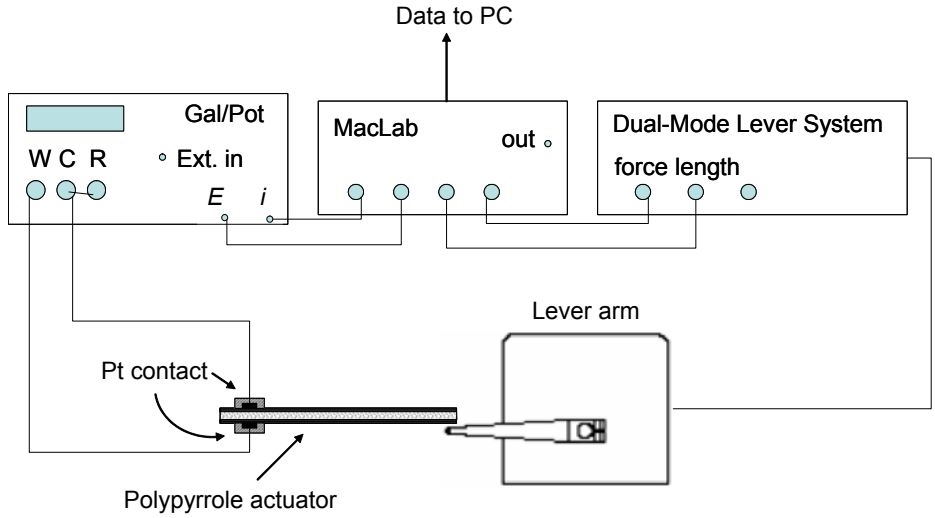

(a)

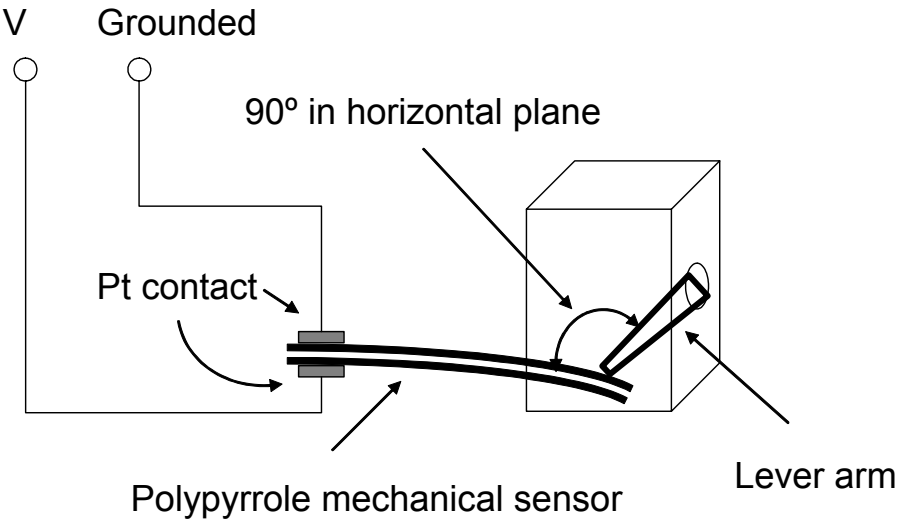

(b)

Figure 2-10 Setup using an Aurora Dual-Mode Lever Arm System for (a) the blocking force measurement and (b) the sensor testing.

2.8 MAGNETRON SPUTTER COATING

Magnetron sputter coating is a powerful and flexible coating technique for atomised material deposition. Almost any material can be coated with a wide range of metals using this technique.

Sputtering occurs as a result of ion bombardment of a target. A voltage of about -300 V is typically applied to the target (the source material

for coating). Positive charged ions that come from the ionisation of a noble gas (usually argon) in the sputtering chamber are then accelerated in this electrical field to collide with the target, resulting in the sputtering of neutral target atoms on to the substrate. Besides the sputtering of target atoms, there are secondary electrons generated from the collision as well. The magnetron means that there is a magnetic field used to trap the secondary electrons. These trapped electrons run within a circle around the magnetic field so that more collisions with the noble gas can occur, generating more positive ions that can bombard the target. The coating thickness can be controlled by the sputtering current and time and the relationship between these parameters may be determined by the EQCM technique [17].

In this study, a Dynavac sputter coater was employed. Platinum and gold targets were used to apply a thin, conductive metal layer to the outer surface of either microporous polyvinylidene fluoride (PVDF) hollow fibres or flat membranes, or polyurethane plastic tubes for subsequent electrochemical deposition of polypyrrole.

2.9 ELECTRICAL CONDUCTIVITY MEASUREMENT

A home-made four point probe was used to measure the sheet resistance or conductivity of various conductive materials including Pt or Au coated PVDF membrane or hollow fibre and polypyrrole coated on those metallised materials. The sheet resistance was usually used as an indicator of the quality of the coating if the conductivity was difficult to determine due to the inhomogeneous coating on a porous structure. This method typically employs four chemically inert metal electrodes symmetrically placed in a linear pattern, as illustrated in Figure 2-11. A constant current was applied between the outer electrodes and the potential drop between the

inner electrodes was measured. This arrangement allows for an accurate determination of the impedance of a conductive material by eliminating contact resistance from the measurement. Depending on the geometrical form of a given material, the sheet resistance and conductivity can be calculated according to:

$$R_s = \frac{V / I}{L / W} \qquad \text{..... 2-14}$$

where V is the potential drop between inner electrodes, I is the current applied between the outer electrodes, L is the spacing distance (cm) between inner electrodes and W is the width of rectangle strip of sample film, which must be smaller than the length of individual electrode).

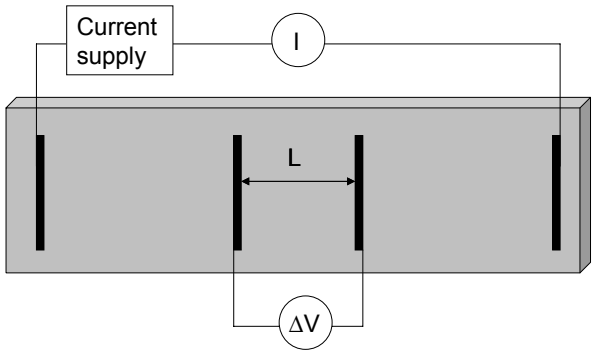

Figure 2-11 The four-point-probe for the measurement of electrical conductivity. Potential drop (ΔV) between inner electrodes was measured while a constant current (*I*) was applied between outer electrodes.

In addition, a commercial Jandel (Model R-2) four point multiheight probe has also been used. According to the manufacture's notes [18], the sheet resistance and bulk resistivity for wafers and films is given by:

$$R_s = 4.532 \times V / I \quad \text{..... 2-15}$$

$$\rho = R_s \times t = 4.532 \times V \times t / I \quad \text{..... 2-16}$$

where the number of 4.532 is the correction factor generally for samples that have a thickness that does not exceed 0.625 mm of the probe spacing and a diameter larger than 6 mm (about 10 times of the probe spacing), t is the thickness of sample in cm.

2.10 REAGENTS AND MATERIALS

Pyrrole (Merck) was distilled, stored at about –20 ºC under $N_{2\ (g)}$ before use. Phosphate buffer (PBS) was freshly prepared according to the manufacture's instructions by dissolving one phosphate buffered saline tablet (Sigma) in 200 mL of Milli-Q water. At 25 ºC, the as-prepared PBS buffer has a pH value of 7.4, containing 0.01 M phosphate buffer, 0.0027 M potassium chloride and 0.137 M sodium chloride. Tetrabutylammonium hexafluorophosphate ($TBA.PF_6$, Aldrich), lithium triflouromethane-sulfonimide (LiTFSI, 3M), sodium perchlorate ($NaClO_4$, Aldrich), potassium chloride (KCl, Aldrich), sodium dodecylbenzenesulfonate (NaDBS, Aldrich), tetrabutylammonium perchlorate (TBAP, Fluka), acetonitrile (ACN, Univar), propylene carbonate (PC, 99.7% anhydrous, Aldrich) were purchased and used without further purification. The ionic liquids, 1-ethyl-3-methylimidazolium (bis) trifluoromethanesulfonimide (EMI.TFSI) and 1-butyl-3-methyl-imidazolium hexafluorophosphate ($BMI.PF_6$) were obtained as a gift from Jakub H. Mazurkiewicz from Intelligent Polymer Research Institute, University of Wollongong [19]. All aqueous solutions were made from Milli-Q water (Millipore) and purged with nitrogen gas for 10 minutes prior to use.

Hydrophobic and hydrophilic polyvinylidene fluoride filter membrane (PVDF, Millipore) of 0.45 μm pore size, 75 % porosity and ~

110 μm thickness was chosen as the backing material for the fabrication of mechanical sensors or actuators. Both of these were purchased from Millipore, in which the hydrophilic version was converted from the hydrophobic version by the manufacture's proprietary surface treatment process.

2.11 COMMON ELECTROCHEMCIAL INSTRUMENTATION SET-UP

Electrochemical methods including CV, chronoamperometry and chronopotentiometry were performed using an EG&G Princeton Applied Research Model 363 Potentiostat/galvanostat or Bioanalytical Systems CV-27 potentiostat. Data was logged using either EChem v1.5.2 or Chart v4 (ADInstrument) through a MacLab 4e (ADInstrument) interface into a PC computer. Data manipulation and presentation were made using EChem, Chart, Microsoft Excel or Origin v6.0 software packages.

A Solartron system including the SI 1287 electrochemical interface and SI 1260 impedance / gain – phase analyser was used for impedance spectra measurements. Data was logged using ZPlot v2.2 (Scribner Associates, Inc.) and manipulated using ZView2 v.2.2 (Scribner Associates, Inc.). This system was also used for CV, pulsed potential and pulsed current experiments for polypyrrole trilayer actuators. In such cases, CorrWare v.2.2 software (Scribner Associates, Inc.) was used for data acquisition and CView2 v. 2.2 (Scribner Associates, Inc.) was used for data manipulation and presentation.

2.12 ELECTROCHEMICAL CELL

Two different electrochemical cells were used in this work. One of these was the two-electrode cell employed in galvanostatic polymerisations. This cell had a volume of 100 ml and was designed for the preparation of polymer actuators and sensors (Figure 2-12). The working lead from a potentiostat was connected to both sides of a metal sputter-coated PVDF membrane working electrode via the stainless steel plates used to maintain a stable electrical contact. Reference and auxiliary leads were coupled together and connected to the stainless steel mesh auxiliary electrode to provide sufficient surface area for galvanostatic deposition of ICP polymers. In addition, a polyethylene mesh served as a cell separator to avoid any possible electrical contact (short circuit) between the working and auxiliary electrodes during electrochemical polymerisation.

Another cell with 20 ml capacity was also designed for standard electrochemical polymerisation and characterisation (Figure 2-13). The general principle in designing this electrochemical cell was that the surface area of the auxiliary electrode should be much larger than the working electrode to ensure that the voltage difference between the working and auxiliary electrodes is smaller than the upper limit of the potentiostat and that the current is always uniform at the working electrode. The set-up used ensures the placement of electrodes in all cells was reproducible.

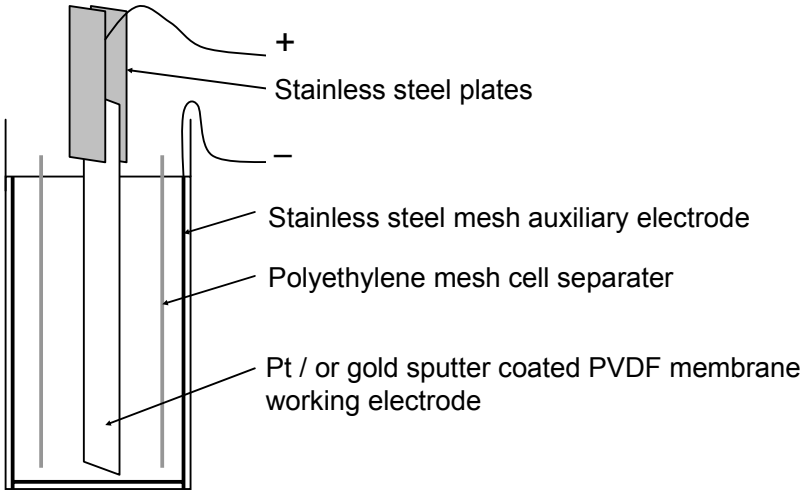

Figure 2-12 The two-electrode cell configuration for the preparation of polymer actuators and sensors.

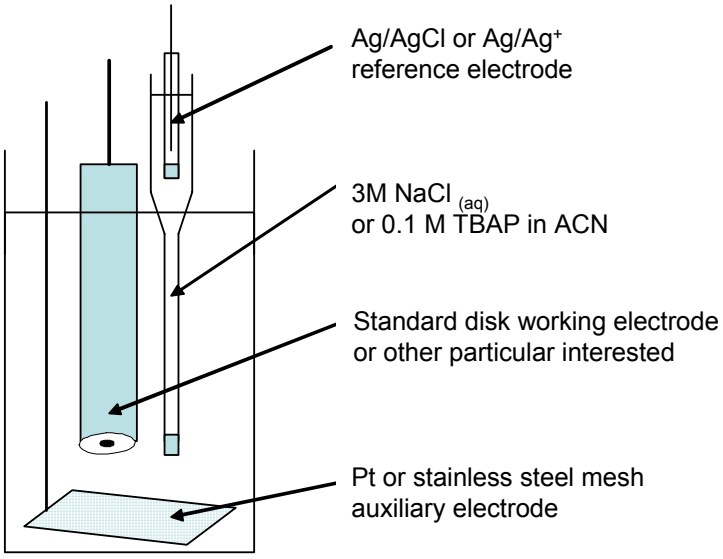

Figure 2-13 The three-electrode cell configuration used for ICP-modified electrode or device preparation and characterisation. Here a Ag/AgCl (3 M NaCl salt bridge) reference electrode was used for aqueous solutions and a Ag/Ag^+ reference electrode (0.1 M TBAP in acetonitrile salt bridge) was used for organic solvents. Platinum or stainless steel mesh was used as the auxiliary electrode.

2.13 REFERENCES

1. Horwood, E. *Instrumental methods in electrochemistry*; Southampton Electrochemistry Group, Halsted Press,: Chichester, New York :, 1985.
2. *Physical electrochemistry : principles, methods, and applications / edited by Israel Rubinstein*; M. Dekker,: New York :, c1995.
3. Skaarup, S., West, K., Gunaratne, L., Vidanapathirana, K.P. and Careem, M.A., *Solid State Ionics*, 136 (Special Issue SI) (2000) 577-582.
4. Millan, K.M. and Mikkelsen, S.R., *Analytical Chemistry*, 65 (17) (1993) 2317-2323.
5. Garnier, F., Korri-Youssoufi, H., Srivastava, P., Mandrand, B. and Delair, T., *Synthetic Metals*, 100 (1) (1999) 89-94.
6. Spinks, G.M., Liu, L., Wallace, G.G. and Zhou, D.Z., *Advanced Functional Materials*, 12 (6-7) (2002) 437-440.
7. Yakovleva, A.A., *Russian Journal of Electrochemistry*, 36 (12) (2000) 1275-1282.
8. Wu, Y., Moulton, S.E., Too, C.O., Wallace, G.G. and Zhou, D., *Analyst*, 129 (2004) 585-588.
9. Parker, J.R., Duan, Y.Y. and Clark, G.M., 1999; Vol. 2002.
10. Nyberg, T., Inganas, O. and Jerregard, H., *Biomedical Microdevices*, 4 (1) (2002) 43-52.
11. Jager, E.W.H., Immerstrand, C., Peterson, K.H., Magnusson, K.E., Lundstrom, I. and Inganas, O., *Biomedical Microdevices*, 4 (3) (2002) 177-187.
12. Yoon, C.O., Sung, H.K., Kim, J.H., Barsoukov, E., Kim, J.H. and Lee, H., *Synthetic Metals*, 99 (3) (1999) 201-212.
13. Cottis, R. and Turgoose, S. *Electrochemical impedance and noise*, V.7 ed.; NACE International: Huston, TX, c1999.
14. Tallman, D.E. *in a tutorial material: Electrochemical Impedance Spectroscopy: A Primer*: Fargo, ND, USA, 2005; pp 7.
15. Brisdon, A.K. *Inorganic spectroscopic methods / Alan K. Brisdon*; Oxford University Press,: Oxford ; New York :, 1998.
16. *Instruction Manual of Dual-Mode Lever Arm Systems*; Aurora Scientific Inc., 2002.

17. Zhou, D. *Development of Conducting Polymer Membrane Structures for Protein and Gas Separation*; PhD thesis, University of Wollongong, 1997.

18. *Maintenance and Use of the Multiheight Probe*; Jandel Engineering Ltd, 2004.

19. Lu, W., Fadeev, A.G., Qi, B., Smela, E., Mattes, B.R., Ding, J., Spinks, G.M., Mazurkiewicz, J., Zhou, D., Wallace, G.G., MacFarlane, D.R., Forsyth, S.A. and Forsyth, M., *Science*, 297 (5583) (2002) 983-987.

PART 1

CHAPTER 3 POLYPYRROLE MECHANICAL SENSORS

3.1 INTRODUCTION

In a study by Takashima *et al.* inherently conducting polymer (ICP) materials were reported to be able to convert mechanical energy to electricity [1]. They observed a mechanically induced electrochemical current in a free-standing film of polyaniline (PAni) and demonstrated that the induced charge was dependent upon the tensioning load and the degree of doping. The authors suggested that the stretching of main chain molecules in ICPs may result in a narrowing of the band gap, which would change the density of states (DOS) near the chemical potential, thereby inducing a redox current.

The effect of the dopant ion (A^- defined in Equation 1-1 and Equation 1-2) was not considered in the above study, and this may play an important role in the mechanism of electrical current generation. In fact, very little work has been done in this respect. It is well known that the dopant ions play an important role in the use of ICPs to convert electricity to mechanical energy [2-4]. Upon electrical stimulation, the polymer undergoes significant volume changes accompanied by the insertion / removal of ions. For small and mobile dopant anions, polymer oxidation predominantly results in the penetration of negatively charged anions from solution into the positively charged polymer backbone causing the polymer to swell. Upon reduction, charge upon the polymer chains are neutralised, electrostatic forces between the polymer-solvent and polymer-counter ions become negligible, and polymer-polymer interactions through Van der Waals forces become strong. As a result, counter-anions can freely diffuse across the polymer/solution interface to the solution, resulting in polymer shrinkage.

At the opposite extreme, if the dopant anion is bulky and immobile, upon polymer reduction, these counter-ions would be entangled within the

polymer matrix and remain inside the neutralised polymer. At this point, mobile cations would be incorporated from solution to balance the negatively charged counter-ions, resulting in polymer expansion. Upon oxidation, the polymer backbone would again become positively charged, promoting the expulsion of mobile cations from the polymer and resulting in polymer shrinkage.

In this Chapter, the reverse process was investigated and the use of polypyrrole to convert mechanical to electrical energy was investigated. It was envisioned that this effect might prove useful as a mechanical sensor for the cochlear implant. The effect of the dopant ions used was studied in order to further elucidate the origins of mechanically induced charge in ICPs. A laminated polypyrrole mechanical sensor was utilised since this is simple to construct and bending induced electrical parameters are readily measured. Using this laminated structure, the effect of dopant ions, redox states, and electrolyte composition were investigated. The effect of the mechanical perturbation frequency and the correlation between displacement and induced charge were also considered.

The observation that the polarity of induced voltage was dependant on the size of the counter-ion used is in disagreement with the theory of Takashima and co-workers [1]. A new mechanism of “stress induced ion flux” is therefore proposed in this Chapter.

3.2 EXPERIMENTAL

In the following sections, the fabrication of laminated polypyrrole mechanical sensors and the experimental set-up for sensor testing are described.

3.2.1 REAGENTS AND MATERIALS

For all reagents and materials mentioned in this Chapter refer to section 2.10 in Chapter 2.

3.2.2 PREPARATION OF MECHANICAL SENSORS

Sensors were constructed as a multilayered laminated structure. PVDF membranes with a thickness of ~ 110 μm and an average pore size of 0.45 μm were employed as the backing material for laminated sensors. On each side of this membrane, a thin layer of platinum was sputter coated at 30 mA for 20 minutes in a magnetron sputter coater where Ar pressure was maintained at 2×10^{-3} mBar. Using these coating conditions, ~ 70 nm of Pt would be deposited on a flat solid surface. Keeping other variables constant, both hydrophobic and hydrophilic versions of PVDF membranes were employed for use with aqueous and organic solvent solutions, respectively.

Polypyrrole was deposited galvanostatically using various current densities from polymerisation solutions containing pyrrole monomer and different dopant ions. All polymerisation solutions were purged with $N_{2(g)}$ for ~ 20 minutes prior to use. A cross-section schematic of the sensor is illustrated in Figure 3-1. Following electrodeposition, all edges of the as-prepared bulk membrane were trimmed off and then cut to small strips using a scalpel blade, ensuring that the two PPy layers on opposite sides of the

PVDF membrane were not in electrical contact. The general structure of the sensors may be denoted as $(PPy^{(+)}/A^-)$/Pt/PVDF/Pt/$(PPy^{(+)}/A^-)$ where the A^- is the dopant ion used. The bulk thickness of sensors was measured using a digital micrometer.

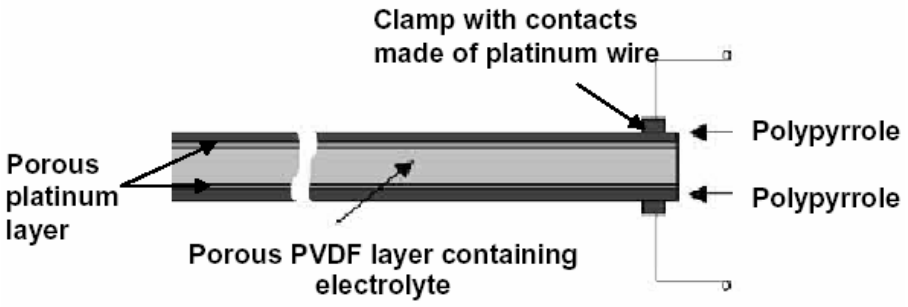

Figure 3-1 Cross-sectional schematic showing the structure of a laminated mechanical sensor. The porous PVDF membrane acted as a backing for the laminated device and as an electrolyte reservoir.

Specifications for each of the mechanical sensors prepared are given in detail below.

(PPy/DBS)/Pt/PVDF/Pt/(PPy/DBS) sensor: Polypyrrole was electrodeposited onto a platinised hydrophilic PVDF membrane at a current density of 1.0 $mA.cm^{-2}$ for 30 minutes from an aqueous solution containing 0.2 M pyrrole monomer and 0.2 M DBS at room temperature. Following electrodeposition, sensor strips were rinsed several times with Milli-Q water to remove any remaining pyrrole monomer. Both sides were potentiostatically conditioned at either –0.8 V or +0.6 V (*vs*. Ag/AgCl) for 5 minutes in aqueous 0.2 M DBS prior to testing in order to probe the effect of oxidation state.

(PPy/ClO_4)/Pt/PVDF/Pt/(PPy/ClO_4) sensors: Polypyrrole was electrodeposited on a platinised hydrophilic PVDF membrane at a current density of 1.0 mA.cm^{-2} for 30 minutes in an aqueous solution containing 0.2 M pyrrole monomer and 0.1 M $NaClO_4$ at room temperature. Following the electrodeposition, sensor strips were rinsed several times with Milli-Q water to remove any remaining pyrrole monomer. Both sides were potentiostatically conditioned at either –0.8 V or +0.6 V (*vs*. Ag/AgCl) for 5 minutes in aqueous 0.1 M $NaClO_4$ prior to testing in order to probe the effect of oxidation state.

(PPy/PF_6)/Pt/PVDF/Pt/(PPy/PF_6) sensor: Polypyrrole was electrodeposited at a current density of 0.10 mA.cm^{-2} for 12 hours from a solution containing 0.06 M pyrrole monomer, 0.05 M TBA.PF_6 and 0.5% (w/w) Milli-Q water in PC at the temperature of ~ –20 ºC (attained by carrying out experiment in a commercial freezer). Following electrodeposition, sensor strips were rinsed several times with PC to remove any remaining pyrrole monomer. The sensor samples were padded dry with tissues and stored in a relatively large volume of electrolyte for 12 hours containing either 0.25 M TBA.PF_6 in PC, pure BMI.PF_6 or various mixtures of BMI.PF_6 and PC.

3.2.3 SENSOR TESTS

The Dual Mode Mechanical Lever Arm system and electrochemical equipment including MacLab interface and a Princeton Applied Research (PAR) EG&G Potentiostat/Galvanostat were employed for sensor testing, and have been described in more detail in Section 2.7 and Section 2.11.

The experimental set-up for sensor testing is illustrated in Figure 3-2. The Dual Mode Lever Arm System was controlled by a conventional

function generator and used to apply a sinusoidal displacement at the desired amplitude and frequency at the free end of the sensor strip where the insulated lever arm tip perpendicularly attached to the sensor tip at a point ~ 2 mm from the sensor's free end. The actual length of the sensor sample between the clamp and the contact point to the lever arm tip was ~ 16 mm. In particular, the consistent attachment of lever arm to the sensor must be met and a small range of sliding of the lever arm along the sensor must be allowed as well.

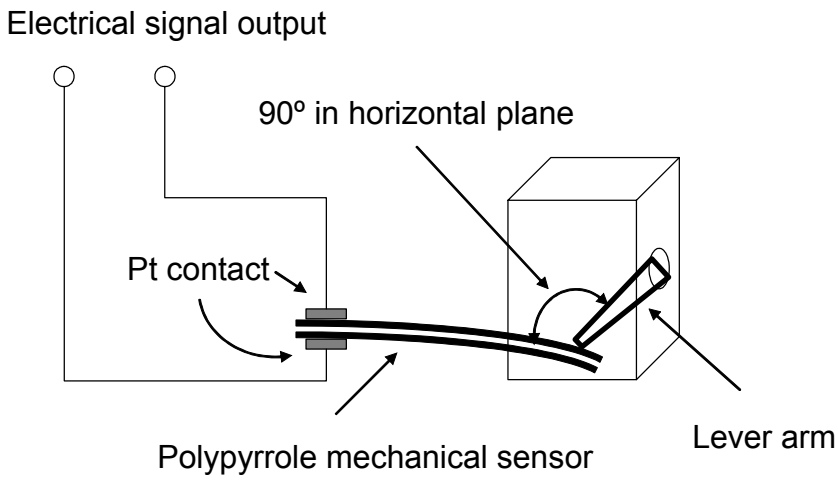

Figure 3-2 Set-up using an Aurora Dual-Mode Lever Arm System to apply sinusoidal displacement at the free end of a laminated polypyrrole mechanical sensor. The tip of the lever arm was insulated and perpendicularly attached to the sensor, where the existence of liquid electrolyte helped this physical attachment during the test.

The upward and downward motions of the lever arm were recorded as positive and negative displacements, respectively. The output voltage (i.e. the potential difference between the two surfaces of the sensor) was monitored directly using MacLab via a BNG cable connection, in which, the upside of the sensor was always connected to the BNG cable's shield lead. When the downward displacement induced a negative voltage, this was

referred to as an "in phase" response. Whereas when a positive voltage was induced, this was referred to as an "out of phase" response.

To measure the charge output from the sensor, a potentiostatic method was employed. A constant potential of 0.000 V was applied by the potentiostat. The induced charge from deflection of the sensor was then determined by the current drawn from the potentiostat in order to maintain the potential. This current was integrated to represent the charge output. In this set-up, the reference and counter electrode leads from the potentiostat were shorted and connected to the upper surface of the sensor strip, while the opposite surface was connected to the working electrode lead.

3.3 RESULTS AND DISCUSSION

Initially the effect of a number of experimental parameters on the output of the conducting polymer based sensor in response to displacement was investigated. The self-contained sensor set-up shown in Figure 3-1 was employed. The effect of the dopant used and the redox state of the polymer as well as the electrolyte was investigated. The effect of frequency of electrical stimulation on output voltage, and the induced charge output was considered. The correlation between the induced charge output and static displacement was also determined.

Note that blank experiments have been performed using platinised PVDF membranes alone in every electrolyte used in this study. Using this structure, no signal output was detectable on the application of mechanical displacement.

3.3.1 THE EFFECT OF DOPANT AND REDOX STATE ON VOLTAGE OUTPUT

The study of the effect of dopant and redox state of the polymer was aimed at probing the electrical signal generation mechanism (Figure 3-3). The sensors produced a sinusoidal voltage output in response to the sinusoidal displacement input at fixed amplitude of 8 mm and a fixed frequency of 0.5 Hz. The effect of the dopant and redox state is discussed below by considering the properties of *(PPy/DBS)/Pt/PVDF/-Pt/(PPy/DBS)* and *(PPy/ClO_4)/Pt/PVDF/Pt/(PPy/ClO_4)* sensors.

An "in phase" voltage output was observed for the *(PPy/DBS)/Pt/PVDF/Pt/(PPy/DBS)* sensor. In other words, during downward displacements the lower electrode was compressed and recorded a negative electrical potential compared with the upper electrode (stretched). The sensor prepared in the reduced form produced a larger voltage output (0.28 mV) than that observed for the sensor prepared in the oxidised form (0.18 mV). In contrast, an "out of phase" voltage output was observed for the *(PPy/ClO_4)/Pt/PVDF/Pt/(PPy/ClO_4)* sensor. Here the compressed electrode gave a more positive electrical potential than the expanded electrode. For the *PPy/ClO_4* sensor, the oxidised form produced a larger amplitude of voltage output (0.21 mV) compared to that observed for the reduced form (0.11 mV). Both the sign of the voltage output and the effect of initial oxidation state was opposite for the two different sensors. A discussion of these results follows.

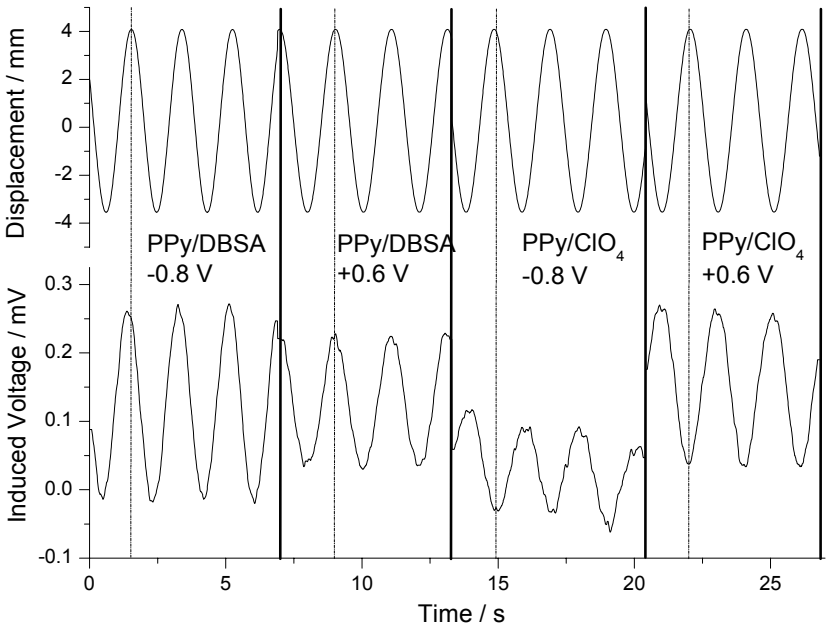

(a)

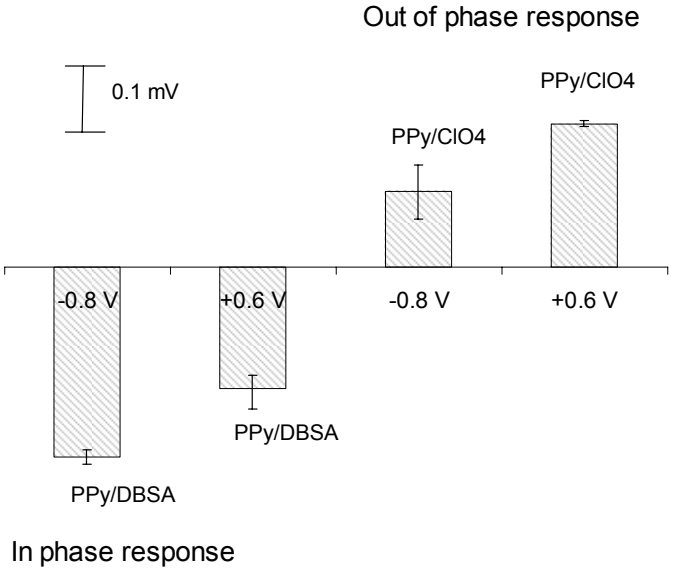

(b)

Figure 3-3 Effect of dopant and redox states on the voltage output of mechanical sensors. The PPy/DBS sensor was preconditioned at either +0.6 V or -0.8 V in aqueous 0.2 M DBS for 5 minutes prior to testing. The PPy/ClO_4 sensor was preconditioned at either +0.6 V and –0.8 V in aqueous 0.1 M $NaClO_4$ for 5 minutes prior to testing. The sensor dimension was 20 mm × 2 mm × ~ 125 μm thick and the sinusoidal displacement was controlled at a constant amplitude of 8 mm and at a constant frequency of 0.5 Hz. (a) Raw data, (b) dependency of induced voltage on dopant and redox state.

The results summarised in Figure 3-3 show that the polarity of the output voltage from a sensor was dependent on the dopant used in the polymer. The change in polarity of the voltage resulted from the difference in the induced surface charge, which means that an excessive charge was induced across the sensor conductive polymer layers. The sensor that used the small and mobile ClO_4^- dopant resulted in a positive charge developing on the compressed side upon displacement, while the sensor with the large and immobile DBS dopant produced a negative charge on the compressed side upon displacement. The model proposed by Takashima *et al* [1] can not explain this phenomenon. In their model, the induced current was attributed to the change in the density of states in the π-conjugated polymer backbone, this would be related to the polymer structure and does not take into account the effect of the dopant ions. These results indicate that the mechanically induced change in the density of states is not the dominant mechanism in the mechanically induced charge generation observed here.

To account for the dopant effect, a new model - stress induced ion flux is proposed (Figure 3-4). Due to the nano-dimensional, entangled conducting polymeric structure, the polymer backbone behaves like an ion filled porous gel, where the unbalanced charged distribution along the backbone is dominated by the movement of dopant ions. In this case, the driving force of ion flux is mechanical deformation. Upon the application of a mechanical stress, an ion flux is generated within the polymer, which would be refilled again upon relaxation. In this process, the dopant ion concentration in close proximity to the charged polymer backbone can be varied, which results in a temporary imbalance in charge on the polymer backbone, inducing a potential difference across the sensor strip.

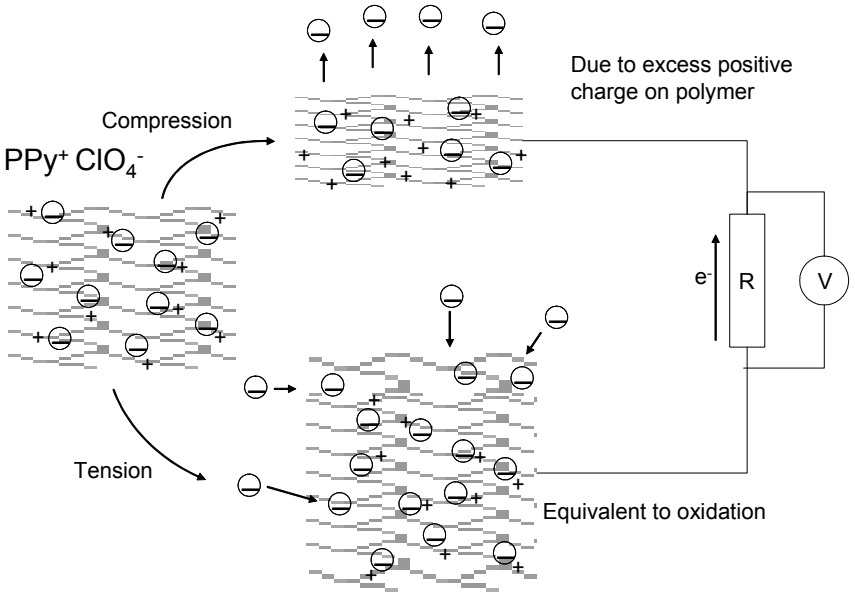

(a)

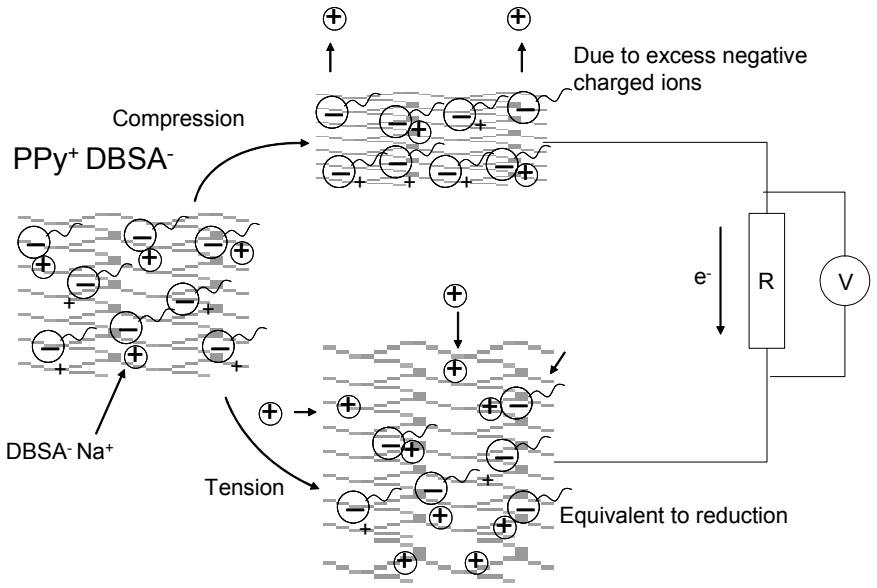

(b)

Figure 3-4 Schematics describing the proposed model of the stress induced ion flux mechanism for (a) small dopants (e.g. ClO_4^-) and (b) large dopants (e.g. DBS^-).

In the case of relatively small dopant ions (e.g. ClO_4^-), mechanical compression pushes the ion flux away from the polymer backbone, decreasing the dopant ion concentration and resulting in a temporarily

unbalanced positive charge on the polypyrrole backbone. This unbalanced positive charge increases the electrochemical potential of the bulk material, resulting in a higher potential on the compressed surface than the tensioned surface of the sensor. This results in what has been called the "out of phase" voltage as shown in Figure 3-3. It was believed that a higher initial doping density of ClO_4^- could generate a larger potential variation across the sensor in response to a given displacement. It is well known that the concentration of the dopant ion ClO_4^- is higher in the oxidised state of the polymer than that in the reduced state. Therefore, the sensor conditioned at + 0.6 V would be expected to generate a larger voltage output than that conditioned at – 0.8 V. This prediction is verified by the results shown in Figure 3-3.

For a bulky and immobile dopant like DBS^-, a mobile cation (i.e. Na^+) is involved in the ion flux to balance the charge. Mechanical compression pushes the cation flux away from the polymer backbone, decreasing the cation concentration, resulting in a temporary unbalanced negative charge (due to DBS^-) in close vicinity to the polymer backbone. This cation movement decreases the electrochemical potential of the bulk material, resulting in a lower potential on the compressed side than on the tensioned side of the bending sensor. This results in an "in phase" voltage as shown in Figure 3-3. It is known that the concentration of Na^+ cations in PPy/DBS is lower in the oxidised state of the polymer than in the reduced state. Therefore, the sensor conditioned at - 0.8 V would be expected to generate a larger amplitude of "in phase" voltage output than that conditioned at + 0.6 V. Again, this prediction is verified by the results shown in Figure 3-3.

The proposed "stress induced ion flux" mechanism has previously been used to explain the stress induced charge generation in ionic polymer/metal composite (IPMC) materials [5, 6]. When the material is placed between two electrodes, the deficit of ion charge in one electrode and

excess in the other can create a voltage in relation to the bending or deformation. Data obtained here suggest that similar behaviour is possible within ICPs.

The mechanically induced electricity in ICPs has been theoretically predicted by Madden [7]. Based on the knowledge on electrochemical actuation behaviour of ICPs, the existence of reversed strain-charge coupling is given by:

$$\Delta\varepsilon = \alpha \cdot \Delta\rho \qquad \text{..... 3-1}$$

where $\Delta\varepsilon$ is the change in strain, α is the strain to charge coefficient, $\Delta\rho$ is the change in charge per volume) [8].

If charge is allowed to transfer, a change in work density can be expressed as [7]:

$$\Delta W_m = \sigma \cdot \Delta\varepsilon = \sigma \cdot \alpha \cdot \Delta\rho \qquad \text{..... 3-2}$$

hence,

$$W_m = \int \sigma \cdot \alpha \cdot \Delta\rho \qquad \text{..... 3-3}$$

According to Madden, Equation 3-2 predicts that applied stress inhibits the insertion of charge and assists in it's removal since the applied stress functions like an applied voltage (called mechanical voltage $V_m \equiv \sigma \cdot \alpha$). Therefore, the sign of the potential is determined by both the sign of the applied stress, σ (i.e. to stretch or compress) and the sign of the strain to charge coefficient, α. With regards to α, if the strain is induced by the insertion of cations rather than anions, the sign of V_m is reversed. The experimental results obtained in this study are consistent with these theoretical predictions:

(1) The sign of measured voltage is dependent on the direction of deformation and the dopant used in the polymer,

(2) The measured voltage output is in the range from 0.1 to 0.3 mV while the predicted V_m is expected to be between 0.15 to 4.5 mV in polypyrrole [7]. Again the theoretical prediction supports the proposed "stress induced ion flux" model.

According to the proposed model, it was quite interesting to consider a situation where cation and anion movement would be competitive upon the application of stress. In this scenario "in phase" and "out of phase" voltage outputs would cancel each other to give a net voltage output of zero. Such a scenario is considered in the following section.

In an attempt to provide more supporting evidence for the "stress induced ion flux" mechanism proposed in this study, a number of *(PPy/PF_6)/Pt/PVDF/Pt/(PPy/PF_6)* sensors (PF_6^- as the anion dopant) were soaked in BMI.PF_6:PC electrolyte and their displacement sensing properties characterised. Figure 3-5 shows the effect of the molar ratio of BMI.PF_6 to PC. The lowest molar ratio of 1:10 produced an "out of phase" voltage output at an amplitude of ~ 0.07 mV. Increasing the molar ratio to 1:2 decreased the amplitude to ~ 0.04 mV. The highest molar ratio of 10:1 produced an "in phase" voltage output at an amplitude of ~ 0.04 mV. Decreasing the molar ratio from 10:1 to 2:1 drastically decreased the output voltage to a negligible amplitude of ~ 0.02 mV. A cancellation effect resulting in zero voltage output was observed when the molar ratio was 1:1. It is known that ions in ionic liquids are associated in clusters [9]. Therefore for the mixed electrolyte of BMI.PF_6 with PC, a higher concentration of BMI.PF_6 would give less mobile anions, producing an "in phase" voltage output, as observed in Figure 3-5. Conversely an "out of phase" voltage output would occur at lower concentrations of the BMI.PF_6, as observed. Due to the breaking up of ion clusters, at the molar ratio of 1:1, no recognisable voltage output was observed, indicating that the "in phase" and

"out of phase" voltage outputs cancelled each other to yield a net voltage output of zero.

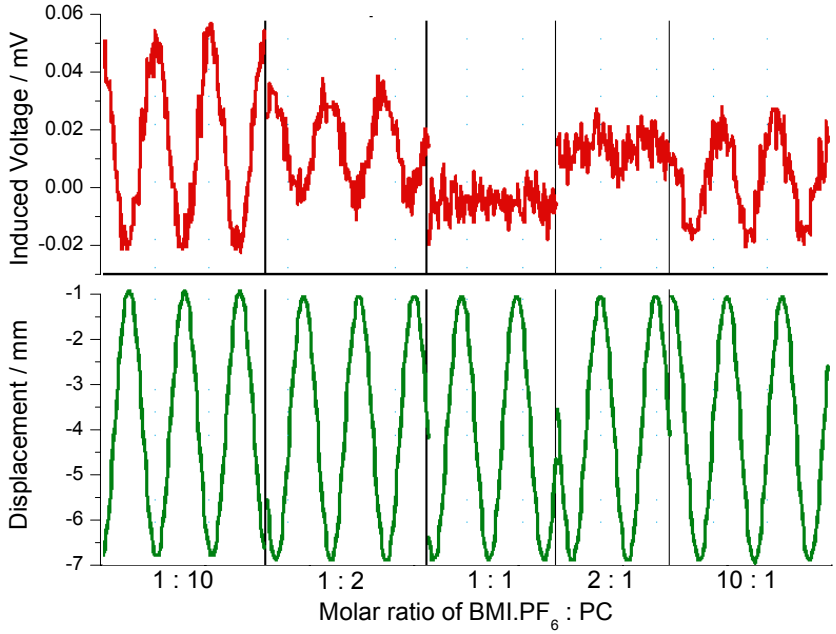

Figure 3-5. The effect of $BMI.PF_6$: PC molar ratio on the displacement sensing properties of polypyrrole mechanical sensors. The sensor dimension was 20 mm × 2 mm × ~ 140 μm thick and the peak-to-peak amplitude of sinusoidal displacement was controlled at 6 mm at a frequency of 0.5 Hz.

The above discussion revealed the phenomenon of ion shifting in response to mechanical stress in ICPs and suggests that the charge is induced at the polymer / electrolyte interface. Considering that the output voltage is dependent on the amount of induced charge as well as the impedance characteristics of the sensor, it would therefore have the output voltage a frequency dependency. The following sections present findings for the PPy mechanical sensor's performance in relation to the frequency of mechanical displacement. Only qualitative analysis of the findings are

discussed as quantitative mathematical treatment was considered beyond the scope of this thesis.

3.3.2 THE EFFECT OF DISPLACEMENT FREQUENCY OF SENSOR ON VOLTAGE OUTPUT

The sensor voltage output of a $(PPy/PF_6)/Pt/PVDF-/Pt/(PPy/PF_6)$ mechanical sensor in response to sinusoidal displacement input at various frequencies is illustrated in Figure 3-6. In general, an "out of phase" sinusoidal voltage output was observed in response to sinusoidal displacement, although there was a slight phase shift observed at lower frequencies (< 4 Hz). The voltage output in this experiment was < 1 mV, with a maximum voltage output of 0.29 mV at a frequency of ~ 0.4 Hz. At frequencies < 0.4 Hz, the amplitude of voltage output decreased steadily until close to zero at the lowest frequency tested of 0.01 Hz. At frequencies > 0.4 Hz, the amplitude of voltage output decreased to 0.18 mV at ~ 3 Hz and stayed constant for frequencies up to and including the highest frequency tested of 10 Hz. Higher frequencies were not possible due to the large inertia of the lever arm. The fact that the maximum amplitude for the voltage output occurred at 0.4 Hz suggested that the mechanically induced ion flux was a relatively slow process. At frequencies < 0.4 Hz, a decrease in the voltage output occurred, probably owning to a parasitic discharging that 'bleeds off' the charge. At frequencies > 0.4 Hz, the rate of ion flux was too slow to keep up with the frequency of displacement, also resulting in a decrease in the voltage output. This explanation was supported by the bending actuator studies that exhibited a significant decrease in actuation amplitude at > 4 Hz [10].

The frequency dependence of the voltage output of polypyrrole mechanical sensors suggested that the galvanostatic mode of operation

would not be suitable for application to displacement sensing. The induced charge output was considered as an alternative approach.

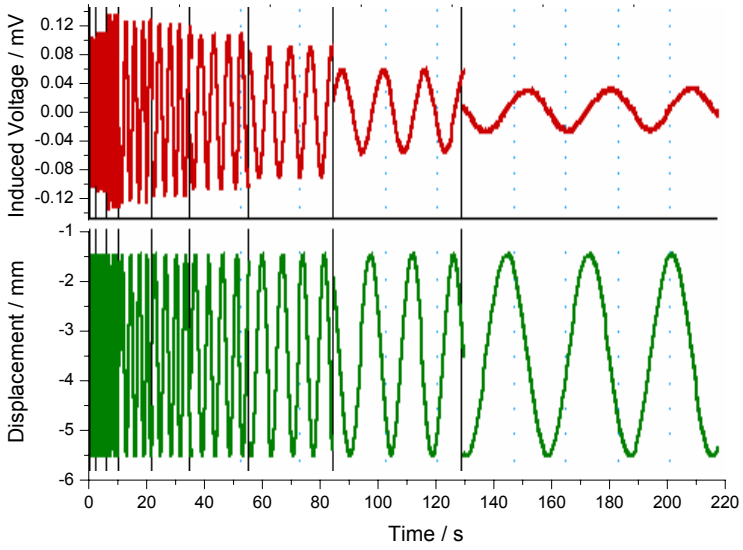

(a)

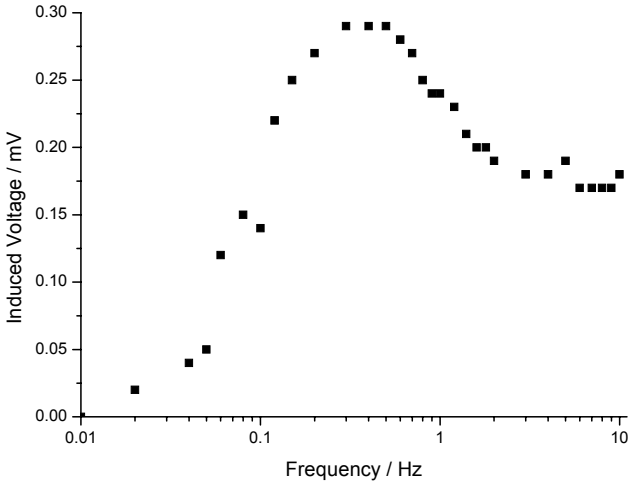

(b)

Figure 3-6 Effect of frequency on the amplitude of sensor voltage output plot: (a) the real time waveform of the induced voltage and (b) relationship between the voltage amplitude and mechanical displacement frequency. A *(PPy/PF_6)/Pt/PVDF/Pt/(PPy/PF_6)* sensor soaked in 0.25 M TBA.PF_6 in PC solution was used with dimensions of 20 mm × 2 mm × 140 μm. Sinusoidal displacement was controlled at a constant peak-to-peak amplitude of 4 mm.

3.3.3 EFFECT OF DISPLACEMENT FREQUENCY ON INDUCED CHARGE

The problem of the slow discharge of the polypyrrole using the voltage output approach was eliminated by using the potentiostatic mode where the induced charge output was monitored instead. At frequency < 0.01 Hz, the signal obtained could not be distinguished from the electrical noise. At the lowest frequency ~ 0.02 Hz, the induced charge was ~ 1.3 μC, which drastically decreased to near zero when the frequency was increased to the maximum 10 Hz (Figure 3-7).

The optimum frequency (~ 0.02 Hz) for displacement sensing using induced charge output suggested that the potentiostatic mode of operation for polypyrrole mechanical sensors was better suited to low frequency applications (e.g. for cochlear implantation) than the galvanostatic mode. In the galvanostatic mode (i.e. measuring the voltage output), the optimum frequency for displacement sensing was considerably higher (~ 0.4 Hz).

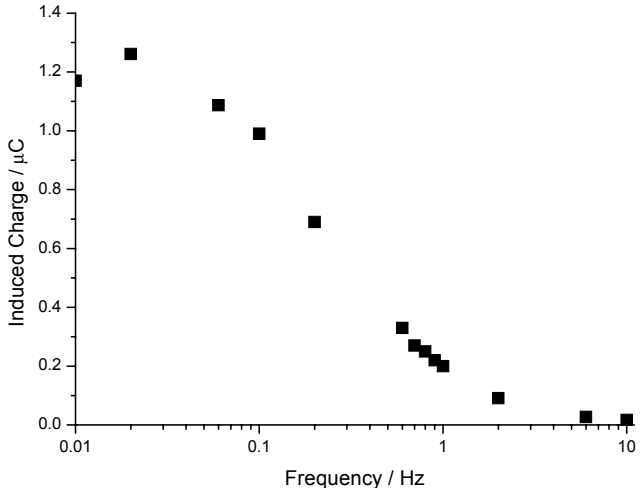

Figure 3-7. The effect of displacement frequency on the induced charge output of a *(PPy/PF_6)/Pt/PVDF/Pt/(PPy/PF_6)* sensor with dimensions of 20 mm × 1 mm × 140 μm. Sinusoidal displacement was controlled at a constant amplitude of 2 mm. The charge measured was the peak-to-peak charge difference.

3.3.4 CORRELATION BETWEEN INDUCED CHARGE OUTPUT AND STATIC DISPLACEMENT

The induced charge output in response to the application of stepped displacements for a *(PPy/PF_6)/Pt/PVDF/Pt/(PPy/PF_6)* sensor is illustrated in Figure 3-8. The induced charge output reproducibly increased and decreased following displacement where the sensor was held in various positions for ~ 20 seconds for both upward and downward displacement (Figure 3-8 (a)). A linear correlation between induced charge output and displacement was obtained with a slope of - 0.65 $\mu C.mm^{-1}$ (Figure 3-8 (b)), given the volume-to-charge coefficient at ~ 2500 $mm^3.C^{-1}$, which is significantly less efficient than its reverse process (0.1 $mm^3.C^{-1}$) according to Madden [7]. Nevertheless, these results show the possibility of using polypyrrole mechanical sensors to consistently monitor the static displacement as opposed to variable frequency displacement. The induced charge output was linearly correlated with displacement in both direction and magnitude.

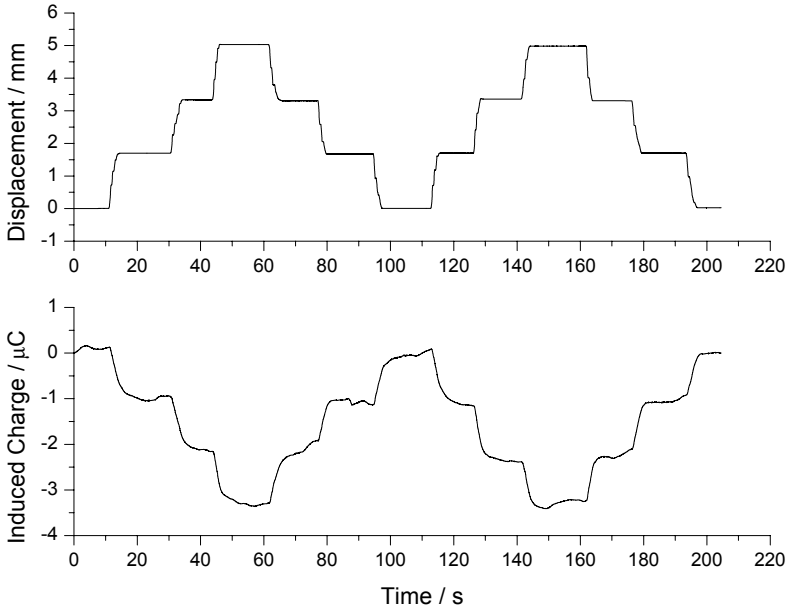

(a)

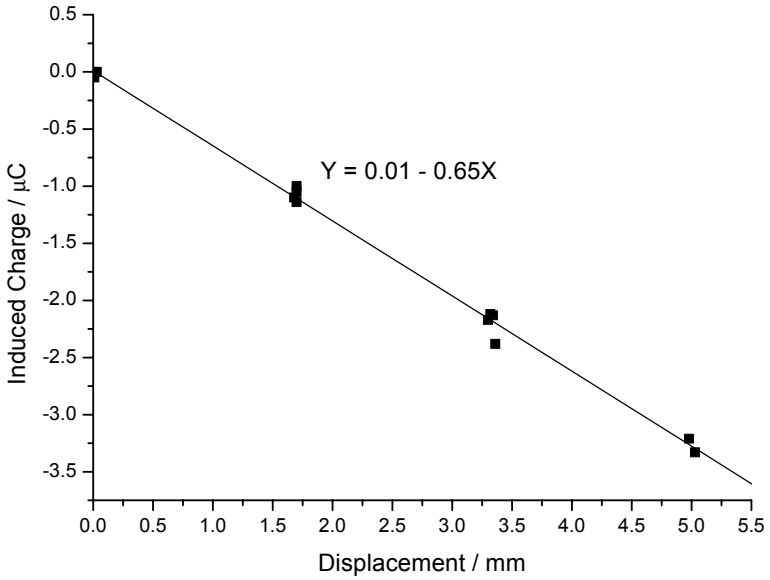

(b)

Figure 3-8. Correlation between induced charge output and displacement for a *(PPy/PF_6)/Pt/PVDF/Pt/(PPy/PF_6)* sensor. Dimensions: 20 mm × 1 mm × 140 μm. (a) Real-time data and (b) plot of sensor displacement *vs.* induced charge output.

3.4 CONCLUSION

Polypyrrole based mechanical sensors were shown to have the ability to detect mechanical displacement by monitoring of the induced voltage or induced charge output. A new model called the "stress induced ion flux" mechanism was proposed to explain the results that considered the effect of dopant and redox state on the displacement sensing properties of polypyrrole mechanical sensors.

It is envisaged that novel polypyrrole mechanical sensors have the ability to be readily scaled down to micro dimensions as has been described for electromechanical actuators [11], yielding compatibility with flexible structures and raising the possibility of biomedical applications.

Future work should investigate the miniaturisation of polypyrrole mechanical sensors for the Cochlear Implant. It is believed that the unique structure of such sensors would be compliant with the microscale cochlear device and would not interfere with the mechanical properties or movement of the cochlear device or structure to which it would be attached. Miniaturisation has the potential to make polypyrrole mechanical sensors particularly applicable to implants or wearable sensing structures.

3.5 REFERENCES

1. Takashima, W., Fukui, M., Uesugi, T., Kaneko, M. and Kaneto, K., *Synthetic Metals*, 85 (1-3) (1997) 1395-1396.
2. Wallace, G.G., Spinks, G.M., Liu, L., Zhou, D., Gao, M. and Dai, L., *SPIE 9th Ann. Intl. Symp. Smart Struct. Mater.*, (2002).
3. Baughman, R.H., *Synthetic Metals*, 78 (3) (1996) 339-353.
4. Otero, T.F. In *Handbook of Organic Conductive Molecules and Polymers*; H. S. Nalwa, Ed.; John Wiley & Sons Ltd.: Chichester, 1997; Vol. 4, pp 558.
5. Shahinpoor, M., *Electrochimica Acta*, 48 (14-16) (2003) 2343-2353.
6. Sadeghipour, K., Salomon, R. and Neogi, S., *Smart Mater. and Struct.*, 1 (1992) 172-179.
7. Madden, J.D. In *PhD thesis "Conducting Polymer Actuators", Mechanical Engineering*; Massachusetts Institute of Technology, 2000, pp 181.
8. Madden, J.D. In *PhD thesis "Conducting Polymer Actuators", Mechanical Engineering*; Massachusetts Institute of Technology, 2000, pp 144.
9. Tokuda, H., Hayamizu, K., Ishii, K., Susan, M.A.B.H. and Watanabe, M., *J. Phys. Chem. B*, 109 (2005) 6103-6110.
10. Wu, Y., Alici, G., Spinks, G.M. and Wallace, G.G., *Synthetic Metals*, Submitted (2006).
11. Smela, E., Ingamas, O. and Lundstrom, I., *Science*, 268 (5218) (1995) 1735-1738.

CHAPTER 4 POLYPYRROLE TRILAYER BENDING ACTUATORS

4.1 INTRODUCTION

Materials that can be operated at low voltage are desirable in the design of electromechanical actuators for biomedical applications, such as the cochlear implant. Suitable materials include ionic electroactive polymers (including inherently conducting polymers and ionomeric polymers), hydrogels [1], carbon nanotubes [2], and shape memory alloys. Hydrogels suffer mainly from relatively slow strain rates and relatively low stress generation. Carbon nanotube papers have only recently been discovered as possible actuators, however their strain generation is low (~ 0.7 %). Shape memory alloys operate through a thermal resistive heating cycle which has restricted their use in some applications due to slow response times and undesirable heat generation. It appears that ionic electroactive polymers represent an attractive prospect for low voltage actuation materials. Applications using such materials have been envisaged in artificial swimming fish, small dimensional robots (micrometer level) and in catheter systems [3] in biomedical devices.

Ionomeric-polymer actuation materials such as Nafion [4] and Flemion [5] use a metal/polymer/metal composite structure. The polymers are made of immobile fluorocarbon backbones (Figure 4-1) and mobile cations. It has been reported [3, 6] that the application of a voltage (< 5 V) on the metal electrode promotes electro-osmosis of cations (such as Na^+) toward the negatively charged electrode (cathode), resulting in a bending of the film towards the positively charged electrode (anode). A drawback of ionomeric actuators is the large relaxation phenomena, where, the actuator will gradually return back to its original position. It has been suggested that this is due to the presence of excess water near the cathode and subsequent back-flux. Although such processes are not obvious in Flemion using the tetrabutylammonium counter-ion due to the large size of the cation and low

mobility [5], the major disadvantage of this type of electroactive actuator is due to dehydration induced failure, hydrolysis and subsequent gas generation.

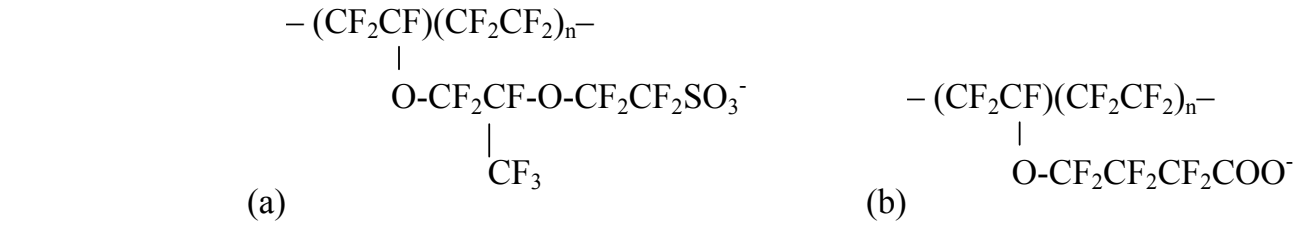

Figure 4-1 Chemical composition of (a) Nafion and (b) Flemion.

Unlike ionomeric polymers, inherently conducting polymers (ICPs) have the advantage of being able to maintain the strain generated [7]. In general, ions in ICPs are incorporated permanently to balance the positive charged polymer backbone (Equation 1-1), and only become mobile during the reduction process. The volume change in ICPs is primarily due to the reversible transport of ions, although solvent molecules also contribute to the overall volume change [8]. Useful mechanical work then can be obtained from this volume change. Extensive research has shown that the maximum stress generated by ICPs is 10 – 20 times greater than that generated by natural muscle [9] and could possibly reach 200 MPa [10]. Strains generated by ICP actuators typically range from 1 % to 10 % [9, 11, 12], however recently it has been reported that strains up to 26 % for polypyrrole (PPy) doped with trifluoromethanesulfonimide (TFSI) anion [13] can be achieved. This compares favourably to the 20% strain in natural muscle. ICP actuator strain rates of ~ 3.2% s^{-1} to give strains of ~ 1.1% [14] are common. Strain rates as high as 16 % s^{-1} have been obtained using polypyrrole doped with PF_6^- anion in a helix tube configuration [15].

Although they have shown many possible advantages, the realisation of practical, long cycle life actuators based on ICPs is still some way off,

and this is partly due to the electrolytes used. Aqueous or common organic solvent based electrolytes have the limitation of a narrow potential window, low environmental stability, and are susceptible to evaporation. A class of alternative electrolytes, ionic liquids, have received particular attention for possible use in ICP based actuators due to advantages of negligible vapour pressure, high ionic conductivities and broad electrochemical window [16]. In a previous study by Lu and co-workers [16], a cathodic expansion was reported for polypyrrole actuators cycled in BMI.PF_6 for which cation incorporation at the reduction state was suggested. It was not clear whether the original doped anions and the additional cations remained incorporated during prolonged application of a negative potential. A study of polypyrrole actuation (in terms of blocking force generation combined with elemental analysis) in ionic liquids at various applied potentials was considered in the present study to determine the extent, if any, to which dopant anions remain within the polymer upon reduction.

Configuration is also important in determining the performance of ICP electromechanical actuators. Otero has described bimorph trilayer actuators [17] that use two ICP films attached to either side of a passive film, such as adhesive tape. These devices have shown advantages in that they have compact structure and utilise oxidation and reduction processes separately, leading to better energy efficiency whilst avoiding parallel electrochemical reactions. However, owing to the high ionic resistivity of the passive backing film used, it can only be used in an electrolyte bath. Although various ionic conductive materials have been used as the backing film, delamination after prolonged bending cycles has often occur due to the poor adhesion of polypyrrole films [18, 19].

In this Chapter, polypyrroles doped with either PF_6^- or $TFSI^-$ were used to construct trilayer actuators. This structure was used previously for

an integrated electrochemical sensor-actuator system [20]. The aim here was to characterise the electrically induced deflection and determine the effect of frequency on displacement as well as the effect of voltage and electrolyte on the blocking force generated. In addition, investigation into improving the cycle life of such actuators and their incorporation into the cochlear implant were considered.

4.2 EXPERIMENTAL

4.2.1 REAGENTS AND MATERIALS

Nucleus® 24 Contour™ electrodes were obtained from Cochlear Ltd. A home-made frame to stretch the PVDF membrane during electrodeposition of polypyrrole was received as a gift from Matt Bennett (Center for Intelligent Material Systems and Structures, Virginia Tech). For all other reagents and materials mentioned in this Chapter refer to section 2.10 in Chapter 2.

4.2.2 FABRICATION METHOD OF TRILAYER ACTUATOR

Au was sputter coated onto each side of porous PVDF membranes at a sputtering current of 30 mA for 30 minutes in a magnetron sputter coater where Ar pressure was maintained at 2×10^{-3} mBar. The as-coated membrane was used as a substrate for the electrochemical deposition of polypyrrole.

The deposition of polypyrrole was carried out in a glass cell (Figure 2-9 in section 2.12,). The PVDF membrane was stretched during electro deposition using a frame as shown in Figure 4-2 in order to maintain a flat configuration. Both sides of Au coated PVDF membranes were shorted and

used as the working electrode. It was placed vertically in parallel between two large pieces of stainless steel mesh, which were shorted together as the counter-electrode. Galvanostatic deposition was carried out at a current density of 0.10 $mA.cm^{-2}$ for different times from a PC solution containing 0.06 M pyrrole, 0.5% water with different salts using an EG & G 363 Potentiostat/Galvanostat. Polypyrrole doped with $TFSI^-$ (denoted as PPy/TFSI) was prepared from PC solution with 0.05 M LiTFSI, while polypyrrole doped with PF_6^- anion (denoted as PPy/PF_6) was obtained from PC solution with 0.05 M TBA.PF_6 salt. Solutions were purged with nitrogen for 10 minutes before use. The entire setup was placed in a freezer and the polymerisation temperature was controlled at ~ – 28 ^oC. As-prepared films were thoroughly rinsed with PC. The edges of bulk film were trimmed off and the bending actuators were prepared as rectangular strips, cut carefully from the bulk film using a scalpel. The actuator samples were padded dry with tissue and stored in either 0.05 M LiTFSI in PC, 0.05 M TBA.PF_6 in PC, or various ionic liquid electrolytes before use.

The wet mass of as-prepared polypyrrole trilayer films was determined using a digital microbalance. The thickness of the polypyrrole layer on each side was determined using a digital micrometer, and additionally using scanning electron microscope (SEM) images of film cross sections. The sheet resistance of Au coated PVDF membranes with and without polypyrrole were determined using the four-point probe method. SEM of polypyrrole coated PVDF membranes was performed using a Leica Scan 440 Microscope.

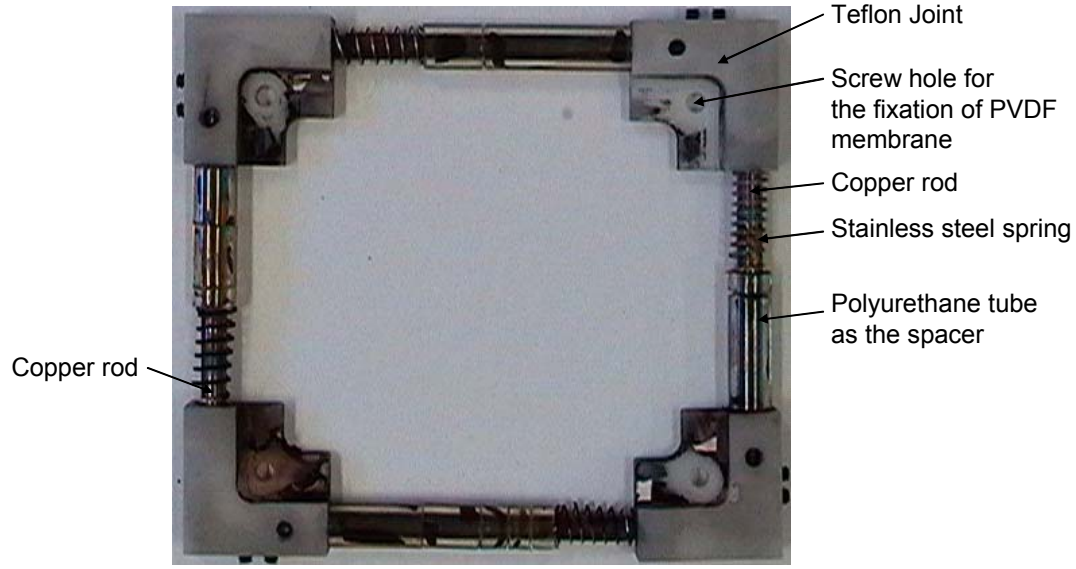

Figure 4-2 The stretching frame (approximate 10 cm × 10 cm in size) used in the fabrication of polypyrrole bending trilayer actuators. Au sputter coated PVDF was fixed by four bolts at each corner on Teflon joints. The frame was fitted with four stainless springs to provide the stretching force along copper rods that were fixed at one end within one Teflon joint and were able to slide freely inside another Teflon joint.

4.2.3 ELECTROCHEMICAL CHARACTERISATION

For electrochemical characterisation methods including cyclic voltammetry (CV), pulsed potential and pulsed current refer to section 2.11. These methods were used to calculate the electrochemical efficiency of polypyrrole trilayer actuators. As such one side of the actuator was used as the working electrode and the other as both the counter- and reference electrodes. For the CV characterisation of the PPy/PF_6 used in the trilayer actuators, a separate sample was electrodeposited under same conditions on a standard Pt disk electrode and CV carried out using a standard 3-electrode setup (refer to Section 2.12). The cell set-up for the ionic conductivity measurement is shown in Figure 4-3.

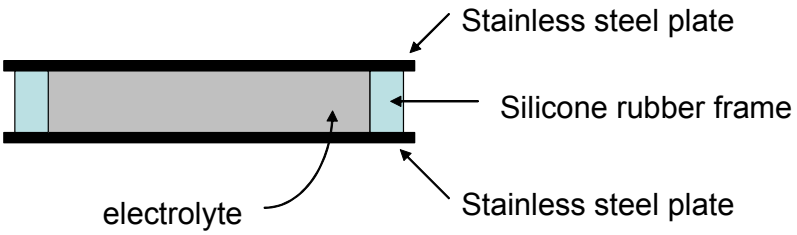

Dimensions: 2 cm × 2 cm × 4 mm

Figure 4-3 Schematic showing set-up used for ionic conductivity measurements. Dimensions of the set-up were 2 cm × 2 cm × 4 mm.

4.2.4 MECHANICAL ACTUATION TESTING

Initial mechanical testing of polypyrrole trilayer actuators involved the visual analysis of the degree of deflection. A commercial digital video camera was used to record the deflection in real time at a speed of 25 frames per second. The strain generated was then obtained by analysis of deflection based on the correlation model established in this study. For the study of the effect of frequency, a function generator was used to supply a sinusoidal signal to trilayer actuators between +/- 1.0 V at various frequencies. The maximum displacement of the free end of bending actuators was measured visually against a metric rule as shown in Figure 4-4. For the measurement of blocking force, a Dual-Mode Lever System from Aurora Scientific Inc. were employed. Trilayer actuators were cut into small strips in order to minimise the bending at the width dimension. The pulsed potential was applied until a stable force or the maximum force output was obtained. The set-up of this piece of equipment is shown in Figure 2-10 (a) in Section 2.7.

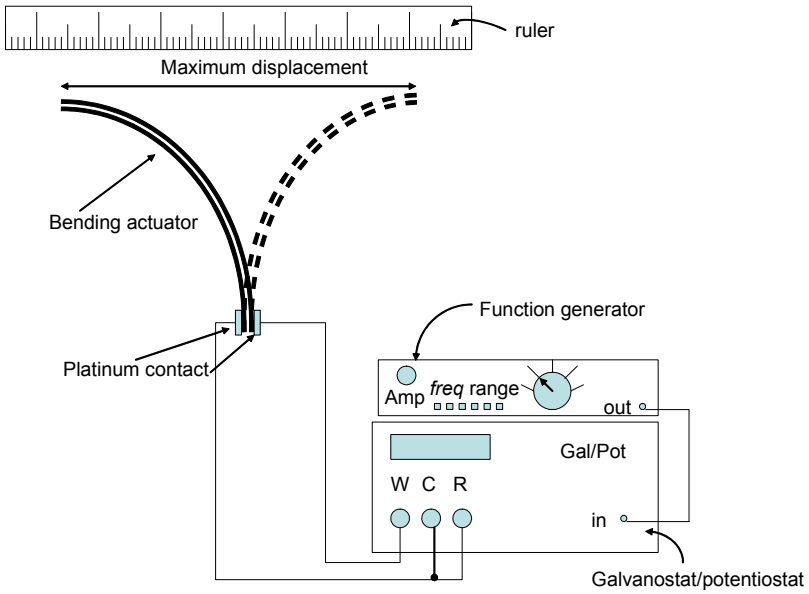

Figure 4-4 Setup for testing the effect of bending frequency. The actuator measured 2 mm wide with various effective lengths between 10 mm and 40 mm, excluding the 2 mm part clamped between the platinum contacts.

The suitability of using the trilayer actuators to straighten the precurled cochlear implant was also considered. The bending force required to straighten the cochlear implant was measured using a microbalance with the set-up illustrated in Figure 4-5. A stainless steel stylet (Ø 125 μm) capable of straightening the curled electrode was inserted into the lumen of the curled part to a given length to hold it straight. The body of the electrode was clamped between two plastic sheets which were then fixed by a piece of double-sided tape onto the tray of the microbalance. A needle was used to apply a force to the stylet to displace the electrode relative to the horizontal plane. The force required to straighten the curled implant electrode was measured as a function of the insertion depth of the stylet, which was adjusted in a step-by-step manner. An angle ~ 15º to the horizontal plane was allowed to avoid over-bending. The force was calculated from the measured mass. In this measurement, the torque generated from the lightweight stylet was ignored.

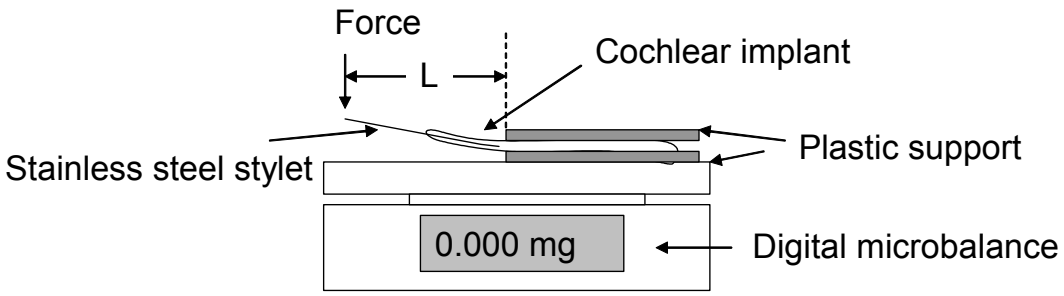

Figure 4-5 Configuration for bending torque measurements of Nucleus® 24 Contour™ electrodes.

4.3 RESULTS AND DISCUSSION

Following construction of the trilayer actuator, the effect of the electrical stimulation waveform used to create a deflection on the energy consumption of the actuator was determined. The correlation between the deflection observed and the strain generated as well as between strain and charge passed were examined. The effect of electrolyte and trilayer structure on actuator working life, effect of frequency on maximum deflection and correlation between blocking force and applied voltage were investigated. The use of ionic liquids and possible mechanisms of actuation were investigated. Finally, the maximum force generated by the trilayer actuator was compared to the torque required to straighten the Nucleus® 24 Contour™ electrodes, thereby determining the feasibility and possible future utilisation of the trilayer actuation for the cochlear implant.

4.3.1 SHEET RESISTANCE AND CROSS-SECTIONAL STRUCTURE OF POLPYRROLE TRILAYER ACTUATORS

Following sputter coating, the surface of the Au coated PVDF remained porous and is electrically conductive. The porosity of Au coating on PVDF was demonstrated when a drop of propylene carbonate was placed on the surface and immediate absorption and spreading over the membrane was observed. Due to the stratified and layered structure of the polypyrrole trilayer actuator, the sheet resistance was determined instead of conductivity (Table 4-1). The average sheet resistance for Au coated PVDF membranes was ~ 0.24 Ω/□. This low resistance indicated that the potential drop over a membrane substrate (measuring 5 cm × 5 cm) during electrodeposition of polypyrrole at 0.1 mA.cm^{-2} would be < 0.24 mV [0.24 Ω/□ × (0.1 mA.cm^{-2} × 5 cm × 5 cm)] without consideration of solution resistance. This negligible potential drop resulted in uniform polypyrrole coatings being deposited over the entire surface. The uniform coating in turn led to uniform bending actuation along the entire length of the polypyrrole trilayer actuators. In addition, the low sheet resistance (< 1 Ω/□) of the polypyrrole trilayer actuators enabled uniform charge / discharge processes to occur during operation even when using a single point electrical contact.

Table 4-1 Thickness and sheet resistance data for Au sputter coated PVDF and electrodeposited polypyrrole on Au sputter coated PVDF.

Sample	Thickness (μm)	Sheet resistance (Ω/□)
Au on PVDF	~ 6 (penetrated into porous PVDF)	0.24
PPy(PF_6) on Au/PVDF	~ 30 (as prepared)	0.59
PPy(TFSI) on Au/PVDF	~ 30 (as prepared)	0.82

When the polypyrrole was deposited simultaneously on both sides of the Au/PVDF/Au membrane, the SEM image of the coated membrane (Figure 4-6) showed that the polypyrrole penetrates into the metallised membrane by a few microns. SEM analysis also revealed that the combined thickness of the trilayer membrane was ~ 140 μm, including ~ 15 μm of polypyrrole on each side of the dried film. Note that samples are dry for SEM. In the case of as prepared samples, an overall thickness of ~ 170 μm was obtained using a micrometer, for which the thickness of polypyrrole was estimated to be ~ 30 μm when swelling of the PVDF membrane was included. The average mass of as-prepared bulk trilayer films was measured to be ~ 20 – 25 mg.cm^{-2}.

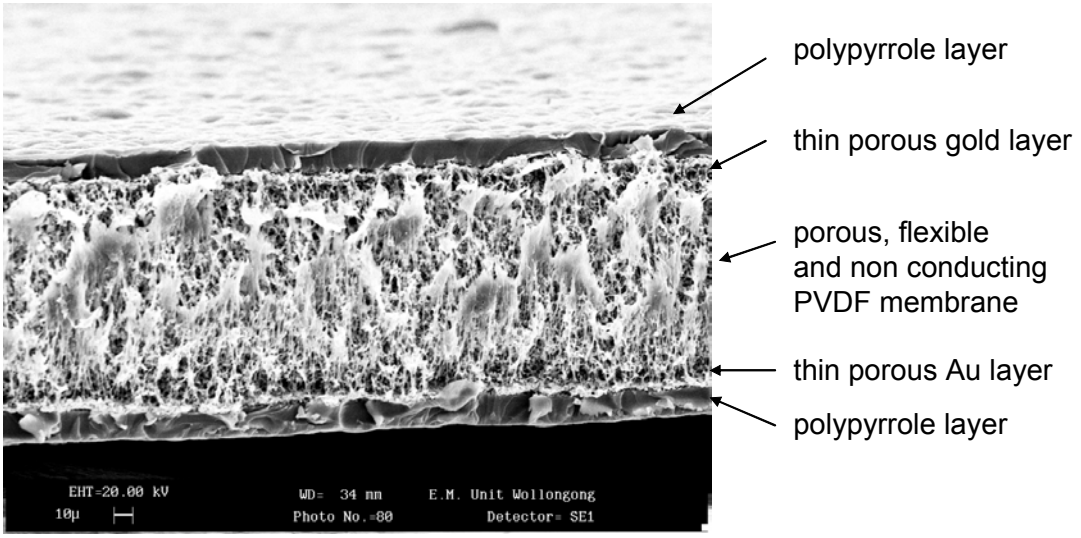

Figure 4-6 Cross-sectional SEM image of electrodeposited polypyrrole on Au coated PVDF membrane. Electrodeposition was carried out in PC solution containing 0.05 M TBA.PF_6, 0.06 M pyrrole and 0.5% water for 12 hours at a constant current density of 0.1 mA.cm^{-2}.

4.3.2 CYCLIC VOLTAMMETRY OF POLYPYRROLE TRILAYER ACTUATOR

Cyclic voltammetry was initially used to determine the voltage range for practical use of polypyrrole trilayer actuators. Polypyrrole was galvanostatically grown on a standard platinum disc electrode for 3 minutes at 1 $mA.cm^{-2}$ in the same solution composition as used for the actuator fabrication. The CV obtained (Figure 4-7) showed well-resolved oxidation / reduction peaks related to the doping and dedoping processes of polypyrrole, respectively. The redox peak separation ~ 0.3 V is believed to be associated with the large portion of doping/dedoping process and indicates significant polymer volume change within 0.3 V potential differences, hence a minimum operating voltage of ~ 0.3V for a PPy/PF_6 based actuator is possible. In fact this has been confirmed by the observed actuation at an applied DC voltage of 0.3 V. The potential window from - 800 mV to + 650 mV (*vs.* Ag/Ag^+ reference) used for CV characterisation suggested that an operation voltage of at least 1.5 V was acceptable.

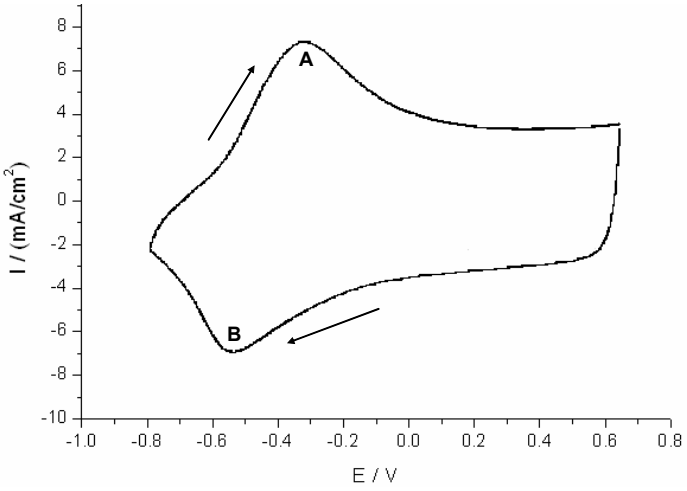

Figure 4-7 CV of PPy/PF_6 film on a standard platinum disc electrode. The third cycle is shown. Potential was scanned between + 650 mV and - 800 mV at 50 $mV.s^{-1}$ *vs.* Ag/Ag^+ in PC solution containing 0.25 M $TBA.PF_6$. (A) The oxidation peak (-0.3 V), (B) the reduction peak (-0.55 V).

CVs were also obtained in a two-electrode configuration using the PPy/PF_6 trilayer actuator (Figure 4-8). A bending actuation towards the reduced polypyrrole side was observed, indicating that the polypyrrole layer contracted at the cathode and expanded at the anode. However, no redox peaks were observed. This is primarily due to the two-electrode configuration, where only the voltage difference was controlled rather than the individual electrode potentials. It would result in the inefficient oxidation and reduction process in the limited duration of the CV experiment. To further explore the later issue, the electrochemical charge efficiency of PPy/PF_6 trilayer actuators was evaluated for this CV experiment.. To further explore this issue, the electrochemical charge efficiency of PPy/PF_6 trilayer actuators was evaluated for this CV experiment.

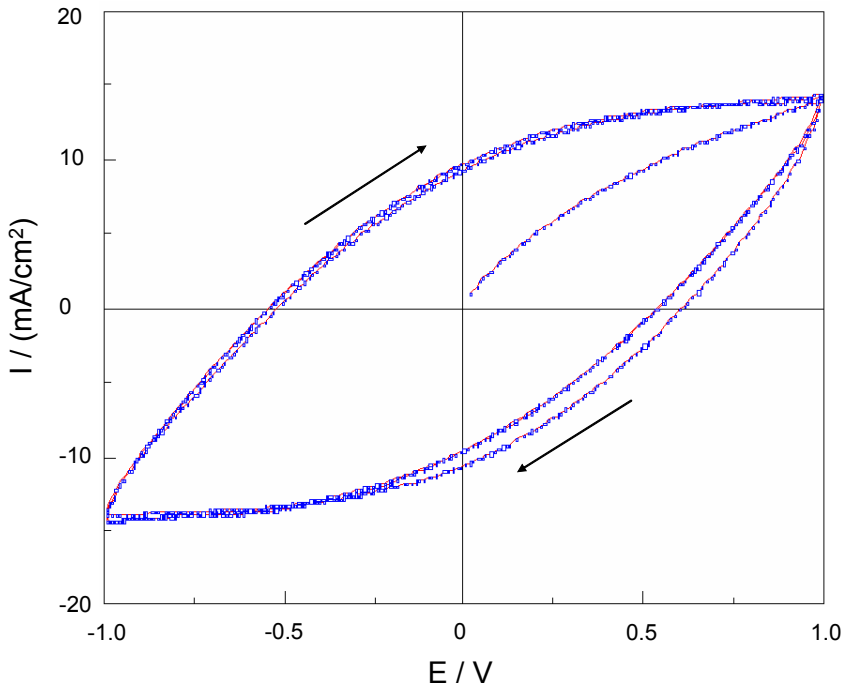

Figure 4-8 CV obtained for PPy/PF_6 trilayer actuator. Lower potential limit = -1.0 V, upper potential limit = + 1.0 V, scan rate = 100 $mV.s^{-1}$. Electrolyte: 0.05 M $TBA.PF_6$ in PC.

The electrochemical efficiency (EE) of an ICP actuator system is an important parameter in assessing device performance and is defined as [15]:

$$EE_{ox} = \frac{charge\ passed\ during\ oxidation}{charge\ for\ complete\ oxidation} \times 100 \qquad \text{..... 4-1}$$

and / or

$$EE_{red} = \frac{charge\ passed\ during\ reduction}{charge\ for\ complete\ reduction} \times 100 \qquad \text{..... 4-2}$$

Charge for complete oxidation / reduction was estimated from the charge consumed during polypyrrole growth and assuming a N:PF_6 ratio of 3.3 in Equation 4-1 (from microanalysis results on PPy/PF_6). Since there are two electrons consumed for each pyrrole ring added to a growing polymer chain, and since each 3.3 pyrrole rings consumes one electron for polymer oxidation, a total of 7.6 electrons ((3.3 × 2) + 1) of charge is consumed during polymerisation to produce the oxidised 'repeat unit' structure. Therefore, the loss or gain of one electron out of 7.6 electrons (consumed during polymerisation) during polymer oxidation or reduction, respectively, would represent 100% EE. For polypyrrole grown at 0.1 $mA.cm^{-2}$ for 12 hours, the total charge passed was 4.3 $C.cm^{-2}$, so that complete reduction / oxidation would be 0.56 $C.cm^{-2}$ (4.3 / 7.6) on each side. The redox charge passed for the CV in Figure 4-8 was determined by the integration of positive and negative current over one cycle, respectively. The average of the absolute values of positive charge and negative charge was then divided

by the surface area of strip on one side. The result was ~ 0.2 $C.cm^{-2}$, representing an EE_{ox} (or EE_{red}) of ~ 36 %. The real EE value would be lower if the electrochemical double layer capacitance was considered. To obtain higher EE value, the applied voltage needs to be held over a prolonged period of time to allow the current to reach equilibrium. This was confirmed by observing that the polypyrrole trilayer actuator could continuously produce bending movement even after being held at 1 V for 20 minutes (at this point, the calculated EE was > 100% which might have been due to the electroactivity of absorbed water and oxygen from the ambient air). To quantify the degree of bending and obtain the correlation between charge and strain, a simplified model was proposed and is described below.

4.3.3 STRAIN DETERMINATION OF POLYPYRROLE TRILAYER BENDING ACTUATION AND CORRELATION WITH CHARGE

The deflection of polypyrrole trilayer actuators was modelled based on experimental observations (Figure 4-9) and Otero's previous work in the theoretical approach to the bending angle analysis of a bilayer ICP actuator [21]. The essentially even strain distribution along the length of the actuator was evidenced by the near ideal arc shape observed. When the trilayer actuator was held vertically, its bending motion could be described in terms of Cartesian plane coordinates, with the origin being the clamping point. In this way, the x-axis was the horizontal plane and the y-axis was the tangent of the bending arc of the polypyrrole trilayer actuator. Therefore, the centre of circle of the bending arc was always located on the x-axis as shown in Figure 4-10.

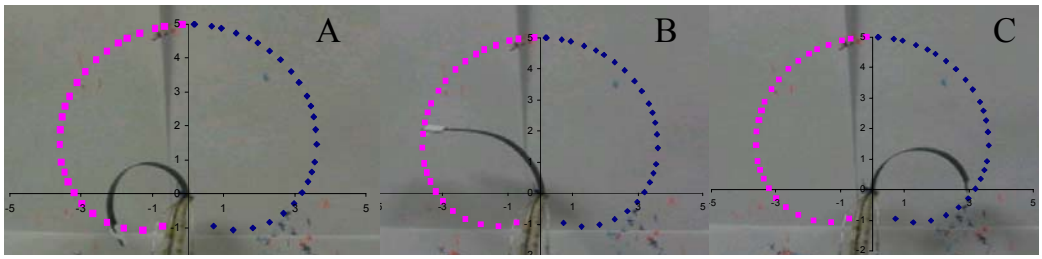

Figure 4-9 The deflection of a polypyrrole trilayer actuator during a CV experiment. Sample dimensions: 10 mm wide, 50 mm long. Polypyrrole was grown galvanostatically for 12 hours at 0.1 $mA.cm^{-2}$. Supporting electrolyte was 0.25 M $TBA.PF_6$ in PC. Mass load at the free end: 25 mg. Voltage cycled between +/- 1.0 V at a fixed scan rate of 100 $mV.s^{-1}$. (A) the outmost left bending position, (B) an intermediate bending position, and (C) the outmost right bending position.

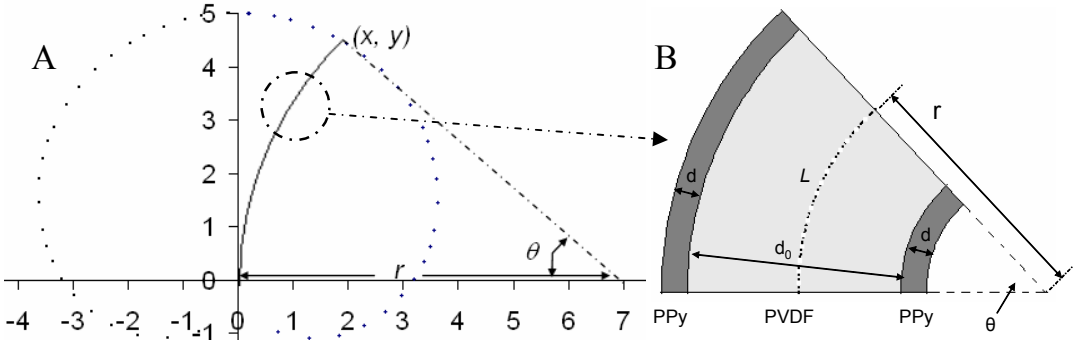

Figure 4-10 Modeling of a bending polypyrrole trilayer actuator. (A) The bending arc of a 50 mm long strip and the tip's locus defined by the coordinates, x and y, r is the radius of bending curve, θ is the angle of bending arc. (B) Cross-section of the actuator. L is the original length, d is the thickness of polypyrrole layer on both sides, and d_0 is the thickness of the porous PVDF layer.

Based on the relationship shown in Figure 4-10, various parameters could be related. Equations below assume the average strain through the thickness of PPy layer to be constant and ignore the formation of a stress gradient [21].

$$\varepsilon = \frac{(d + d_0) \times 10^{-4}}{2 \times r} \quad \text{..... 4-3}$$

$$\theta = L / r \quad \text{..... 4-4}$$

$$x = r - r\cos\theta \quad \text{..... 4-5}$$

$$y = r\sin\theta \quad \text{..... 4-6}$$

where ε is the average strain for the strains being the average of the contracted and expanded sides; r is the radius of actuator bending curve in cm; d is the thickness of polypyrrole layer on each side in μm; d_0 is the thickness of PVDF layer in μm. θ is the bending angle as indicated in the Figure 4-10 and L is the original length of trilayer actuator in cm. Note that Equations 4-5 and 4-6 can be used to describe the tip position for any value of the bending angle θ.

By analysing the time sequenced video images and synchronising these with the charge passed, the relationship between the strain ε and the charge during CV characterisation could be obtained. Figure 4-11 shows strain in relation to time and Figure 4-12 shows strain in relation to charge. The results showed that the strain generated decreased almost linearly from the maxima of + 0.58 % to - 0.46 %, corresponding to when 0.19 mC of charge was passed. When the direction of current inverted, the strain increased to almost the same value (+ 0.55 %) when the same amount of charge (0.19 mC) was passed in the reverse direction. These results indicated that strain was proportional to the charge passed between the two polypyrrole layers, in agreement with the theory that the strain generated from ICPs is proportional to the total amount of charge passed [22, 23]. In addition, the strain curve obtained here seemed to show hysteresis. When the direction of current was switched from positive to negative, the slope decreased slightly, presumably due to the contribution of the double layer charging effect or parasitic electrochemical reactions. It was noted that the obtained strain was not the same on both sides (i.e. + 0.58% for the right side and – 0.46 % for the left side). This may due to the initial curvature of

the actuator to the right side, which was formed by the unbalanced surface stress after the electrodeposition of polypyrrole.

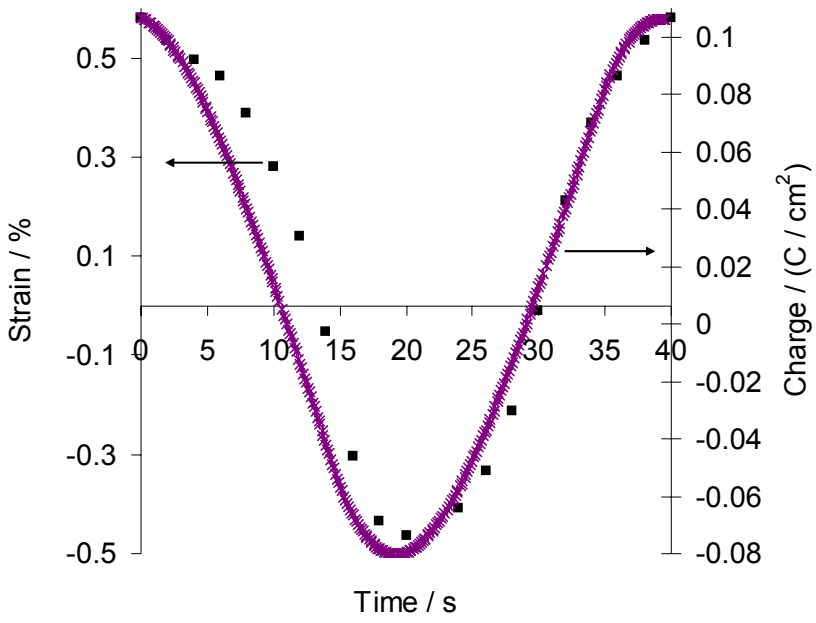

Figure 4-11 One cycle of charge passed and strain produced in a CV experiment, where the voltage was scanned between +/- 1.0 V at a fixed rate of 100 mV.s^{-1}.

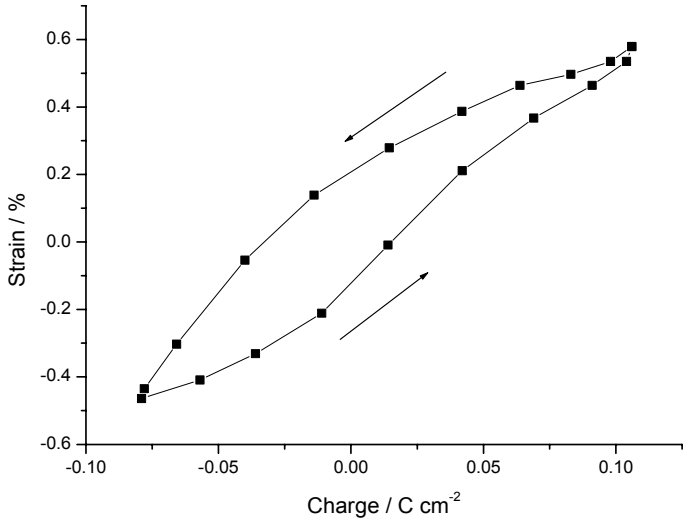

Figure 4-12 Plot of strain *vs.* charge data from Figure 4-11.

4.3.4 ELECTRICAL ENERGY CONSUMPTION OF POLYPYRROLE TRILAYER ACTUATORS

Energy consumption is an important parameter in the design of actuators. For an investigation into electrical energy consumption, a piece of plastic (~ 25 mg) was attached to the tip of a polypyrrole trilayer actuator (~ 115 mg) and the average energy consumption per cycle for bending between the two outmost positions A and B (Figure 4-9) was evaluated.

The average energy consumption per cycle was compared by using different electrical stimuli, including CV, square wave pulsed potential, and square pulsed current. This comparison was based on the assumption that by adjusting the amplitude and duration of electrical stimulation to ensure precise bending between points A and B, the same amount of mechanical energy output would be produced in each cycle. In this way the different types of electrical stimuli could be compared.

To obtain a precise bending between point A and B, CV was carried out between +/- 1 V with a cycle duration of 40 second (i.e. scan rate = 100 $mV.s^{-1}$), square wave pulsed potential was carried out between +/- 1 V with a cycle duration of 12 seconds, and square wave pulsed current was carried out between +/- 20 $mA.cm^{-2}$ with a cycle duration of ~ 12 seconds. The voltage, current, charge passed and power consumption obtained for CV, square wave pulsed potential and square wave pulsed current inputs were plotted against time and are illustrated in Figure 4-13, Figure 4-14 and Figure 4-15, respectively. The total consumed electrical energy was calculated by the integration of the power consumption *vs.* time graphs.

Averaging over three input cycles gives average energy consumptions of 170 $mJ.cm^{-2}$ per cycle for CV, 147 $mJ.cm^{-2}$ per cycle for square wave pulsed current and 270 $mJ.cm^{-2}$ per cycle for square wave pulsed potential. To simplify the comparison, the energy consumed by the possible parasitic

reaction and the mechanical kinetic energy were ignored. Note that the former is correlated to the charging time over one cycle and the amplitude of voltage, therefore CV over 40 s per cycle longer than the 12 s for either square wave pulsed current or pulse potential may consume more electrical energy in parasitic reactions; the square wave pulsed current at higher potential > 1 V may also consume more electrical energy in parasitic reactions in comparison to others. The mechanical kinetic energy was evaluated by the speed of the tip at the end of each cycle according to the recorded video clip, which was found slower than 2 $cm.s^{-1}$. Given the speed of 2 $cm.s^{-1}$ at the tip, a total mass ~ 140 mg including the bending actuator, the overall kinetic energy per half cycle should be < 2.8×10^{-5} mJ ($\frac{1}{2}mV^2$), hence the unit kinetic energy consumption per cycle is less than 2×10^{-5} $mJ.cm^{-2}$ per cycle, obviously negligible compared to the electrical energy consumption. Therefore, the highest energy consumption associated with the square wave pulsed potential input (nearly double that observed for other input types) can be established.

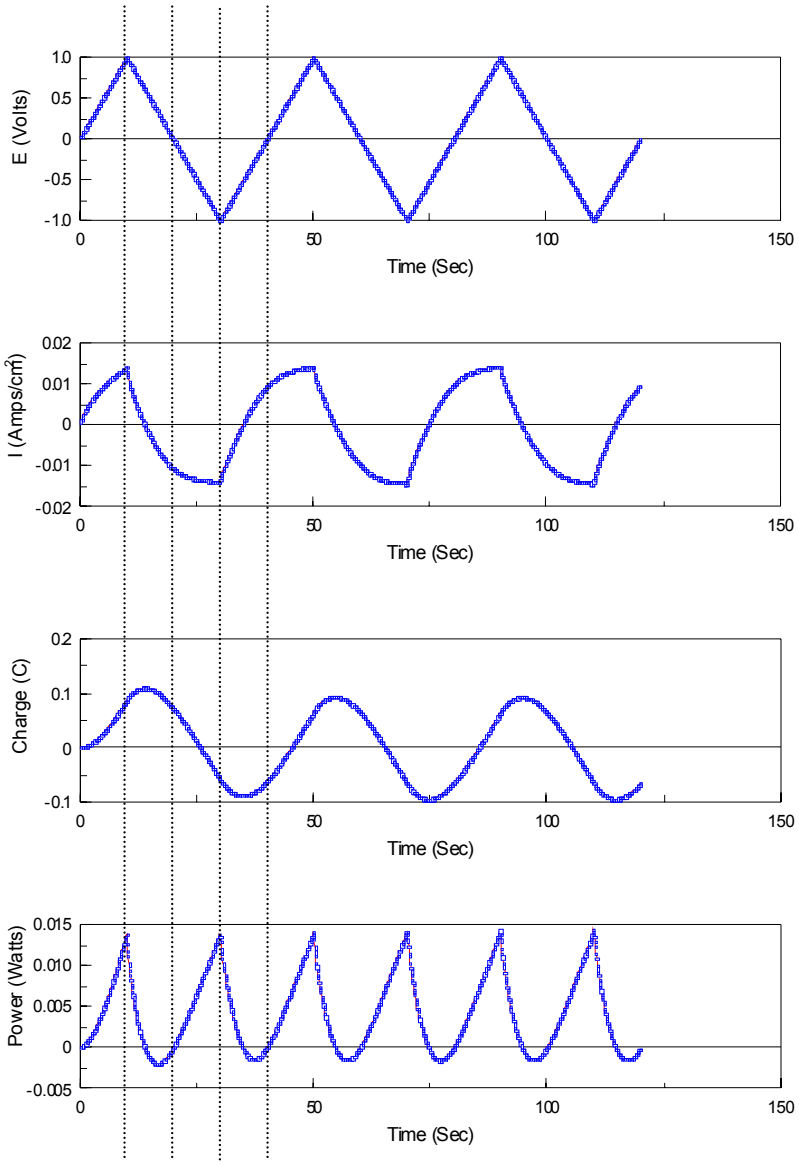

Figure 4-13 CV of polypyrrole trilayer actuator between +/- 1.0 V at scan rate of 100 $mV.s^{-1}$. PPy/PF_6 was grown galvanostatically at a current density of 0.1 $mA.cm^{-2}$ for 12 hours from a solution containing 0.06 M pyrrole monomer, 0.05 M $TBA.PF_6$ and 0.5% (w/w) Milli-Q water in PC at the temperature of ~ -20ºC.

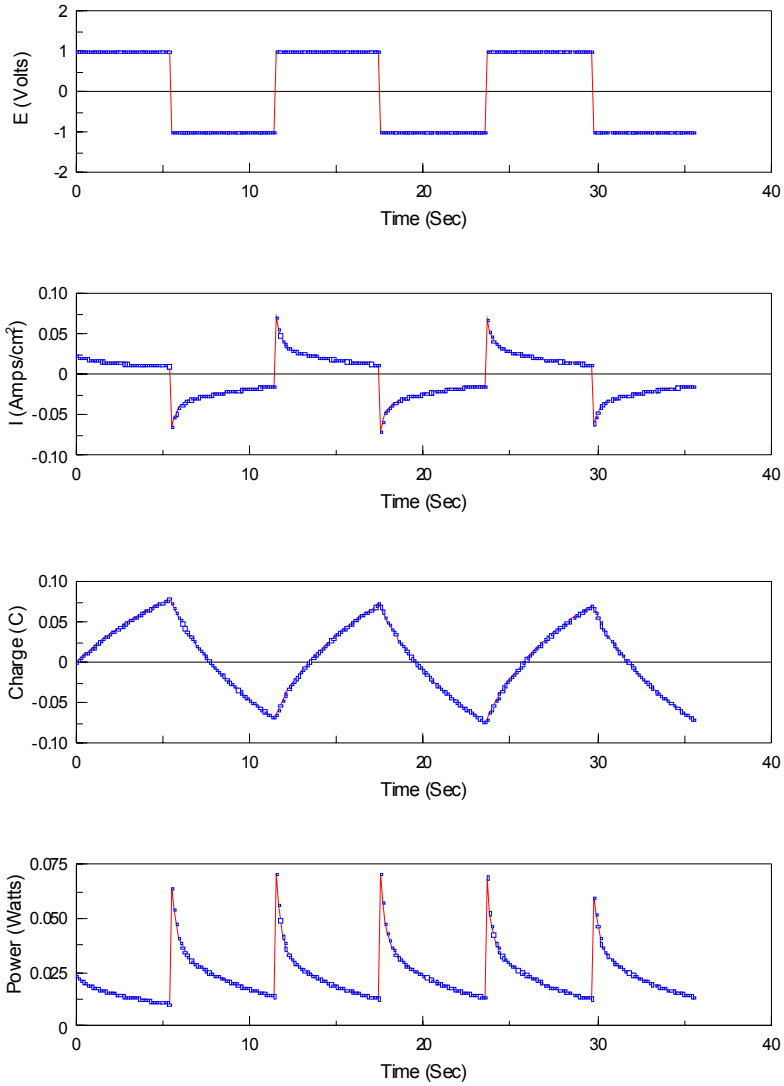

Figure 4-14 Polypyrrole trilayer actuator subject to square wave pulsed potential input between +/- 1.0 V. Each pulse was ~ 6 seconds (i.e. cycle time ~ 12 seconds). PPy/PF_6 was grown galvanostatically at a current density of 0.1 mA.cm^{-2} for 12 hours from a solution containing 0.06 M pyrrole monomer, 0.05 M TBA.PF_6 and 0.5% (w/w) Milli-Q water in PC at the temperature of ~ -20ºC.

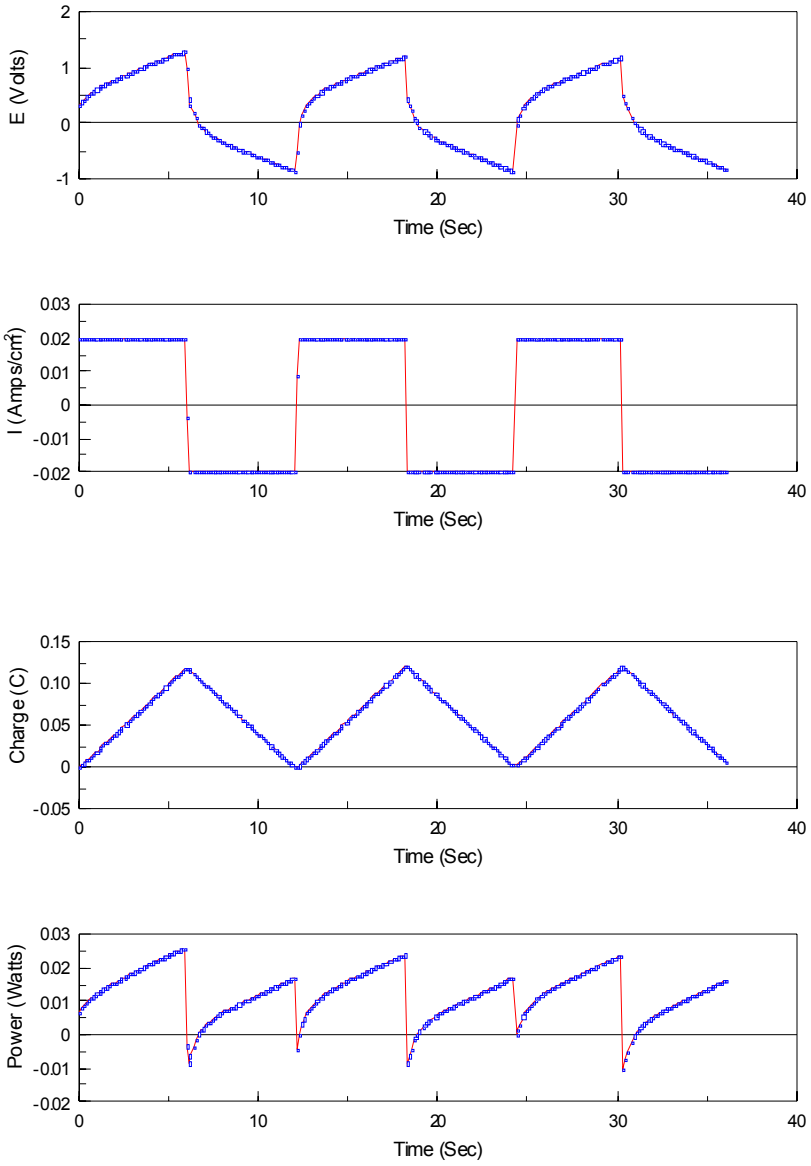

Figure 4-15 Polypyrrole trilayer actuator subject to square wave pulsed current input between +/- 20 $mA.cm^{-2}$, Each pulse was ~ 6 seconds (i.e. cycle time ~ 12 seconds). PPy/PF_6 was grown galvanostatically at a current density of 0.1 $mA.cm^{-2}$ for 12 hours from a solution containing 0.06 M pyrrole monomer, 0.05 M $TBA.PF_6$ and 0.5% (w/w) Milli-Q water in PC at the temperature of ~ -20ºC.

The electrical energy consumption measurements carried out above revealed that polypyrrole trilayer actuators require much more electrical energy when a square wave pulsed potential input was used. According to the experimental results, large current spikes up to 75 mA were observed when the voltage was suddenly switched between + / - 1 V in the square wave pulsed potential experiment. It should be noted that the apparent negative power consumption that was observed for both CV and square wave pulsed current experiments, was probably due to the recovery of some stored electrical charge from the previous electrical stimulation. This process is analogous to the well-known energy loss associated with the charging and discharging of a capacitor [24], where here it is the large capacitance of polypyrrole.

To improve actuator efficiency, instantaneous changing of the voltage across a capacitor should be avoided as much as possible. Solutions suggested in the literature [24] include using an inductor in series or switching voltage polarity when the voltage across a capacitor reaches zero. The energy losses incurred when using a square wave pulsed potential input has been shown here to be significant for ICP actuators; however, this issue has failed to draw attention in the scientific literature. Perhaps this is due to the overall low energy conversion rates of ICP actuators, usually < 1% [12]. Moreover it is also the case that the problem is not just the loss of energy, but also the fact that the majority of energy loss is possibly converted to thermal heat at the contacts, drastically decreasing the life cycle of polypyrrole trilayer actuators. This was observed in this study as the burning of holes in the polypyrrole layers of trilayer actuators when subjected to continuous square wave pulsed potential input.

4.3.5 CYCLE LIFE

Although square wave pulsed potential actuation was found to burn the polypyrrole actuator at the contacts due to the current spiking induced thermal heating, it was found that the actuator was still able to work due to the presence of the Au layers. The presence of Au layers provided a significant advantage since the square wave pulsed-potential actuation often generates faster strain rates and more rapid mechanical movement compared to CV and square wave pulsed current actuation.

Other factors besides thermal heating that may affect the cycle life of polypyrrole trilayer actuators include the delamination of polypyrrole from the supporting substrate and the evaporation of solvent from the supporting electrolyte. The following sections investigate the possible advantages of mechanical anchoring of polypyrrole within PVDF pores and using ionic liquids as ways of addressing the other factors influencing cycle life.

4.3.5.1 Improved adhesion of polypyrrole to the substrate

For polypyrrole trilayer actuators, delamination is often a problem that can greatly reduce cycle life. Delamination results in the loss of electrical contact to the polypyrrole and device failure. Therefore, the adhesion of the polypyrrole layer to the substrate is crucial for maintaining long-term high performance. Several approaches have been used to try to minimise delamination problems, including the use of rough electrochemically deposited Au on top of thermally evaporated Au/polyimide substrate [18] and the use of asymmetric membranes [19]. However, these approaches related to actuators that operate while immersed in electrolyte, unlike the actuators considered in this chapter for which porous PVDF membranes were used as electrolyte reservoirs to allow

actuation in air. It was shown here that the polypyrrole layers on either side of trilayer actuators could be subjected to extensive bending deflection without either breaking or delamination. It was shown above that the Au-coated porous PVDF structure allowed polypyrrole to grow within the pores of the PVDF to a depth of a few microns (Figure 4-6). The absence of any delamination problem here indicated that the mechanical anchoring of the polypyrrole layer to the substrate effectively extended the cycle life of polypyrrole trilayer actuators. Actuators were successfully operated for 1400 cycles in air, which is similar to the long-term cycle life reported previously for PPy/Au/polyimide bending actuator [18].

4.3.5.2 Use of Ionic Liquid

The problem of loss of solvent owing to evaporation from polypyrrole trilayer actuators can lead to shortened cyclic life. The effect of electrolyte on the cycle life of polypyrrole trilayer actuators was investigated at ambient conditions by comparing 0.05 M LiTFSI in PC and the hydrophobic ionic liquid EMI.TFSI.

It was found that the cycle life for polypyrrole trilayer actuators varied significantly depending on the electrolyte used. When cycled between - 1 V and + 1 V at a frequency of 0.05 Hz, the actuator using 0.05 M LiTFSI in PC electrolyte, generated peak-to-peak strains that decreased significantly (by ~ 92%) after 5 hours (or 900 cycles) (Figure 5-15). Conversely, for the same batch of actuator, using EMI.TFSI as the electrolyte, strain generation was much more stable over a prolonged time, although the initial strain of ~ 3.9 % was lower than that using LiTFSI in PC (~ 6.4%). After 8 hours (i.e. 1444 cycles), actuators using the EMI.TFSI electrolyte were still able to produce peak-to-peak strains of ~ 1.8 % (i.e. a decrease in strain of ~ 50%. This decrease may have been due to the

irreversible conformational change of polymer). The reason for the longer lasting performance when using the EMI.TFSI electrolyte was the non-volatile nature of the ionic liquids. Although PC has a relatively high boiling point (241.7 ºC) and low vapor pressure (0.039 mmHg), it was still susceptible to evaporation, especially due to the thermal heat generated by the continuous square wave pulsed potential. Solvent loss was evidenced by the observation that the actuator using the 0.05 M LiTFSI in PC electrolyte slowly dried after several hours of continuous operation, while analogous actuators using EMI.TFSI as the electrolyte maintained wetness.

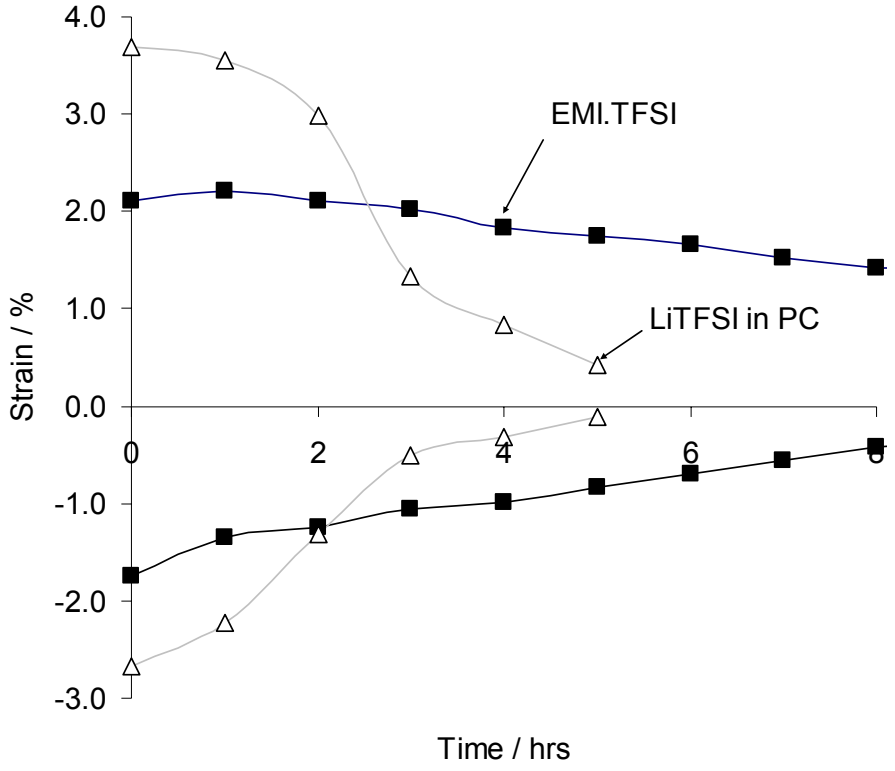

Figure 4-16 Effect of electrolyte on the free bending strain generation of polypyrrole trilayer actuators using CV input. The potential was scanned between –1.0 V and +1.0 V at 0.05 Hz. Actuator dimensions: 30 mm long, 3 mm wide. The strain was estimated based on the loops and diameter of the coiled actuator according to the Equations 4-3 and 4-4.

4.3.6 EFFECT OF FREQUENCY OF ELECTRICAL STIMULATION ON BENDING ACTUATION

The effect of varying the frequency of electrical stimulation on both PPy/PF6 and PPy/TFSI actuators was investigated. It is also important to consider the relationship between the displacement between two outmost bending positions and the frequency of electrical stimulation. The results presented below were obtained with the application of a sinusoidal potential waveform between + / - 1.0 V at various frequencies.

Figure 4-17 and Figure 4-18 show the tip displacement of the trilayer actuators as determined at different input frequencies. The applied potential was a sine wave with amplitude of +/- 1.0 V and several different actuator lengths were assessed for each doped form of PPy. In all cases, the tip displacement tended to decrease initially as the frequency of the input voltage increased. Over a certain frequency range, however, the tip displacement sharply increased which indicates that the actuation process coincided with the natural frequency of the trilayer bending beam structure. This behaviour has not been previously observed in the frequency response of bilayer aqueous or dry PPy actuators [25]. For both dopant types, these resonance peaks appeared at higher frequencies when the actuator length was decreased. In comparing the TFSI doped PPy with the PPy/PF_6 actuators, it can be seen that the PPy/TFSI produced larger tip displacements but at lower resonance frequencies than the PPy/PF_6 actuators of similar size. The largest tip displacements were produced by the 40 mm long PPy/TFSI actuator, which generated ~60 mm of tip displacement and showed a resonance at ~4 Hz. In comparison, the 40 mm long PPy/PF_6 actuator generated only ~20 mm of tip displacement and showed a resonance peak at 6.4 Hz.

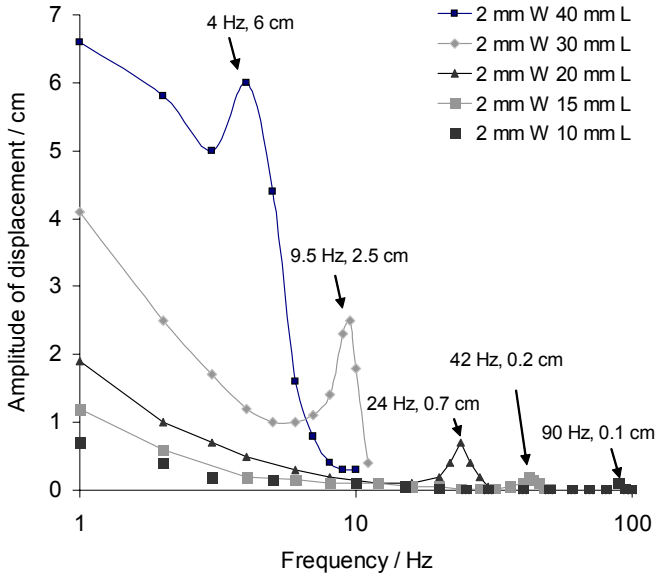

Figure 4-17 Frequency bending displacement response of the PPy/TFSI bending actuator. The applied potential was a sine wave with amplitude of +/- 1.0 V and frequencies ranging from 1 to 100 Hz. The width (W) of actuator was 2 mm, but its length (L) was varied from 10 mm to 40 mm, as indicated.

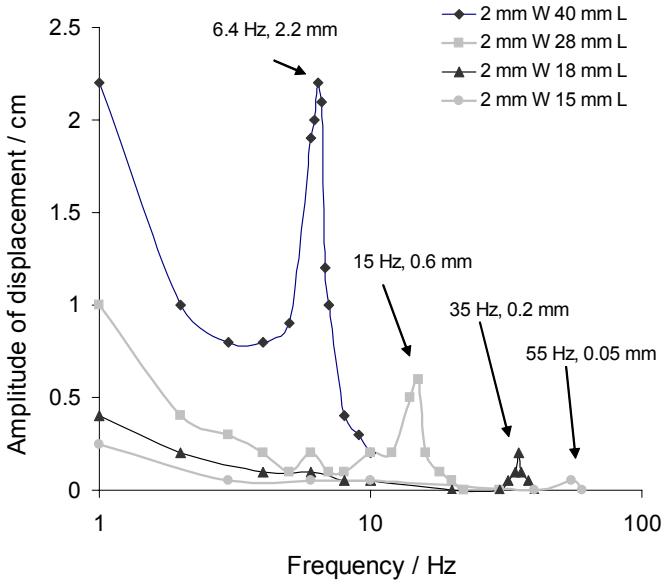

Figure 4-18 Frequency bending displacement response of the PPy/PF_6 bending actuator. The applied potential was a sine wave with amplitude of +/- 1.0 V and frequencies ranging from 1 to 60 Hz. The width (W) of the actuator was 2 mm, but its length (L) was varied from 10 mm to 40 mm, as indicated.

The faster actuation response of the PPy/TFSI is also illustrated by the step response shown in Figure 4-19. In this case, the blocking forces at the tip of 20 mm long actuators were determined when a +1 V stimulus was applied at t = 0 second. The PPy/TFSI produced a higher and faster tip force than the PPy/PF_6. If we assume that the dynamics of the actuators are dominated by a single real pole as in a typical first order system [26], the time constant concept can be used to determine the response time of the actuators. The time constant is the time needed to reach 63.2% of the steady state value under a step input [26]. With reference to the step responses depicted in Figure 4-19, the time constants are 0.47 second and 0.77 second for the PPy/TFSI and PPy/PF_6 actuators, respectively.

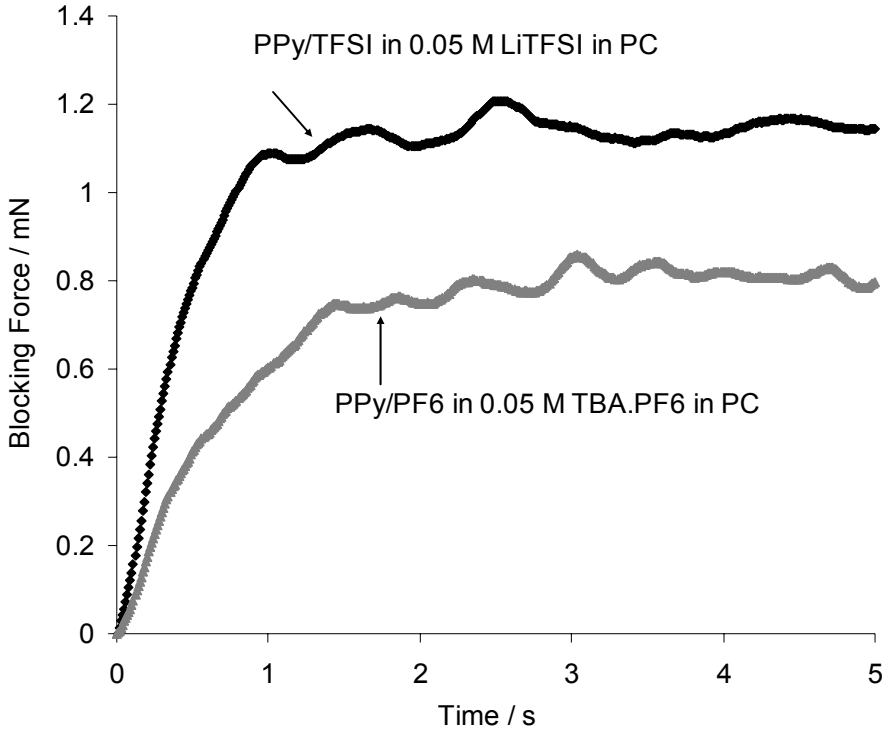

Figure 4-19 The step responses of the PPy/TFSI and PPy/PF_6 actuators under a step potential of 1.0 V. Both actuators have a width of 2 mm and an effective length of 20 mm.

The current and charge passed during the same step responses are shown in Figure 4-20 and Figure 4-21, respectively. A significantly faster rate of charging and a much higher amount of charge were observed for the PPy/TFSI compared to the PPy/PF_6. It should also be noted that the charge continues to increase for a long time after the actuation is complete (as shown by the force plateau in Figure 4-19). It is possible that secondary parasitic electrochemical reactions continue in the trilayer structure that is not related to the PPy electrochemistry and actuation mechanism.

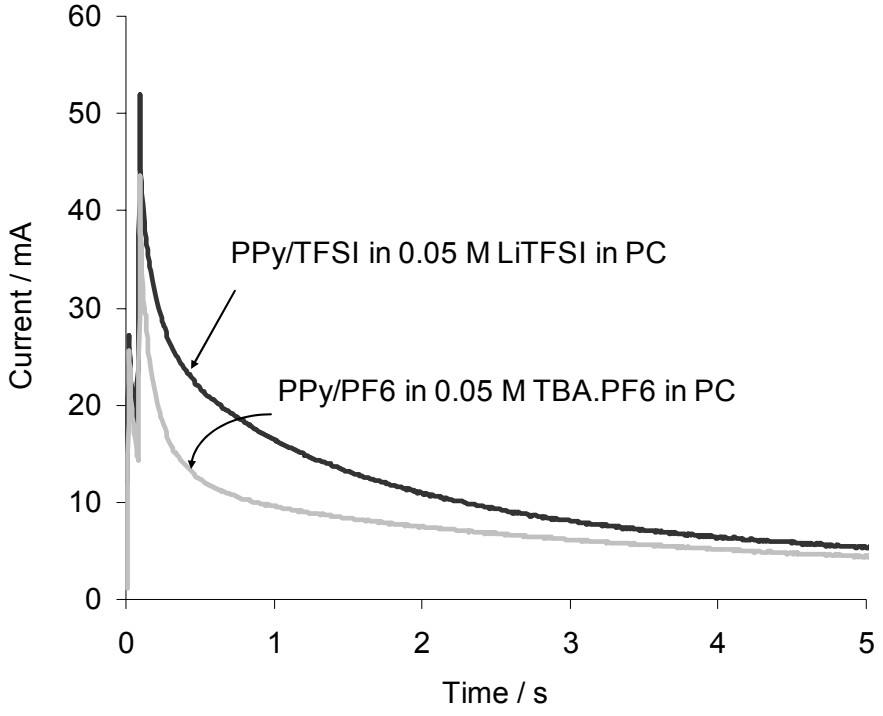

Figure 4-20 The current passed through the PPy/TFSI and PPy/PF_6 actuators under a step potential of 1 V. Both actuators have a width of 2 mm and an effective bending length of 20 mm.

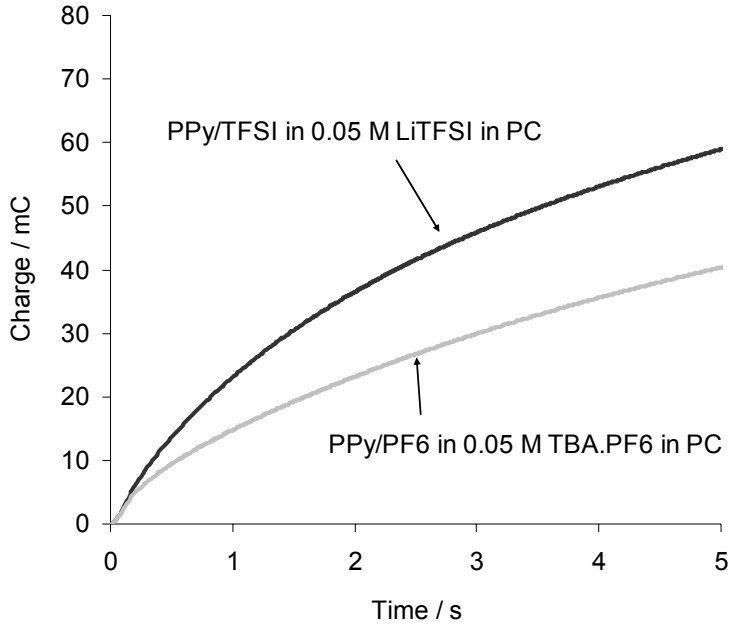

Figure 4-21 The charge transferred to the PPy/TFSI and PPy/PF_6 actuators under a step potential of 1.0 V. Both actuators have a width of 2 mm and an effective bending length of 20 mm.

The experimental data clearly shows a resonance type bending response occurring in both TFSI and PF_6 doped polypyrrole trilayer actuators. In addition, the tip amplitudes (250%) and force generated (30%) were shown to be significantly higher in the PPy/TFSI compared to the PPy/PF_6 when operated under identical conditions. The resonance peaks were observed to occur at higher frequencies for shorter actuator lengths, but at the same length the PPy/PF_6 actuator showed resonance at a higher frequency than the PPy/TFSI actuator. Each of these observations will be discussed with reference to beam mechanics and the fundamental actuator mechanisms.

The natural frequency ω_n of a one end-cantilevered beam with a mass of m_b and length L is given by [27]:

$$\omega_n = \sqrt{\frac{3EI}{\frac{33}{140} m_b L^3}} \qquad \text{..... 4-7}$$

where E and I are the Young's modulus and area moment of inertia of the beam – the actuator in this case.

With reference to Equation 4-7, the peak frequency (which is approximately the natural frequency) in the frequency response is proportional to the -3/2 power with respect to the actuator length, provided that the mass and flexural rigidity (*EI*) do not change. Figure 4-22 shows the relationship between the resonance frequency and $L^{-3/2}$ for each type of actuator. The relationships are nearly linear, which supports the bending beam analysis of these systems.

The appearance of resonance amplification in these actuator systems can only occur when the actuation processes occur faster than the natural frequency of the system. We assume that the actuation principle is based on the voluminous movement of ion and solvent molecules in and out of the polymer layers [22, 23, 28, 29]. While the deflection in conducting polymer actuators has been attributed in part to the electrostatic forces between displaced ions and the polymer backbone [28, 30], it has been suggested that the dominant actuation mechanism is due to the voluminous displacement of ion and solvent molecules [28, 29]. Since the actuation mechanism in conducting polymers is dominated by mass transfer, the inherent speed of actuation will be determined by diffusion rates, diffusion distances and number of diffusing ions and as stated earlier that actuation is proportional to charge. Full actuation (and maximum tip displacement) will only occur when there is sufficient time available to allow complete doping/de-doping of the polymer and the associated ion/solvent movement. As shown in Figure 4-17 and Figure 4-18, even at the lowest speeds tested, the actuation

had not attained the maximum value, since a plateau in tip displacement is expected at low frequency. However, in the trilayer geometry used, there was sufficient tip displacement to produce a definite resonance amplification when the actuator was operated near the natural frequency of the system. A larger resonance amplification occurred when the tip displacement just prior to resonance was higher. Resonance would not be observed if thicker or wider beam structures were used (increasing I and m_b in Equation 4-7) such that the natural frequency coincided with very small tip displacements.

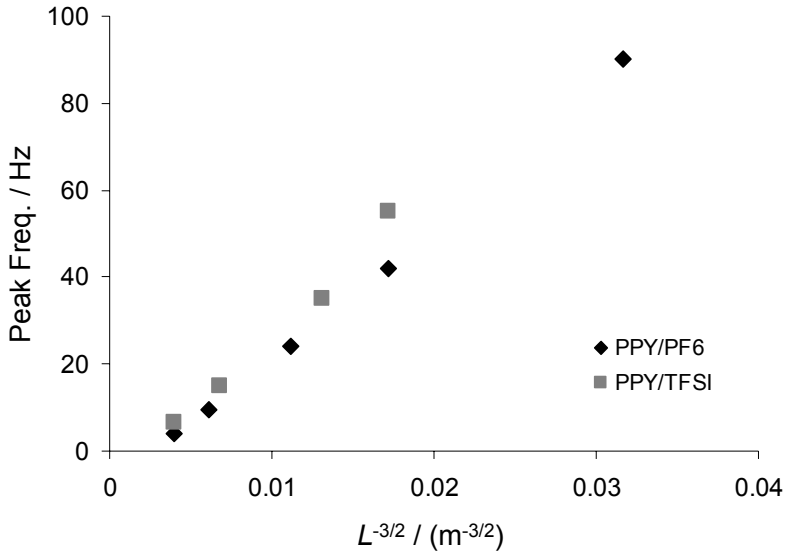

Figure 4-22 Frequencies at the sharp maxima in Figure 4-17 and Figure 4-18 plotted against $L^{-3/2}$ where L is the length of the trilayer actuator. As predicted by bending beam theory (Equation 4-7) the relationships are linear.

The difference in actuation behaviour observed for the two different doped forms of PPy studied may be attributed to different mass transfer rates and different Young's moduli. Tip displacements for TFSI doped PPy were much larger under identical test conditions than PPy/PF_6, in agreement with recent results from Hara *et al* [13]. The larger strains in PPy/TFSI may

either be due to a higher strain-to-charge ratio or due to faster charging rates. The strain-to-charge ratio reflects the efficiency of conversion of electrical energy to mechanical energy by the actuator. As reported in the literature [7, 22, 23, 25], the strain is proportional to the charge passed. Similarly, the stress generated in a bending actuator is directly proportional to the charge passed [31, 32]. Comparing the data given in Figure 4-19 and Figure 4-21, the force-to-charge relationships were found to be approximately linear, as depicted in Figure 4-23, with a larger force-to-charge ratio for PPy/TFSI compared to PPy/PF_6. These results show that approximately 50% more stress is generated by the PPy/TFSI compared with PPy/PF_6 for a given amount of charge injected into the polymer.

The data in Figure 4-21 clearly shows that faster charging occurs in the PPy/TFSI so that the electron and ion transfer occurs much faster in this polymer compared with PPy/PF_6. The faster charging occurs in PPy/TFSI despite it having a lower electronic conductivity than PPy/PF_6. These results suggest that faster ion diffusion occurs in the PPy/TFSI. The speed of electrochemical charging of PPy is determined by the slowest charge transfer process: electrons or ions. In the present geometry it appears that ion movement through the film thickness is the rate determining step. The faster ion movements of $TFSI^-$ compared to PF_6^- produce faster rates of charging in this polymer and larger tip displacements during a given time period.

Another clear observation from Figure 4-17 and Figure 4-18 is that the position of the resonance peaks occurs at higher frequencies for PPy/PF_6 than in the PPy/TFSI actuators of similar length. This result seems anomalous at first, since the rate of actuation is clearly faster in the PPy/TFSI than the PPy/PF_6. The position of the resonance peak, however, depends directly on the square root of the beam stiffness. It is possible that

the PPy/TFSI layers are more fully swollen with electrolyte and have a lower Young's modulus than the PPy/PF_6. The lower moduli of the PPy/TFSI layers would produce a lower beam stiffness and lower resonance frequency. The more swollen nature of the PPy/TFSI may also account for its faster charging speed and step response since ion diffusion is likely to be faster in the more open and molecularly-porous structure. These arguments are supported by the force response results shown in Figure 4-19. Although the tip displacements for PPy/TFSI are as much as 300% higher than the equivalent PPy/PF_6 actuator, the tip force is only ~30% higher. The tip force will be a product of the tip displacement and the beam stiffness. The displacement and force results are explainable if the PPy/TFSI layers have a lower Young's modulus than the PPy/PF_6. Thus, the position of the resonance peaks, the amount of tip force produced and the faster charging in PPy/TFSI all support the concept that this polymer is more fully swollen with electrolyte than the PPy/PF_6 polymer.

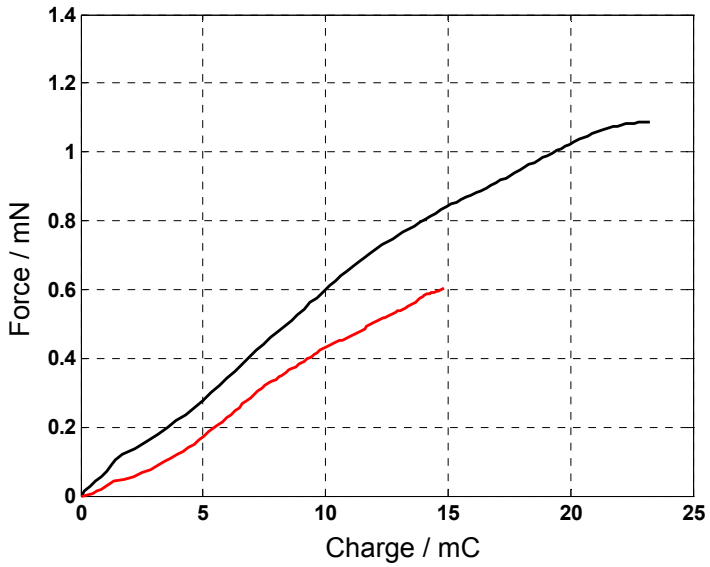

Figure 4-23 Force generated (Figure 4-19) against charge injected (Figure 4-21) for the first 1 second after a step voltage of +1.0 V was applied.

4.3.7 CORRELATION BETWEEN THE BLOCKING FORCE AND APPLIED VOLTAGE IN VARIOUS ELECTROLYTES

The primary motivation of this study was to develop a miniaturised actuator that would have the capability to straighten the curled cochlear implant electrode and control recurling for safe surgical implantation. The blocking force produced from polypyrrole trilayer actuators in relation to the polypyrrole coating thickness, applied voltage, polymer dopant, and electrolyte used was investigated here.

The results on the effect of polypyrrole coating thickness (Figure 4-24) showed that the blocking force increased with thickness from 12.5 μm up to 100 μm. In addition, the maximum force of ~ 2.6 mN produced here was significant in that it was ~ 60 × its own weight.

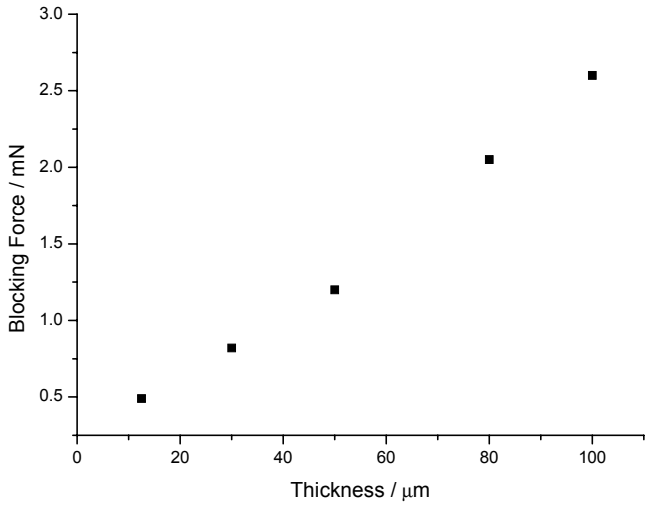

Figure 4-24 Blocking force *vs.* polypyrrole film thickness for a PPy/PF_6 trilayer actuator using 0.05 M TBA.PF_6 in PC electrolyte. Voltage applied: + 1.0 V. Actuator dimensions: 1 mm wide, 10 mm long.

Besides the effect of coating thickness, the blocking force also increased with the amplitude of applied voltage and was also affected by the

use of different dopants and electrolytes. For a PPy/PF_6 trilayer actuator with polypyrrole thickness of 30 μm, the blocking force increased proportionally with the applied voltage up to 1.2 V and then gradually leveled off (Figure 4-25). The maximum blocking force obtained was ~ 1 mN at 1.5 V. For a PPy/TFSI trilayer actuator, a similar linear relation was found up to 1.2 V where the maximum blocking force was ~ 1.26 mN (Figure 4-26). Increasing the applied voltage resulted in a decreased blocking force to ~ 1.16 mN at 1.6 V, which might have been due to over-oxidation of the polypyrrole [33]. The maximum blocking force produced at 1.2 V for the PPy/TFSI trilayer actuator was ~ 26 % higher than that for the PPy/PF_6 trilayer actuator at 1.5 V.

Interesting results in relation to the blocking force were found when ionic liquids were used as supporting electrolytes. Besides the unusual actuation of anodic contraction reported previously [16], the maximum blocking forces observed using ionic liquids were much lower than those using PC-based electrolyte. The maximum blocking force produced by a PPy/PF_6 trilayer actuator electrolyte using BMI.PF_6 was ~ 0.58 mN (Figure 4-25) compared to ~ 1.0 mN for the same type of actuator using 0.05 M TBA.PF_6 in PC electrolyte. In addition, the blocking force leveled off at a relatively lower voltage of ~ 1V compared to ~ 1.5V. Similarly, the maximum blocking force produced by a PPy/TFSI trilayer actuator using EMI.TFSI electrolyte was lower at ~ 0.6 mN compared to the ~ 1.26 mN produced for the same type actuator using 0.05 M LiTFSI in PC electrolyte (Figure 4-26). Similarly to the PPy/PF_6 trilayer actuator, the blocking force produced by the PPy/TFSI trilayer actuator leveled off at a much lower voltage of ~ 0.8 V compared to ~ 1.2 V.

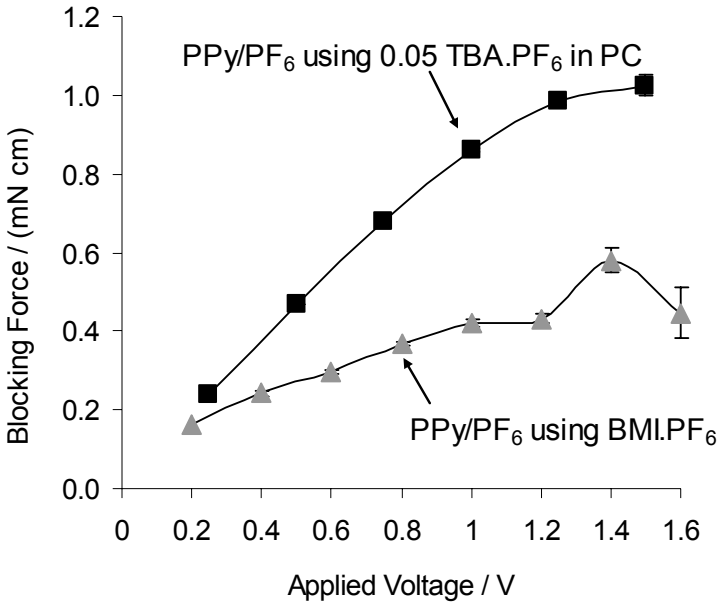

Figure 4-25 Blocking force *vs.* applied voltage for PPy/PF_6 trilayer actuator using 0.05 M $TBA.PF_6$ in PC or $BMI.PF_6$ electrolytes. PPy/PF_6 thickness: 30 μm. Actuator dimensions: 1 mm wide, 10 mm long.

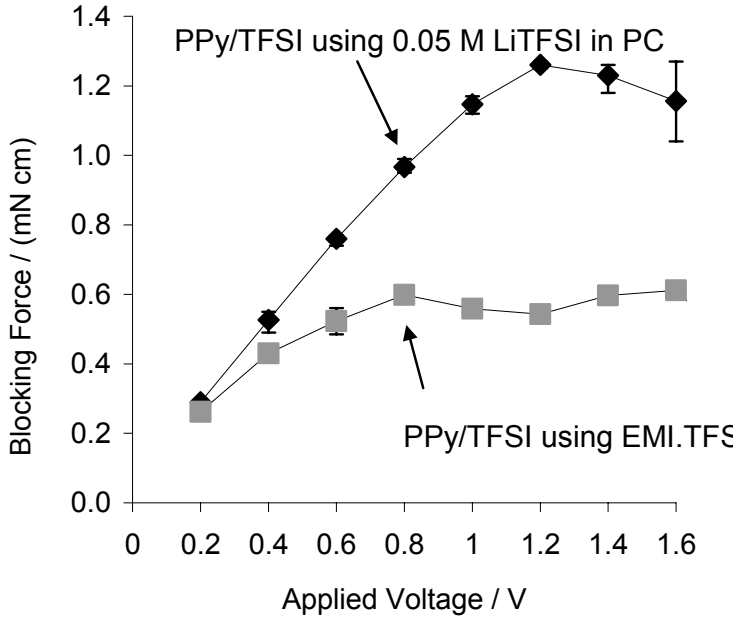

Figure 4-26 Blocking force *vs.* applied voltage for PPy/TFSI trilayer actuator using 0.05 M LiTFSI in PC or EMI.TFSI electrolyte. PPy/TFSI thickness: 30 μm. Actuator dimensions: 1 mm wide, 10 mm long.

The unusual opposite direction of bending when using ionic liquids electrolytes indicated that the polypyrrole expanded during reduction and contracted during oxidation. This may be explained by a cation dominated actuation mechanism. It is believed that EMI or BMI cations would be incorporated during electrochemical reduction, leading to expansion of the polypyrrole. The lower blocking forces that leveled off at relative lower voltage (Figure 4-25 and Figure 4-26) for polypyrrole trilayer actuators using ionic liquid electrolytes instead of PC-based electrolytes suggested that the reduced polypyrrole might not have been able to hold the incorporated cation species, and that dopant anions and incorporated cations might gradually diffuse out of the polypyrrole and into the bulk solution, depending on the duration and amplitude of the applied voltage. This detrimental effect over extended times in the reduced state has been discussed previous as the 'salt draining' phenomenon [34, 35], reflecting the thermodynamic equilibrium of the solvent activity and the salt activity. Further evidence was based on the experimental observation that the blocking force decreased with time for continuously applied voltage. This was contrary to the very stable blocking force observed when using PC-based electrolyte, which was steady for the duration of applied voltage. Note that above analysis was based on an assumption that at a particular applied voltage, the mechanical properties of PPy layer in every electrolyte used are similar.

To confirm the possible diffusion of cations and anions out of polypyrrole when using ionic liquid electrolytes, micro elemental analysis was performed to probe the density of PF_6 dopant in PPy/PF_6 films at two extreme redox states. The result showed that the % weight of PF_6 was significantly decreased from 18.89 % (P: 4.04 % + F: 14.85 %) to 3.61% (P: 0.78 % + F: 2.86 %) when the PPy/PF_6 film was reduced in $BMIPF_6$ from +

0.65 V to – 0.8 V (Figure 4-27). According to calculated data, if the charge compensation was achieved by the incorporation of cation, the % weight of dopant PF_6 would decrease slightly from 18.89% to the minimum of 15.9% at the point that the polymer was fully reduced and BMI^+ (Fw: 141) was incorporated at the molar ratio of 1:1 to the dopant PF_6^- (Fw: 145). Therefore, the decrease in the % weight of PF_6^- to 3.61% would only be made possible by the loss of dopant PF_6^- from the polymer. This suggests that, although cation incorporation may have dominated during the initial stages of reduction, prolonged (10 min) application of the reducing potential resulted in diffusion of paired cation and anions from the polypyrrole. This may explain the decay in blocking force with time for polypyrrole trilayer actuators using ionic liquid electrolytes.

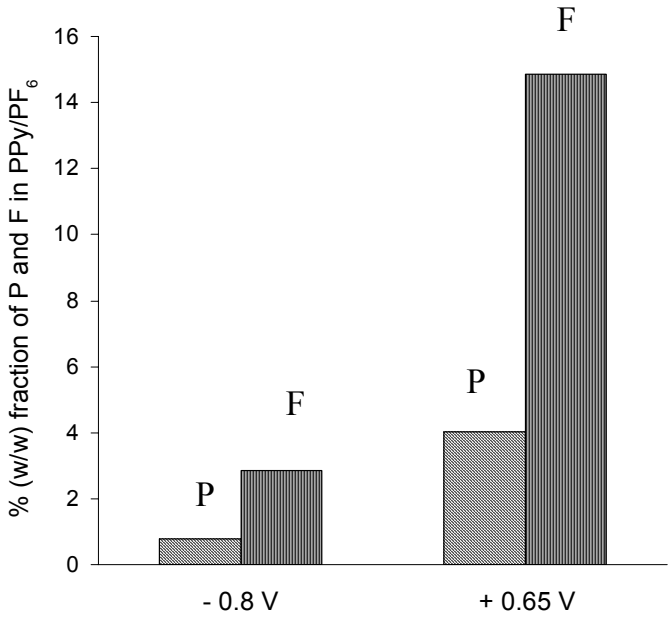

Figure 4-27 % (W/W) fraction of P and F in PPy/PF_6 by microanalysis of the fully oxidized (+ 0.65 V applied potential) and fully reduced (-0.80 V applied potential) states.

With reference to the above results, it appears that when using LiTFSI in PC electrolyte in polypyrrole trilayer actuators, $TFSI^-$ was dominant during actuation, while the EMI^+ was dominant when using the EMI.TFSI electrolyte. Similarly, when using the TBA.PF_6 in PC electrolyte, PF_6^- was dominant during actuation, while BMI^+ was dominant when using the BMI.PF_6 electrolyte in agreement with Lu *et al.* [16], for which, the low cation transport number can be ascribed to ion paring effect [36, 37]. The resulting actuation was therefore dominated by the anion when using the LiTFSI in PC electrolyte. For ionic liquids, such as EMI.TFSI, it has been shown that cations diffuse faster than anions, even if cation radii were larger than anion radii [38-40]. The resulting actuation was therefore cation dominant when using ionic liquid electrolytes.

4.3.8 BENDING TORQUE REQUIRED TO STRAIGHTEN THE NUCLEUS®24 CONTOUR™ ELECTRODE

To assess the possibility of using polypyrrole trilayer actuators in the cochlear implant, it was first necessary to know the torque required to straighten the curled electrode array. The torque necessary to straighten the curled electrode of the most commonly used cochlear implant electrode, Nucleus® 24 Contour™ was determined (Figure 4-28). At least ~ 1.6 mN.cm torque was required to straighten the implant tip and this increased linearly with the increasing diameter of implant as the point at which the force was applied was moved further from the tip. The maximum required strengthening torque required of ~ 12.65 mN.cm was for force application to the bottom part of the ring electrode array (inset in Figure 4-28), ~ 10 cm from the tip. Considering that the maximum diameter of an actuator for the cochlear implant should be < 150 μm, and since a maximum blocking force of 1.26 mN for a PPy/TFSI trilayer actuator with an effective length of 1 cm

(i.e. 1.26 mN.cm torque) was achieved for an actuator width of 1 mm, the blocking force generated from this polypyrrole trilayer actuator is not sufficient to straighten the Nucleus® 24 Contour™ electrode. To achieve this task, further development in configuration and materials of and for polypyrrole trilayer actuators is required.

Although not able to straighten the Nucleus® 24 Contour™ electrode, polypyrrole trilayer actuators, such as those prepared in this study, may be used for the future thin film cochlear implant electrode (currently under development). Further studies on the encapsulation of polypyrrole trilayer actuators in such a device to avoid electrolyte and DC current leakage are required.

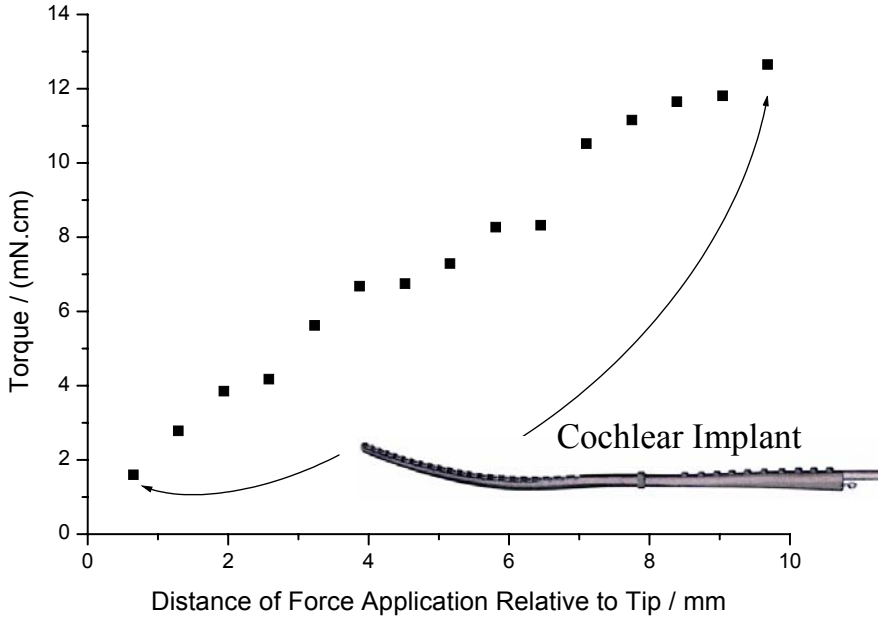

Figure 4-28 Torque required to straighten the Nucleus® 24 Contour™ electrode as a function of the distance relative to the electrode tip at which force was applied.

4.4 CONCLUSIONS

In this study, polypyrrole trilayer actuators were successfully constructed. Polypyrrole trilayer actuators are easy to fabricate and the use of a porous PVDF membrane backing enables their practical use in air and effectively eliminates the delamination problem. It was demonstrated that the choice of electrical stimulation method is important in determining both energy consumption and cycle life.

A high amplitude harmonic vibration was obtained for the first time using a PPy/TFSI trilayer actuator. A plot of exerted force in response to a 1 V step potential showed that the time constant using a PPy/TFSI actuator was much smaller (~ 0.47 s) that that using a PPy/PF_6 actuator (~ 0.76 s), indicating the more rapid actuation response of the former compared to the latter.

The study of blocking force showed that the maximum blocking force was proportional to the thickness of PPy and the amplitude of applied voltage when an organic salt dissolved in PC was used as the electrolyte. In comparison, when a pure ionic liquid (EMI.TFSI or BMI.PF_6) was used as the electrolyte, the blocking force was in the opposite direction, in agreement with cathodic expansion behaviour reported previously. However the blocking force was much smaller. Microanalysis of the PPy/PF_6 film when using BMI.PF_6 as the electrolyte showed the expulsion of the dopant anion (PF_6^-) after prolonged application of a reducing potential (- 0.8 V *vs.* Ag/Ag^+). It was suggested that switching from cathodic expansion initially to cathodic contraction may occur under reducing potentials depending on the amplitude and duration of the electrical stimulation. An ion diffusion controlled mechanism was proposed to explain this.

Finally, the possibility of using PPy trilayer actuators to straighten the cochlear implant was evaluated. The results suggested that at their current stage of development, PPy trilayer actuators are not able to give a controlled steering of a Nucleus® 24 Contour™ electrode, however their use in thin film electrodes to be developed in the future might be possible.

4.5 REFERENCES

1. Beebe, D.J., Moore, J.S., Bauer, J.M., Yu, Q., Liu, R.H., Devadoss, C. and Jo, B.H., *Nature*, 404 (6 April) (2000) 588-590.
2. Baughman, R.H., Cui, C., Zakhidov, A.A., Iqbal, Z., Barisci, J.N., Spinks, G.M., Wallace, G.G., Mazzoldi, A., Rossi, D.D. and Rinzler, A.G., *Science (Washington, D. C.)*, 284 (5418) (1999) 1340-1344.
3. Sewa, S., Onishi, K., Asaka, K., Fujiwara, N. and Oguro, K. In *Proc. IEEE 11th Workshop on Microelectronic Mechanical Systems (MEMS 98)*, 1998, pp 148-153.
4. Tant, M.R. and Mauritz, K.A. *Ionomers: Synthesis, Structure, Properties and Applications*; Blackie Academic and Professional Press, 1997.
5. Oguro, K., Fujiwara, N., Asaka, K., Onishi, K. and Sewa, S., *Smart Materials and Structures, Proc. SPIE*, 3669 (1999) 64-71.
6. Nasser, S.N. and Thomas, C. *Ionic Polymer-Metal Composite (IPMC)*; SPIE Press, 2001; pp 139-191.
7. Otero, T.F. In *Handbook of Organic Conductive Molecules and Polymers*; H. S. Nalwa, Ed.; John Wiley & Sons Ltd.: Chichester, 1997; Vol. 4, pp 558.
8. Grande, H., Otero, T.F. and Cantero, I., *Journal of Non-Crystalline Solids*, 235-237 (1998) 619-622.
9. Della Santa, A., Rossi, D.D. and Mazzoldi, A., *Smart Materials and Structures*, 6 (1997) 23.
10. Baughman, R.H., Shacklette, I.W. and Elsenbaumer, R.L. *Microelectromechanical actuators based on conducting polymers*; Kluwer, Dordrecht, 1991; pp 267.
11. Spinks, G.M., Liu, L., Wallace, G.G. and Zhou, D.Z., *Advanced Functional Materials*, 12 (6-7) (2002) 437-440.

12. Baughman, R.H., *Synthetic Metals*, 78 (3) (1996) 339-353.

13. Hara, S., Zama, T., Takashima, W. and Kaneto, K., *J. Mater. Chem.*, 14 (2004) 1516-1517.

14. Madden, J.D., Cush, R.A., Kanigan, T.S., Brenan, C.J. and Hunter, I.W., *Synthetic Metals*, 105 (1999) 61-64.

15. Ding, J., Liu, L., Spinks, G.M., Zhou, D., Wallace, G.G. and Gillespie, J., *Synthetic Metals*, 138 (2003) 391-398.

16. Lu, W., Fadeev, A.G., Qi, B., Smela, E., Mattes, B.R., Ding, J., Spinks, G.M., Mazurkiewicz, J., Zhou, D., Wallace, G.G., MacFarlane, D.R., Forsyth, S.A. and Forsyth, M., *Science*, 297 (5583) (2002) 983-987.

17. Otero, T.F. In *Handbook of Organic Conductive Molecules and Polymers*; H. S. Nalwa, Ed.; John Wiley & Sons Ltd.: Chichester, 1997; Vol. 4, pp 553.

18. Pyo, M., Bohn, C.C., Smela, E., Reynolds, J.R. and Brennan, A.B., *Chem. Mater.*, 15 (2002) 916-922.

19. Sansinena, J.-M., Gao, J. and Wang, H.-L., *Adv. Funct. Mater.*, 13 (9) (2003) 703-709.

20. Andrews, M.K., Jansen, M.L., Spinks, G.M., Zhou, D. and Wallace, G.G., *Sensors and Actuators A: Physical*, 114 (1) (2004) 65-72.

21. Otero, T.F. In *Handbook of Organic Conductive Molecules and Polymers*; H. S. Nalwa, Ed.; John Wiley & Sons Ltd.: Chichester, 1997; Vol. 4, pp 549.

22. Otero, T.F. and Cortes, M.T., *Chemistry Communications*, (2004) 284-285.

23. Otero, T.F. and Cortes, M.T. In *SPIE Smart Structures and Materials: Electroactive Polymer Actuators and Devices*, 2001; Vol. 4329, pp 93-100.

24. Foutz, J. In *SMPS Technology Knowledge Base*; J. Foutz, Ed., 2004; Vol. 2004.

25. Madden, J.D., Cush, R.A., Kanigan, T.S. and Hunter, I.W., *Synthetic Metals*, 113 (1-2) (2000) 185-192.

26. Ogata, K. *System dynamics / Katsuhiko Ogata*, 4th ed. ed.; Prentice Hall,: Upper Saddle River, N.J. :, c2004.

27. Steidel, R.F.R.F., 1926- *An introduction to mechanical vibrations / Robert F. Steidel, Jr*, 3rd ed ed.; Wiley,: New York :, c1989.

28. Madden, J.D.W., Madden, P.G.A. and Hunter, I.W. In *SPIE Smart Structures and Materials: Electroactive Polymer Actuators and Devices*, 2001; Vol. 4329, pp 72-83.

29. Smela, E., Kallenbach, M. and Holdenried, J., *IEEE Jounal of Microelectromechanical Systems*, 8 (4) (1999) 373-383.

30. Kaneko, M., Fukui, M., Takashima, W. and Kaneto, K., *Synthetic Metals, International Conference on Science and Technology of Synthetic Metals*, 84 (1-3) (1997) 795-796.

31. Alici, G., Mui, B. and Cook, C., *Sensors and Actuators A: Physical*, 126 (2006) 396-404.

32. Alici, G., Metz, P. and Spinks, G.M., *Journal of Smart Materials and Structures*, 15 (2006) 243-252.

33. Lewis, T.W., Spinks, G.M., Wallace, G.G., Mazzoldi, A. and De Rossi, D., *Synthetic Metals*, 122 (2) (2001) 379-385.

34. Pei, Q. and Inganas, O., *J. Phys. Chem. B*, 96 (1992) 10507.

35. Jager, E.W.H., Smela, E. and Inganas, O., *Science*, 290 (November) (2000) 1540-1545.

36. Hayamizu, K., Aihara, Y., Arai, S. and Martinez, C., *J. Phys. Chem. B*, 103 (1999) 519-24.

37. West, K. *Personal Communications*, The Danish Polymer Centre, Department of Chemical Engineering, The Technical University of Denmark, Lyngby, Den. 2006.

38. Tokuda, H., Hayamizu, K., Ishii, K., Susan, M.A.B.H. and Watanabe, M., *J. Phys. Chem. B.*, 108 (2004) 16593-600.

39. Noda, A., Hayamizu, K. and Watanabe, M., *J. Phys. Chem. B*, 105 (2001) 4603-10.

40. Hayamizu, K., Aihara, Y., Nakagawa, H., Nukuda, T. and Price, W., *J. Phys. Chem. B*, 108 (2004) 19527-32.

CHAPTER 5 POLYPYRROLE-BASED MICROPUMP FOR CONTROLLED FLUID TRANSPORT

5.1 INTRODUCTION

The development of low power fluid management systems underpins the realisation of efficient microfluidic and controlled release systems. Fluid management systems that have been used to date fall into two classes [1]. The first class is reciprocating micropumps, which require actuators to displace liquid and generate pressure, and which actively control inlet and outlet valves. Reciprocating micropumps based on piezoelectric [2, 3], thermopneumatic [4–6], electrostatic [3, 7] and electromagnetic [3] systems have been developed. The second class is continuous flow micropumps, distinguished by their ability to provide constant fluid transport. Continuous flow systems employ different pumping principles, including ultrasonic [8], electrokinetic [9], magnetohydrodynamic (MHD) [10], electrohydrodynamic (EHD) [11–13], electroosmotic and magneto-driven ferrofluidic [14]. Despite the myriad of approaches investigated to date, the development of low power systems capable of delivering accurate and sustained flow rates in the nl–µl min^{-1} range is still required. Inherently conducting polymers (ICPs) such as polypyrrole undergo significant volume changes upon oxidation/reduction through the accompanying insertion/removal of ions (refer to Equation 1-1).

Volume changes in ICPs associated with redox switching have been used in the development of electromechanical actuators, often referred to as artificial muscles [15, 16]. It has been demonstrated that ICPs provide more than an order of magnitude advantage in achievable dimensional changes, electrically generated stresses and work densities per cycle compared with piezoelectric polymer actuators [17]. Using this approach, ICPs have been recently used in the construction of valves [18, 19] for microfluidic systems.

In this Chapter, the electromechanical properties of polypyrrole have been utilised in the design and development of a novel microfluidic

pumping system. A "Tube In Tube Actuator Nodule" (TITAN) micropump structure was successfully constructed to exploit the advantages of polypyrrole including low operational voltage, low power requirements, mechanical flexibility and even intrinsic resistance. The effects of backpressure, applied voltage and charge on the volume displacement were investigated. A novel approach of allowing the resistive and electrochemical properties of polypyrrole to do the 'sequential' shifting of the actuation was considered. The potential use of the TITAN micropump for the controlled delivery of drugs in biomedical applications such as the cochlear implant is envisaged.

5.2 EXPERIMENTAL

5.2.1 REAGENTS AND MATERIALS

Aromatic, polyether-based thermoplastic polyurethane tubing (PU, provided as a gift from BSI) has an inner diameter of 950 μm and an outer diameter of 1050 μm. Stainless steel mesh (W500-50) was purchased from Metal Mesh Pty Ltd., and used as received. For all other reagents and materials mentioned in this Chapter refer to section 2.10 in Chapter 2.

5.2.2 CONSTRUCTION OF TITAN MICROPUMP

The first part of the TITAN micropump (Figure 5-1) was prepared using a porous PVDF fibre (650 μm outer diameter) (Figure 5-1 "A") as a mechanical support inside a PU tube (Figure 5-1 "B"). The PU tube was sputter coated with platinum (~ 72 nm as calculated from the deposition rate of 1.2 $Å.s^{-1}$) before polypyrrole was electrodeposited onto it in an electrochemical cell as shown in Figure 5-2. To achieve an even coating along the surface of a tube, a 6 cm long, 50 μm diameter platinum wire was

wound around the outside of the 4 cm long platinised PU tube to enhance its electrical conductivity. This platinised PU tube was used as a working electrode in the electrochemical cell containing 0.05 M TBA.PF_6 and 0.06 M pyrrole in PC. The platinised PU tube working electrode was also filled with deionised water and sealed at both ends. Electropolymerisation was carried out at −20 ºC, with the shape of the PU tube maintained by the internal frozen water. Polypyrrole was grown galvanostatically for 12 hours at a constant current density of 0.1 $mAcm^{-2}$, after which a ~ 30 μm thick coating around the tube was obtained. The second part of the TITAN micropump (Figure 5-1, "C") was the electrochemical cell separator, made of an inert porous PVDF membrane (110 μm thickness, 0.45 μm pore size) of size 30 mm × 12 mm and rolled into a thin hollow tube (diameter □3 mm). The third part of the TITAN micropump (Figure 5-1, "D") was the auxiliary electrode, prepared on a PVDF membrane substrate. The PVDF membrane was sputter-coated on both sides with platinum before polypyrrole was electrodeposited using the same conditions as for the PU tube. The resulting laminate was cut to a size of 30 mm × 12 mm and then rolled to form a hollow tube (3.5 mm outer diameter, 3.1 mm inner diameter). This laminated PVDF hollow tube was then connected to a piece of stainless steel mesh (SS) to complete the auxiliary electrode. The TITAN working electrode was inserted inside the inert PVDF hollow tube, which in turn was placed inside the TITAN auxiliary electrode assembly. The entire system was encased with a plastic tube composition, (4 mm inner diameter, 5 mm outer diameter) after soaking in TBA.PF_6/PC electrolyte for 30 minutes.

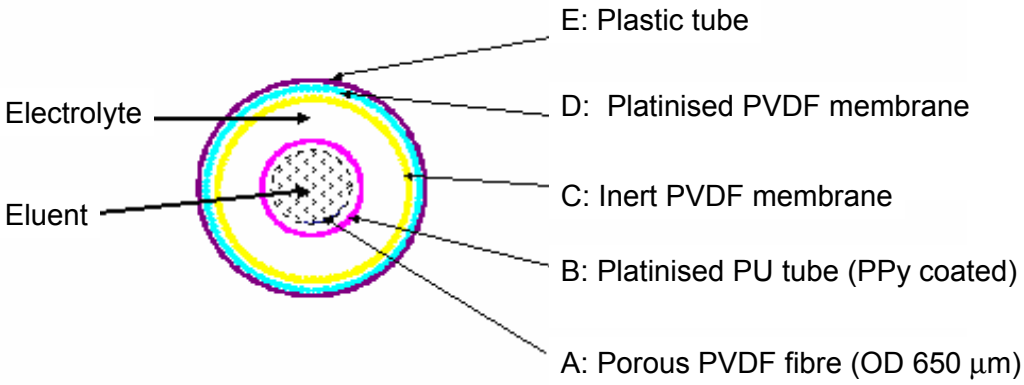

Figure 5-1 Schematic diagram showing the TITAN assembly. A: porous PVDF fibre (OD: 650 μm) used to maintain the micropump cylindrical shape. B: platinised PU tube (OD: 1050 μm, ID: 950 μm) wrapped with *Φ* 50 μm platinum wire and coated with polypyrrole, used as the TITAN working electrode. C: inert PVDF membrane, used as an inert electrochemical cell separator and to hold the 0.25 M $TBA.PF_6$/PC supporting electrolyte. D: platinised PVDF membrane coated with polypyrrole connected via stainless steel mesh, used as the TITAN auxiliary electrode. E: plastic tube (3 cm long, OD: 5 mm, ID: 4 mm) used to pack the electrode assembly.

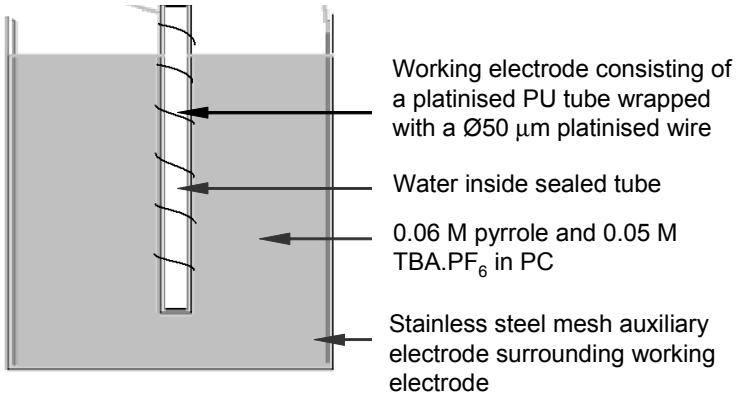

Figure 5-2 Schematic diagram showing the electrochemical cell used to electrodeposit polypyrrole onto a platinised polyurethane tube with surrounding Pt wiring.

5.2.3 CHARACTERISATION OF THE TITAN MICROPUMP

The fully assembled TITAN micropump was connected at one end with a glass pipette. This was used as an outlet to a water column in order to apply a backpressure via a plastic tube (ID: 1000 μm) to the TITAN outlet channel. The height difference between the upper level of the water column and the open end of the outlet channel was adjusted to apply the required backpressure. At the other end of the TITAN pump, a 100 μl glass syringe was connected and used to supply fluid into the TITAN internal chamber. In this experiment, high vacuum grease (Dow Corning) was used as the joint sealing material. A diagram of the fully assembled TITAN mciropump is shown in Figure 5-3.

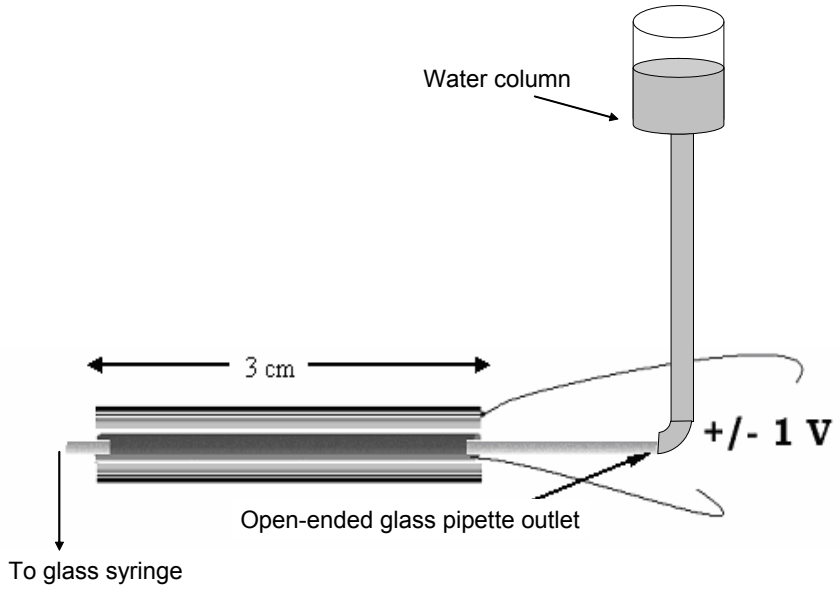

Figure 5-3 The TITAN assembly. A water column was used to apply backpressure.

The bulk conductivity of the TITAN electrodes was measured using a four-point probe (model RM2, JANDEL). Electrochemical properties were characterised by cyclic voltammetry (CV) in a three-electrode cell with a Ag/Ag^{+} reference electrode and a stainless steel mesh auxiliary electrode.

The electrolyte was 0.25 M TBA.PF_6 in PC. The potential during CV characterisation was cycled between + 650 mV and − 1000 mV at a scan rate of 10 mV s^{-1}.

In an additional experiment, 8 individual TITAN components (1 cm each separated by a 0.3 cm blank section) were constructed on a single 10 cm PU tube by a sectional masking technique during sputter coating (Figure 5-4). A solid wire (Ø 800 μm) was inserted into the TITAN tube to reduce the dead volume. Prior to the electrochemical deposition of polypyrrole (same conditions as used previously), platinum lead wires (Ø 25 μm) were intentionally attached to each segment and embedded in the polypyrrole layer after deposition, so that a reliable electrical connection could be achieved. Every TITAN electrode was electrically isolated from each other and simultaneously stimulated at DC +/- 1.0 V by using 8- relay circuitry. This 8- relay circuitry was controlled by a switching cluster program (Figure 5-5, written in LabView) at a programmed sequential switching frequency of 0.5 Hz with a 4-segment interval.

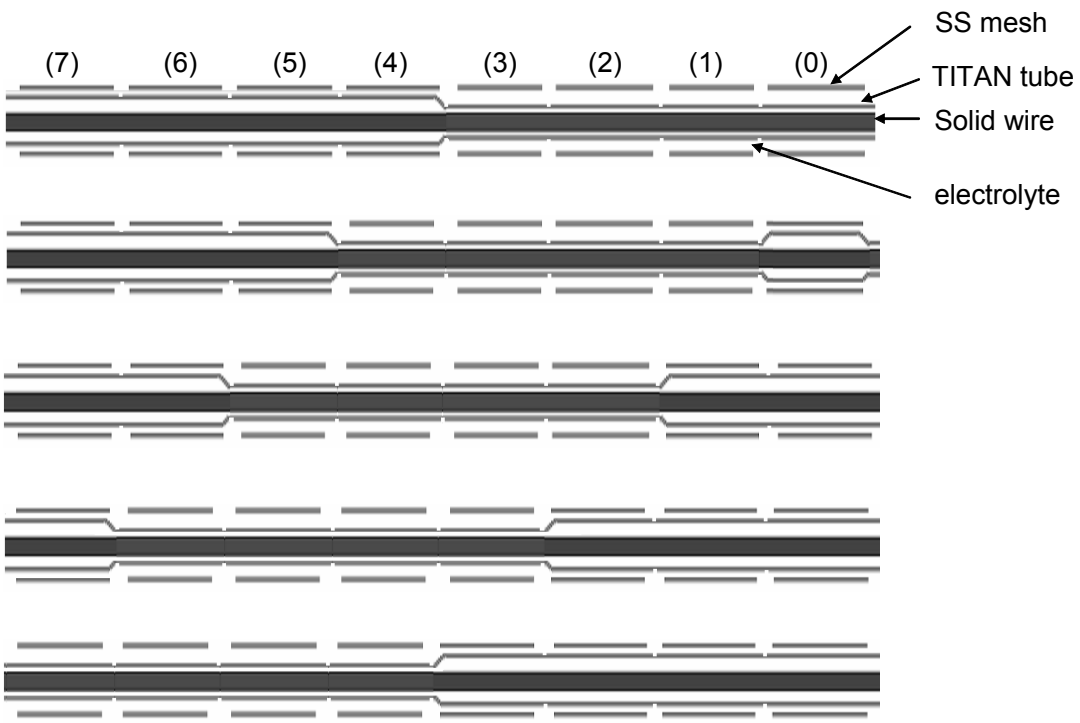

Figure 5-4 Schematics showing 8 TITAN working electrodes constructed in series on a single polyurethane tube and their volume change in response to sequential switching of voltage.

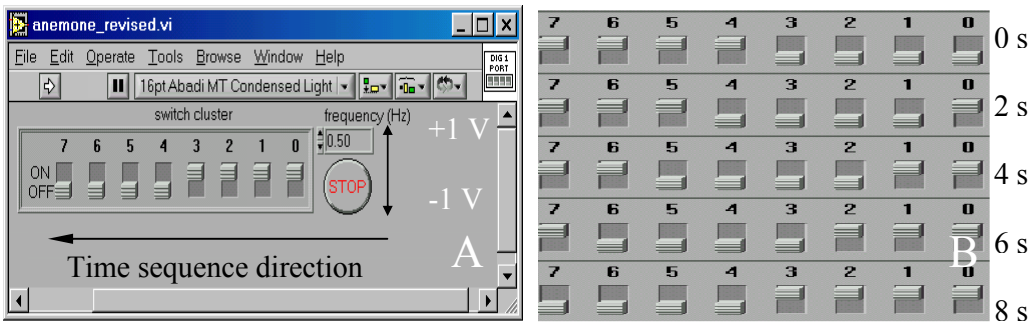

Figure 5-5 LabView switching cluster program for the dynamic switching of TITAN tube segments at +/- 1.0 V.

5.3 RESULTS AND DISCUSSION

The following sections present findings in regard to the use of cyclic voltammetry to probe the electrochemical properties of the TITAN components. The effect of applied voltage, charge transferred and applied backpressure on the volume displaced using the TITAN micropump was then investigated. In addition, preliminary results in regard to trials using an electronic switching cluster and the intrinsic resistance of the TITAN micropump to create a peristaltic pumping regime are also presented.

5.3.1 CYCLIC VOLTAMMETRY OF TITAN COMPONENTS

Electrochemically prepared TITAN electrodes were shown to have conductivities of ~ 240 S cm^{-1}, as determined by four point probe measurements. This property of electrical conductivity (or resistance) was later utilised in the development of a peristaltic pumping regime. The operational voltage range of the TITAN components was determined by CV in a 3-electrode cell. Well-resolved oxidation/reduction peaks for polypyrrole deposited on either the platinised PU tube electrode (Figure 5-6 "A") or for polypyrrole deposited on a platinised PVDF membrane (Figure 5-6 "B") were observed. The significantly higher current observed for the TITAN auxiliary electrode compared to the TITAN working electrode was primarily attributed to the higher geometric surface area of the former (12 mm^2) compared to the latter (4.7 mm^2). In addition, the porous nature of the PVDF membrane substrate onto which polypyrrole was deposited in order to give the auxiliary electrode also contributed to the higher current observed. CV was also carried out on the TITAN micropump assembly (Figure 5-7). Again well-defined oxidation/reduction responses were observed even when the TITAN was removed from the electrolyte solution

with electrolyte still filling the porous PVDF separator between the electrode components. CV of the TITAN micropump components and of the entire TITAN micropump assembly showed that the application of a square wave potential waveform with limits of + 1.0 V and – 1.0 V would be sufficient to induce complete oxidation and reduction of polypyrrole.

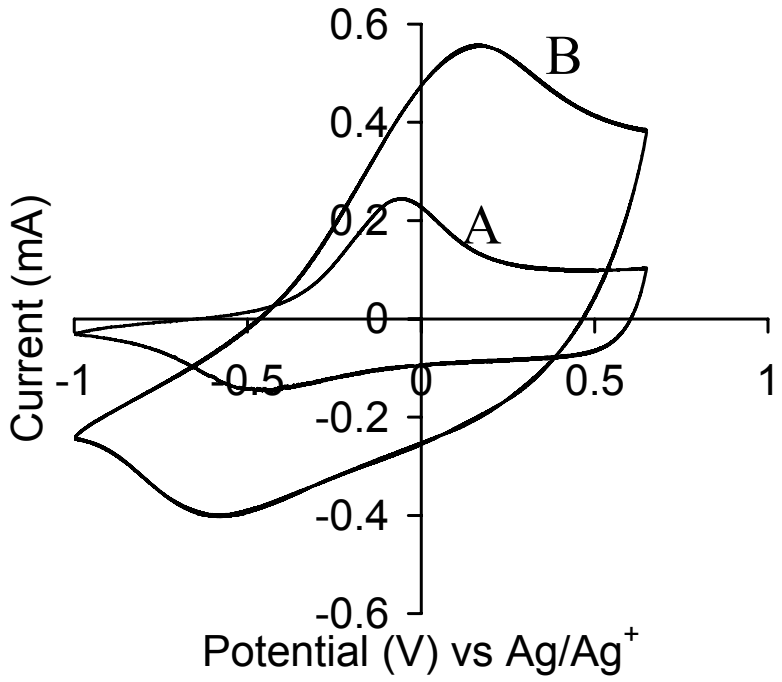

Figure 5-6 CV characterization of (A) TITAN micropump working electrode (polypyrrole coated PU tube), and (B) TITAN micropump auxiliary electrode (polypyrrole coated PVDF membrane); lower potential limit = -1.0 V, upper potential limit = + 0.65 V, scan rate = 50 $mV.s^{-1}$; electrolyte: 0.25 M $TBA.PF_6$ in PC.

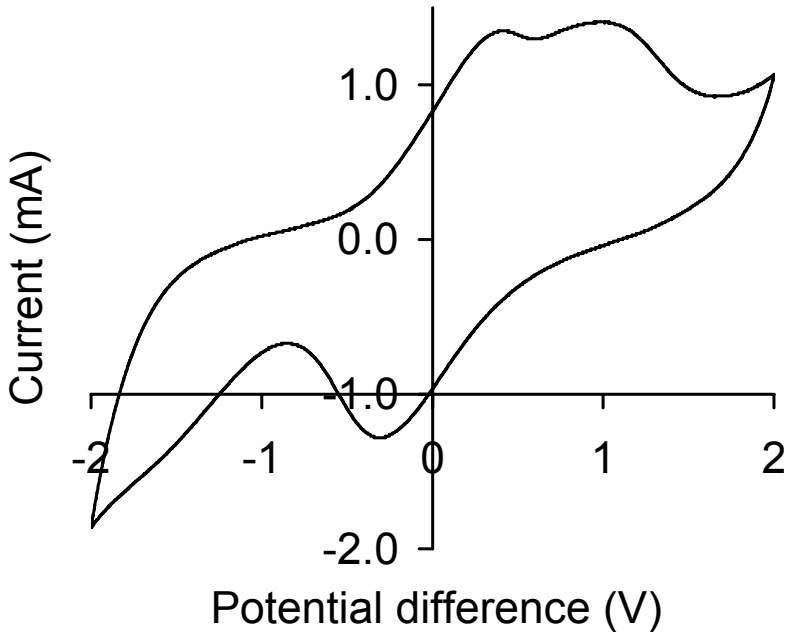

Figure 5-7 CV of TITAN assembly using two-electrode setup. Potential (*vs.* auxiliary electrode) was swept from +2.0 V to –2.0 V at 50 $mV.s^{-1}$ in 0.25 M $TBA.PF_6$ / PC.

5.3.2 FLUID MOVEMENT USING TITAN MICROPUMP

Initial fluid movement studies involved the use of a 3 cm long TITAN micropump segment and a pulsed voltage waveform where the polarity of the applied voltage was switched every 30 s. An example of the resulting fluid displacement is shown in Figure 5-8, which shows the displacement of a dyed liquid plug through the open ended capillary, when the voltage applied to the TITAN working electrode was switched from + 1.0 V to - 1.0 V. To investigate the effect of applied voltage on flow rate, positive pulses were kept constant at +1.0 V, and negative pulses were varied between 0.0 and −1.0 V as shown in Figure 5-9. Higher volumes of fluid were displaced at more negative potentials as shown in Figure 5-10. A maximum volume displacement of 2.5 µl was achieved for a 30 s pulse at -1.0 V. This 2.5 µl displacement corresponded to a change in volume of 12 % in the inner

chamber, which in turn reflected a circumferential strain of ~ 4.2 % in diameter. A diagram representing the changes in cross-sectional geometry of the TITAN micropump is illustrated in Figure 5-11. During the subsequent 30 s pulse at + 1.0 V, the displaced fluid returned to the pump reservoir. This reverse inflow indicated that it was not possible to create directional flow when using a single TITAN micropump. Continuous movement of the fluid back and forth was achieved without significant loss of performance for at least 300 cycles.

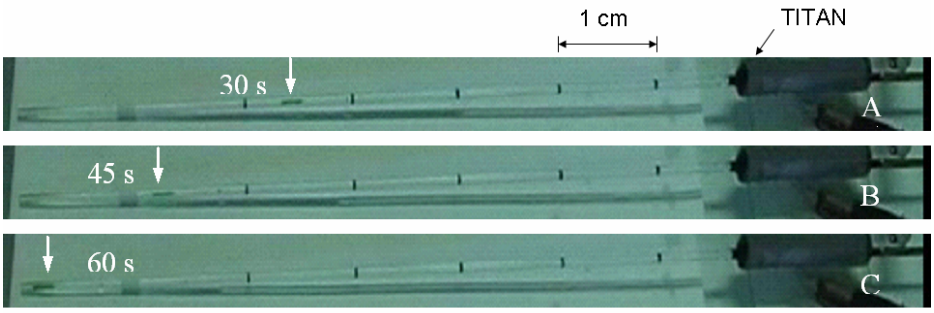

Figure 5-8 Sequence of video frames showing the displacement of dyed plug through an open-end glass capillary. (A) +1.0 V applied (0-30 s), the TITAN working electrode expands and plug moves towards the pump. (B) voltage switched to –1.0 V (30-60 s), the TITAN working electrode contracts and plug moves away from the pump. (C) displacement reached after -1.0 V applied for 30 s.

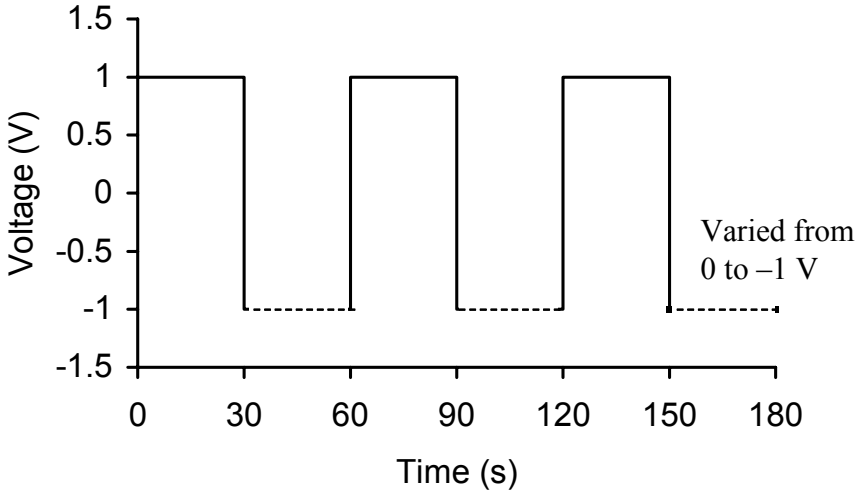

Figure 5-9 Pulsed potential waveform. Upper potential was held at +1.0 V and the lower potential was varied to optimise the pump operating potential (-1.0 V shown as an example).

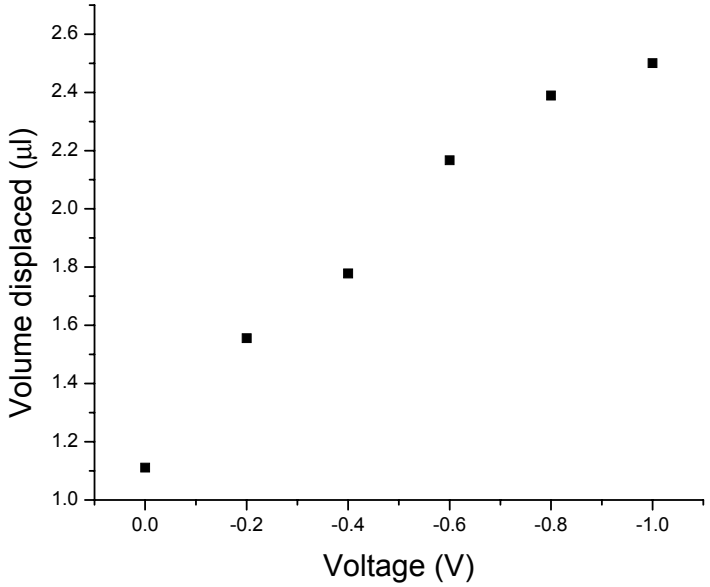

Figure 5-10 Volume of fluid displaced as a function of the voltage applied to a TITAN micropump; volume taken as the amount of fluid displaced after 30 s for each applied voltage.

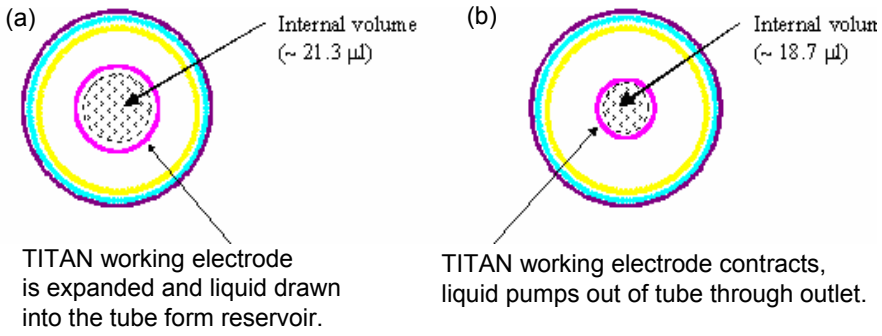

Figure 5-11 Diagram representing the dimensional changes in the polypyrrole coated platinised PU tube working electrode of the TITAN micropump, for applied voltages of (a) +1.0 V and (b) -1.0 V.

The volume change in the TITAN working electrode is caused by expansion/contraction of the polypyrrole coating in the inner chamber as a result of electrochemical redox cycling. This expansion/contraction occurs in both length and cross-sectional diameter although dimensional changes in length will be restricted by the substrate onto which the polymer is deposited. From the charge passed during oxidation/reduction the electrochemical efficiency (% of polymer oxidized/reduced, refer to section 4.3.2 in Chapter 4) of the TITAN micropump was calculated to be 46%. Charge is the key parameter in determining the extent of electrochemically generated strain [21] and hence fluid movement. For the TITAN micropump investigated in this study, data between the volume of fluid displaced and the charge integrated over 30 s intervals for the application of 0, -0.2, -0.4, -0.6, -0.8 and -1.0 V was plotted (Figure 5-12) and the polynomial fitting illustrates that the charge is related to the volume displaced via a quadratic polynomial.

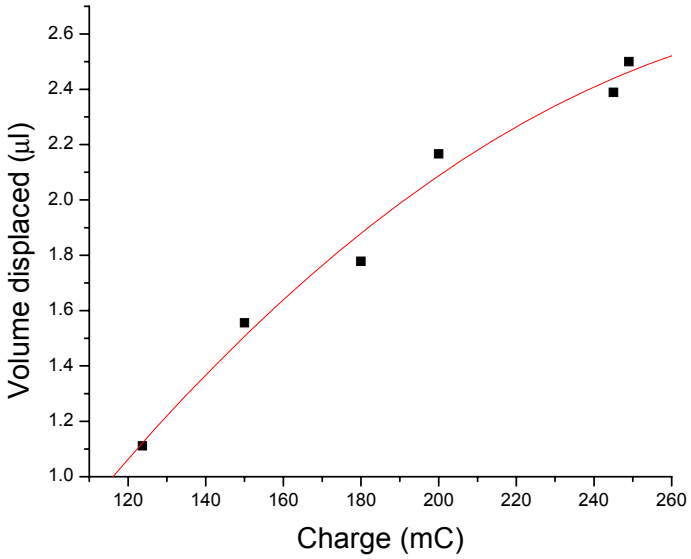

Figure 5-12 Volume of fluid displaced by TITAN micropump as a function of charge. The charge was the integration of the current obtained from the experiment shown in Figure 5-10.

However, based on the known relation that strain is proportional to charge transferred, relatively independent of load, the theoretical calculation indicated the relationship is a reversal, in that the volume displaced should be the trinomial of charge according to the following Equations:

$$\varepsilon = \alpha \times Q \qquad \text{..... 5-1}$$

$$\varepsilon = \frac{r_1 - r_2}{r_1} = \frac{l_1 - l_2}{l_1} \qquad \text{..... 5-2}$$

$$\Delta V = \pi \times r_1^2 \times l_1 - \pi \times r_2^2 \times l_2 \qquad \text{..... 5-3}$$

re-arrange the above Equations,

$$\Delta V = (\pi r_1^2 l_1 \alpha^3) Q^3 - 3(\pi r_1^2 l_1 \alpha^2) Q^2 + 3(\pi r_1^2 l_1 \alpha) Q \qquad \text{..... 5-4}$$

where ε is the strain where the circumferential strain and longitudinal strain of polypyrrole on the TITAN tube were assumed the same, α is the strain to charge coefficient, Q is the charge, r_1 and l_1 is the original diameter and length respectively of

the TITAN tube, r_2 and L_2 is the diameter and length respectively of the TITAN tube after charge passed over and ΔV is the volume change.

Equation 5-4 indicates that the slope should increase with the charge rather than decrease as shown in Figure 5-12. A possible reason for the large variation between the experimental and theoretical results might be the parasitic reactions that consume charge without producing strain and mechanical work. Further study might need to address the origin and effect of such possible parasitic reactions.

The effect of backpressure on the performance of a TITAN micropump was also investigated, showing that the volume displaced decreased by ~ 50% from ~ 2.50 μl to ~ 1.25 μl as the backpressure increased from 0 to 50 mbar (Figure 5-13). This decrease in the volume of fluid displaced corresponds to a ~ 30% reduction in actuation strain. The stress within the polypyrrole at a backpressure of 50 mbar (ignoring the polyurethane tube) is approximately 170 kPa. Spinks *et al* reported a comparable decrease in actuation strain for linear polypyrrole actuators under load, where the actuation strain decreased from 4.0% to 2.5% (40% decrease) for a load of 600 kPa [22]. It is thought that work against the substrate, in this case a polyurethane tube, may account for some of reduction in the actuation strain.

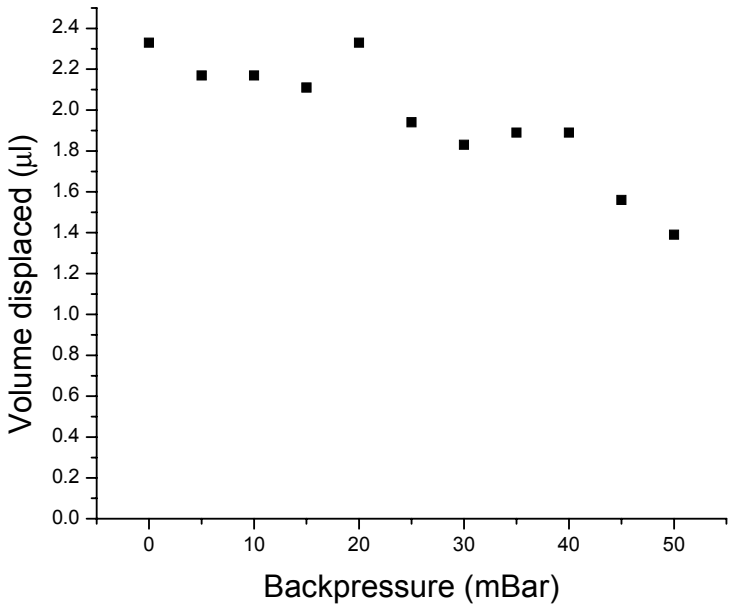

Figure 5-13 Volume of fluid displaced by a TITAN micropump as a function of applied back pressure.

5.3.3 APPLICATION OF THE TITAN MICROPUMP TO PERISTALTIC PUMPING

5.3.3.1 Utilisation of the electrical circuitry for sequential switching

When the voltages of the switch cluster along the 8 segments were switched from right to left at a frequency of 0.5 Hz with an interval of 4 segments as illustrated in Figure 5-4, a 0.2 $\mu l.min^{-1}$ flow rate was observed when the two ends of the pump were open to air. This was much lower than the 2.5 $\mu l.min^{-1}$ displacement using a single 3 cm length of TITAN micropump tube. The flow rate did not increase when the applied voltage was gradually increased to higher levels up to +/- 2.0 V where overoxidation occurred. It was also observed that the performance of the TITAN peristaltic pump was rather poor in that it was not able to generate any fluid movement with the application of backpressure. The low flow rate and inability to

generate fluid movement against backpressure may have been due to the non-ideal shape of the tube where the TITAN micropumps were segmented by areas not coated with polypyrrole. These non-coated, soft and flexible tube segments led to a large dead volume which was comparable to the volume displaced from the contracted segments, resulting in insufficient pressure to push the fluid forward along the segments. Improvements were made in subsequent experiments to eliminate the dead volume induced by the segments of the tube that were not coated with polypyrrole.

5.3.3.2 Utilisation of the intrinsic resistance and electrochemical properties of the TITAN micropump for sequential switching

In the previous section, a platinum helix wire was used to provide effective electrical contact along the entire length of the polypyrrole-coated working electrode in order to increase electrical conductivity and to allow efficient reduction and oxidation. The TITAN micropump was segmented to achieve peristaltic pumping characteristics using external electronic circuitry. In this section, platinum wire was intentionally attached only at the very end of a TITAN micropump working electrode (pump inlet end) prior to electrochemical polymerisation. The resulting polypyrrole-coated platinised PU tube demonstrated a potential drop along the tube from one end to another (0.1 V), raising the possibility of peristaltic contraction and expansion as depicted in Figure 5-14. A stainless steel wire was also inserted into the tube in order to provide a means of closing off the tube when the pump was fully contracted.

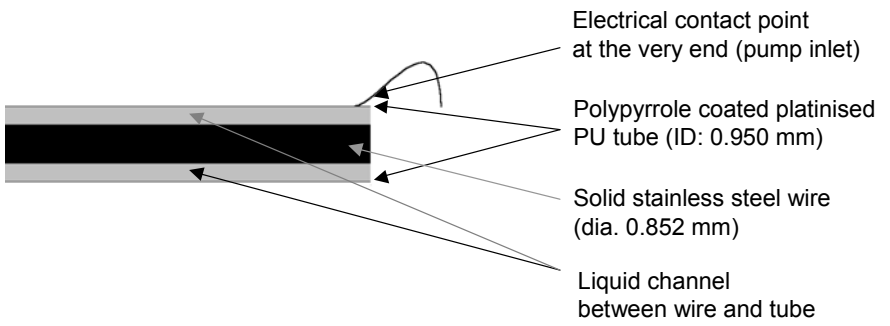

(a)

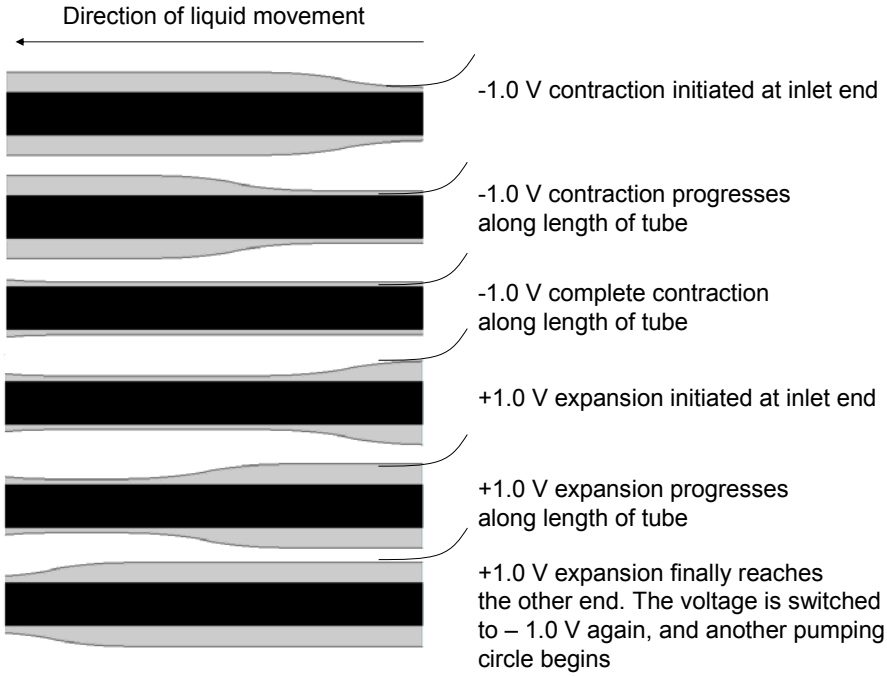

(b)

Figure 5-14 (a) Diagram of the valveless TITAN micropump in the oxidised (expansion) state, (b) schematic illustrating the pumping sequence of the valveless TITAN micropump.

When a − 1.0 V pulse was applied, the TITAN working electrode initially contracted at one end (pump inlet end) where the platinum wire was attached. This contraction then progressed along the working electrode to the other end (pump outlet) until the TITAN had contracted completely along the full length of the steel wire. When a subsequent + 1.0 V pulse was

applied, the TITAN inlet end expanded first, allowing the tube to be refilled with fluid from the external reservoir. As the above process was repeated, constant fluid flow was observed. It is envisaged that the most important parameter affecting the pumping performance would be the diameter of the stainless steel wire. The diameter of the wire must be small enough to allow sufficient fluid flow when the tube is expanded (at + 1.0 V) and at the same time must be large enough to allow the tube to close up completely onto the wire when contracted (at – 1.0 V). For the diameter of wire used in this study (850 μm), a maximum flow rate of 0.5 $\mu l.min^{-1}$ was obtained, which is slightly higher than the 0.25 $\mu l\ min^{-1}$ obtained for the peristaltic pump set up in the previous section. In addition, this superior rate of fluid flow (0.50 $\mu l.min^{-1}$ *vs.* 0.25 $\mu l.min^{-1}$) was achieved for a shorter overall pump length of 3 cm compared to 10 cm. However, like the peristaltic TITAN micropump that utilised external circuitry to deliver fluid movement, the pump prepared here was unable to provide fluidic motion when a backpressure was applied. This was presumably due to the non-ideal prepared nature of the intrinsic 'valve' system. Besides the superior flow rate of the pump in this section, compared to the previous section, advantages included that optimal pumping conditions required, only 1.0 V operating voltage and 8.7 mW power, and the absence of somewhat complicated external circuitry in order to generate a peristaltic pumping action.

5.3.4 FUTURE STUDIES

Further studies are needed to elaborate on the idea of using the inherent resistance and electrochemical properties of polypyrrole to produce 'sequential' actuation. With advances in micro fabrication technology, the structure of the TITAN micropump may eventually be integrated with biomedical devices at the micro level, in particular with the cochlear

implant, for possible controlled drug release applications. Moreover, the novel TITAN micropump structure opens up a possible alternative approach to the design of ICP actuators. In contrast to the common beam structure, in which the mechanical force is limited by the cross-sectional thickness of the polymer, the thin ICP coating of the TITAN micropump would raise electrochemical efficiency, thereby providing the pump with the ability to generate a substantial pneumatic actuation force.

5.4 CONCLUSIONS

In this Chapter, it was successfully demonstrated that a polypyrrole-based TITAN micropump could be used for the movement of small volumes of fluid. The system provides obvious advantages such as simple structure and ease of construction. The pump is robust and has no side effects and no limitations on the type of fluid to be transported because of the use of PU tubing. A 3 cm TITAN micropump was shown to reversibly transport 2.5 µl of fluid in 30 s at an applied voltage of only ~ 1.0 V and without significant performance decrease in the presence of a 50 mbar backpressure. A novel idea of using the inherent resistance and electrochemical properties of polypyrrole to achieve 'sequential' actuation has also been demonstrated, together with the use of an electronic switching cluster to achieve peristaltic switching. It is envisaged that the TITAN micropump may be useful for the cochlear implant as a means of controlled drug release. In addition, investigations into the TITAN micropump may yield an alternative approach to the design of ICP actuators.

5.5 REFERENCES

1. Woias, P., *Sensors and Actuators B: Chemical*, In Press, Corrected Proof. 2004.
2. Carrozza, M.C., Croce, N., Magnani, B. and Dario, P., *Journal of Micromechanics and Microengineering*, 5 (2) (1995) 177-179.
3. Bohm, S., Olthuis, W. and Bergveld, P., *Sensors and Actuators A: Physical*, 77 (3) (1999) 223-228.
4. Van de Pol, F.C.M., Van Lintel, H.T.G., Elwenspoek, M. and Fluitman, J.H.J., *Sensors and Actuators A: Physical*, 21 (1-3) (1990) 198-202.
5. Acero, M.C., Plaza, J.A., Esteve, J., Carmona, M., Marco, S. and Samitier, J., *Journal of Micromechanics and Microengineering*, 7 (3) (1997) 179-182.
6. Wego, A. and Pagel, L., *Sensors and Actuators A: Physical*, 88 (3) (2001) 220-226.
7. Bourouina, T., Bosseboeuf, A. and Grandchamp, J.P., *Journal of Micromechanics and Microengineering*, 7 (3) (1997) 186-188.
8. Moroney, R.M., White, R.M. and Howe, R.T., in *Proceedings of the MEMS '91, Nara, Japan*, (30 January–2 February 1991) 277–282.
9. Manz, A., Verpoorte, E., Raymond, D.E., Effenhauser, C.S., Burggraf, N. and Widmer, H.M., *Micro Total Analysis Systems*. A. van den Berg and P. Bergveld, Eds.; Kluwer Academic Publishers: Dordrecht, 1995; Vol. 1, pp 5–27.
10. Bohm, S., Timmer, B., Olthuis, W. and Bergveld, P., *Micro Total Analysis Systems*, A. van den Berg. 2000, Dordrecht: Kluwer Academic Publishers. pp 347–350.
11. Bart, S.F., Mehregany, M., Tavrow, L.S. and Lang, J.H., *Microfabricated electrohydrodynamic pumps*. Transducers, Book of Abstract. 1989, Montreux, Switzerland. p113.
12. Richter, A. and Sandmaier, H., in *Proceedings of the MEMS '90, Napa Valley*, (11–14 February 1990) 104.
13. Richter, A., Plettner, A., Hoffmann, K.A. and Sandmaier, H., in *Proceedings of the MEMS '91, Nara, Japan*, (30 January–2 February 1991) 271–276.
14. Hartshorne, Herb, Backhouse, Christopher J. and Lee, W.E., *Sensors and Actuators B: Chemical*, 99 (2-3) (2004) 592-600.

15. Gandhi, M., Spinks, G. M., Burford, R. P. and Wallace, G. G., *Polymer*, 36 (25) (1995) 4761-4765.

16. Wallace, G.G., Spinks, G.M. and Teasdale, P.R., *Conductive Electroactive Polymers - Intelligent Materials Systems*. 1997, Switzerland: Technomic Publishing.

17. Baughman, R. H., *Synthetic Metals*, 78 (3) (1996) 339-353.

18. Fang, Q., Chetwynd, D.G., Gardner, J. W., Toh, C. and Bartlett, P. N., *Materials Science and Engineering A*, 355 (1-2) (2003) 62-67.

19. Low, L.M., Seetharaman, S., He, K.Q. and Madou, M.J., *Sensors and Actuators B: Chemical*, 67 (1-2) (2000) 149-160.

20. Lewis, T.W., Spinks, G.M., Wallace, G.G., Mazzoldi, A. and De Rossi, D., *Synthetic Metals*, 122 (2) (2001) 379-385.

21. Otero, T.F., Grande, H. and Rodriguez, J., *Synthetic Metals*, 76 (1-3) (1996) 293-295.

22. Spinks, G.M., Liu, L., Wallace, G.G. and Zhou, D.Z., *Advanced Functional Materials*, 12 (6-7) (2002) 437-440.

.

CHAPTER 6 CONTROLLED RELEASE USING POLYPYRROLE-COATED HOLLOW FIBRES

6.1 INTRODUCTION

Various methods and devices have been developed for controlled drug delivery applications. These include systems that utilise diffusion from a polymer matrix [1], from a reservoir across a polymer membrane [2], or the controlled degradation of a polymer matrix [3]. With these approaches, however, the release rate is pre-determined and control of the release profile *in-situ* is not readily achieved.

In many applications, the ability to adjust the release rate based on a feedback mechanism [4] is desirable. For this purpose, inherently conducting polymers (ICPs) have drawn considerable attention due to the redox switching in response to simple electrical stimulation [5-8] according to Equation 1.1 and Equation 1.2 (refer to Section 1.2 in Chapter 1). Ions can be incorporated into the polymer in one redox state and released in another, so that the current passed enables control of the amount released. Miller *et al.* [7, 8] have demonstrated that electrochemically-controlled release of both cationic drugs, such as dopamine and phenothiazine, from a poly(N-methylpyrrole) film doped with poly(styrene sulfonate) or anionic drugs, such as salicylate, from a poly(3-methoxy-thiophene) film is possible. Recently, Kontturi *et al.* [9, 10] have demonstrated that PPy can be employed as a model ion gate membrane for the controlled delivery of drugs such as salicylate, naproxen and nicoside. However, in all cases the amount of drug released was small and obviously limited to the amount originally incorporated into the polymer matrix, therefore restricting this approach to drugs with high therapeutic activity.

For electrochemically-controlled release of substantial amounts of ionic drugs over prolonged periods of time, a novel PPy-coated hollow fibre system was developed herein. The cavity within the porous hollow fibre served as an ionic drug reservoir so that the amount of ionic drug would no

longer be limited to that initially present in the polymer matrix, while the PPy functioned as an ion gate membrane to control the release rate. In this Chapter, the construction of a PPy-coated platinised polyvinylidene fluoride (PVDF) hollow fibre system was described and an anionic dye was used as a model for ionic drugs. The performance of the system was characterised and the release mechanism was discussed for electrochemically controlled release using three- or two-electrode setups.

6.2 EXPERIMENTAL

6.2.1 REAGENTS AND MATERIALS

Sulforhodamine B (Figure 6-1) (SB, Aldrich) were used as received without further purification. PVDF hollow fibre was received as a gift from US filtration. According to the manufacture's information, the porous PVDF hollow fibre had an average external diameter of ~ 1018 μm, an average internal diameter of ~ 644 μm and a wall thickness of ~ 167 μm with an inhomogeneous porosity of ~ 85 %. For other reagents and materials mentioned in this Chapter refer to Section 2.10 in Chapter 2. All experiments were performed at room temperature in this study.

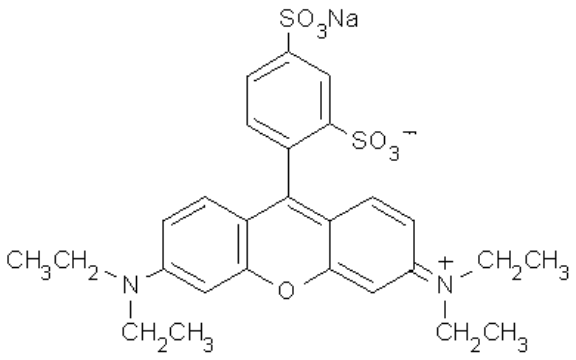

Figure 6-1 Chemical structure of sulforhodamine B, Mwt = 580.7.

6.2.2 PREPARATION OF PLATINISED PVDF HOLLOW FIBRE

PVDF hollow fibres were sputter-coated with platinum in order to completely cover the external surface. Platinised PVDF hollow fibres were used as electrodes for the electrochemical deposition of PPy. The platinised PVDF hollow fibre was denoted as Pt/PVDF_HF in this study. A four-point probe was employed to measure the sheet resistance of Pt/PVDF_HF electrodes.

6.2.3 SYNTHESIS OF PPY ON PLATINISED HOLLOW PVDF FIBRES

As prepared Pt/PVDF_HF was cut to 40 mm lengths and used as the anode for the electrochemical deposition of PPy. One end of 40 mm Pt/PVDF_HF samples was clamped by platinised stainless steel tweezers and the rest dipped into a polymerisation solution to a depth of 35 mm in a three-electrode cell (refer Figure 2-10). PPy was deposited galvanostatically using a constant current density of 1.0 $mA.cm^{-2}$ for 1, 3 or 6 minutes. Resultant fibres were denoted as 1min PPy/Pt/PVDF_HF, 3min PPy/Pt/PVDF_HF and 6min PPy/Pt/PVDF_HF, respectively.) PPy doped with *p*TS was prepared from an aqueous solution containing 0.1 M pyrrole monomer and 0.1 M *p*TS and used as the ion gate membrane coating, while PPy doped with DBS was prepared from an aqueous solution containing 0.1 M pyrrole monomer and 0.1 M DBS for comparison. Coated fibres were denoted as (PPy/A^-)/Pt/PVDF_HF, where A^- was the dopant anion). After electrodeposition of PPy, hollow fibres were thoroughly rinsed with Milli-Q water and dried using paper tissue in order to carefully remove solution retained in the lumen of the hollow fibres. Complete drying of PPy/Pt/PVDF_HF samples was achieved in ambient atmosphere prior to use.

6.2.4 PRIMING OF MODEL ANION INTO THE LUMEN OF POLYPYRROLE-COATED PLATINISED HOLLOW FIBRES

SB anionic dye was used as the model anion in this study. The solution concentration of SB was determined by the UV absorption intensity at 560 nm (λ_{max} = 560 nm) and using a calibration curve. 10 μL of aqueous 10 mM SB solution was injected into the lumen of hollow fibres using a micro syringe, while the other end (~ 5 mm) was firmly clamped using the platinised tweezers. The needle of the micro syringe was then carefully withdrawn and the open end immediately sealed by dipping it into molten lab wax. After this procedure, ~ 25 mm of the lumen length was filled with dye solution. Extra care were taken for PPy-coated hollow fibres, whereby tweezers were clamped at the end not coated with PPy in order to ensure that only the PPy-coated part was immersed inside the receiving solution during controlled release experiments. Figure 6-2 illustrates the configuration of a primed PPy-coated hollow fibre.

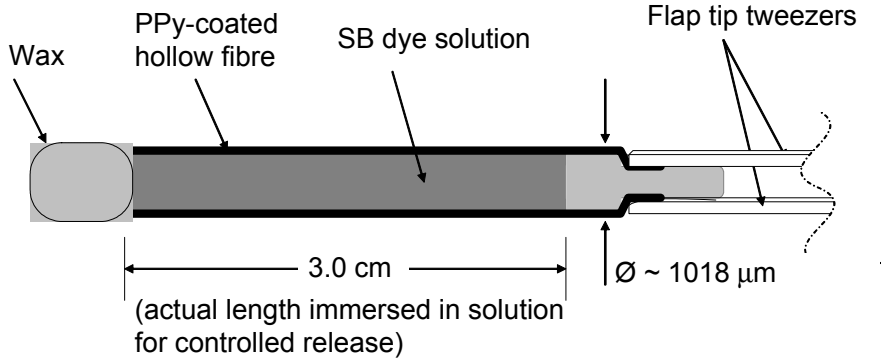

Figure 6-2 Schematic showing the configuration of a PPy-coated hollow fibre primed with aqueous SB dye solution for controlled release experiments.

6.2.5 SET-UP FOR CONTROLLED RELEASE STUDIES

The controlled release of SB from PPy-coated hollow fibres into receiving solutions was carried out in a glass cell containing 18 mL PBS buffer. The PPy-coated hollow fibre filled with aqueous SB solution was dipped into the PBS buffer to a depth of 30 mm and a magnetic stirrer bar was employed to gently mix any released SB into the bulk solution. A small aliquot of bulk solution (~ 1 ml) was periodically taken using a micropipette for the UV-Vis analysis of SB concentration using a Shimadzu UV-1601 spectrophotometer. After UV-Vis measurement of SB concentration, the aliquot was gently transferred back to the bulk solution using a micropipette in order to maintain a constant receiving solution volume.

For the study of electrochemically-controlled release, the tweezers connected to the hollow fibre (either platinised or further coated with PPy) filled with aqueous SB solution was used as the working electrode. In one type of experiment, a three-electrode set-up was employed (Figure 6-3) including a Ag/AgCl reference electrode and an external Pt mesh auxiliary electrode. A pulsed potential (pulse width = 30 s) was applied between – 500 mV and + 600 mV (*vs.* Ag/AgCl) to the working electrode.

In another type of experiment, the Ag/AgCl reference electrode and the Pt mesh auxiliary electrode were removed from the receiving solution and a miniaturized "wire in fibre" two-electrode set-up was tested (Figure 6-4). 3min (PPy/*p*TS)/Pt/PVDF_HF samples were used as working electrodes that had been conditioned at 0.0 V *vs.* Ag/AgCl for 5 minutes after electrodeposition of PPy. The auxiliary electrode was made by electrodepositing an equal amount of PPy/DBS over a 3.0 cm length at one end of a piece of platinum wire (Ø 125 μm). PPy/DBS-coated Pt wire was used as the auxiliary electrode instead of bare Pt wire in order to reduce the problem of gas evolution. Electrodeposition was carried out

galvanostatically at 1.0 $mA.cm^{-2}$ for 24 minutes from an aqueous solution containing 0.1 M pyrrole monomer and 0.1 M DBS before the PPy was conditioned at 0.0 V *vs.* Ag/AgCl for 5 minutes. The PPy/DBS-coated Pt wire auxiliary electrode was thoroughly rinsed with Milli-Q water and dried under ambient atmosphere prior to use. The working electrode was primed with aqueous SB solution and sealed by wax at one end as described previously before the auxiliary electrode was inserted from the open end into the lumen. Finally, the top end of the two-electrode set-up was clamped using tweezers. For controlled release studies using the two-electrode set-up, the potential applied between the working and auxiliary electrodes was switched between +/– 1000 mV at 30 s intervals. The two-electrode set-up is illustrated in Figure 6-3. For the electrochemistry equipment set-up, refer to Section 2.12 in Chapter 2.

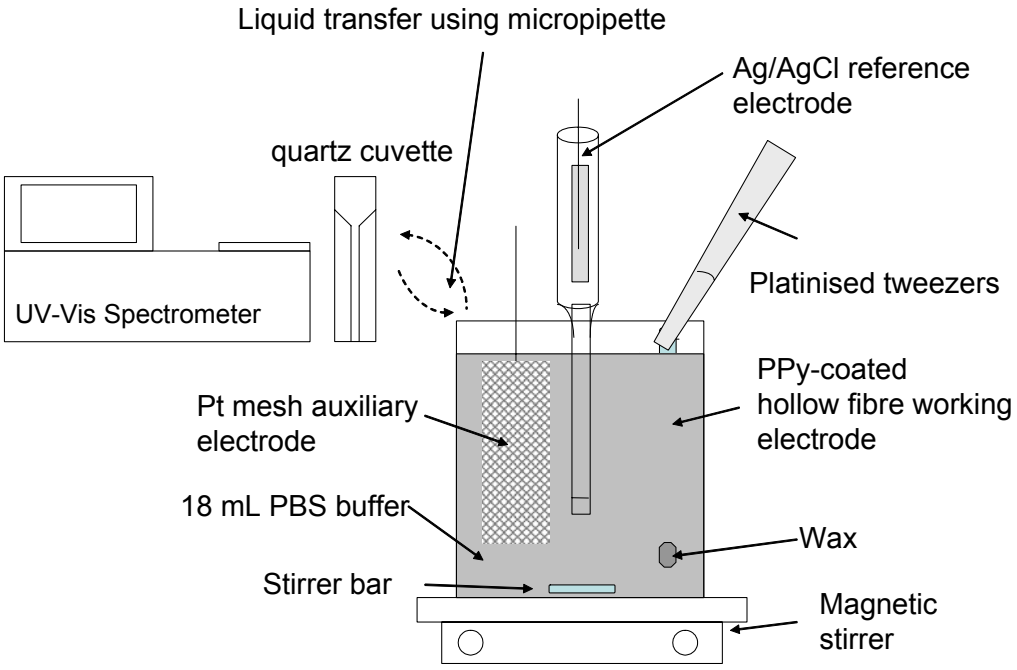

Figure 6-3 Schematic showing the three-electrode set-up for controlled release experiments.

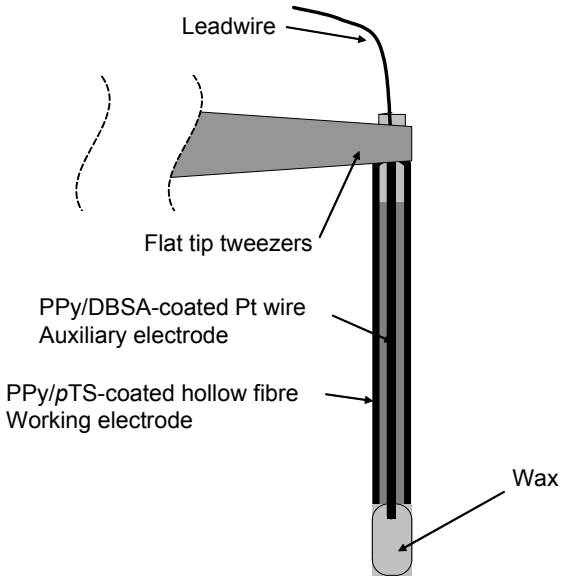

Figure 6-4 Schematic showing the "wire in fibre" two electrode set-up for controlled release experiments. The electrode assembly was immersed in PBS buffer as shown in Figure 6-3.

6.3 RESULTS AND DISCUSSION

The following sections present findings in regard to characterisations of the model anionic dye SB, Pt/PVDF_HF and PPy/Pt/PVDF_HF electrodes, the effect of PPy thickness on controlled release, and the electrochemically-controlled release of SB using a three-electrode or two-electrode set-up.

6.3.1 CHARACTERISATION OF THE ANIONIC DYE SULFORHODAMINE B

For the purpose of convenient determination of concentration, an anionic dye (SB) was used as a model compound in this study. The dye also contains hydrophobic components and water solubilised sulphonic groups as do many drugs [11]. As a first step a calibration curve was established. It was thought that for the calibration plot to hold true, the dye should be pH

insensitive in case the pH of the receiving solution were to change during long term electrochemical stimulation. More importantly, SB should be electrochemically stable at least over the potential needed for PPy to be oxidised / reduced. It was found that the UV-Vis absorption intensity of SB at 560 nm was pH independent (Figure 6-5). In regard to cyclic voltammetry (CV) characterisations, it was found that SB was not electroactive from - 500 mV to at least + 600 mV (Figure 6-6), which is the potential range to be used for controlled release. Moreover, using a 30 second pulsed potential between - 500 mV and + 600 mV on a PPy coated platinised hollow fibre electrode in a three-electrode cell containing 5 $\mu g.ml^{-1}$ SB in 18 ml aqueous PBS buffer, the measured UV-vis absorption intensity at 560 nm remained constant over 30 minutes. It was concluded that SB could indeed be used as a model anion for the electrochemically controlled release study.

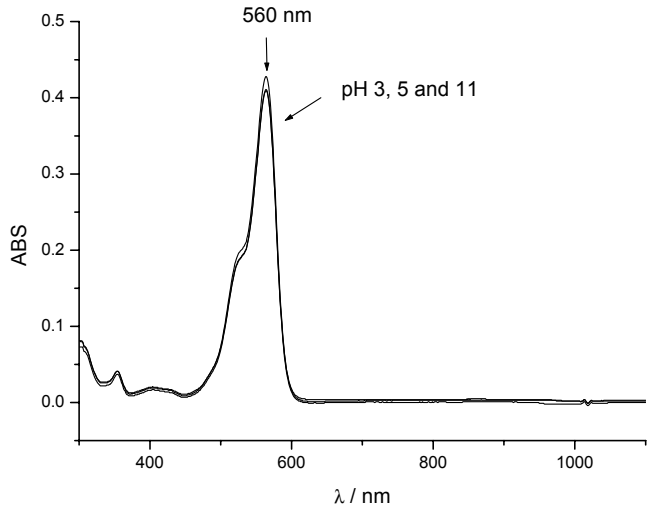

Figure 6-5 Overlay of the UV-Vis spectra of a ~ 5 ppm aqueous SB solution at pH of 3, 5 and 11. Solution pH was carefully adjusted by adding 0.1 M $NaOH_{(aq)}$ or 0.1 M $HCl_{(aq)}$ and monitored using pH paper.

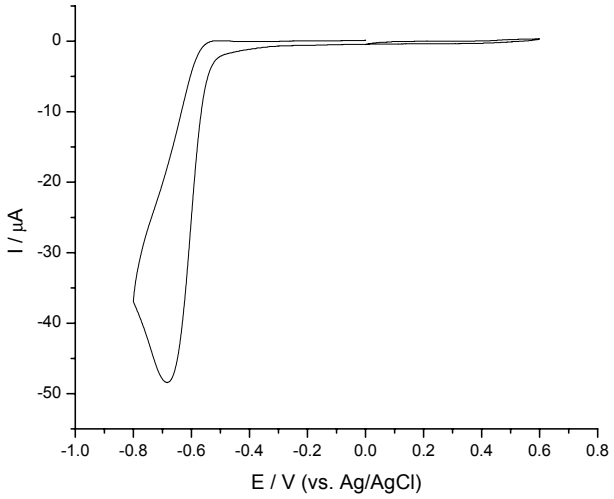

Figure 6-6 CV of aqueous 0.01 M SB on a standard glassy carbon electrode (Ø 3mm); 0.1 M $KCl_{(aq)}$ was used as the supporting electrolyte. Potential was scanned between - 800 mV and + 600 mV (*vs.* Ag/AgCl) at a scan rate of 10 $mV.s^{-1}$ for 5 cycles.

6.3.2 CHARACTERISATION OF PLATINISED PVDF HOLLOW FIBRE

PVDF hollow fibres were sputter coated with platinum for use as a conductive substrate for the electrodeposition of PPy. It was shown that thicker Pt coatings resulted in lower sheet resistances (Figure 6-7), where Pt coating thickness was calculated based on a deposition rate of 2 $Å.s^{-1}$. A drastic decrease of sheet resistance from ~ 40 Ω/□ to ~ 10 Ω/□ was observed when the coating thickness increased from 45 to 148 nm, followed by a moderate decrease in sheet resistance to ~ 5 Ω/□ at the maximum thickness of 290 nm. Ideally, lower sheet resistance is desirable since this can minimise the potential drop along the length of the hollow fibre and result in a more even coating of PPy. However, this preference for low sheet resistance is balanced by the need for an open porous structure that is critical for the release of ions through the hollow fibre.

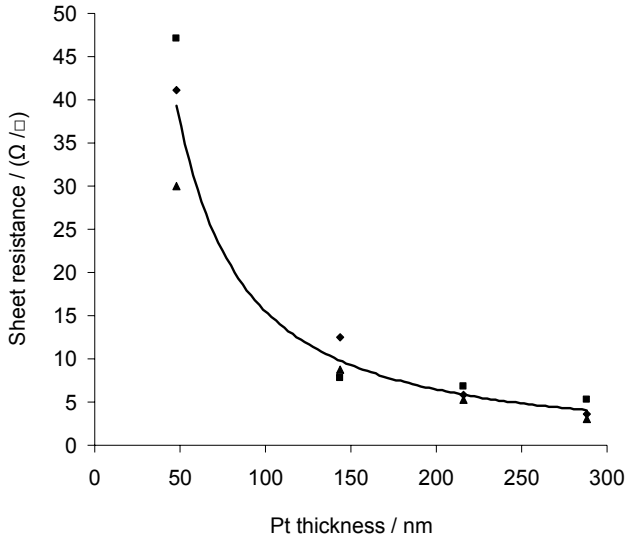

Figure 6-7 Plot of the sheet resistance of platinised PVDF hollow fibres at various Pt coating thicknesses.

The release of SB from PVDF hollow fibres with and without a Pt coating was investigated in PBS buffer solution to probe whether platinised PVDF hollow fibres remained porous. The results showed that both bare and platinised hollow fibres allowed the transport of SB to the receiving solution (Figure 6-8), which indicated that platinised PVDF hollow fibres retained an open porous structure. In the first 10 minutes, the amount of SB dye released increased linearly with time for all three hollow fibres used. The non-platinised hollow fibre had the highest release rate of ~ 3 μg/min compared to ~ 1 μg/min for the hollow fibre coated with a 145 nm platinum (Pt) coating. The hollow fibre with the thickest Pt coating of 288 nm showed the lowest release rate of ~ 0.6 μg/min. The results suggested that Pt coatings reduced the average pore size of hollow fibres and thereby inhibited the transport of ions. Remembering the need to balance lower sheet resistance with higher ion mobility, the hollow fibre with a 145 nm coating of Pt was chosen for further investigations into controlled release.

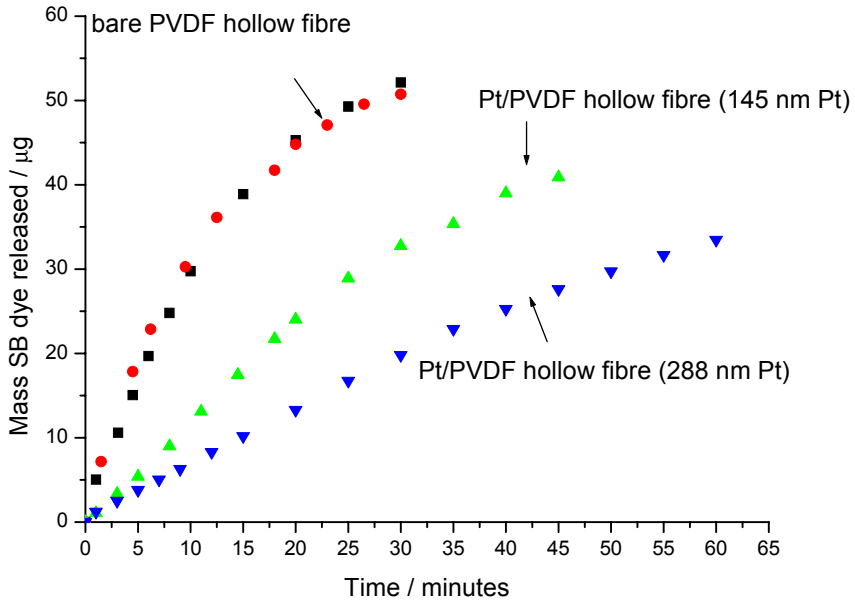

Figure 6-8 Release of SB with time from a bare PVDF hollow fibre, a PVDF hollow fibre coated with 145 nm of Pt or a PVDF hollow fibre coated with 288 nm of Pt. The receiving solution was 18 ml of PBS buffer. 10 µL of 10 mM aqueous SB solution (total mass SB = 58 µg) was loaded inside each of the hollow fibres prior to testing.

6.3.3 CHARACTERISATION OF POLYPYRROLE-COATED PLATINSED PVDF HOLLOW FIBRE

PPy/*p*TS was chosen as the model ion gate membrane in this study because it has previously been used for the electrochemically controlled transport of electroinactive ions [12]. For PPy/*p*TS, the dopant can be electrochemically incorporated and excluded from the polymer matrix in response to electrical stimulation. PPy was galvanostatically deposited on PVDF hollow fibres with 145 nm thick Pt coatings. The recording of chronopotentiogram during electrodeposition and post-growth CV was aimed at monitoring PPy quality and to probe the suitable potential range for electrochemically-controlled release using PPy-coated platinised PVDF hollow fibre. Figure 6-9 shows a typical chronopotentiogram recorded during electrodeposition of PPy on a platinised PVDF hollow fibre at a

current density of 1.0 mA/cm^2 from an aqueous solution containing 0.1 M pyrrole monomer and 0.1 M *p*TS at room temperature. A sharp increase of electrode potential followed by a steady decrease with deposition time was observed. The relatively high initial electrode potential of ~ + 0.74 V is believed to be related to the initial formation of the very first monolayer of PPy on the platinised PVDF hollow fibre since the oxidation potential for the pyrrole monomer is higher than that of pyrrole oligomers. Subsequent PPy film growth proceeded at a lower potential of ~ + 0.67 V. This result together with visual observations indicated that PPy was successfully electrodeposited on the platinised PVDF hollow fibre.

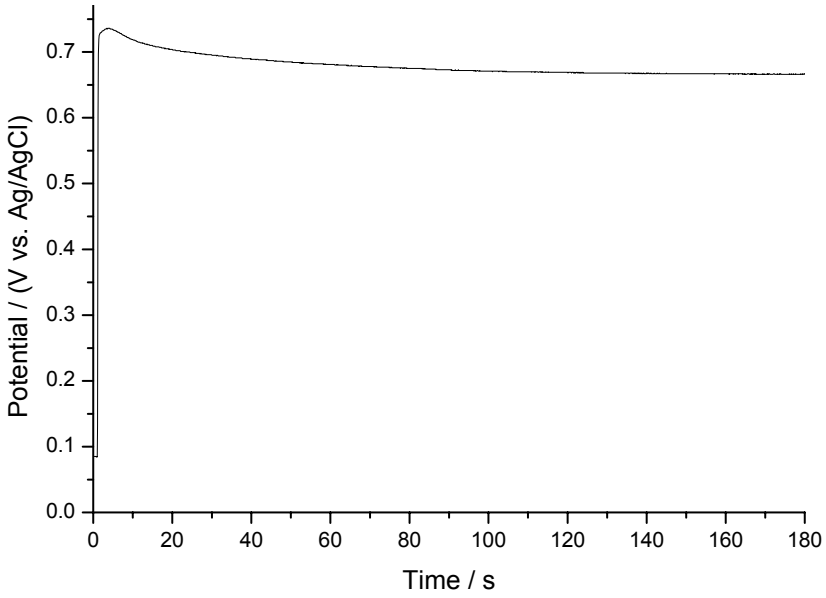

Figure 6-9 Chronopotentiogram recorded during the electrodeposition of PPy onto a platinised PVDF hollow fibre at a current density of 1.0 mA.cm^{-2} from an aqueous solution containing 0.1 M pyrrole monomer and 0.1 M Na *p*TS.

The as-prepared PPy/*p*TS-coated platinised PVDF hollow fibre was subsequently characterised by CV. Reproducible CVs were obtained (Figure 6-10), with the broad oxidation and reduction features believed to be related to the redox processes of PPy accompanied with the incorporation and

expulsion, respectively, of the anions within a potential range between – 500 mV and 600 mV [12]. The broad nature of redox peaks was likely due to the iR drop associated with the large surface area of the working electrode and further distorted by the large capacitive effect of the conductive and porous PPy/Pt layer (for details refer to Section 2.2.2). According to the above results, electrodeposited PPy/*p*TS was electroactive and could be reversibly oxidised and reduced for the incorporation and expulsion of anions within the potential range between - 500 mV to + 600 mV, which corresponded to the stable electrochemical window of SB.

SEM studies revealed that PPy was successfully electrodeposited along the length and completely across the circumference of platinised PVDF hollow fibres (Figure 6-11). It was also shown that the porosity of PVDF hollow fibres was inhomogeneous in that the pore size in the middle layer was much larger than that in the inner or outer layers of PPy-coated platinised PVDF hollow fibres.

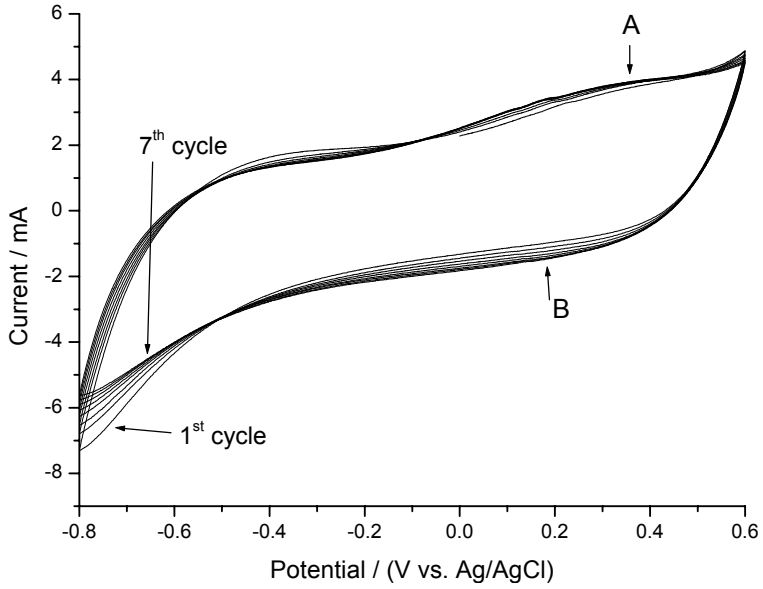

Figure 6-10 CV of PPy/*p*TS-coated PVDF hollow fibre in PBS buffer. A: the oxidation peak, B: the reduction peak. Potential was scanned between – 800 mV and + 600 mV (*vs.* Ag/AgCl) at a scan rate of 50 $mV.s^{-1}$ for 7 cycles.

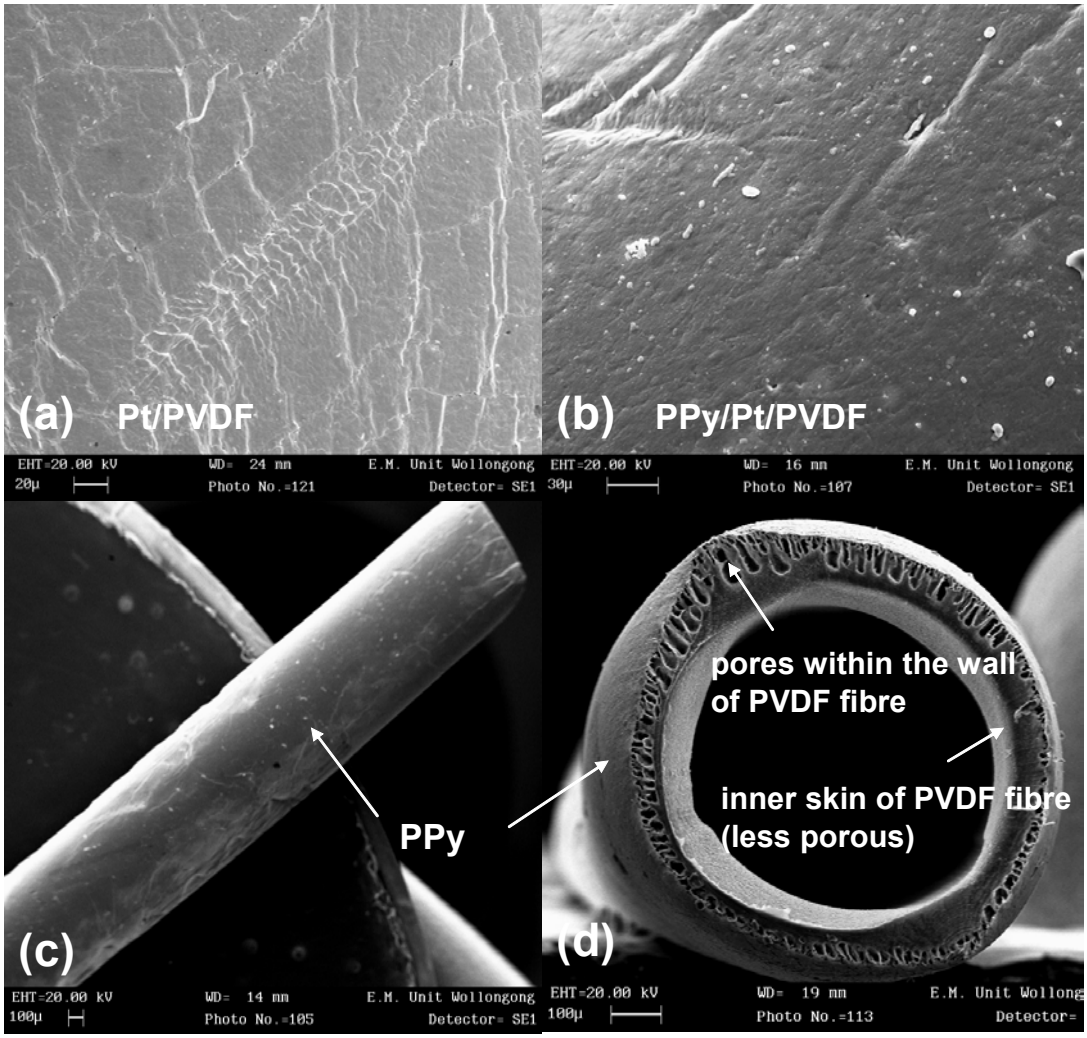

Figure 6-11 SEM images of Pt/PVDF_HF and 3min (PPy/*p*TS)/Pt/-PVDF_HF showing (a) the outer surface of Pt/PVDF, (b) the outer surface, (c) the outer surface over ~ 5 mm length and (d) the cross section of 3min (PPy/*p*TS)/Pt/PVDF_HF.

6.3.4 EFFECT OF POLYPYRROLE THICKNESS ON DIFFUSION CONTROLLED RELEASE

The release of SB dye across PPy/Pt/PVDF_HF by natural diffusion was initially studied for three thicknesses of PPy. Figure 6-12 shows that PPy coatings drastically reduced the linear range release rate from ~ 1 µg / min for uncoated platinised PVDF hollow fibre to 0.1 µg / min, 0.018 µg / min or 0.006 µg / min depending on PPy thickness. It was clearly established that the thicker the PPy, the lower the ion release rate. It was understood from the diffusion experiment that the PPy coating had a much smaller pore size compared to the platinised PVDF hollow fibre substrate and also increased in overall wall thickness. The observed increase in release rate after ~ 15 minutes for the PVDF hollow fibre coated with the thinnest PPy coating might be due to the initial swelling of the PPy matrix.

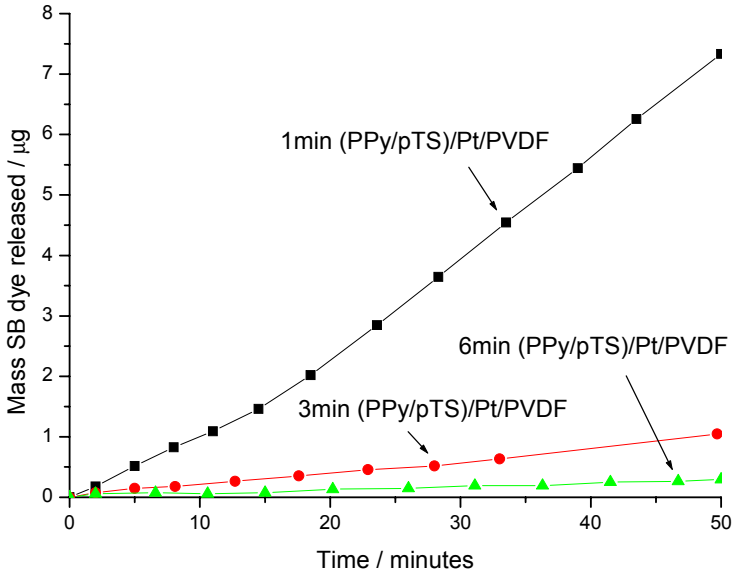

Figure 6-12 Amount released of SB dye from PPy-coated platinised PVDF hollow fibres, where PPy was galvanostatically deposited for 1, 3 or 6 minutes.

Under diffusion-controlled release, the rate of release generally decreases exponentially with time because the concentration gradient across the hollow fibre decreases. An example of this is the diffusion release properties when using bare hollow fibres (Figure 6-8). This represents a typical first order release under diffusion control. The initial rate for first order release is dependent on the thickness and pore size of the membrane if other conditions are maintained constant. For the hollow fibre reservoir-type device investigated here, a constant release rate can be maintained if the concentration of ions within the hollow fibre can be more or less maintained during the experiment. This was demonstrated here using the thicker PPy-coated PVDF hollow fibre for which the release rate was slow (Figure 6-12). Alternatively, if the loaded solution is saturated, a near constant release rate can also be observed since the concentration of dissolved chemical in the reservoir is constant. Such a constant release rate is zero order and is preferred for most drug release applications. This study of the effect of PPy thickness verified that the release of SB from PPy/Pt/PVDF_HF was diffusion controlled in the absence of an applied electrical stimulation.

6.3.5 ELECTROCHEMICALLY-CONTROLLED RELEASE

Electrochemically-controlled release was investigated using a 3min(PPy/*p*TS)/Pt/PVDF_HF sample. The experiment was performed in a three-electrode cell using a 30 second pulsed potential between - 500 mV and + 600 mV. Upon the application of this electrical stimulation, the amount of SB released was simultaneously measured *vs.* time (Figure 6-13). Compared to the release rate of ~ 0.018 μg / min under natural diffusion, the application of electrical stimulation dramatically increased the release rate by more than 7 times to ~ 0.15 μg / min. Such a release rate is believed to be

due to the redox processes occurring with PPy [6, 7]. With the application of + 600 mV, the PPy backbone was oxidised and anions including SB were incorporated by electrostatic force to balance the positively charged polymer. The anionic SB involved came mainly from the inner lumen because its concentration is much higher than in the bulk solution. Upon reduction at – 500 mV, the incorporated SB anion was excluded from the neutral polymer to the bulk solution due to the existence of the concentration gradient across the PPy membrane. The pulsed potential electrical stimulation therefore promoted the controlled transportation of the anion SB from the inner lumen of the hollow fibre through the membrane wall to the receiving solution. The results illustrated in Figure 6-13 also showed that a reproducible release pattern can be achieved using such a hollow fibre reservoir device. After 6 hours, the rate of release decreased drastically, which maybe due to the decreased concentration gradient of SB across the hollow fibre. At this point, ~ 70% SB was released into the bulk solution (40μg / 58μg). Note that such pulsed potential-controlled release from a reservoir over 6 hours would not be readily achievable with other membrane devices, where the total extent of release would be limited by the small amount of ionic drug doped inside the polymer. Although only in the preliminary stage of development, PPy-coated hollow fibre devices demonstrate the potential for the controlled release of electroinactive anionic drugs in biomedical applications where the release rate needs to be modulated and where relatively large amounts of drugs need to be released.

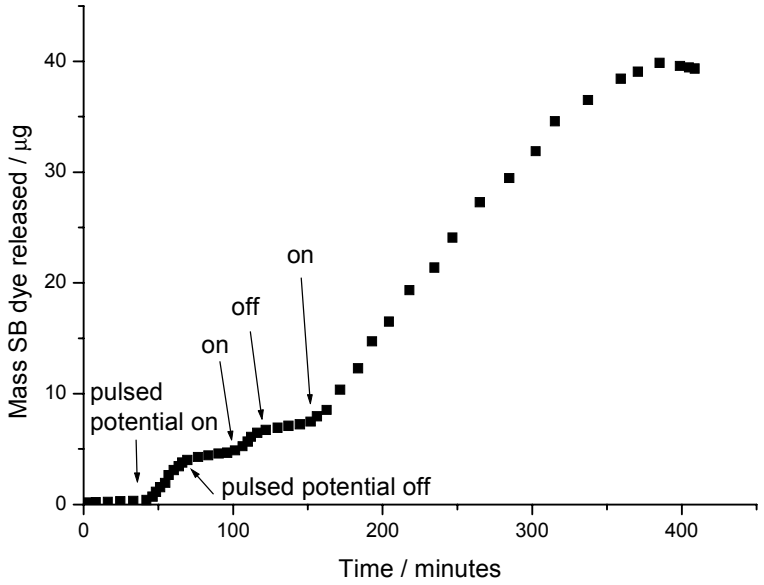

Figure 6-13 Release of the anionic SB from a sample of 3min(PPy/*p*TS)/Pt/PVDF_HF in response to a pulsed electrical stimulation. The applied potential was pulsed between – 500 mV and + 600 mV at 30 s intervals.

To confirm the mechanism above used to describe the electrochemically-controlled release of the anionic dye SB from PPy-coated platinised PVDF hollow fibres, a bulky anion was used as the dopant for PPy in place of *p*TS. It was thought that using a bulky anionic dopant instead of *p*TS would result in cation dominated redox cycling of PPy. This would represent a competitive ion flux that would inhibit the release of SB. DBS is a well known bulky anionic dopant used to induce cation dominated redox cycling of PPy.

The application of a pulsed potential electrical stimulation to a PPy/DBS-coated platinised PVDF hollow fibre inhibited the release of the loaded anion SB (Figure 6-14). Specifically, the average release rate of SB over 90 minutes was ~ 0.03 μg/min under diffusion control, while the application of a pulsed potential electrical stimulation resulted in a dramatic

decrease in the average release rate over the same 90 minute period to ~ 0.006 μg/min. These findings confirmed that electrochemically-controlled release using PPy/Pt/PVDF_HF reservoir devices was dominated by the redox processes of PPy.

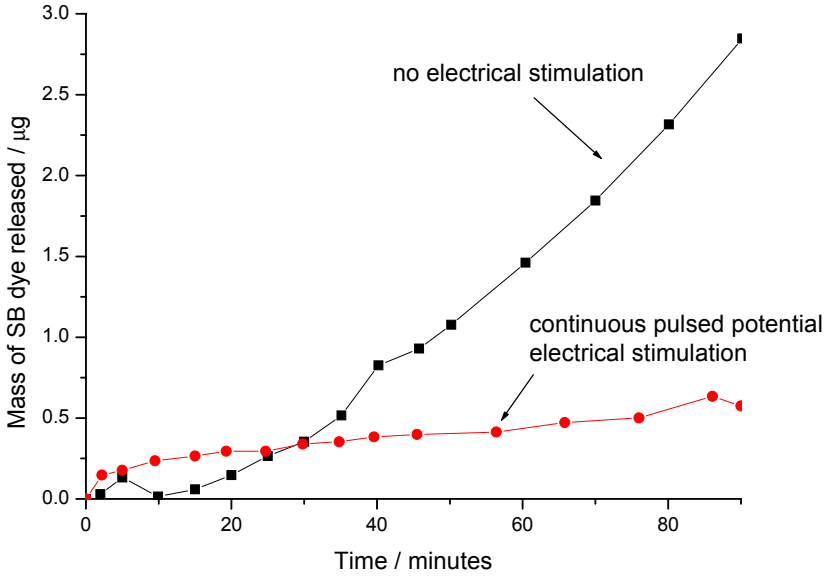

Figure 6-14 Release of the anionic dye SB from a sample of 3min(PPy/DBS)/Pt/-PVDF_HF with and without electrical stimulation. For the electrically stimulated sample, the applied potential was continuously pulsed between –500 mV and +600 mV at 30 s intervals.

6.3.6 CONTROLLED RELEASE USING THE TWO-ELECTRODE "WIRE IN FIBRE" SET-UP

The previous section showed the potential of PPy/Pt/PVDF_HF reservoir devices for the controlled release of electroinactive anionic drugs. However, it would be preferable for the external auxiliary and reference electrodes to be integrated into the hollow fibre in order to have a smaller, more practical device. In the following, a miniaturised "wire in fibre" device was developed and investigated for this purpose.

The release of SB *vs.* time using the "wire in fibre" set-up with or without electrical stimulation is shown in Figure 6-15. The use of a pulsed potential between – 1.0 V and + 1.0 V was based on the redox potential range of PPy that lies between - 500 mV and + 500 mV (*vs.* Ag/AgCl). It was assumed that at the beginning of stimulation, the potential of the working electrode and the auxiliary electrode was maintained at zero (*vs.* Ag/AgCl), and that upon the application of + 1.0 V, the potential of the working electrode would be approximately + 500 mV and the potential of the auxiliary electrode would be – 500 mV and vice versa. Considering Figure 6-15 (a), the release rate at the beginning was lower at ~ 0.04 μg/min for both cases before increasing. This initial period of slow release was ~ 15 min with electrical stimulation and ~ 25 min without electrical stimulation. The application of electrical stimulation might increase the rate at which the PPy membrane was swollen.

After ~ 15 minutes of electrical stimulation, a slightly higher release rate of ~ 0.07 μg/min was observed, presumably due to anion transport promoted by the redox cycling of PPy. The insignificance of the observed electrochemically-facilitated anion transport across the PPy membrane was believed to be related to an electrophoretic / ion migration effect. The auxiliary electrode in the "wire in fibre" two-electrode set-up was placed inside the hollow fibre, resulting in a very short separation distance (< 500 μm) to the working electrode. Therefore, a large potential gradient (> 2000 V / m when 1.0 V applied) would likely have resulted in a large ion migration effect. This issue is discussed in more detail below. In addition, the observed peak current responses shown in Figure 6-15 (b) suggested that the swelling of polymer increased the interfacial surface area between the PPy and the electrolyte.

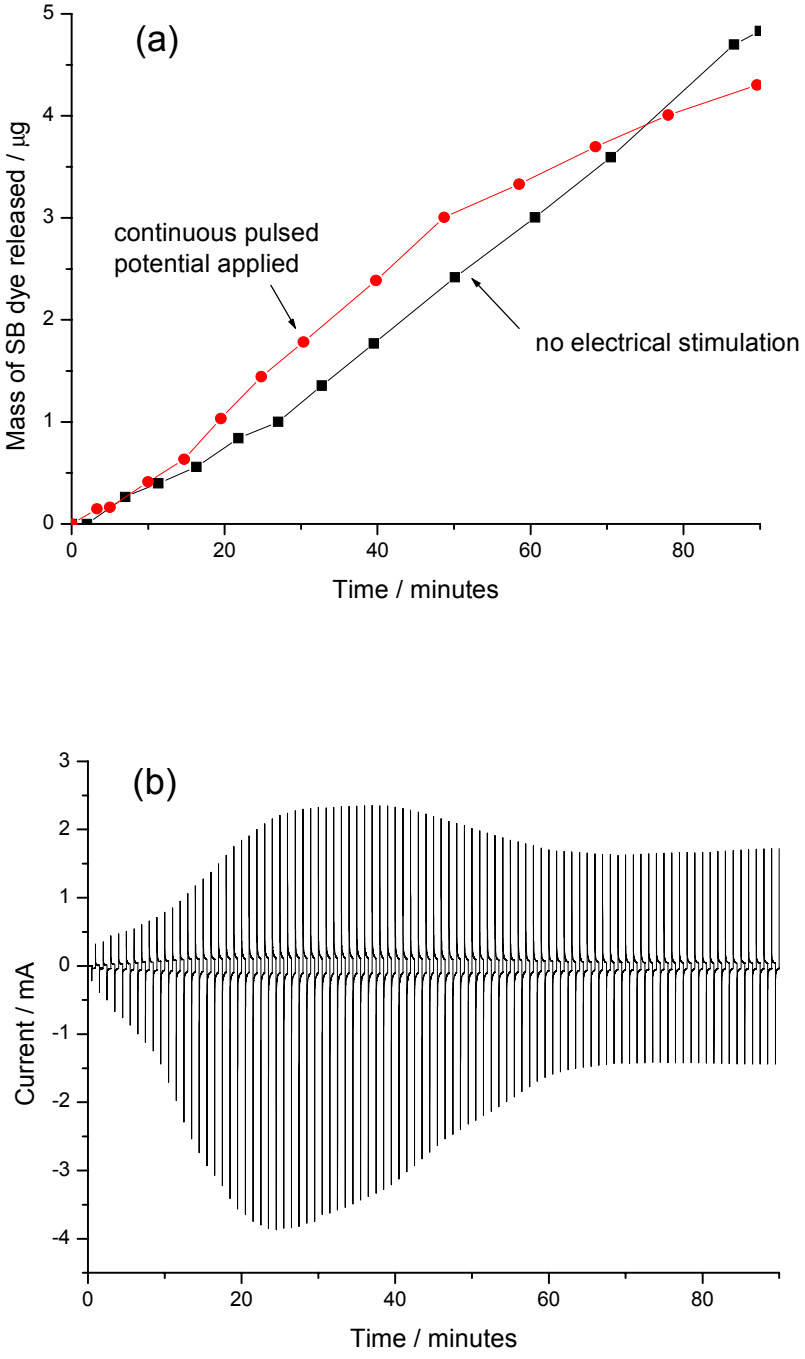

Figure 6-15 (a) Release of the anionic dye SB using "wire in fibre" two-electrode set-up including a 3min(PPy/*p*TS)/Pt/PVDF_HF working electrode with and without electrical stimulation. Electrical stimulation was achieved by applying a pulsed potential between +/– 1.0 V at 30 s intervals. (b) Current response during electrical stimulation experiment.

Theoretically, in the presence of an electric field across a membrane and in the absence of convection, the flux (J_j) of a charged species across the membrane is given by Equation 7-1 [13]:

$$J_j = -D_j \frac{\partial C_j}{\partial x} - z_j \frac{F}{RT} D_j C_j \frac{\partial \phi}{\partial x} \qquad \text{..... 6-1}$$

where D_j is the diffusion coefficient of the charged species, C_j is the concentration of the charged species, z_j is the valence of the charged species (including sign of charge), $\frac{\partial C_j}{\partial x}$ is the concentration gradient of the charged species in the solution-filled pores of the membrane, and $\frac{\partial \phi}{\partial x}$ is the potential gradient of the electric field in the solution filled pores of the membrane.

In the case of the "wire in fibre" set-up stimulated by pulsed potential, the overall flux of the anion SB is determined by diffusion in the presence of a concentration gradient represented by the first term in Equation 7-1 and electromigration in the presence of an electrical field represented by the second term in Equation 7-1. The electromigration is dependant upon the sign of the potential gradient and the sign of the charged species. The sign of the potential gradient can be changed by reversing the polarity of the applied potential at the outer PPy working electrode and at the inner PPy/Pt wire auxiliary electrode. At the oxidising potential (i.e. + 1.0 V), the anion SB was incorporated into the positively-charged PPy via migration and diffusion. At the reducing potential (i.e. – 1.0 V), the neutralised PPy promoted the diffusion of incorporated SB anion to the bulk solution. However, it was found that the potential gradient was not favourable for the release of the anion SB from the lumen of the hollow

fibre to the receiving solution. At the reducing potential, SB would be forced to migrate towards the inner lumen and positively charged auxiliary electrode. Therefore, anionic migration of SB was likely to be competing with the electrically-induced transport, resulting in an overall insignificant increase in release rate (Figure 6-16).

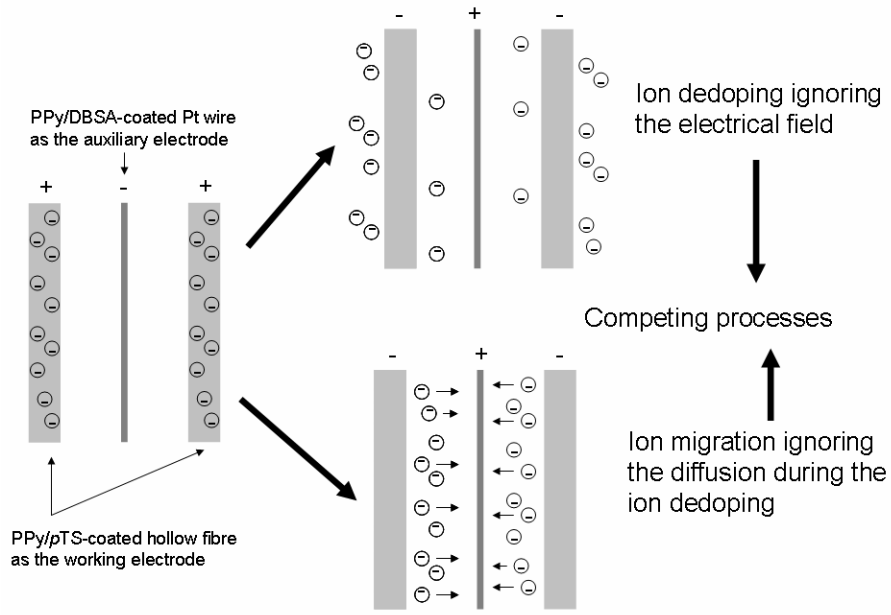

Figure 6-16 Schematic showing the competing ion flows using the "wire in fibre" set-up.

Figure 6-15 (a) indicated that after 50 minutes, the release rate had decreased to ~ 0.03 μg/min, which is lower than the ~ 0.06 μg/min release rate observed under natural diffusion. This might have been due to the degradation of the PPy and the resulting decrease in electrochemical efficiency. It is believed that the electrochemistry of the two-electrode device was complicated due to the absence of a standard reference electrode. After the first – 1.0 V reduction pulse, the working electrode would be at – 0.5 V and the auxiliary electrode would be at + 0.5 V. At the very beginning of the following + 1.0 V oxidation pulse, the potential applied to the working electrode would be + 1.5 V (*vs.* Ag/AgCl) in

reference to the auxiliary electrode, which would immediately result in overoxidation of the PPy and subsequent degradation. Such a decrease in the electrochemical efficiency of PPy would have led to a decrease in the contribution of electrically-induced transport of SB across the PPy membrane, resulting in the observed overall decrease in release rate.

6.3.7 FUTURE STUDIES

Further studies are needed to find a better electrical stimulation method for the miniaturised "wire in fibre" device. This would have to include a way of minimising the adverse ion migration effect and promoting more efficient redox switching characteristics. Moreover, although it is expected that the controlled release of cationic species would also be possible with hollow fibre reservoir devices using a PPy doped with bulky anions, detailed investigation in this respect is still required. This may also include determination of the largest possible ion size that can be controllably released using such devices.

6.4 CONCLUSIONS

In this Chapter, it was successfully demonstrated that PPy-coated platinised PVDF hollow fibre reservoir devices could be used for electrochemically-controlled release of the model anion SB. The advantage of such devices is that anionic drugs could be released in a controlled way and that large amounts could be released over long periods of time. In addition, such hollow fibre devices are simple to produce and are flexible. It was shown that a 3 cm long hollow fibre device could reproducibly release the anionic dye SB at a rate ~ 6 times that achieved under natural diffusion in response to the application of pulsed potential between – 500 mV and +

600 mV using 30 s intervals. The study showed that the dominant mechanism for the three-electrode device was ion transport induced by the doping / dedoping process of PPy. An adverse ion migration effect occurred in the miniaturised "wire in fibre" configuration that worked against the electrochemically-induced ion transport and owing to the close proximity of working and auxiliary electrodes. Nevertheless, PPy-coated hollow fibre devices showed potential application to the controlled release of electroinactive anionic drugs in biomedical applications where the release rate needs to be modulated and relatively large amounts need to be released.

6.5 REFERENCES

1. Davis, S.S. and Illum, L., *Biomaterials*, 9 (1) (1988) 111-115.
2. Lehmann, K.O.R., Bossler, H.M. and Dreher, D.K. In *Niol Macromol. Monogr.*, 1979, pp 111-119.
3. Leong, K.W., Brott, B.C. and Langer, R., *J. Biom. Mater. Res.*, 19 (1985) 941-955.
4. Kost, J.; CRC Press: Boca Raton, FL, 1990.
5. Beck, F., Braun, P. and Schloten, F., *Journal of Electroanalytical Chemistry*, 267 (1-2) (1989) 141-148.
6. Massoumi, B. and Entezami, A., *European Polymer Journal*, 37 (5) (2001) 1015-1020.
7. Miller, L.L., Smith, G.A., An-Cheng Chang and Qin-Xin Zhou, *Journal of Controlled Release*, 6 (1) (1987) 293-296.
8. Zinger, B. and Miller, L.L., *J. Am. Chem. Soc.*, 106 (22) (1984) 6861-6863.
9. Kontturi, K., Pentti, P. and Sundholm, G., *Journal of Electroanalytical Chemistry*, 453 (1-2) (1998) 231-238.
10. Kontturi, K., Murtomaki, L., Pentti, P. and Sundholm, G., *Synthetic Metals*, 92 (2) (1998) 179-185.
11. *Smith and Williams' introduction to the principles of drug design and action / edited by H. John Smith*, 4th ed ed.; Taylor & Francis,: Boca Raton :, 2005; pp 77.
12. Zhao, H., Price, W.E., Too, C.O., Wallace, G.G. and Zhou, D., *Journal of Membrane Science*, 119 (2) (1996) 199-212.
13. Bard, A.J. and Faulkner, L.R. *Electrochemical Methods, Fundamentals and Applications*; John Wiley & Sons: New York, 1980.

PART 2

CHAPTER 7 MICRO FORCE SENSOR USING THE COCHLEAR IMPLANT ELECTRODE

7.1 INTRODUCTION

The use of a micro force sensor (transducer) could enable the monitoring of resistive forces in order to minimise the risk of insertion trauma during surgical implantation of the cochlear implant. This chapter summarises a number of possible methods for force transduction and considers the use of existing cochlear implant components for the monitoring of resistive forces.

Force transducers, may take a number of forms as reviewed by Cobbold [1]. These include:

- balancing against the gravitational force of a standard mass,
- measuring the acceleration of a known mass to which the force is applied,
- balancing the force against a known electromagnetically developed force,
- converting the force to a fluid pressure and measuring that pressure, or
- measuring the strain produced in an elastic material

For miniaturised force transducers, a number of techniques have been employed to convert strain / displacement to an electrical signal. These include as resistive [2], inductive (well known in Linear Variable Differential Transformer (LVDT)) [3], optical [4-6], and capacitive [7, 8] transducers.

In the resistive type force transducer, metal wire, foil or thin-film semiconductor strain gauges are often employed and the application of strain causes the resistance to increase. This increased resistance includes two terms: one is a dimensional change induced resistance and the other is

the resistivity change due to the piezoresistive effect [9-11]. The gauge factor of a resistive force transducer is defined by:

$$G = \frac{\Delta R / R}{\Delta L / L} \qquad \text{..... 7-1}$$

where G is the gauge factor, ΔR is the change in resistance, R is the original resistance, ΔL is the change in length and L is the original length of the resistive gauge.

These resistive force transducers have a wide range of gauge factors from 2.1 ($Ni_{45}Cu_{55}$) to 170 (Silicon, p-type) [12]. Warnick and Drake [2] have described the novel configuration of an implantable resistive strain-gauge-type force / pressure transducer in a catheter tip (Figure 7-1). It consists of a thin, hollow elastic cylinder wound around four unbonded strain-gauge wires, two of these wires are tightly wound on spacers to measure the strain in the cylinder, and the other two are loosely wound to provide temperature compensation. Recently ultra-miniature semiconductor gauges have been integrated into a catheter tip as small as 0.05 mm in diameter for pressure and force measurement [13].

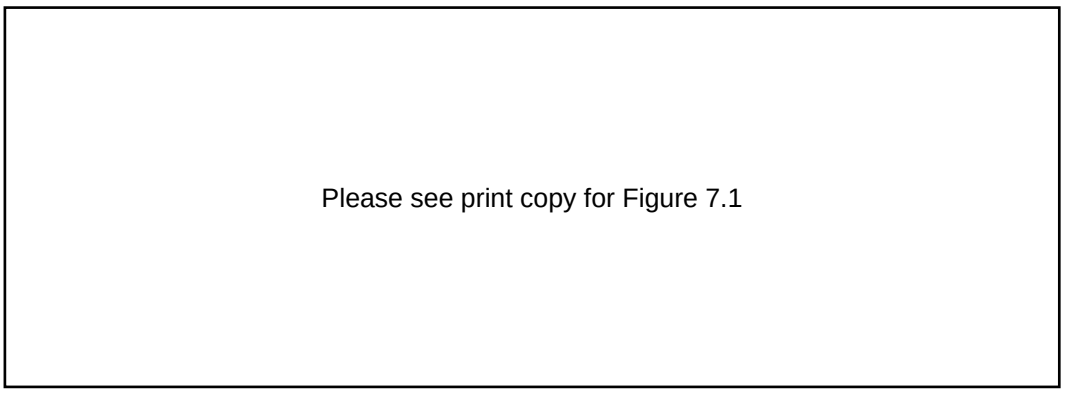

Figure 7-1 Sectional view of a catheter tip transducer using a cylindrical elastic member and unbonded strain gauges [2].

For inductive type force transducers, the application of force induced displacement is measured based on the variation in the inductance of one or

more coils. One of the most widely employed is the Linear Variable Differential Transformer (LVDT) which has the advantage of a large output for a small movement. Commercial systems have sensitivities from 0.5-2.0 mV per 0.01 mm displacement [14].

Fibre optic force / pressure sensors are often used in biomedical devices. One such device used for measuring blood pressure (Figure 7-2) has a sensor tip with a diameter of 0.59 mm and a length of 5 mm. Inside the sensor tip, there is a cavity that can be deformed by external pressure. By measuring the changes in length of the cavity based on white light interferometry, blood pressure can be determined. The very attractive features of this force transducer are that the measurement tip is virtually insensitive to any pulling or manipulation of the fibre and all materials used in the sensor tip are bio-compatible and are anti-thrombogenic [6].

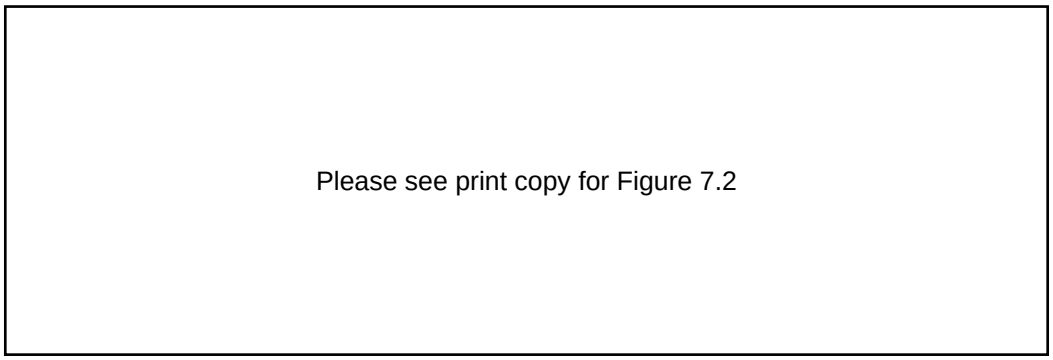

Figure 7-2 The fibre optic sensor used to measure blood pressure [6].

Capacitance transducers have been widely used in the measurement of displacement, motion and force [1] and the theoretical basis of operation has been studied for measuring the displacement of liquids [15, 16]. The general principle of such devices relies on the fact that the capacitance is dependant on electrode area, electrode separation and permittivity of the medium between the two electrodes. This can be used to convert the strain / displacement to an electrical signal, with which, the correlation between the

applied force and measured capacitance can be established. Due to the large capacitance of the electrochemical double layer, electrodes of this type can be miniaturised to small dimensions. According to the model (Figure 7-3) provided by Grahame [17], the double layer formed on an electrode comprises two planes: one for specifically adsorbed ions (such as the absorbed amino acid and proteins on the detection electrode) and one for non-specifically adsorbed ions with an additional diffuse layer region extending into the bulk electrolyte phase. Therefore, for use in physiological media containing amino acids and proteins, the effect of compositional change on the measured capacitance should be considered.

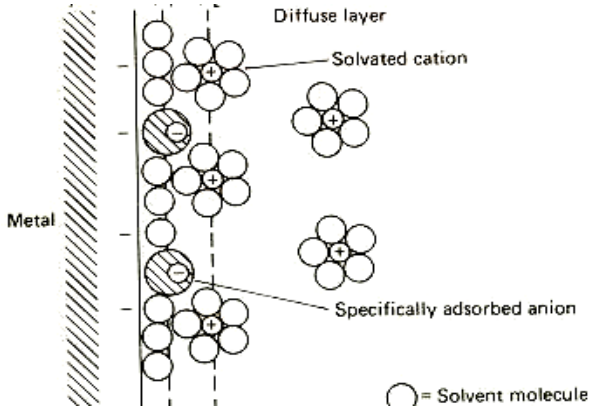

Figure 7-3 Grahame's model of the interfacial region in the immediate vicinity of the electrode.

With the force transducers described above, they would all require an additional structure, which would increase cost, fabrication difficulties and also the dimensions of the cochlear implant. Moreover, after surgical implantation, the force transducer is redundant and ideally should be easily removed from the implant. Therefore, the use of the ring electrodes within the cochlear implant to function as a capacitive force sensor during implantation was envisaged. Immediate advantages include simplicity and

biocompatibility. The underlying idea is that the impact force on the tip of the cochlear implant might be able to exert an elastic compression force from the surrounding silicone rubber onto the ring electrode, resulting in a reduced surface area, which can be correlated to the electrochemical double layer capacitance.

In this chapter, the capacitance change of the ring electrodes (that are already an integral part of the implant) in response to impact force has been investigated. Electrochemical and impedance spectroscopy studies using the ring electrode have been carried out. The correlation between the impedance and the impact force, between the capacitance and the impact force, between the capacitance and the bulk resistive force during a simulated implantation has been studied. In addition, complications arising from the compositional change of the surrounding biological fluid during implantation are also discussed.

7.2 EXPERIMENTAL

7.2.1 REAGENTS AND STANDARD SOLUTIONS

Artificial perilymph was prepared by adding 2 $mg.ml^{-1}$ HSA (Sigma), 175 mM L-phenylalanine (Merck), 396 mM Glycine (Analar) and 40 mM L-proline (Sigma) to PBS buffer [18]. In this work, all experiments were performed in artificial perilymph buffer unless otherwise stated. For all other reagents and materials mentioned in this Chapter refer to Section 2.10 in Chapter 2.

7.2.2 PREPARATION OF IMPLANT ELECTRODE

A Pt stylet (Ø125 μm) was inserted into the implant lumen in order to straighten the coiled electrode tip along the electrode array. The stylet

loaded implant was then fixed onto a circuit board (dimensions: 2.5 cm × 3.5 cm) with super glue so that the fine lead wires (Ø25 μm) attached to the ring electrodes could be connected to the individual copper leads for subsequent electronic link to measurement instrumentation. The ring electrodes were denoted E1, E2, E3, … , E20, E21, E22 as shown in Figure 7-4.

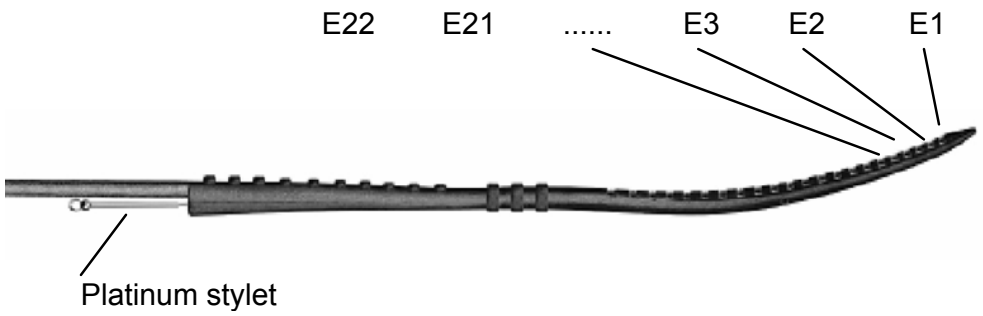

Figure 7-4 The cochlear implant showing the 22 ring electrodes from E1 to E22.

7.2.3 ELECTROCHEMICAL CHARACTERISATION

Cyclic voltammetry (CV) and electrochemical impedance spectroscopy (EIS) were performed in PBS buffer and artificial perilymph, respectively.

7.2.4 STANDARD IMPACT FORCE SENSING TEST

The set-up that can be used to apply a standard vertical impact force to the implant tip is shown in Figure 7-5. The distance from the tip to the bottom of a rigid glass container was finely adjusted using a cantilever. The implant electrode was held straight by a stylet as it would be during implantation [19]. The force exerted on the implant tip was determined by a digital mass balance placed underneath the glass container. The electrical

capacitance or impedance between the ring electrodes induced by the exerted force was recorded.

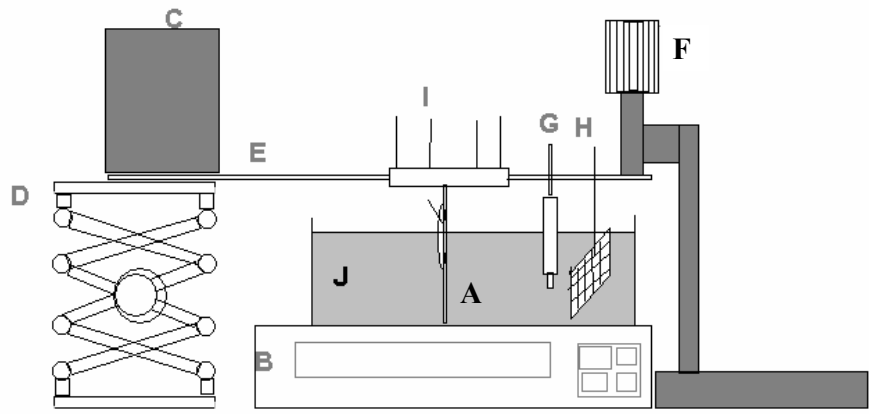

Figure 7-5 Schematic of custom set-up for the impedance / capacitance measurement as a function of impact force. (A) the cochlear implant electrode, (B) a digital mass balance used to measure the compressive force of implant tip, (C) weight on the fixed end of the ruler cantilever, (D) screw jack, (E) stainless steel cantilever, (F) screw used to adjust the distance between the implant tip and the cell bottom through a cantilever, (G) Ag/AgCl reference electrode, (H) platinum mesh counter-electrode, (I) lead wires, (J) the electrochemical cell containing PBS or artificial perilymph solution.

7.2.5 SIMULATED INSERTION WITH COCHLEAR REPLICA

Simulated insertion was performed using a cochlear replica obtained from Cochlear Ltd (Figure 7-6). The replica was placed upside down, clamped and moved at a constant speed towards the implant. The insertion was controlled by an Instron tensile tester (model 4302) and the insertion depth was controlled to 20 mm. The 10 N load cell within the Instron Tensile Tester was used to measure the force. The overall bulk resistance, ring electrode capacitance and force were measured simultaneously in respect to the insertion depth. In the standard procedure, the electrode was loaded with a stylet and then inserted into the cochlear replica at a controlled speed of 1 $mm.min^{-1}$.

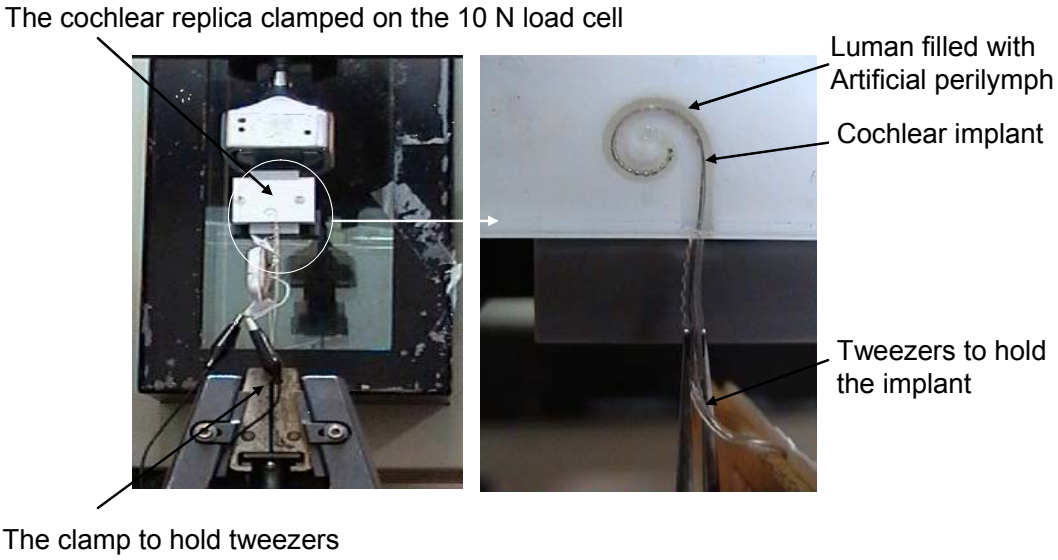

Figure 7-6 The experimental set-up for a simulated implantation: (a) the cochlear replica made of Teflon (dimension: 3 cm × 5.2 cm × 1.1 cm) was placed upside down and clamped on the 10 N load cell and the cochlear implant was held by tweezers straightly aligned and pointed upwards toward the replica entry (b) The final position of the cochlear implant electrode in the replica after the simulated implantation.

7.3 RESULTS AND DISCUSSION

The following sections present findings in regard to cyclic voltammetry experiments carried out using the ring electrode and impedance spectroscopy of the ring electrode. The correlation between capacitance and applied force on the electrode tip, as well as simulated insertion and influence of buffer composition were investigated.

7.3.1 CYCLIC VOLTAMMETRY OF RING ELECTRODE

The cyclic voltammetry study of the ring electrode was used to study the electrochemical interface. Cyclic voltammograms for E1 were obtained in artificial perilymph and PBS buffer (Figure 7-7). Responses observed (A/A`) (B/B`) are attributed to oxide layer formation (A/B) and reduction (A`/B`) on the Pt electrode [18, 20]. The shift in potentials observed in

artificial perilymph solution suggested that protein adsorption affected the processes. However, in artificial perilymph solution the cyclic voltammograms obtained were stable with time (50 cycles) indicating that the electrodes may be suitable as sensor probes during implantation.

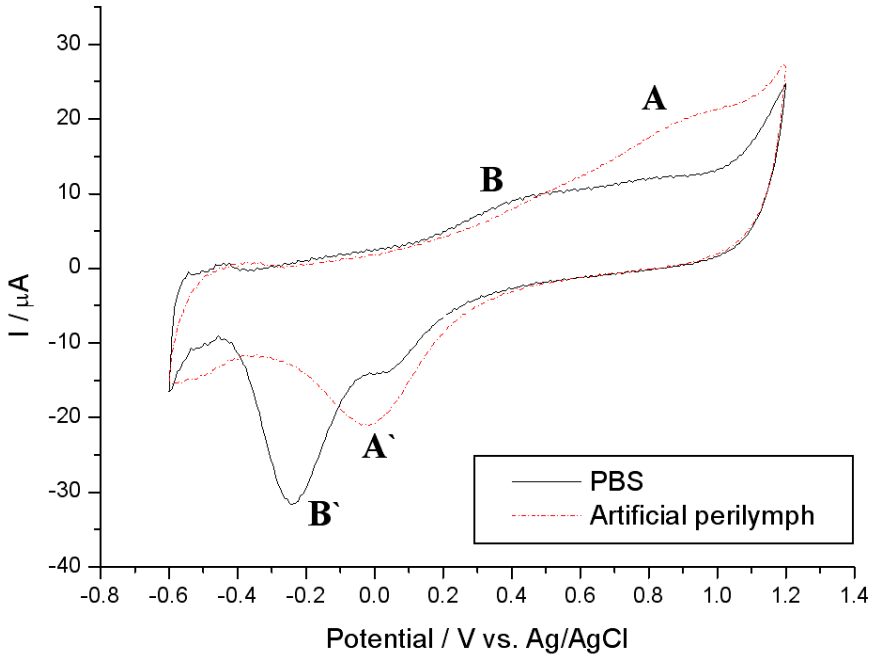

Figure 7-7 Cyclic voltammograms of the ring electrode in artificial perilymph or PBS solution. Lower potential limit = -0.60 V, upper potential limit = +1.2 V, scan rate = 500 $mV.s^{-1}$. The 50^{th} cycle is shown for each solution.

7.3.2 ELECTROCHEMICAL IMPEDANCE SPECTROSCOPY

To establish equilibrium time, the impedance between electrodes E1 and E2 was determined in artificial perilymph (Figure 7-8). In the first 10 minutes, |Z| drastically decreased from 13500 Ω to 8900 Ω before reaching a relatively steady state at about 8600 Ω in the following 10 minutes. It was therefore considered that at least 20 minutes has to be allowed before any impedance measurements could be taken.

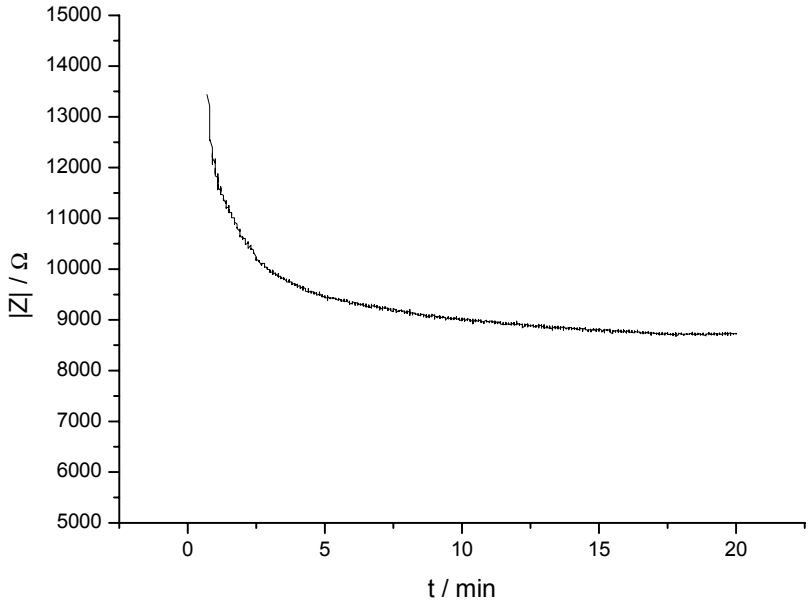

Figure 7-8 Impedance between E1 and E2 *vs.* Time after immersion in artificial perilymph solution at 1000 Hz. DC potential is set at open circuit potential, AC amplitude was set at 10 mV.

After 20 minutes equilibration, impedance spectra between pairs of ring electrodes were obtained in artificial perilymph solution at open circuit potential (Figure 7-9). The complex plane plot showed a slope of 75º from the real axis and the Bode plots showed that |Z| started from a constant at around 700 Ω in the higher frequency region between 10^6 to 10^5 Hz before gradually increasing to around 10^6 Ω at 1 Hz. At the same time, θ continuously increased to about 75 º at 1 Hz perturbation. A positive θ angle was observed at very high frequencies of around 10^6 Hz, likely due to the inductance of the coiled lead wire of the implant. The large amplitude of fluctuation observed in the low frequency region from 10^0 to 10^2 Hz may have been due to the large impedance encountered increasing the errors of the impedance analysis system.

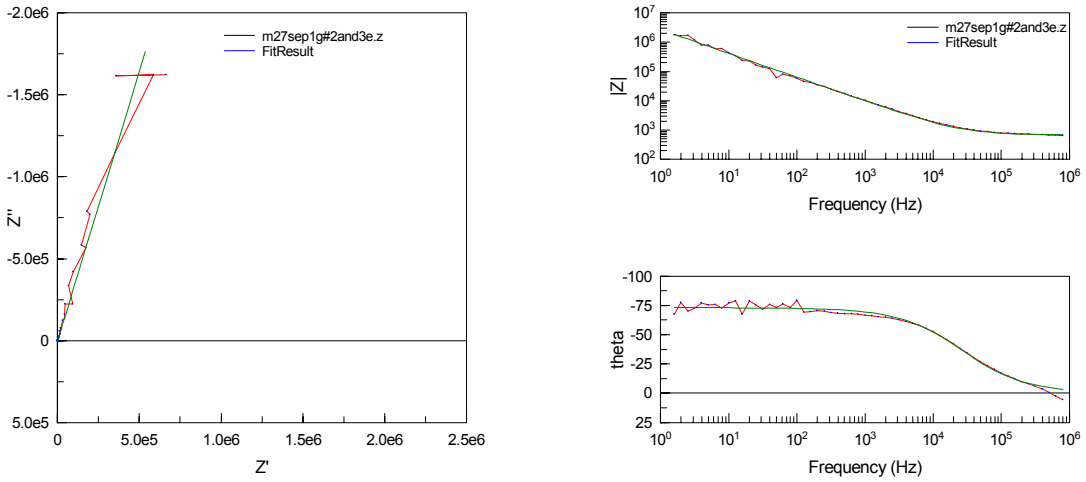

Figure 7-9 Complex and Bode plots of impedance between two ring electrodes in buffer solution. DC: 0.000 V, AC: 10 mV in rms, Frequency: 10^0 to 10^6 Hz.

The ring electrode system was modelled and fitted by an equivalent circuit (Figure 7-10), in which the solution resistance (R_s) was connected in series to the constant phase element (CPE) for the two ring electrode double layers. In turn, the CPE was connected in parallel to the polarisation, or charge transfer, resistance (R_p). The results showed that the solution resistance between two adjacent ring electrodes was about 680 Ω and that the CPE-T (the magnitude of CPE) is about 8×10^{-8} F with a CPE-P of about 0.81 (the correction factor for the constant phase angle of CPE, which is calculated by 90º×CPE-P). This suggested that the CPE behaviour is close to that of a capacitor. The value of the polarisation resistance in parallel was huge and can be ignored because there would be no charge transfer at the electrode / solution interface at open circuit potential.

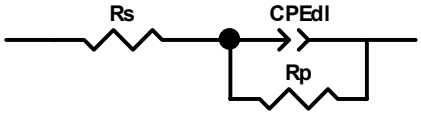

Figure 7-10 Equivalent circuit model and data fitting.

Considering the |Z| in the Bode plot (Figure 7-9) and the equivalent circuit (Figure 7-10), it was known that the contribution of solution resistance (R_s) to the overall |Z| is constant and independent of perturbation frequency, therefore the % contribution to |Z| of the double layer of the ring electrodes (CPE) increased at lower frequency. For the initial use of |Z| (later the capacitance) to probe the expected correlation between the double layer of the ring electrode and the impact force, the largest percent contribution from the CPE is desirable since it can increase the signal sensitivty. However, this preference is balanced by the requirement for less data fluctuation. It was shown that the obtained |Z| was relatively stable in the frequency region close to 1000 Hz. By calculation, the percent contribution of CPE at 1000 Hz to the overall |Z| was > 90 %. Therefore, 1000 Hz was chosen for further investigation.

The relationship between the bulk impedance and standard impact forces at 1000 Hz is illustrated in Figure 7-11. The impedance increased at both real and imaginary directions along with the applied force. The impedance increased from around 6500 to 6650 Ω in the real axis and from around 3280 to 3370 Ω in the imaginary axis for impact forces from 0 to 40 mN, while the total |Z| increased stepwise from 7280 Ω, 7325 Ω, 7370 Ω, 7405 Ω and 7438 Ω in response to 10 mN increments in force. A reproducible magnitude of impedance was observed when the force was decreased stepwise by 10 mN from 40 to 0 mN. This result clearly demonstrated that the impact force can change the impedance between any two ring electrodes.

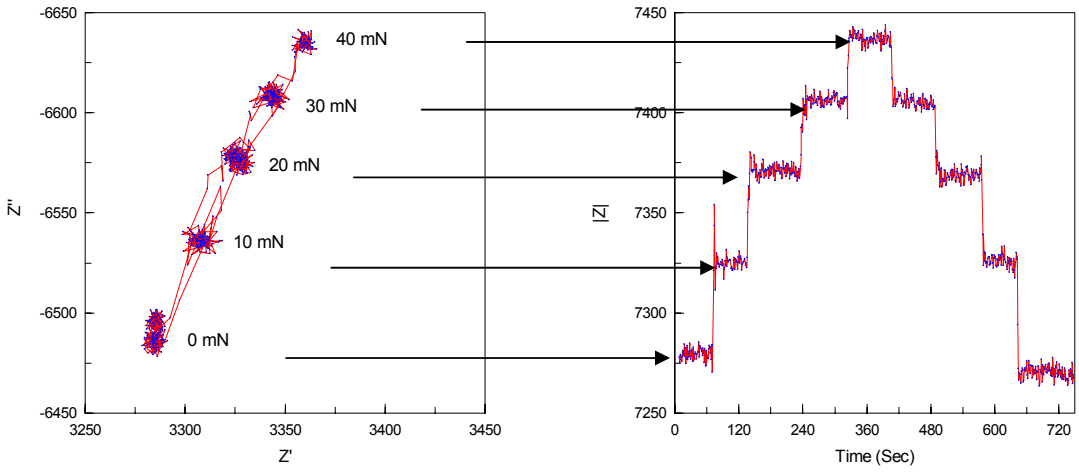

Figure 7-11 Complex and Bode plots of impedance for stepwise change in impact force applied to the implant electrode tip from 0 mN to 40 mN at a fixed frequency of 1000 Hz. Impedance was measured for the first ring electrode (E1) at the open circuit potential relative to Ag/AgCl.

By visual observation, the observed pattern of increased impedance in response to increasing impact force was mainly due to a reduction in the electrode surface area. The body of the cochlear implant is made of insulating silicon rubber, which covers the edges of the platinum ring electrode array. When the cochlear implant ring electrode array is straightened by a stylet, the insulating silicon rubber is pulled away, exposing a greater surface area. The impact force is able to partially reverse this process by exerting an elastic compression force from the surrounding silicone rubber onto the ring electrode, resulting in a reduced electrode surface area as shown in Figure 7-12.

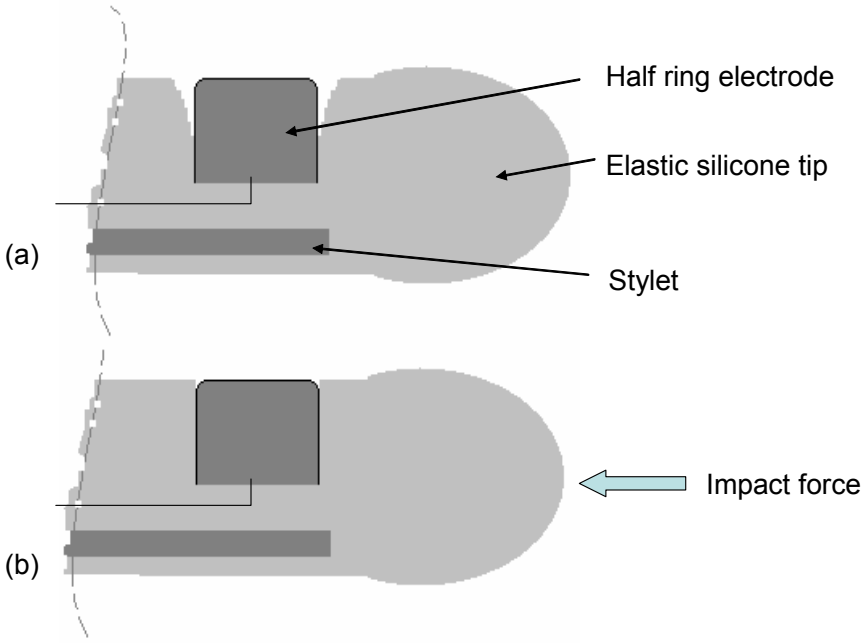

Figure 7-12 Cross-sectional schematic of the mechanism of surface area change of the cochlear implant ring electrode when (a) straightened by a stylet and (b) when subjected to an impact force.

7.3.3 CORRELATION BETWEEN THE CAPACITANCE / AND APPLIED FORCE ON THE ELECTRODE TIP

In the equivalent circuit shown in Figure 7-10, the constant phase element (CPE) can be simplified as a capacitor and the parallel polarisation resistance (R_p) can be removed due to its extremely large value at the fixed frequency of 1000 Hz. Therefore the circuit becomes a simple series circuit and relationships between the impedance, capacitance and effective surface area of the ring electrode can be described by the following equations:

$$Z = \frac{V}{I} = R_s - \frac{j}{2\pi f \times C} \quad \text{..... 7-2}$$

$$C = K \times A \quad \text{..... 7-3}$$

where V is a sine-wave AC voltage at the frequency f. I is the response current, R_s is the buffer solution resistance, j is the vector indicating a $-\pi/2$ phase shift, C is the capacitance, K is the correlation factor related to the dielectric constant, thickness and

structure of the electrochemical double layer formed at the electrode / solution interface (normally 10 to 40 $\mu F.cm^{-2}$ in aqueous solution), and A is the effective electrode area.

Due to the presence of the buffer solution, a resistive component was added in series to the double layer capacitance in the proposed equivalent circuit. According to the results in Figure 7-9, since the buffer resistance (700 Ω) between two ring electrodes was less than 7% of the bulk impedance (10229 Ω) at a fixed frequency of 1000 Hz, the contribution of buffer resistance was ignored in order to reduce measurement complexity.

Since the solution resistance (R_s) was less than 7% of the bulk impedance, the capacitance measured by a portable digital multimeter (working at 1000 Hz perturbation frequency) was then directly used and reported. Figure 7-13 shows the correlation plots for three ring electrode pairs. The initial capacitance started at 15.95 nF, 17.10 nF, and 18.40 nF for the ring electrode pairs E1/E2, E1/E3, and E1/E4, respectively. This increase in capacitance was due to the configuration of the implant electrode, where, the surface area of the ring electrode gradually increases from the tip (E1→E2→E3 …). For all ring electrode pairs, the capacitance decreased by approximately 0.5 ~ 0.6 nF while the force increased from 0 to 40 mN. The most sensitive region was from 0 to 25 mN, where the sensitivity was approximately 0.02 $nF.mN^{-1}$. However, the reproducibility was not ideal, whereby the capacitance continuously decreased following repeated testing for ring electrode pairs E1/E2 and E1/E3. Only the E1/E4 ring electrode pairs showed relatively reproducible results for the triplicate measurements.

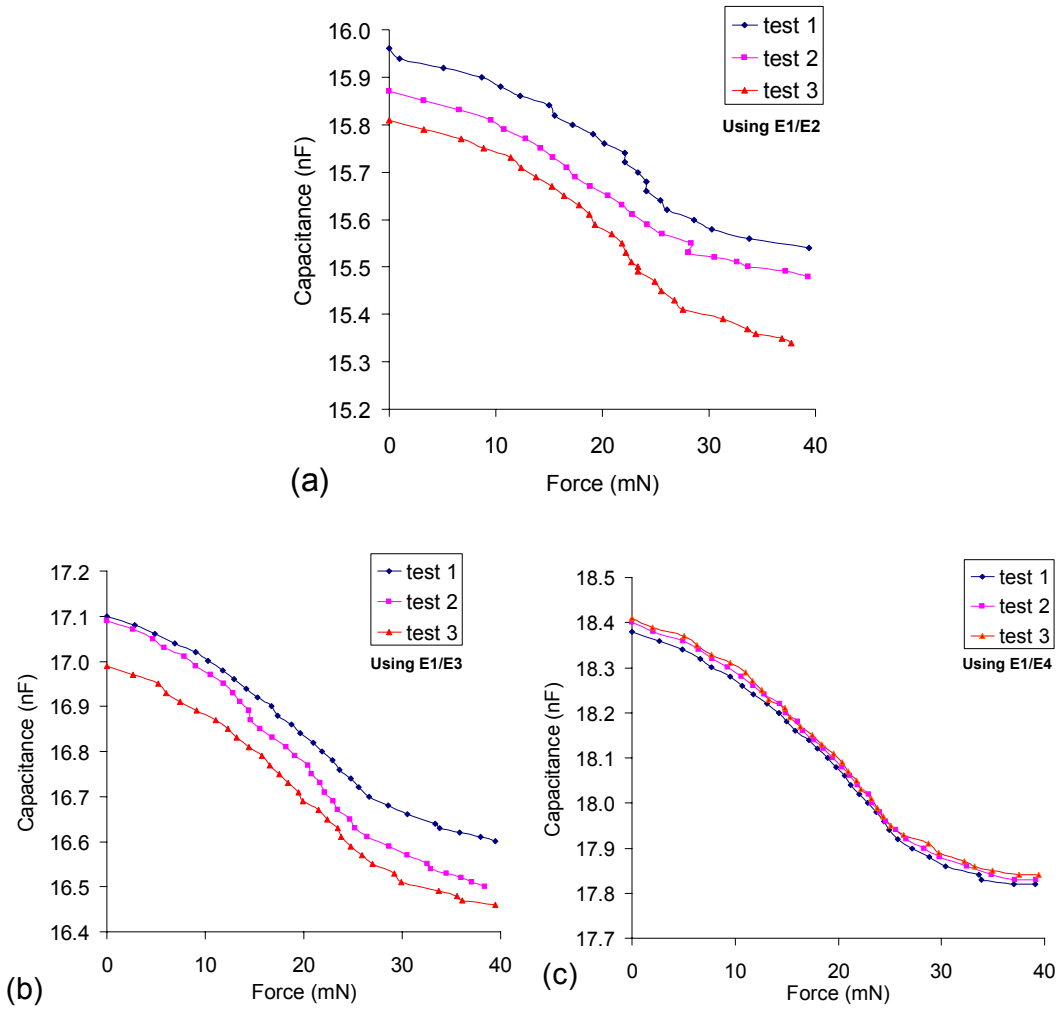

Figure 7-13 Triplicate experimental plots of capacitance *vs.* vertical impact force for ring electrode pairs on an implant electrode array. (a) E1/E2, (b) E1/E3 and (c) E1/E4.

The results shown in Figure 7-11 and Figure 7-13 demonstrated that this reduction in electrode surface area was detectable through capacitance measurements. The lack of reproducibility in capacitance measurements may be partially attributed to the fact that the cochlear implant was not designed for this purpose. It is possible that a partial redesign of the cochlear implant with capacitance measurements in mind may greatly improve reproducibility.

7.3.4 SIMULATED INSERTION

For the first trial using the ring electrode pair E1/E2, the combined plot of insertion force and capacitance in relation to the insertion depth is shown in Figure 7-14. When the implant progressed into the lumen of the cochlear replica without contact to the lumen wall (from 0 to 7.7 mm), the total resistive force reading was about 0 mN; however, it was observed that the capacitance increased slightly from 16.25 nF to about 16.46 nF. This might have been due to further wetting of the implant upon entry although it had been in the buffer solution for over 20 minutes prior to testing. From 7.7 to 8.6 mm insertion depth, the implant tip interacted with the outer wall of the lumen and started to bend. The total resistive force rapidly increased from 0 to 60 mN and the capacitance rapidly decreased from 16.46 to 16.33 nF. When the insertion depth was increased from 8.6 mm to 13.0 mm, the implant tip started to slide along the lumen wall. This caused the total resistive force to continuously increase from ~ 60 mN to ~ 90 mN and the capacitance to slightly increase from 16.33 nF to 16.38 nF. Presumably this is due to the temporary reduction of tip impact force during the progress of sliding (e.g. the temporarily reduced attachment of the tip to the wall of the lumen). From 13 to 20 mm insertion depth, the spiral shaped lumen progressively increased the curvature of the implant, forcing it to bend further in order to conform. The total force therefore rapidly increased from 90 mN to 480 mN and the capacitance rapidly decreased from 16.38 nF to 15.78 nF.

(A)

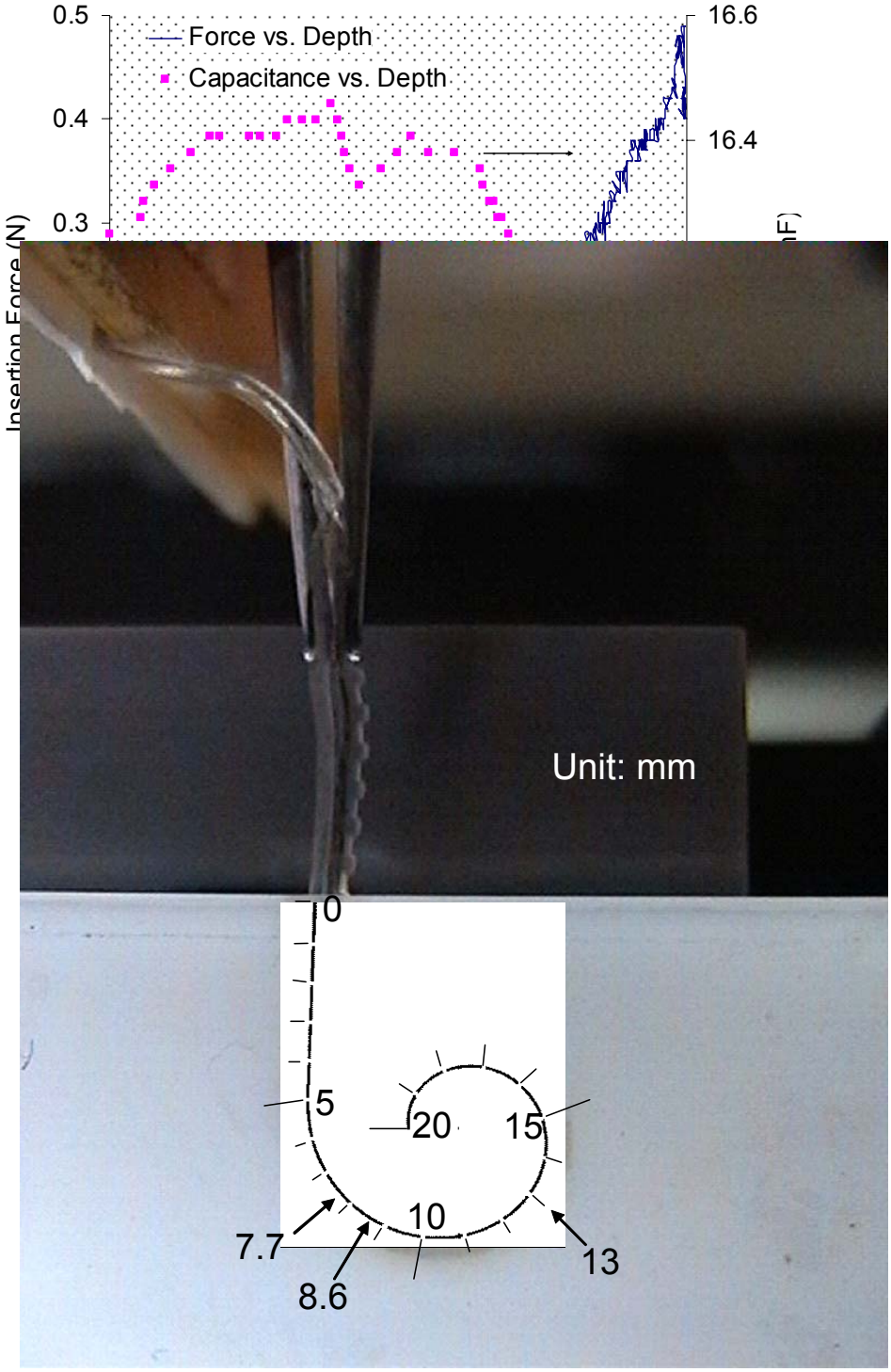

Figure 7-14 (A) Correlations between the insertion force, insertion depth and capacitance of a cochlear implant in a simulated insertion into a cochlear replica. A constant insertion speed of 1 mm.min^{-1} was used, (B) a diagram illustrating the relative insertion depth along the cochlear replica.

In another trial (Figure 7-15), the implant freely entered the lumen over an insertion depth of 0.0 mm to 6.7 mm. The total resistive force remained at around 0 mN and the capacitance increased from 17.49 nF to 17.77 nF. From 6.7 to 9.3 mm insertion depth, the implant was in contact with the side wall of the lumen, which is slightly earlier than that in the first trial, and slided in approximately 1 mm before reaching the bottom wall of the lumen and beginning to bend. The total resistive force increased from 0 to 70 mN and the capacitance initially slowly decreased from 17.77 nF to 17.73 nF during the 1 mm sliding period before rapidly decreasing to 17.37 nF until a depth of 9.3 mm was reached. The changes in capacitance occurred at a deeper insertion point than in the first trial, indicating that the curvature of bending was larger than that in the first trial. For the insertion depth of 9.3 mm to 11.9 mm, the implant started to slide along the lumen wall, however, due to the large degree of bending, the tip of the implant did not return back to closely contact the lumen wall and the total resistive force decreased slightly from 70 mN to ~ 59 mN and the capacitance rapidly increased to ~ 17.81 nF. From 11.9 to 17.8 mm insertion depth, the increased curvature of the spiral-shaped lumen forced the implant to bend further to conform. The total resistive force increased from 57 mN to 273 mN and the capacitance remained at ~ 17.81 nF with only a small amplitude of fluctuation. For depth of insertion between 17.8 mm and 20.0 mm, close to the centre of the spiral lumen with the highest curvature, the tip of the implant started to firmly contact the lumen wall, the insertion force continuously increasing to 450 mN from 273 mN and the capacitance decreasing from 17.81 nF to 17.66 nF.

(A)

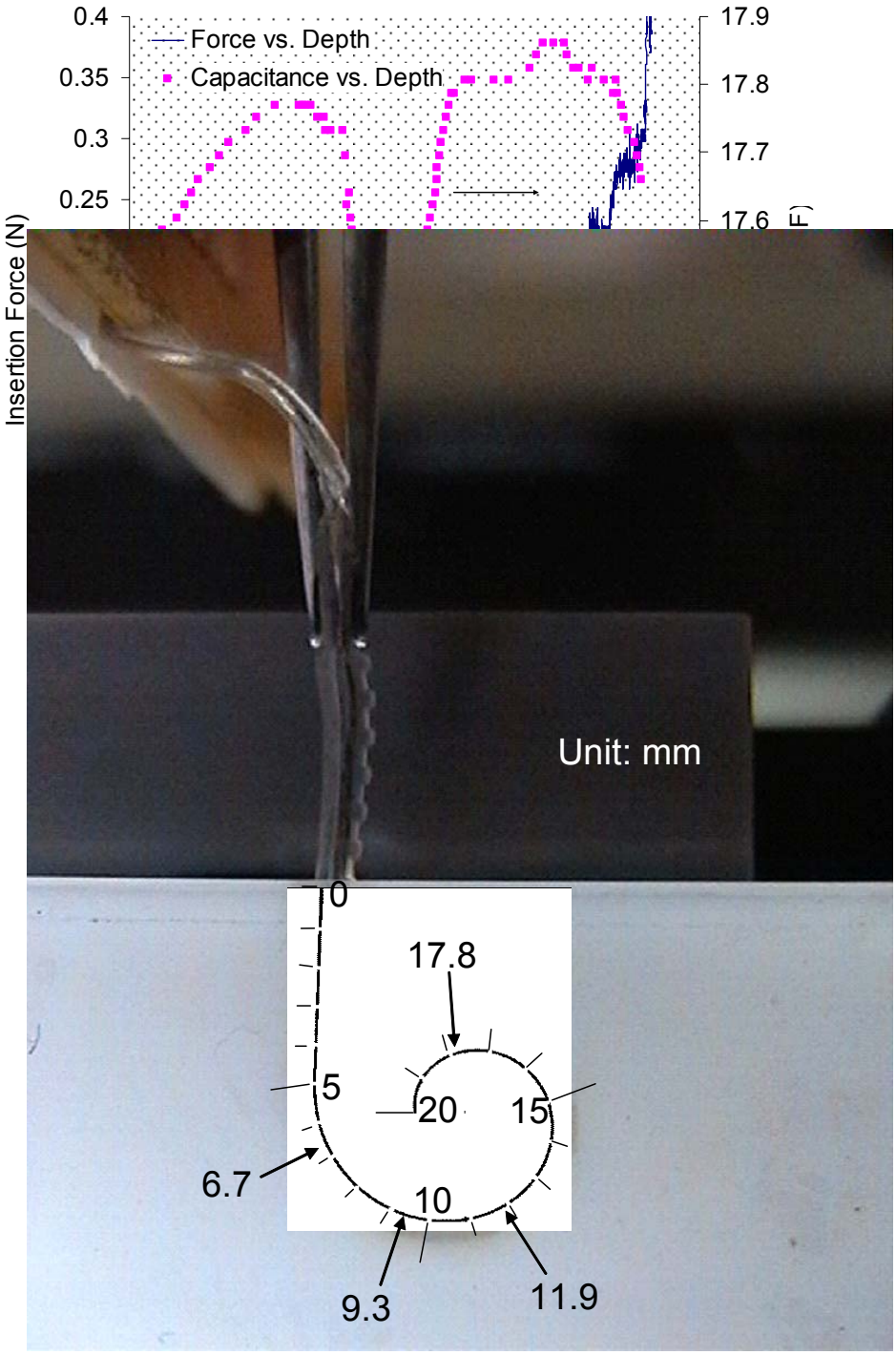

Figure 7-15 (A) Correlations between the resistive force, insertion depth and capacitance of implant E in a simulated insertion into a cochlear replica. A constant insertion speed of 1 mm.min^{-1} was used. (B) A diagram illustrating the relative insertion depth along the cochlear replica.

The insertion of a cochlear implant into a cochlear replica is a complicated process where various forces are encountered at various orientations to the implant body. Figures 7-14 and 7-15 show that the capacitance response curve did not always correlate to the total resistive force due to slight differences in the initial shape of the implant (straightened by a stylet) and orientation at entry into the cochlear replica. In general, three major stages of insertion have been proposed (Figure 7-16):

(1) The implant electrode is inserted into the straight part of the lumen of the cochlear replica, corresponding to an insertion depth of 0 mm to around 8 mm. Only a negligible friction force was encountered at this stage.

(2) The implant electrode begins to buckle as the lumen starts to curve and the tip of the electrode touches the bottom of the first turn. This stage corresponds to an insertion depth of 8 mm to 14 mm. The total resistance force increased to around 100 mN towards the end of this second stage.

(3) Further buckling of the implant electrode occurs and this stage corresponding to an insertion depth of 14 mm to 20 mm. The increased diameter of the electrode from the tip, the increased curvature of the lumen and the deeper insertion at this stage leads to a larger buckling force. The increase in insertion depth of the implant electrode in the lumen results in an increased frictional force against the sidewall of lumen.

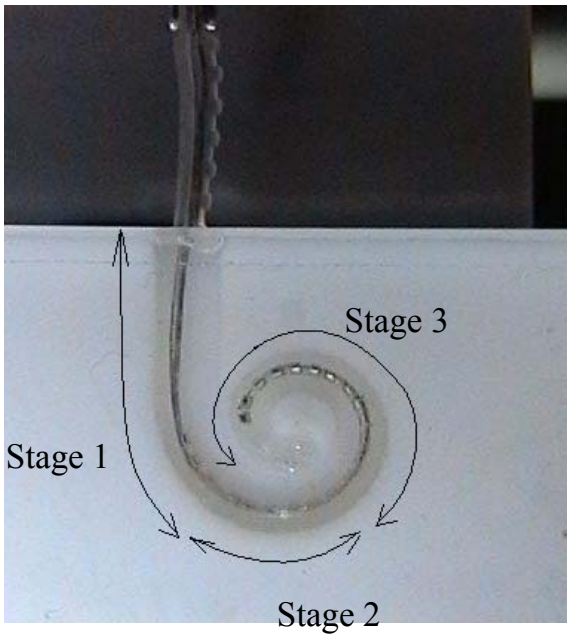

Figure 7-16. The three major insertion stages during implant insertion into a cochlear replica.

Significantly, this study revealed that the most surgically risky impact force, that is, at the first turn was detectable. Although such detection was largely qualitative, quantitative information would also be available if the electrodes of the implant could be redesigned for improved reproducibility.

7.3.5 INFLUENCE OF BUFFER COMPOSITION

Figure 7-17 shows that the impedance at 1000 Hz decreased from 7750 Ω to 7367 Ω in the first 6 minutes following transfer of the implant from the PBS buffer to the artificial perilymph. This change is quite significant because it is larger than the impedance change from 7280 Ω to 7438 Ω in response to a 40 mN standard impact force as shown previously in Figure 7-11.

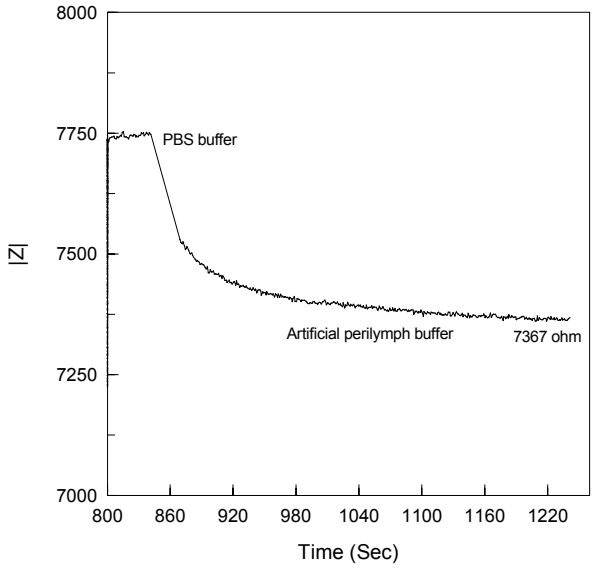

Figure 7-17 Impedance / time plot of a ring electrode transferred from PBS buffer to artificial perilymph at 1000 Hz. Impedance measured for one ring electrode at open circuit potential relative to Ag/AgCl.

If the ionic composition of a buffer is not constant, the most significant influence determining the effective surface area of an electrode is structural changes in the electrical double layer. The results in Figure 7-17 confirmed the effect of protein and amino acid adsorption by comparing PBS buffer solution and artificial perilymph solution. The adsorbed protein and amino acid from artificial perilymph solution may establish a more closely compacted anion layer on the electrode than a diffuse layer, which increased the electrical double layer capacitance. It has reduced the bulk impedance by more than 383 Ω, which was much larger than the 158 Ω increase in bulk impedance by the application of 40 mN force on the electrode tip as observed in Figure 7-11.

The effect of fluid composition may be problematic in relation to the application of this novel force transducer in an implant. To minimise the

effect of the buffer solution, two possible approaches were envisaged. Figure 7-18 shows the use of an additional pair of electrodes to compensate for the variations in ion composition. The #3 and #2 electrodes are purposefully designed, for which, their surface area is constant with respect to the impact force and the curvature change of the implant. Therefore, the difference in the capacitance per unit area between the electrode pairs of #3/#2 and #2/#1 would directly reflect the change of surface area at the electrode #1; hence, the correlated impact force on the tip or the curvature change of the implant.

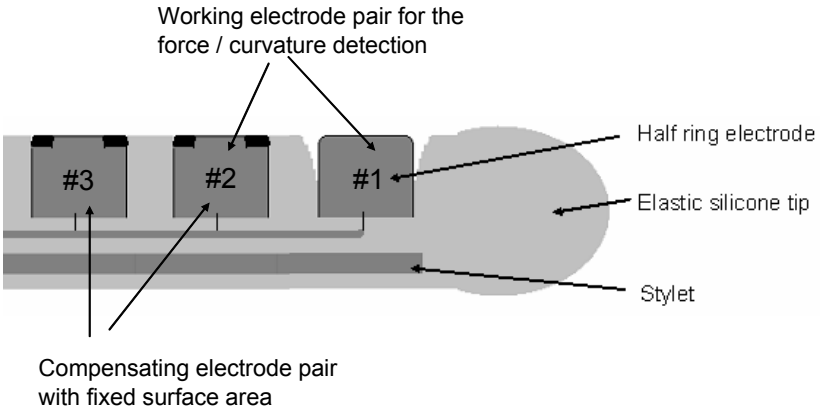

Figure 7-18 Schematic of a new cochlear implant electrode and the configuration of the ring electrodes showing the strategy for the compensation of ion compositional change.

Another possible approach is to deposit an extremely thin layer of a dielectrical insulation coating onto the electrode. The magnitude of the overall coating capacitance would be enough to measure; however, it would be 10% or less of the electrochemical double layer capacitance so that the influence of the buffer solution could be largely ignored. The capacitance in such a set-up is illustrated in Figure 7-19 where C_1 is the capacitance between the ring electrode and buffer solution separated by the thin

dielectical insulation layer and C_2 is the double layer capacitance of the buffer solution. The overall capacitance C_T of such a circuit would be given by Equation 7-4.

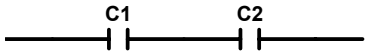

Figure 7-19 The equivalent circuit for the capacitance of a ring electrode with a thin layer non-conductive coating in buffer solution.

$$\frac{1}{C_T} = \frac{1}{C_1} + \frac{1}{C_2} \qquad \text{..... 7-4}$$

Equation 7-4 can be rearranged to give C_T as given in Equation 7-5.

$$C_T = \frac{C_1 C_2}{C_1 + C_2} \qquad \text{..... 7-5}$$

If C_1 is small (e.g. C_1 is 10% or less of C_2), then Equation 7-5 would simplify to Equation 7-6, where C_T essentially ignores the electrical double layer capacitance (C_2):

$$C_T = C_1 \qquad \text{..... 7-6}$$

Note that this dielectrical insulation coating should biologically degrade within several days to enable the use of the electrode for stimulation purposes.

Therefore, further development of the as-described force transducer using the cochlear implant ring electrode itself requires improvement of the structural consistency of the cochlear implant and modification of the electrode in order to achieve better detection performance. Currently the utilisation of cochlear implant ring electrodes to measure impact force during implant insertion may only be useful for surgical training purposes, where the liquid composition would be kept constant.

7.4 CONCLUSIONS

The results in this Chapter have shown the possibility of using the cochlear implant electrode array as an integrated force transducer. The study revealed that the impact force can exert an elastic compression force from the surrounding silicone rubber onto the ring electrode. This results in a reduction in the effective surface area, which can be measured in terms of the capacitance of the electrochemical double layer. The magnitude of the change in capacitance could therefore be used to measure the impact force during implantation.

Cyclic voltammetry showed that the ring electrode can be used as a common platinum electrode to probe solution electrochemistry. The impedance spectra confirmed the formation of an ionic double layer on the ring electrode. The impedance / time relationship observed at a fixed frequency of 1000 Hz indicated that the ring electrode needed to be soaked in buffer solution for at least 20 minutes prior to measurement to allow for equilibrium.

The strong correlation observed between the impact force on the array tip and impedance in the standard set-up was highly significant. A stable correlation was obtained for impedance measured at 1000 Hz perturbation in response to impact force, and similar trends were also obtained for capacitance measurements.

The insertion using a cochlear implant into a cochlear replica is a rather complicated process, in which, the forces encountered are not “standard”. The initial curvature of the implant electrode array, insertion orientation and tip positioning at the first turn of the cochlear replica were shown to result in very different insertion force profiles. The results demonstrated qualitatively that the most risky impact force at the first turn

during implantation could be detected. It demonstrates that an integrated force transducer could be used in a way that would make the surgical implantation of the cochlear implant safer for patients.

The composition of the buffer solution was shown to significantly affect the credibility of the measurement since the response due to the impact force was overwhelmed by the change in double layer capacitance. Therefore, constant buffer composition during the measurement is required. However, if the buffer composition could not be kept constant during measurement, possible solutions to this problem would include the use of an additional pair of electrodes to compensate the buffer composition change or a dielectrical insulation coating on the ring electrode.

Finally, it was proposed that the implant electrode array be redesigned to further explore the advantages of a self-monitoring implant with improved reproducibility.

7.5 REFERENCE

1. Cobbold, R.S.C. *Transducers for Biomedical Measurements: Principles and Applications*; John Wiley & Sons: Toronto, 1974; pp 175.
2. Warnick, A. and Drake, E.H., *IRE Nat. Conv. Record*, Pt. 9 (1958) 68-73.
3. Doebelin, E.O. *Measurement Systems: Application and Design*; McGraw-Hill: New York, 1966; pp 233-242.
4. Kapany, N.S. *Fiber Optics: Principles and Applications*; Academic: New York, 1967.
5. Lindstrom, L.H., *IEEE Trans. Bio-Med. Eng.*, BME-17 (July 1970) 207-219.
6. *The fibre optic sensor to measure blood pressure*; World Precision Instruments Ltd: Aston Stevenage. SG2 7EG. UK., 2005.
7. Sydenham, P.H., *J. Phys.*, E (5) (1972) 721-733.

8. Wolfendale, P.C.F., *J. Sci. Instrum.*, 1 (1968) 817-818.
9. *Semiconductor and Conventional Strain Gauges*; Academic: New York, 1962.
10. Geyling, F.T. and Forst, J.J., *Bell Syst. Tech.*, 39 (May 1960) 705-731.
11. Cobbold, R.S.C. *Transducers for Biomedical Measurements: Principles and Applications*; John Wiley & Sons: Toronto, 1974; pp 119.
12. Cobbold, R.S.C. *Transducers for Biomedical Measurements: Principles and Applications*; John Wiley & Sons: Toronto, 1974; pp 121.
13. *MIKRO-tip Catheter Transducer*; Millar Instruments, Inc., 2005.
14. Cobbold, R.S.C. *Transducers for Biomedical Measurements: Principles and Applications*; John Wiley & Sons: Toronto, 1974; pp 135.
15. Holbo, H.R., Miller, E.L. and Sidle, R.C., *Journal of Hydrology*, 79 (3-4) (1985) 311-318.
16. Revesq, G., *RE Trans. Ind. Electron., PGIE-7,*, (1958) pp. 11--16.
17. Horwood, E. *Instrumental methods in electrochemistry*; Southampton Electrochemistry Group, Halsted Press,: Chichester, New York :, 1985; pp p152.
18. Hibbert, D.B., Weitzner, K. and Carterb, P., *Journal of The Electrochemical Society*, 148 (1) (2000) E1-E7.
19. Briggs, R. and Saunders, E. *The Nucleus 24® Contour Electrode Array - A training guide*; Cooperative Research Centre for Cochlear Implant & Hearing Aid Innovation, 2002.
20. Hibbert, D.B., Weitzner, K., Tabor, B. and Carter, P., *Biomaterials*, 21 (21) (2000) 2177-2182.

CHAPTER 8 GENERAL CONCLUSIONS

This study aimed to develop sensors and actuators that could possibly be utilised in the cochlear implant. The devices developed included PPy mechanical sensors, PPy trilayer actuators, TITAN microfluidic pumps and PPy-coated hollow fibres for electrochemically controlled release. In addition, simple capacitive force sensors using the cochlear implant itself were also developed.

Studies into PPy mechanical sensors were described in Chapter 3, and a "stress induced ion flux" mechanism is proposed to explain the mechanically induced electrical signals in ICPs. Initial testing showed that the polarity of the voltage output was dependent on the dopant ion used. The amplitude of the voltage output was found to relate to the oxidation state and was also dependent on the concentration of mobile dopants within PPy. The "stress induced ion flux" model was further verified using different molar ratios of BMI.PF_6 in PC as the electrolyte to consider the situation where both cationic and anionic dopants were mobile and where the doping processes were competitive. As expected, when the molar concentration of BMI.PF_6 in PC changed from 1:10 to 10:1, a switch in the polarity of the voltage output was obtained, while a near zero voltage output was observed at the molar ratio of 1:1. A linear static displacement of PPy mechanical sensors of 0.65 $\mu C.mm^{-1}$ was demonstrated. Finally, further investigations into device miniaturisation and integration into the cochlear implant were suggested since the results obtained in this study have demonstrated the possibility of monitoring implant curvature changes during surgical insertion of the cochlear implant.

PPy trilayer bending actuators were also fabricated and tested (Chapter 4). A high amplitude harmonic vibration was obtained using a PPy/TFSI trilayer actuator. A plot of exerted force in response to a 1.0 V step potential showed that the time constant for response of a PPy/TFSI

actuator was much smaller (~ 0.47 s) than that using a PPy/PF_6 actuator (~ 0.76 s), indicating a more rapid actuation response. The study of blocking force showed that the maximum blocking force was proportional to the thickness of the PPy and the amplitude of the applied voltage when an organic salt dissolved in PC was used as the electrolyte. In comparison, when a pure ionic liquid (EMI.TFSI or BMI.PF_6) was used as the electrolyte, the blocking force was smaller and in the opposite direction, in agreement with a previously reported system involving cathodic expansion. Microanalysis of the PPy/PF_6 film when using BMI.PF_6 as the electrolyte showed the expulsion of the dopant anion (PF_6^-) after prolonged application of a reducing potential (- 0.8 V *vs.* Ag/Ag^+), which did not support the previously reported cathodic expansion phenomenon. It was suggested that switching from cathodic expansion initially to cathodic contraction may occur under reducing potentials depending on the amplitude and duration of the electrical stimulation. An ion diffusion controlled mechanism was proposed to explain this. Finally, the possibility of using PPy trilayer actuators to straighten the cochlear implant was evaluated. The results suggested that at their current stage of development, PPy trilayer actuators are not able to give a controlled steering of a Nucleus® 24 Contour™ electrode, however their use in thin film electrodes to be developed in the future might be possible.

An investigation into PPy-based microfluidic pumps led to the significant finding that the intrinsic resistance along a tubular PPy actuator can be used to induce a peristaltic actuation for fluid transport (Chapter 5). The construction of a novel "tube in tube actuator nodule" (TITAN) structure was undertaken. This structure consisted of a PPy-coated polyurethane thin film tube surrounded by another PPy film. Without the use of a valve, initial results based on the displacement of fluid showed that

a 3 cm TITAN micropump could reversibly transport 2.50 μL of fluid in 30 s at an applied voltage of only + 1.0 V, with an estimated power consumption of 8.7 mW. When the applied backpressure was raised from 0 to 50 mBar, the displaced volume decreased from 2.50 μL to 1.25 μL, with a corresponding ~ 30 % reduction in actuation strain being observed. The diameter of the internal wire and the circumferential strain of the actuation pump are of critical importance.

PPy-coated platinised PVDF hollow fibres were considered as novel drug reservoir devices for electrochemically controlled release of a model anion (Chapter 6). Results showed that without electrical stimulation, the release of the anionic dye species SB from PPy-coated hollow fibres was diffusion controlled at 0.018 $\mu g.min^{-1}$, while upon application of electrical stimulation, the release rate was dramatically increased to ~ 0.15 $\mu g.min^{-1}$. Such enhanced release could be switched on and off many times due to the very small decreases in the concentration of the anionic species SB in the internal reservoir. The controlled release of SB was believed to be due to the electrochemical switching properties of PPy, for which electrochemically activated incorporation / expulsion of small anions resulted in enhanced ion transport from the internal reservoir of the hollow fibre to the receiving solution. Such a mechanism was further verified by using the bulky anion DBSA in place of *p*TS as the dopant for PPy. With electrical stimulation, the use of DBSA in place of *p*TS inhibited the release of SB into the receiving solution and reduced the release rate from ~ 0.03 $\mu g.min^{-1}$ (using *p*TS dopant) to 0.006 $\mu g.min^{-1}$ (using DBSA dopant). The electrochemically controlled release of anions using a miniaturised "wire in fibre" two-electrode configuration was not successful and might have been due to an adverse ion migration effect and the loss of the precise control of potential. Finally, it was suggested that the PPy-coated platinised hollow PVDF fibres

are possibly well-suited for the release of electroinactive anionic drugs, where the release rate needs to be modulated frequently over relatively long time periods.

The study of a novel force sensor using the cochlear implant itself was described in Chapter 7. It was demonstrated that a stable correlation between electrode capacitance and impact force on the tip can be established over the range of 0 mN to 40 mN. This was the result of ring electrode surface area decrements due to increased coverage by the silicone body in which the ring electrodes are embedded upon the application of impact forces. In a simulated insertion test, the results suggested that the qualitative detection of impact force was possible; however, no stable correlation could be established since the orientations of the forces encountered were not "standard". Finally, it was considered that the development of future cochlear implant electrode arrays could provide a platform from which such a self-monitoring could become a reality.

In summary, several novel devices have been developed for possible use with the cochlear implant. However, due to limited time and resources, this study focused mainly on the structural novelty and the working mechanism of such devices, meaning that the integration of these devices into the cochlear implant and biocompatibility studies are left to future researchers.